THE UNIVERSITY OF CHICAGO

PHOTOSENSITIZING THE REVERSE WATER-GAS SHIFT REACTION

A DISSERTATION SUBMITTED TO

THE FACULTY OF THE DIVISION OF THE PHYSICAL SCIENCES

IN CANDIDACY FOR THE DEGREE OF

DOCTOR OF PHILOSOPHY

DEPARTMENT OF CHEMISTRY

BY

NATHAN TODD LA PORTE

CHICAGO, ILLINOIS

DECEMBER 2015

To my family

"On the arid lands there will spring up industrial colonies without smoke and without smokestacks; forests of glass tubes will extend over the plains and glass buildings will rise everywhere; inside of these will take place the photochemical processes that hitherto have been the guarded secret of the plants, but that will have been mastered by human industry which will know how to make them bear even more abundant fruit than nature, ***for nature is not in a hurry and mankind is****. And if in a distant future the supply of coal becomes completely exhausted, civilization will not be checked by that, for life and civilization will continue as long as the sun shines!"* −G. L. Ciamician, *Science* 36, 385-394 (1912)

Table of Contents

List of Figures vi
List of Tables x
List of Schemes xi
List of Equations xii
Acknowledgements xiii
Abstract xv
Chapter 1 Introduction 1
1.1 Background 1
1.2 Chapter Summary 5
1.3 References 8
Chapter 2 Electron-Transfer Sensitization of H_2 Oxidation and CO_2 Reduction Catalysts Using a Single Chromophore 11
2.1 Introduction 11
2.2 Experimental 12
2.3 Results and Discussion 20
2.4 Conclusion 37
2.5 References 38
Chapter 3 Photoinduced reductive trapping of carbon dioxide without a sacrificial electron donor 41
3.1 Introduction 41
3.2 Experimental 47
3.3 Results and discussion 54
3.4 Conclusion 77
3.5 References 78
Chapter 4 Dual photoredox sensitization of CO_2 and H_2 activating complexes in a self-assembled triad 81
4.1 Introduction 81
4.2 Experimental 85
4.3 Results 98
4.4 Discussion 111
4.5 Conclusion 115
4.6 References 116
Appendix A Crystal Structure of $[NEt_4][CpCr(CO)_3]$ 121
A.1 Experimental 121
A.2 Structure solution and refinement 121
A.3 References 128
Appendix B Crystal Structure of $[Co(HMD)(CH_3OH)][BF_4]_2 \cdot CH_3OH$ 129
B.1 Experimental 129
B.2 Structure solution and refinement 129
B.3 References 138
Appendix C Crystal structure of $[Pd(triphos)(CH_3CN)][BF_4]_2$ 139
C.1 Experimental 139
C.2 Structure solution and refinement 140

C.3 References 149
Appendix D Spectroelectrochemistry of $[NEt_4][Cp^*Cr(CO)_3]$ 150
D.1 Experimental 150
D.2 Results 150
D.3 References 151

List of Figures

Figure 1.1 The photodriven reverse water-gas shift reaction. 4

Figure 2.1 Schematic representation of the photodriven reverse water-gas shift reaction. 20

Figure 2.2 Electronic-absorption spectra of [NEt_4]**1a**, **2a**, and ZnTPP in DMF solution at room temperature. 23

Figure 2.3 Jablonski diagram showing intermolecular electron-transfer processes among ZnTPP, $\mathbf{1}^-$, and **2** initiated by excitation of the S_1 state of ZnTPP in DMF. Relative energies of redox states are determined from electrochemical data shown in Table 2.1. 24

Figure 2.4 Left: Fluorescence intensity of ZnTPP in THF as a function of the concentration of $1a^-$ (λ_{ex} = 567 nm). Right: Stern-Volmer analyses of the fluorescence lifetime of ZnTPP as a function of the concentration of $\mathbf{1}^-$ ($\mathbf{1a}^-$, THF, λ_{ex} = 595 nm; $\mathbf{1b}^-$, DMF, λ_{ex} = 558 nm). The lines are fits of the data to the equation $\tau_0/\tau = 1 + k_q\tau_0[\mathbf{1}^-]$. 26

Figure 2.5 Temporally integrated transient-absorption spectra of ZnTPP (0.07 mM; λ_{ex} = 558 nm) in the absence (Δt = 1−100 μs) and presence of $\mathbf{1a}^-$ (3.5 mM, Δt = 1−200 μs) in DMF solution. The smooth curve is the ground-state absorption spectrum of $ZnTPP^-$ (adapted from ref. [17]). 28

Figure 2.6 Temporally integrated transient-absorption spectra of ZnTPP (0.07 mM; λ_{ex} = 555 nm) in the absence (Δt = 1−100 μs) and presence of $\mathbf{1a}^-$ (4.6 mM, Δt = 1−200 μs) in THF solution. Also shown is the ground-state absorption spectrum of $ZnTPP^-$ in THF (determined by spectroelectrochemistry). 29

Figure 2.7 Quenching of the ZnTPP T_1 state by $\mathbf{1a}^-$ in DMF. Left: Transient-absorption kinetic profiles of the ZnTPP T_1 state (λ = 818 nm) with [$\mathbf{1a}^-$] = 0 and [$\mathbf{1a}^-$] = 0.46 mM. Right: Stern-Volmer analysis. 30

Figure 2.8 Left: Transient-absorption kinetic profile showing decay of photo-generated $ZnTPP^-$ (λ = 705 nm) via back electron transfer to **1a•** in DMF (λ_{ex} = 558 nm). Right: Second-order rate plot for these data. 32

Figure 2.9 Plot of $[ZnTPP^-]^{-1}$ versus time, showing the second-order back electron transfer between photogenerated **1b•** and $ZnTPP^-$. 32

Figure 2.10 Left: Temporally integrated transient-absorption spectra of $ZnTPP^-$ (λ_{ex} = 558 nm) in the absence (black, Δt = 1−100 μs) and presence of **2a** (red, [**2a**] = 0.6 mM, Δt = 80−7500 ns) in DMF solution. Right: Transient-absorption kinetic profile showing decay of photo-generated $ZnTPP^-$ (λ = 705 nm) via electron transfer to **2a** ([**2a**] = 0.6 mM) in DMF; the red curve is a single-exponential fit. Inset: Transient-absorption kinetic profile showing decay of photo-generated $ZnTPP^-$ (λ = 705 nm) via back electron transfer to **1a•** in DMF in the absence of **2a** (data from Figure 2.8). 34

Figure 2.11 Temporally integrated (Δt = 6−400 μs) transient-absorption spectrum of a mixture of ZnTPP (0.070 mM; λ_{ex} = 558 nm), $\mathbf{1a}^-$ (3.5 mM), and **2a** (2.4 mM) in DMF. The transient-

absorption bands of photogenerated $ZnTPP^-$ have completely decayed prior to this time window. The spectrum of $\mathbf{2a}^-$ (adapted from ref. [18]) is overlaid. 34

Figure 2.12 Decay rate of photogenerated $ZnTPP^-$ as a function of the concentration of **2** (see Figure 2.13); [ZnTPP] = 0.070 mM (**2a**, **2c**) and 0.140 mM (**2b**, **2d**), [$\mathbf{1a}^-$] = 3.7 mM (**2a**−**c**) and 3.5 mM (**2d**). The lines are fits of the data to the equation $1/\tau = A + k_{ET}[\mathbf{2}]$. 36

Figure 2.13 Plot of log k_{ET} vs ΔG for electron transfer from photogenerated $ZnTPP^-$ to **2a**−**d** in DMF. 36

Figure 2.14 Plot of $[\mathbf{2a}^-]^{-1}$ versus time, showing the second-order back electron transfer between photogenerated **1a•** and $\mathbf{2a}^-$. The red line is a linear fit to the data. 37

Figure 3.1 Photoreduction of CO_2 to CO, shown proceeding through a reductive quenching mechanism. 42

Figure 3.2 Schematic representation of the photocatalysed reverse water-gas shift reaction. 43

Figure 3.3 ORTEP drawings of crystal structure of $\mathbf{Co}^{2+}(CH_3OH)$. Structures are drawn with thermal ellipsoids at 40% probability. 54

Figure 3.4 Electronic absorption spectra of $\mathbf{Co}^+$ (prepared in situ by Na/Hg reduction of $\mathbf{Co}^{2+}$) in acetonitrile under various conditions. 57

Figure 3.5 Differential pulse voltammograms of $\mathbf{Co}^{2+}$ in DMF under CO_2 atmosphere, with 0.1 M $[^nBu_4N][PF_6]$ and other reagents as listed, referenced to the $Fc^{0/+}$ couple. 59

Figure 3.6 Cyclic voltammagrams of $\mathbf{Co}^{2+}$ in DMF under CO (green), CO_2 (blue), and N_2 (red) with 0.1 M $[^nBu_4N][PF_6]$, 70 mM pyrrolidine, 200 mM MeOH and 17 mM $Mg(ClO_4)_2$, with internal $FeCp^*_2$ (potential adjusted for reference to the $Fc^{0/+}$ couple). All CVs were acquired at a scan rate of 400 mV/s. 61

Figure 3.7 Stern-Volmer plot showing quenching of ZnTPP T_1 state by $\mathbf{Ni}^+$, in DMF with 3.1 mM $\mathbf{Co}^{2+}$. 63

Figure 3.8 *Top*: Transient-absorption spectrum (λ_{ex} = 547 nm) of solution of $\mathbf{Ni}^+$ ([$\mathbf{Ni}^+$] = 1.1 mM), $\mathbf{Co}^{2+}$ ([$\mathbf{Co}^{2+}$] = 3.1 mM), and ZnTPP in DMF containing 70 mM pyrrolidine under N_2 atmosphere. Spectra are integrated and averaged over the time ranges shown to allow intensities to be compared over different time windows. Spectrum from 20−40 μs magnified 10× to show faint band of Co^+. *Bottom*: Transient-absorption spectrum (λ_{ex} = 551 nm) of solution of $\mathbf{Ni}^+$ ([$\mathbf{Ni}^+$] = 1.2 mM), $\mathbf{Co}^{2+}$ ([$\mathbf{Co}^{2+}$] = 3.1 mM), and ZnTPP in DMF containing 70 mM pyrrolidine under 100% H_2 atmosphere. Spectra are integrated and averaged over the time ranges shown to allow intensities to be compared over different time windows. .. 65

Figure 3.9 Kinetic trace at 690 nm, showing decay of $\mathbf{Co}^+$. The black line is the fit of the data to a single exponential decay. 67

Figure 3.10 Transient-absorption spectrum (λ_{ex} = 551 nm) of solution of **Ni**$^{+}$ ([**Ni**$^{+}$] = 1.2 mM), **Co**$^{2+}$ ([**Co**$^{2+}$] = 3.1 mM), and ZnTPP in DMF containing 70 mM pyrrolidine under 28% CO_2 in H_2 atmosphere. Spectra are integrated and averaged over the time ranges shown to allow intensities to be compared over different time windows. 69

Figure 3.11 Energy-level diagram showing the possible decay pathways following S_1 excitation of ZnTPP in solution containing **Ni**$^{+}$ and **Co**$^{2+}$, with and without CO_2 present in the reaction atmosphere. 71

Figure 3.12 Transient-absorption spectrum (λ_{ex} = 547 nm) of solution of **Ni**$^{+}$ ([**Ni**$^{+}$] = 1.1 mM), **Co**$^{2+}$ ([**Co**$^{2+}$] = 3.1 mM), and ZnTPP in DMF under H_2 atmosphere. Spectra are integrated and averaged over the time ranges shown to allow intensities to be compared over different time windows. Spectrum from 20−40 μs magnified 10× to show faint band of **Co**$^{+}$. 73

Figure 4.1 Spectra (blue) and fits (red) for representative TA samples, corrected to 1 cm pathlengths, showing extent of ligation of **ZnP−Re**$^{+}$ by **W**. 91

Figure 4.2 Fits to the transient-absorption band of **1** at 594 nm (left) and 1297 nm (right) provided by global kinetic analysis of the spectrum (τ_{S1} = 106 ± 1 ps). Inset: Residuals from global fit. 92

Figure 4.3 Calculated (DFT) model structure of **ZnP−Re**$^{+}$. The average Zn−bpy(C) distance is 10.5 Å. Calculations performed in Gaussian 09[45] with the B3P86 functional and 6-31G* (H, C, N, O)[46,47] and LANL2DZ (Zn, Re)[48,49] basis sets. LANL2DZ effective-core potentials were used for Zn and Re.[48,49] 96

Figure 4.4 Jablonski diagram for **ZnP−Re**$^{+}$ (adapted from ref. [29]) 99

Figure 4.5 IR absorption spectrum of **ZnP−Re**$^{+}$ in CH_2Cl_2. 100

Figure 4.6 (a) TR-IR spectra of **ZnP−Re**$^{+}$ in CH_2Cl_2 solution (λ_{ex} = 565 nm, Q(0,0)). (b) Kinetic analyses of the bands at 2035 cm^{-1}, 2041 cm^{-1}, and 1945 cm^{-1}; the solid lines are fits to the data (open markers) (c) Kinetic analyses of the bands at 2035 cm^{-1} and 2012 cm^{-1}; the red lines are fits to the data (open markers). Data in purple is masked from the fit. 101

Figure 4.7 Electronic-absorption spectra of **ZnP−Re**$^{+}$ and its mixtures with 1% pyridine (quantitatively forming **Zn$_{py}$P−Re**$^{+}$) and 1.33 mM **W** (forming a 91:9 mixture of **1** and **ZnP−Re**$^{+}$) in CH_2Cl_2. Intensities are normalized to the peak of the Q(1,0) band. 105

Figure 4.8 Visible and near-IR transient-absorption spectrum of 1 in CH_2Cl_2 (λ_{ex} = 565 nm, Q(1,0), 89% selective excitation of 1 based on [**1**]:[**ZnP−Re**$^{+}$] = 78:22). Values of ΔA cannot be compared between spectra since they were recorded on different instruments with different laser powers. 107

Figure 4.9 (a) TR-IR spectrum of **1** in CH_2Cl_2 with 2 mM **W** (λ_{ex} = 565 nm, Q(1,0)). (b) Kinetic analyses of bands attributable to the **Re•** moiety. (c) Kinetic analysis of S_1 induced absorption feature in TRIR spectrum of 1. Data points go below ΔA = 0 due to overlap of this induced absorption and the ground state bleach. 108

Figure 4.10 Jablonski diagram for **1**, based on excited-state energies deduced from **W−ZnTPP** and $\mathbf{Zn_{py}P-Re^{+}}$,[9,29] color coded as follows: (black) states common to **W−ZnTPP** and $\mathbf{Zn_{py}P-Re^{+}}$; (blue) state of $\mathbf{Zn_{py}P-Re^{+}}$; (dark green) states of **W−ZnTPP**; (red) terminal photoproduct of 1. Rate constants measured in studies of **W−ZnTPP** and $\mathbf{Zn_{py}P-Re^{+}}$ are similarly color coded. Energies and rates were determined from experiments conducted in CH_2Cl_2 ($\mathbf{Zn_{py}P-Re^{+}}$, **1**) and fluorobenzene (**W−ZnTPP**). Shaded boxes indicate ranges of dπ* excited-state energies for coordinated **W**, as deduced previously.[41] Rates shown in red are calculated for **1** based on TA observations, as discussed in the main text..... 112

Figure A.1 ORTEP views of the two repeating subunits of the $[NEt_4][Cp^*Cr(CO)_3]$ crystal. Thermal ellipsoids are drawn at 35% probability. 123

Figure A.2 Depiction of the unit cell of $[NEt_4][Cp^*Cr(CO)_3]$..... 124

Figure B.1 ORTEP drawings of crystal structure of $[Co(HMD)(CH_3OH)][BF_4]_2$. Structures are drawn with thermal ellipsoids at 40% probability. 132

Figure B.2 Two space-filling views at different sides of the $[Co(HMD)(CH_3OH)][BF_4]_2$ molecule: Co green, N blue, O red 133

Figure B.3 Methanol molecule attached to a Co atom is also involved in further intermolecular H-bonding with another solvent methanol molecule. 134

Figure B.4 Depiction of the unit cell of $[Co(HMD)(CH_3OH)][BF_4]_2$. 135

Figure C.1 ORTEP drawings of crystal structure of $[Pd(triphos)(CH_3CN)][BF_4]_2$. Structures are drawn with thermal ellipsoids at 40% probability. 142

Figure C.2 Depiction of the unit cell of $[Pd(triphos)(CH_3CN)][BF_4]_2$. Two independent Pd-complexes, 4 $[BF_4]^-$ anions and 2 acetonitrile molecules are present in the unit cell. All disordered moieties are shown. 143

Figure D.1 Spectrum of $[Cp^*Cr(CO)_3]$ as potential is scanned across the $[Cp^*Cr(CO)_3]^{-/0}$ couple. 151

List of Tables

Table 2.1 Ground-State and Excited-State Redox Potentials and Electron-Transfer Reaction Free Energies for $\mathbf{1}^{-}$, **2**, and ZnTPP 25
Table 3.1 Redox potentials of ZnTPP, $\mathbf{Ni}^{+}$, and $\mathbf{Co}^{2+}$ in DMF with 0.1 M [$^{n}Bu_4N$][PF_6], referenced to the $Fc^{0/+}$ couple. Redox couples are reversible unless specified. 56
Table 3.2 Reduction potentials of $\mathbf{Co}^{2+}$ in DMF under CO_2 atmosphere unless otherwise specified, with 0.1 M [$^{n}Bu_4N$][PF_6], referenced to the $Fc^{0/+}$ couple. 60
Table 3.3 Driving forces in DMF (given in eV) for the electron transfer reactions shown 71
Table 3.4 Summary of bulk photolysis experiments using GC detection. Concentrations are given in mM, CO produced is given in μmols per 3.0 mL of headspace gas. Volume of solution photolyzed is 2.0 mL 76
Table 4.1 Excited-state energy levels for $\mathbf{ZnP{-}Re}^{+}$ with various ligands. 93
Table 4.2 Redox Potentials for Triad Compounds and Model Complexes 95
Table 4.3 Gibbs Free Energy for Photochemical Charge Separation and State Energy for Relevant Charge-Separated States. 96
Table 4.4 CO Stretching Frequencies of $[Re(bpy)(CO)_3L]^{n+}$ Compounds. 102
Table 4.5 Electronic Absorption Spectroscopic Data for $\mathbf{ZnP{-}Re}^{+}$, $\mathbf{Zn_{py}P{-}Re}^{+}$, and **1** 105
Table A.1 Crystal data and structure refinement for $[NEt_4][Cp^*Cr(CO)_3]$ 122
Table A.2 Bond lengths [Å] and angles [°] for $[NEt_4][Cp^*Cr(CO)_3]$. 125
Table B.1 Crystal data and structure refinement for $[Co(HMD)(CH_3OH)][BF_4]_2$. 131
Table B.2 Bond lengths [Å] and angles [°] for $[Co(HMD)(CH_3OH)][BF_4]_2$. 136
Table C.1 Crystal data and structure refinement for $[Pd(triphos)(CH_3CN)][BF_4]_2$. 141
Table C.2 Bond lengths [Å] and angles [°] for $[Pd(triphos)(CH_3CN)][BF_4]_2$. 144
Table C.3 Torsion angles [°] for $[Pd(triphos)(CH_3CN)][BF_4]_2$. 148

List of Schemes

Scheme 1.1 H_2 oxidation catalyst $\mathbf{1}^-$ and CO_2 reduction catalyst **2** 6
Scheme 1.2 H_2 oxidation catalyst $[Ni(P^{Cy}_2N^{tBu}_2)]^+$ and CO_2 reduction catalyst $[Co(HMD)]^{2+}$ 7
Scheme 1.3 Self-assembled triad consisting of a tungsten−benzylidyne H_2 oxidation catalyst and a $Re(bpy)(CO)_3$ CO_2 reduction catalyst assembled around a zinc tetraarylporphyrin..... 8
Scheme 3.1 Structures of the **HMD** ligand (as the diprotonated $\mathbf{H_2HMD^{2+}}$) and compounds $\mathbf{Ni^{n+}}$ and $\mathbf{Co^{n+}}$. 44
Scheme 3.2 Photoelectrochemical oxidation of H_2 by $\mathbf{Ni^+}$. Adapted from ref [19] 44
Scheme 3.3 Reduction of $\mathbf{Co^{2+}}$ in the presence of L and CO_2. 46
Scheme 3.4 Hypothesized stabilization of $\mathbf{(L)Co(CO_2)^+}$ by Mg^{2+}. 58
Scheme 4.1 Triad **1** and its components **W** and $\mathbf{ZnP{-}Re^+}$. 85
Scheme 4.2 Model compound WPh, used to determine redox potentials of compound **W**. 95

List of Equations

$\frac{d[ZnTPP^-]}{dt} = k_{FET}[\mathbf{2}][ZnTPP^-] + k_{BET}[\mathbf{1}\bullet][ZnTPP^-]$ Equation 2.1 18

$[ZnTPP^-] = [ZnTPP^-]_0 e^{-\frac{[\mathbf{2}]t}{\tau_{FET}}}$ Equation 2.2 18

$\Delta A = Be^{-\frac{t}{\tau_{obs}}} + C$ Equation 2.3 18

$\frac{1}{\tau_{obs}} = k_{FET}[\mathbf{2}]$ Equation 2.4 19

$\frac{\tau_0}{\tau} = 1 + \tau_0 k_q [Ni^+]$ (Stern-Volmer Equation) Equation 3.1 50

$\frac{1}{\tau} = C + k_q [Ni^+]$ Equation 3.2 50

$F(\lambda) = A\mathbf{1}(\lambda) + B\mathbf{2}(\lambda) + C\mathbf{3}(\lambda)$ Equation 4.1 90

$\Delta A(t) = A_{rise}(e^{-t/\tau_{rise}}) + A_{decay}(e^{-t/\tau_{decay}}) + A_0$ Equation 4.2 91

$\Delta A(t) = A_{S_1,background}(e^{-t/\tau_{S_1}}) + A_{S_1}(e^{-t/\tau_{decay}}) + A_0$ Equation 4.3 92

$\Delta G_{CS} = e[E_{ox} - E_{red}] - E_{00}$ Equation 4.4 94

$\Delta G_{CS} = e[E_{ox} - E_{red}] - \frac{e^2}{4\pi\varepsilon_0\varepsilon R_{WZn}} - \frac{e^2}{4\pi\varepsilon_0\varepsilon R_{ZnRe}} + \frac{e^2}{4\pi\varepsilon_0\varepsilon R_{WRe}} - E_{00}$ Equation 4.5 94

$k_{FRET} = \frac{9000\ln(10)\kappa^2\Phi_D J_F}{128\pi^5\eta^4 N_A \tau_D R_{DA}^6}$ Equation 4.6 96

$k_{FRET,DCM} = k_{FRET,tol}\frac{\eta_{tol}^4}{\eta_{DCM}^4}$ Equation 4.7 97

$k_{ET} = \sqrt{\frac{\pi}{\hbar^2\lambda k_b T}}|V|^2 e^{\frac{-(\Delta G^\circ + \lambda)^2}{4\lambda k_B}}$ Equation 4.8 97

$\lambda = \lambda_i + \lambda_o = \lambda_i + \frac{e^2}{4\pi\varepsilon_0}\left(\frac{1}{r} - \frac{1}{R_{CC}}\right)\left(\frac{1}{\eta^2} - \frac{1}{\varepsilon_s}\right)$ Equation 4.9 97

$k_q = \tau_{S_1}^{-1} - \tau_0^{-1}$ Equation 4.10 104

$\tau_{obs}^{-1} = \tau_{s_1}^{-1} - (k_{OxQ} + k_{FRET} + k_{RedQ})$ Equation 4.11 113

Acknowledgements

The path through graduate school winds and branches, and without a steadfast group of guides to see me through I would never have made it to the other side. First and foremost I owe thanks to my advisor, Prof. Michael Hopkins, for his patient guidance and intellectual stimulation during the course of my graduate work. Without him none of this would have been possible. I am also grateful to Profs. Richard Jordan, Dmitri Talapin, and Richard Schaller for serving on my thesis committee. I am indebted to Prof. Richard Dallinger and Dylan Lynch for their assistance with constructing the transient-absorption spectrometer used for the majority of this work, and to Prof. Richard Schaller for his assistance with the time-resolved spectrometers at the Center for Nanoscale Materials at Argonne National Lab. Working with the CNM is always a pleasure, in large part due to the hard work of Rich and his colleagues.

The other students in the Hopkins lab with whom I have overlapped have been invaluable friends and co-workers. I am particularly grateful for my collaborations with Davis "supposed to be here today" Moravec and Dan "Kat to my Bianca" O'Hanlon on the photophysics of porphyrins, and with Mark Westwood on the catalysis of hydrogen oxidation. The other members of the lab—Ben Lovaasen, Sarah Shaner, Cameron Iverson, Wayne Lau, Judith Kamm, Hunter Vibbert and Chris Hansen—made the lab a place I looked forward to spending time.

Without a supportive social environment I would never had had the emotional fortitude to make it through grad school. To Landon, James, Ken and the other members of the Lewis lab, lunch with you is the best part of every workday. To my friends who are not chemists, you have kept me grounded in something more closely resembling reality. To my family, you have supported and believed in me my entire life. To my son Cyrus, thank you for waiting until after my defense to be born. And finally, to my wife, Leah—words cannot adequately express how much your presence in my life has meant to me. Thank you for everything.

This research was supported by the U.S. Department of Energy, Office of Basic Energy Sciences, Solar Photochemistry Program, under Grant DE-FG02-07-ER15910. Ultrafast spectrometry was carried out at the Center for Nanoscale Materials at Argonne National Lab under user proposal CNM 33927. Fluorescence lifetime measurements were performed in the Institute for Biophysical Dynamics NanoBiology Facility, which is supported in part by NIH Grant 1S10RR026988-01. I was supported for three years by NSF GRFP Grant #DGE-0638477.

Abstract

Due to the ever-increasing global demand for energy and the looming disaster of climate change fueled by the increase in atmospheric carbon dioxide concentration, there is a pressing need for non-fossil-fuel energy sources. Among the renewable energy sources, solar energy presents the largest potential capacity, provided that it can be efficiently captured and stored for offline use. Storage of solar energy as a liquid fuel is attractive both in terms of energy density and as fuel source easily integrated into existing infrastructure. To this end, an artificial photosynthetic system must be developed that integrates the oxidation of water and the reduction of carbon dioxide. Photochemical integration of these two redox catalytic cycles is the problem at the heart of any solar fuel system.

The systems presented in this dissertation are homogeneous, integrated chromophore/two-catalyst systems that are thermodynamically capable of photochemically driving the energy-storing reverse water-gas shift reaction ($CO_2 + H_2 \rightarrow CO + H_2O$), where the reducing equivalents are provided catalytic oxidation of renewable H_2, a proxy for water. In this thesis, zinc tetraarylporphyrin, a broadly absorbing chromophore, is used as the photosensitizer. In Chapters 2 and 3, the systems described are freely dispersed in solution, while the system in Chapter 4 is based on self-assembly using rigid spacers with soft contacts.

Using time-resolved spectroscopic methods, a comprehensive mechanistic and kinetic picture of the photoinitiated reactions of these systems has been developed. It has been found that absorption of a single photon by a broadly absorbing zinc porphyrin sensitizes intercatalyst electron transfer to produce the substrate-active forms of each catalyst. The initial photochemical step in Chapters 2 and 3 is the heretofore unobserved reductive quenching of the low-energy T_1 state of ZnTPP. In Chapter 3, reductive binding of CO_2 by the sensitized form of the CO_2

reduction catalyst is observed under conditions that are catalytic for H_2 oxidation. Insights regarding the ability to tune the rates of charge separation and charge recombination for each system are discussed.

Chapter 1 Introduction

1.1 Background

At present, 87% of the energy used globally is generated by the combustion of fossil fuels.[1] In 2006, Nocera and Lewis estimated that global energy use would double in the period 2001 to 2050, from 13.5 to 27 TW.[2] By 2013, global energy use was estimated at 16.9 TW, confirming this growth trend.[1] At the same time, combustion of fossil fuels has caused atmospheric CO_2 levels to increase from around 280 ppm before 1850 to over 390 ppm in 2011.[3] This increase in CO_2 carries with it a variety of environmental consequences including ocean acidification and large-scale changes to the climate which will lead to decreased biodiversity, desertification of arable lands, a rise in the sea level due to melting of polar ice caps, and an increase in the rate of formerly rare severe weather events, wildfires, and other natural disasters.[3] The result will be an environmental and human disaster as natural food webs are disrupted, resource scarcity increases and populated coastal land is flooded or submerged.[3] This seemingly inexorable growth of global energy consumption and increased concern over its attendant environmental consequences has spurred considerable research into developing renewable energy sources.[4]

Among the alternative sources of energy to fossil fuels, including geothermal, tidal, hydroelectric, wind, biomass and solar energy,[3] only solar energy offers the capacity to meet the projected growth in energy demand.[2] Annual global insolation totals 120,000 TW,[2] meaning that all the energy needs for the coming centuries could be met by capturing the solar radiation falling on a very small fraction of the Earth's surface. However, simply using solar energy to generate electricity is not sufficient; in order to meet our energy needs during nighttime hours and in off-grid uses such as transportation, we require a means to store solar energy. The densest form of

energy that is compatible with our current energy-distribution infrastructure is some form of chemical fuel.[5] Among the potential feedstocks for these solar fuels, CO_2 is a desirable target because it is the end product of the combustion of fossil fuels. Thus, developing solar-driven mechanisms for chemically reducing CO_2 to energy-rich products holds the potential to recycle conventional fuels and mitigate their carbon impact.[6-10]

Numerous studies over the past 30 years have investigated homogeneous artificial-photosynthetic systems for CO_2 reduction, in which a photoexcited chromophore accomplishes the transfer of electrons from a source of reducing equivalents to a CO_2 reduction catalyst.[11-17] With very rare exceptions,[18] the reducing equivalents consumed in these photochemical CO_2 reduction reactions have been supplied by sacrificial electron donors. These reagents are employed because their prompt decomposition following photoinitiated oxidation suppresses unproductive back-electron-transfer pathways, which are generally fast compared to substrate transformation, and because their decomposition products can provide additional reducing equivalents needed for some CO_2 reduction reactions, thus circumventing the one-photon/one-electron limit of molecular photosensitizers. Offsetting these practical advantages, however, is the fact that the stoichiometric consumption of conventional sacrificial donors in these reactions negates their energy-storing potential. In order for homogeneous systems to drive CO_2 reduction reactions that store energy, these sacrificial reagents must be replaced by a second catalytic cycle that extracts the reducing equivalents from a renewable source.[19] In practice, the only sources of renewable reducing equivalents inexpensive and abundant enough to serve this purpose are water or hydrogen generated by water splitting.

The reverse water-gas shift reaction (RWGS), $CO_2 + H_2 \rightarrow CO + H_2O$, is an attractive target reaction as an entry point for CO_2 into a fuel-generating series of reactions. The reaction is

endothermic at room temperature, requiring 41.2 kJ/mol. Even at 700 K, the reaction is still endothermic, requiring 3.05 kcal/mol (K_{eq} = 0.11).[20] This reflects the extreme thermodynamic stability of the CO_2 molecule. Indeed, the water-gas shift reaction, run in its forward direction, is a principal commercial source of H_2 for ammonia synthesis, using CO produced by steam reforming of methane.[21] The majority of catalysis of the RWGS reaction has focused on using catalysts developed for the WGS reaction, and exploiting the increased favorability of the reverse reaction as temperature increases. Unfortunately, the catalysts typically employed for the reaction, usually Cu supported on alumina or silica, are optimized for stability at the lower temperatures of the WGS reaction, and rapidly deactivate at the higher temperatures required to shift the equilibrium towards CO + H_2O.[22] Addition of Fe has been shown to confer some stability to Cu catalysts, and noble metal catalysts on solid supports have been shown to be efficient, although their performance is highly dependent on the precursors used for their preparation. Moreover, in no case is the mechanism of heterogeneous catalysis of the (R)WGS reaction well-understood, and it is therefore difficult to selectively catalyze the production of CO.

A further advantage of the RWGS reaction is that the carbon-containing product, CO, can be converted into a wide range of industrially-useful compounds, such as long-chain hydrocarbons and alcohols, through the well-developed Fisher-Tropsch process. In addition, by utilizing H_2 as a source of reducing equivalents, the RWGS reaction also presents a solution to the problem of storing H_2 generated from water splitting. To date, no H_2-storage system, whether based on simple gas compression, adsorption onto porous molecular frameworks, or formation of hydride compounds, has come close to matching the energy density of hydrocarbon fuels.[23,24] Furthermore, liquid hydrocarbon fuels generated from CO_2 and H_2 (itself derived from water)

can easily replace oil-derived liquid fuels without significant modification to the distribution infrastructure already in place such as pipelines, fuel tanks, fueling stations and so forth.

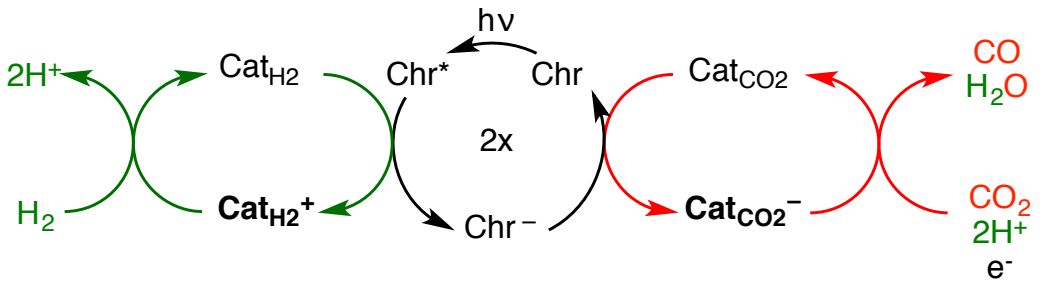

Figure 1.1 The photodriven reverse water-gas shift reaction.

Shown above in Figure 1.1 is a schematic representation of the the photodriven RWGS. An excited chromophore (Chr) is reductively quenched by an H_2 oxidation catalyst (Cat_{H2}), activating that catalyst towards H_2 binding and oxidation. The reduced chromophore (Chr^-) subsequently reduces a CO_2 reduction catalyst (Cat_{CO2}), activing that catalyst towards CO_2 binding and reduction and returning the chromophore to its ground state.

The crucial parameters that determine whether a system sensitized in this manner will be functional are the lifetime and yield of the doubly sensitized state, in which both catalysts have been activated for substrate binding and transformation. Both of these are determined by the competing kinetics of forward (productive) and back (or otherwise unproductive) electron transfer. Research into artificial photosynthetic systems has been directed at achieving rapid charge separation while reducing the rate of charge recombination. Many systems have been explored in which the chromophore, electron donor, and electron acceptor are covalently linked within a single supramolecular assembly, and the rates of charge separation and recombination are controlled by the geometric and electronic properties of the molecular linkages.[16,25-30] This approach allows for very precise tuning of the electron transfer kinetics, but frequently involve lengthy, low-yield synthetic pathways. In addition, replacement of any one component of the

system to tune its catalytic properties requires synthesis of an entire new supramolecular assembly.

In this dissertation, we explore several types of systems that offer potential advantages over a covalently linked donor-chromophore-acceptor triad. First, we hypothesized that under the right conditions, a system of freely diffusing components could be designed in which the kinetics of forward- and back-electron transfer could be controlled purely by the energetics of electron transfer. This system would offer the advantages of simple syntheses and the ability to replace each component individually if necessary. We also hypothesized that a system with rigid spacers could be designed in which the different components self-assemble into a triad of defined geometry. This system would offer the possibility of replacing one component of the system without repeating the entire synthesis, as well as the ability to tune the electron-transfer properties by changing the geometry of the system.

1.2 Chapter Summary

In Chapter 2 we present a proof-of-concept system that demonstrates for the first time that in a freely diffusing solution, a pair of catalysts can be sensitized by electron transfer initiated by the absorption of a single photon by a chromophore. Zinc tetraphenylporphyrin (ZnTPP) was chosen as the chromophore for a number of reasons: first, it exhibits strong absorptivity at long wavelengths, a useful property for capturing solar energy. Second, its excited and reduced states are well-characterized by spectroscopic methods and offer a facile probe of electron-transfer kinetics. Finally, the ZnTPP T_1 state, which is produced in high yield upon excitation, is both long-lived and high in energy, offering the possibility of high-yield electron transfer reactions from that state. The system in chapter 2 employs H_2 oxidation catalysts of the form $[Cp^RCr(CO)_3]^-$ (**1**$^-$, R = H, CH_3), and CO_2 reduction catalysts of the type Re(bpy-4,4′-

$R_2)(CO)_3Cl$ (**2**, R = H, Me, ^tBu, $COOCH_3$), as shown in Scheme 1.1. Upon excitation of the porphyrin, rapid reductive quenching of both the S_1 and T_1 excited states by $\mathbf{1}^-$ is observed, producing the porphyrin anion in nearly quantitative yield. The porphyrin anion is then observed to thermally reduce **2**. The rates for each electron transfer step, as well as for the back-electron transfer from $\mathbf{2}^-$ to **1•**, are found by transient-absorption spectroscopy and are observed to vary with the electrochemical driving force. This work represents the first time two redox catalysts have been observed to undergo photoinduced electron transfer in freely diffusing solution, and the first time reversible electron-transfer quenching of the ZnTPP T_1 state has been observed.

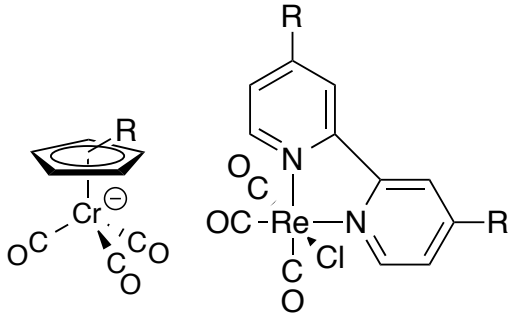

Scheme 1.1 H_2 oxidation catalyst $\mathbf{1}^-$ and CO_2 reduction catalyst **2**

The system in Chapter 3 expands on the system described in Chapter 2 by employing catalysts (shown in Scheme 1.2) with improved activity. The system incorporates the H_2 oxidation catalyst $[Ni(P^{Cy}_2N^{tBu}_2)]^+$ ($\mathbf{Ni^+}$), which has been shown to photocatalyze H_2 oxidation under the conditions of our experiments.[31] This catalyst is one of the the fastest-known electrocatalysts for H_2 oxidation and was chosen because its mechanism has been extensively characterized. As a CO_2 reduction catalyst, we chose $[Co(HMD)]^{2+}$ ($\mathbf{Co^{2+}}$), whose electrochemistry and CO_2-binding properties have been extensively investigated and whose different oxidation and substrate-bound states have been thoroughly spectroscopically characterized. This catalyst has been shown to reductively bind CO_2 extremely rapidly upon oxidation. Transient-absorption experiments under different gas mixtures observe the production

of reduced **Co**$^+$ in the absence of CO_2, and the trapping of **Co**$^+$ in the presence of CO_2. Electrochemical experiments suggest that a second reduction of the complex **Co**$^+$**−CO**$_2$ produces a **Co**$^+$**−CO**, which releases CO upon reoxidation. Bulk photolysis experiments show the production of subcatalytic amounts of CO.

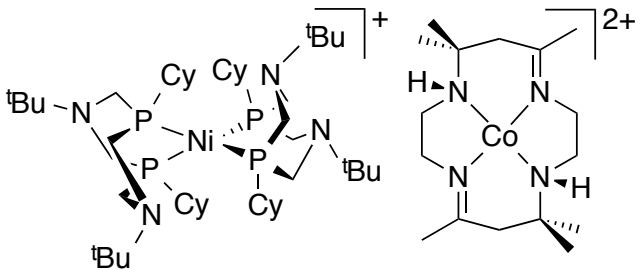

Scheme 1.2 H_2 oxidation catalyst $[Ni(P^{Cy}_2N^{tBu}_2)]^+$ and CO_2 reduction catalyst $[Co(HMD)]^{2+}$

The catalysts in Chapter 4 consist of a tungsten−benzylidyne H_2 oxidation catalyst **W** and a Re(bpy)(CO)$_3$L CO_2 reduction catalyst **Re**$^+$. Tungsten−benzylidynes have been investigated as ground- and excited-state strong electron donors, and in their oxidized forms they are capable of oxidizing H_2.[32] These catalysts self-assemble around a zinc tetraarylporphyrin using pyridyl linkers as shown in Scheme 1.3. Electron transfer is observed to proceed via oxidative quenching of the porphyrin by the appended **Re**$^+$ moeity, followed by thermal reduction of the porphyrin cation by the coordinated tungsten−benzylidyne. The lifetime of the charge-separated state is observed by time-resolved mid-IR experiments to be greater than 3.5 ns.

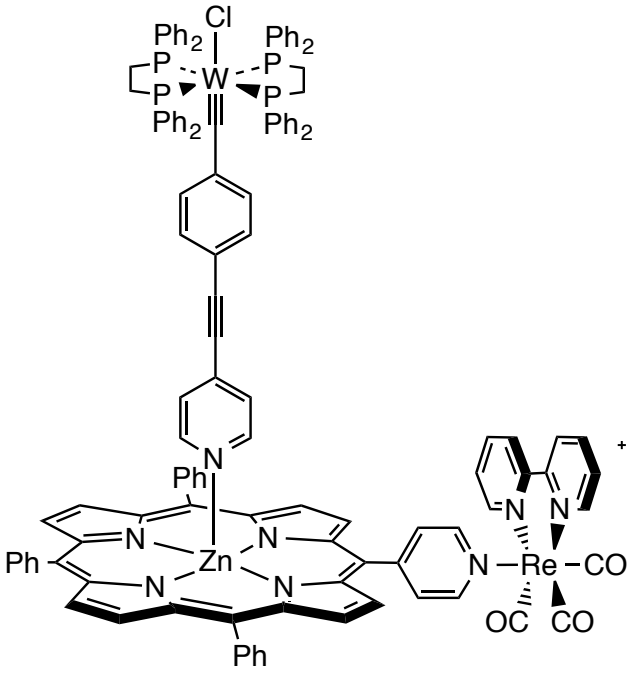

Scheme 1.3 Self-assembled triad consisting of a tungsten−benzylidyne H_2 oxidation catalyst and a Re(bpy)$(CO)_3$ CO_2 reduction catalyst assembled around a zinc tetraarylporphyrin

In the Appendices, crystal structures and spectral data for several of the catalysts employed in this work are presented. The structure of $[NEt_4][CpCr(CO)_3]$ is presented in Appendix A. The structure of $[Co(HMD)][BF_4]_2$, used to confirm the stereochemical conformation of the ligand, is presented in Appendix B. The structure of $[Pd(triphos)(CH_3CN)][BF_4]_2$ is presented in Appendix C. The spectroelectrochemically determined spectrum of the $[Cp^*Cr(CO)_3]$• radical is presented in Appendix D.

1.3 References

(1) BP In *BP Statistical Review of World Energy* 2014, p 1.

(2) Lewis, N. S.; Nocera, D. G. *Proc. Natl. Acad. Sci. U. S. A.* **2006**, *103*, 15729.

(3) *Climate Change 2014: Synthesis Report. Contribution of Working Groups I, II and III to the Fifth Assessment Report of the Intergovernmental Panel on Climate Change* 1ed.; Pachauri, R. K.; Meyer, L. A., Eds. Geneva, Switzerland, 2014.

(4) Faunce, T. *Aust. J. Chem.* **2012**, *65*, 557.

(5) Concepcion, J. J.; House, R. L.; Papanikolas, J. M.; Meyer, T. J. *Proc. Natl. Acad. Sci. U. S. A.* **2012**, *109*, 15560.

(6) Appel, A. M.; Bercaw, J. E.; Bocarsly, A. B.; Dobbek, H.; Dubois, D. L.; Dupuis, M.; Ferry, J. G.; Fujita, E.; Hille, R.; Kenis, P. J.; Kerfeld, C. A.; Morris, R. H.; Peden, C. H.; Portis, A. R.; Ragsdale, S. W.; Rauchfuss, T. B.; Reek, J. N.; Seefeldt, L. C.; Thauer, R. K.; Waldrop, G. L. *Chem. Rev.* **2013**, *113*, 6621.

(7) Cokoja, M.; Bruckmeier, C.; Rieger, B.; Herrmann, W. A.; Kühn, F. E. *Angew. Chem., Int. Ed.* **2011**, *50*, 8511.

(8) Mikkelsen, M.; Jørgensen, M.; Krebs, F. C. *Energ. Envir. Sci.* **2010**, *3*, 43.

(9) Saveant, J. *Chem. Rev.* **2008**, *108*, 2348.

(10) *Carbon dioxide as a chemical feedstock*; Aresta, M., Ed.; Wiley-VCH Verlag: Weinheim, Germany, 2010.

(11) Aresta, M.; Dibenedetto, A.; Angelini, A. *Philos. Trans. R. Soc. London, A* **2013**, *371*, 20120111.

(12) Barton Cole, E.; Bocarsly, A. B. In *Carbon dioxide as a chemical feedstock*; Aresta, M., Ed.; Wiley-VCH Verlag: Weinheim, Germany, 2010, p 291.

(13) Kumar, B.; Llorente, M.; Froehlich, J.; Dang, T.; Sathrum, A.; Kubiak, C. P. *Annual Review of Physical Chemistry* **2012**, *63*, 541.

(14) Morris, A.; Meyer, G.; Fujita, E. *Acc. Chem. Res.* **2009**, *42*, 1983.

(15) Reithmeier, R.; Bruckmeier, C.; Rieger, B. *Catalysts* **2012**, *2*, 544.

(16) Takeda, H.; Ishitani, O. *Coord. Chem. Rev.* **2010**, *254*, 346.

(17) Windle, C. D.; Perutz, R. N. *Coord. Chem. Rev.* **2012**, *256*, 2562.

(18) Ettedgui, J.; Diskin-Posner, Y.; Weiner, L.; Neumann, R. *J. Am. Chem. Soc.* **2010**, *133*, 188.

(19) Singh, W. M.; Pegram, D.; Duan, H.; Kalita, D.; Simone, P.; Emmert, G. L.; Zhao, X. *Angew. Chem., Int. Ed.* **2011**, *51*, 1653.

(20) Jacobs, G.; Davis, B. H.; Royal Society of Chemistry: Cambridge, 2007; Vol. 20, p 122.

(21) Crabtree, G. W.; Dresselhaus, M. S.; Buchanan, M. V. *Physics Today* **2004**, *57*, 39.

(22) Wang, W.; Wang, S.; Ma, X.; Gong, J. *Chem. Soc. Rev.* **2011**, *40*, 3703.

(23) Durbin, D. J.; Malardier-Jugroot, C. *Int J Hydrogen Energy* **2013**, *38*, 14595.

(24) Jena, P. *J. Phys. Chem. Lett.* **2011**, *2*, 206.

(25) Albinsson, B.; Mårtensson, J. *J. Photochem. Photobio. Rev. C* **2008**, *9*, 138.

(26) Artero, V.; Fontecave, M. *Chem. Soc. Rev.* **2013**, *42*, 2338.

(27) Balzani, V.; Credi, A.; Venturi, M. *Chem. Eur. J.* **2008**, *14*, 26.

(28) de la Torre, G.; Bottari, G.; Sekita, M.; Hausmann, A.; Guldi, D. M.; Torres, T. *Chem. Soc. Rev.* **2013**, *42*, 8049.

(29) Falkenström, M.; Johansson, O.; Hammarström, L. *Inorg. Chim. Acta* **2007**, *360*, 741.

(30) El-Khouly, M. E.; Wijesinghe, C. A.; Nesterov, V. N.; Zandler, M. E.; Fukuzumi, S.; D'Souza, F. *Chem. Eur. J.* **2012**, *18*, 13844.

(31) Westwood, M.; Hopkins, M. D. *in preparation* **2015**.

(32) Morales-Verdejo, C. A.; Newsom, M. I.; Cohen, B. W.; Vibbert, H. B.; Hopkins, M. D. *Chem. Commun.* **2013**, *49*, 10566.

Chapter 2 Electron-Transfer Sensitization of H_2 Oxidation and CO_2 Reduction Catalysts Using a Single Chromophore

2.1 Introduction

As discussed in Chapter 1, the photodriven reverse water-gas shift reaction (RWGS: $CO_2 + H_2O \rightarrow CO + H_2O$) represents one of the simplest artificial photosynthetic reactions. As shown in equations 1−3, H_2 is used as a source of reducing equivalents to reduce the carbon in CO_2, producing CO, while the protons produced by oxidation of H_2 balance the reaction by producing H_2O. Unlike photochemical reactions that consume sacrificial donors, this energy-storing system ($\Delta H_f = 41.2$ kJ mol^{-1})[1] catalytically extracts renewable reducing equivalents that can be sourced to water:

$$H_2 \rightarrow 2e^- + 2H^+ \quad (1)$$

$$CO_2 + 2e^- + 2H^+ \rightarrow CO + H_2O \quad (2)$$

$$CO_2 + H_2 \rightarrow CO + H_2O \quad (3)$$

A system which performs this reaction was reported by Neumann and co-workers. In their system the reducing equivalents are derived from the oxidation of H_2 by colloidal platinum, and CO_2 is reduced by a $[Re^I(phen)(CO)_3L]^+$ (phen = 1,10-phenanthroline) CO_2 reduction catalyst linked with a polyoxometalate cluster.[2] This system was the first report of homogenous molecular CO_2 reduction which did not employ a conventional sacrificial electron donor. However, the system presented is not amenable to enhanced understanding of the catalytic mechanism. There are few spectroscopic signatures for catalytic intermediates in the heterogeneous oxidation of H_2 on platinum, and the spectroscopy of the CO_2 reduction reaction was not explored. Nevertheless, this system proves the concept that two catalytic cycles can be integrated in a set of energy-storing photodriven redox reactions.

The mechanistic, thermodynamic, and kinetic integration of two catalytic cycles with a chromophore is a general challenge that cuts across homogeneous molecular approaches to forming solar fuels from CO_2 and H_2O. A photochemical system for the RWGS reaction that employed a homogeneous H_2O oxidation catalyst would both provide insights into the fundamental factors that govern this integration and opportunities to exert greater control over them than possible with heterogeneous catalysts. Motivated by these possibilities, this chapter reports the photochemistry of a fully homogeneous system comprised of a photosensitizer, CO_2-reduction catalyst, and H_2-oxidation catalyst that, upon excitation with long-wavelength light ($\lambda > 590$ nm), yields a product state thermodynamically capable of accomplishing the RWGS reaction. The system operates via reductive quenching of the low-energy T_1 excited state of the common chromophore zinc tetraphenylporphyrin (ZnTPP) by a compound of the form $Cp^RCr(CO)_3^-$ (**1**$^-$; Cp^R = η^5-cyclopentadienyl), followed by thermal electron transfer from the product $ZnTPP^-$ radical to a complex of the type $Re(bpy\text{-}4,4'\text{-}R_2)(CO)_3Cl$ (**2**; bpy = 2,2′-bipyridyl). The electron-transfer-sensitized radical products of these reactions—$Cp^RCr(CO)_3$ (**1**•) and $[Re(bpy\text{-}4,4'\text{-}R_2)(CO)_3Cl]^-$ (**2**$^-$)—can initiate the oxidation of H_2 and reduction of CO_2, respectively. The ligand substituents within each of these classes of compounds allow control over the driving forces and, thus, the rates of the productive (and unproductive) electron-transfer reactions available to the components. A comprehensive picture of the mechanism and kinetics of this system has been elucidated using time-resolved spectroscopic methods.

2.2 Experimental

2.2.1 General Procedures.

All experiments were performed at room temperature under a nitrogen atmosphere using standard Schlenk and glovebox techniques. Acetonitrile and THF used for electrochemical

experiments (HPLC grade, stored under nitrogen) were purified by passing them under nitrogen pressure through an anaerobic, stainless-steel system consisting of two 4.5 in. × 24 in. (1 gal) columns of activated A2 alumina.[3] THF for spectroscopic and photophysical measurements (Burdick and Jackson brand) was dried over 4A molecular sieves and then stored over NaK (1:2) alloy. Acetonitrile for photophysical measurements (Burdick and Jackson brand, photophysical grade) was refluxed over CaH_2, and then stored on 4A molecular sieves. DMF (Acros, peptide synthesis grade, free amine content < 0.001%) was dried over 4A molecular sieves. THF-d_8 (Cambridge Isotope Laboratories) was stored over NaK (1:2) alloy. CD_3CN and DMF-d_7 (Cambridge Isotope Laboratories) were stored over 4A molecular sieves. $[NBu^n_4]PF_6$ (Sigma-Aldrich, 98%) was recrystallized from methanol and dried under vacuum at room temperature. Ferrocene was recrystallized from 95% ethanol and then sublimed under vacuum. $[NEt_4][Cp^*Cr(CO)_3]$ ($[NEt_4]$**1a**),[4] $Re(bpy)(CO)_3Cl$ (**2a**),[5] $Re(bpy\text{-}4,4'\text{-}(CO_2Me)_2)(CO)_3Cl$ (**2b**),[6] $Re(bpy\text{-}4,4'\text{-}Bu^t_2)(CO)_3Cl$ (**2c**),[5] $Re(bpy\text{-}4,4'\text{-}(OMe)_2)(CO)_3Cl$ (**2d**),[5] and ZnTPP[7-9] were synthesized according to literature procedures. $[NEt_4][CpCr(CO)_3]$ ($[NEt_4]$**1b**) was synthesized analogously to $[NEt_4]$**1a**, replacing $Cp^*Cr(CO)_3H$ with $CpCr(CO)_3H$;[10] the ^{1}H-NMR spectrum of **1b**$^-$ matches that reported for samples prepared by alternative procedures.[11,12] All other reagents and solvents were obtained from commercial sources and used as received.

2.2.2 Crystal Structure of $[NEt_4]$1b

Crystals of $[NEt_4]$**1b** were grown under N_2 by cooling of a saturated acetonitrile solution to −30 °C overnight. Details of the crystal structure are given in Appendix A.

2.2.3 Supplemental NMR Data for Re(bpy-4,4′-$(CO_2Me)_2$)$(CO)_3Cl$ (2b).

δ (acetone-d_6): 4.06 (s, 6 H; COOC$\underline{H}_3$), 8.25 (dd, J_{56} = 5.7 Hz, J_{35} = 1.7 Hz, 2 H, 5,5′-bpy), 9.21 (dd, J_{35} = 1.7 Hz, J_{36} = 0.5 Hz, 2 H, 3,3′-bpy), 9.34 (dd, J_{56} = 5.7 Hz, J_{36} = 0.5 Hz, 2 H, 6,6′-bpy).

2.2.4 Electrochemical Measurements.

Cyclic-voltammetry experiments were performed at room temperature under a nitrogen atmosphere in a glovebox using a Bioanalytical Systems (BAS) 100 B/W Electrochemical Workstation and C3 cell stand. A three-electrode configuration was used, consisting of a Pt-disk working electrode (area = 0.2 cm^2), Pt-disk auxiliary electrode (area = 0.2 cm^2), and Ag-wire quasi-reference electrode. The electrodes were polished prior to each experiment. Samples consisted of 0.3−5.0 × 10^{-3} M analyte in THF or DMF containing 0.1 M [NBu^n_4][PF_6]. Cyclic-voltammetric experiments were conducted over a range of scan rates (0.05−0.40 V s^{-1}). Electrochemical data were analyzed using BAS 100W version 2.0 software. Ferrocene was used as an internal electrode-potential standard[13] for all compounds except [NEt_4]**1a** and [NEt_4]**1b**, for which it overlapped with an irreversible second oxidation. For these compounds the $CoCp_2^{+/0}$ couple (of [$CoCp_2$][PF_6]) was used as an internal electrode-potential standard[14]; relative to $FeCp_2^{0/+}$, the $CoCp_2^{+/0}$ couple was observed under our conditions at −1.35 V in THF and −1.33 V in DMF.

2.2.5 Optical spectroscopic samples

Solution samples for optical experiments were prepared on a vacuum line in sealable cuvettes; those for photophysical measurements were degassed by at least five freeze−pump−thaw cycles and sealed under purified nitrogen. Transient-absorption

spectroscopic experiments were performed using $\lambda \geq 670$ nm probe light to ensure that transient **1a•** and **1b•** were not irradiated, since they are reported to be photosensitive.[15]

2.2.6 Steady State Emission Spectroscopy

Emission spectra were recorded with a PTI Quantmaster fluorimeter equipped with Peltier-cooled R928 photomultiplier tube. The emission monochrometer was wavelength-calibrated using the emission lines of an Ar lamp; wavelength accuracy is < 0.5 nm over the entire detection range. The excitation monochrometer was wavelength-calibrated using the calibrated emission monochrometer. Emission intensities were corrected for instrument response using data supplied by PTI.

2.2.7 Fluorescence Lifetime Measurements

Fluorescence lifetimes were measured with a ChronosBH time-domain fluorometer (ISS, Inc.) using time-correlated single photon counting methods. The fluorometer contained Becker-Hickl SPC-130 detection electronics and an HPM-100-40 hybrid PMT detector. Tunable picosecond pulsed excitation (λ_{ex} = 595 nm) was provided by a Fianium SC400 supercontinuum laser source and integrated acousto-optic tunable filter. Emission wavelengths were selected with bandpass filters (641BP75 or 725BP150, Semrock and Chroma). The instrument response function was measured to be approximately 120 ps FWHM, using a 1% scattering solution of Ludox LS colloidal silica. Lifetimes were fit via a forward convolution method using the Vinci control and analysis software of the instrument.

2.2.8 Spectroelectrochemistry

Spectroelectrochemical measurements were performed on ZnTPP and [NEt_4]**1a** in THF using an optically transparent thin-layer electrochemical cell equipped with CaF_2 windows.[16] The electrode potential was controlled using the BAS 100B potentiostat described above. The applied

potential was ramped at a slow rate (1 mV s^{-1}) across the redox couple of interest, during which time spectra were recorded at regular intervals.

2.2.9 Nanosecond Transient-Absorption Spectroscopy

Excitation was provided by an integrated Nd:YAG−optical-parametric-oscillator pulsed laser (Opotek Vibrant 355 LD; 10 Hz, 10 ns pulse width, 0.5−1.5 mJ/pulse energy at the sample) that produced tunable output between 410−710 nm. The laser beam sent to the sample was not focused. The white-light probe was provided by a 75 W xenon lamp (PTI model A1010) that was passed through a 0-51 Schott filter (to remove much of the infrared radiation) and a 670 nm long-pass filter. The toroidal-shaped probe beam was focused onto the sample with a concave mirror; the transmitted light was focused onto the input slit of a monochromator (Horiba Scientific model iHR320) with a second concave mirror. Laser excitation was collinear with and counter-propagating to the probe beam, passing through holes in the centers of the concave mirrors (where the probe lamp intensity was zero); this allowed overlap of the laser and focused probe beams in the sample. The monochromator output was detected by a 6-stage Hamamatsu R928 PMT and processed with a digital oscilloscope (Tektronix model TDS 3032C). Transient decay traces at each wavelength were typically averaged for 512 laser pulses; these were analyzed to determine the transient lifetime and absorbance (ΔA). Automated data acquisition was controlled by LabView software. Electronic-absorption spectra recorded before and after transient absorption measurements indicated that all samples were photochemically stable.

2.2.10 ZnTPP S_1 Quenching Measurements.

The quenching of the S_1 state of ZnTPP by **1a**$^-$ (in THF) and **1b**$^-$ (in DMF) was studied by steady-state emission spectroscopy and fluorescence-lifetime measurements (Figure 2.4). Samples containing systematically varied concentrations of **1a**$^-$ (0−8 mM) or **1b**$^-$ (0−6.15 mM)

were prepared from a stock solution of ZnTPP ([ZnTPP] = 0.007 mM). The samples were excited in the ZnTPP Q band region, at which the $\mathbf{1}^-$ ions do not absorb (Figure 2.2).

2.2.11 ZnTPP T_1 Quenching Measurements.

The products and kinetics of the reductive quenching of the T_1 state of ZnTPP by $\mathbf{1}^-$, and of back electron transfer between $ZnTPP^-$ and **1•**, in DMF solution were examined by transient-absorption spectroscopy (λ_{ex} =558 nm, ZnTPP Q(1,0)) in the wavelength range 670−820 nm. Kinetic profiles for T_1 quenching were measured at 818 nm, which is the blue edge of an intense ZnTPP T_1 band at 840 nm. The lifetime of the T_1 state was determined as a function of the concentration of $\mathbf{1}^-$ ([$\mathbf{1a}^-$] = 0−0.56 mM; [$\mathbf{1b}^-$] = 0−0.65 mM) of samples prepared from a stock solution of ZnTPP in DMF ([ZnTPP] = 0.070 mM). The kinetics of back electron transfer between $ZnTPP^-$ and **1a•** were determined for a sample containing 0.070 mM ZnTPP and 3.7 mM $\mathbf{1a}^-$; the decay of the 705-nm TA band due to $ZnTPP^-$ was monitored.

2.2.12 ZnTPP S_1 Quenching Control Experiments with 2.

The possible quenching of the S_1 state of ZnTPP by **2a** in DMF was excluded by the observation that the fluorescence lifetime of ZnTPP ([ZnTPP] = 0.007 mM, λ_{ex} = 598 nm) is 1.94 ns in both the absence and presence of **2a** ([**2a**] = 0 and 5 mM). Similarly, S_1 quenching by **2b** in DMF was excluded by the observation that the fluorescence lifetime of ZnTPP ([ZnTPP] = 0.015 mM, λ_{ex} = 605 nm) of samples containing **2b** ([**2b**] = 0.43, 0.86, 1.7, and 3.5 mM) ranged from 1.90−1.93 ns, which is within experimental error of that found for ZnTPP under identical conditions (1.86 ns).

2.2.13 Kinetics of Electron Transfer reactions involving ZnTPP and 2a-d.

The products and kinetics of the reaction of $ZnTPP^-$ and **2a**−**2d** in DMF solution were studied using transient-absorption spectroscopy in the λ > 670 nm region. Samples contained

constant concentrations of ZnTPP and **1a**$^-$ ([ZnTPP] = 0.070 mM (**2a**, **2c**) or 0.140 mM (**2b**, **2d**); [**1a**$^-$] = 3.7 mM (**2a**–**2c**) or 3.5 mM (**2d**)) and varied in concentration of **2**. The samples were excited at 558 nm (**2a**, **2c**) or 598 nm (**2b**, **2d**). The ZnTPP$^-$ ion, formed via reductive quenching of the ZnTPP T_1 state by **1a**$^-$**,** exhibits a characteristic band at 705 nm, which was monitored to obtain kinetic information.

The rate of oxidation of ZnTPP$^-$ by **2** was monitored by observation of the transient-absorption band of ZnTPP$^-$ at 705 nm (see Figure 2.5). The consumption of ZnTPP$^-$ is governed by the following rate law:

$$\frac{d[ZnTPP^-]}{dt} = k_{FET}[\mathbf{2}][ZnTPP^-] + k_{BET}[\mathbf{1}\bullet][ZnTPP^-] \qquad \text{Equation 2.1}$$

where k_{FET} is the rate of electron transfer from ZnTPP$^-$ to **2** and k_{BET} is the rate of back electron transfer from ZnTPP$^-$ to **1**•. In these experiments [**1**•] = [ZnTPP$^-$] ≅ 8 μM, based on the observation of $\Delta A_{705nm} \cong 0.1$ at t = 0, the first data point after the laser flash (ε_{705nm} = 12000 M^{-1} cm^{-1} for ZnTPP$^-$ in DMF).[17] The concentration of **2** was varied from 0.12 to 3.6 mM (see Figure 2.12); therefore, the assumption [**1**•] ≪ [**2**] is valid. In the limit $k_{FET} \approx k_{BET}$, the rate expression simplifies to:

$$[ZnTPP^-] = [ZnTPP^-]_0 e^{-\frac{[\mathbf{2}]t}{\tau_{FET}}} \qquad \text{Equation 2.2}$$

where $\tau_{FET} = k_{FET}^{-1}$ and $[ZnTPP^-]_0$ is the concentration of ZnTPP$^-$ at t = 0. To fit the observed decay traces, we substitute ΔA for [ZnTPP$^-$], B for $[ZnTPP^-]_0$, τ_{obs} for $[B]/\tau_{FET}$ and add a baseline correction term C, to give:

$$\Delta A = Be^{-\frac{t}{\tau_{obs}}} + C \qquad \text{Equation 2.3}$$

The decay kinetics of $ZnTPP^-$ were determined at several wavelengths between 690−720 nm, with the fits sharing the term τ_{obs} and fitting A, B and C as unshared coefficients.

The electron-transfer rate between $ZnTPP^-$ and **2** (k_{FET}) was determined from the relationship between τ_{obs} and the concentration of **2** using the expression:

$$\frac{1}{\tau_{obs}} = k_{FET}[\mathbf{2}] \qquad \text{Equation 2.4}$$

The decay kinetics of $ZnTPP^-$ at the highest achievable concentrations of **2d** did not conform to a single-exponential function, due to the fact that under these conditions the oxidation of $ZnTPP^-$ by **2d** is not faster than that by **1a•** (for which the decay obeys second-order kinetics, vide supra). Therefore, values of $t_{1/2}$ were estimated as being the decay times at which $\Delta A(ZnTPP^-)$ was one-half of the initial value; these are used in place of τ_{obs} in the Stern-Volmer analysis (see Figure 2.12).

2.2.14 Kinetics of Electron Transfer between 2^- and 1a•.

. Electron-transfer kinetics between $\mathbf{2a}^-$ and **1a•** were monitored in a separate experiment using the same samples and excitation conditions, but in which the 670-nm cut-off filter on the probe beam was removed to allow monitoring of the 505-nm band of $\mathbf{2a}^-$.

Both $\mathbf{2a}^-$ and **1a•** absorb in the region 450−550 nm. The spectrum of $\mathbf{2a}^-$ (Figure 2.11) exhibits a band at 505 nm (ε = 5700 M^{-1} cm^{-1}).[18] Spectroelectrochemical measurements of **1a•** (Appendix D) show a broad band from 450−550 nm with ε = 600 M^{-1} cm^{-1}. Therefore, the transient concentration of each species was found by dividing ΔA at 505 nm by the sum of the two extinction coefficients. Since [**1a•**] = [$\mathbf{2a}^-$] under the conditions of the experiment, the ordinate axis of Figure 2.14 represents the reciprocal concentrations of $\mathbf{2a}^-$ and of **1a•**.

2.3 Results and Discussion

2.3.1 Design Criteria.

Shown in Figure 2.1 is a general scheme for accomplishing the RWGS reaction via photochemical electron-transfer sensitization of H_2-oxidation (Cat_{H2}) and CO_2-reduction catalysts (Cat_{CO2}) by a chromophore (Chr). This scheme imposes a number of fundamental and practical constraints on the components of the system, which are described here in order to explain the particular chromophore and catalysts chosen for the present study. These constraints include the obvious thermodynamic requirements for the pairs of chromophore−catalyst electron-transfer reactions, and that the pK_as of catalyst intermediates must be matched such that there is a Brønsted conjugate acid−base pair that can transfer protons from the H_2 oxidation cycle to the CO_2 reduction cycle. In addition, the excited chromophore should react by electron transfer with only one of the two catalysts (here, Cat_{H2}) to ensure unidirectional operation of the overall cycle (Figure 2.1), and possess lower-energy photoactive excited states than those of the catalysts to prevent chromophore→catalyst energy transfer. Finally, the catalysts should be sensitized by one-electron-transfer reactions to be commensurate with the intrinsic one-electron processes of the chromophore.

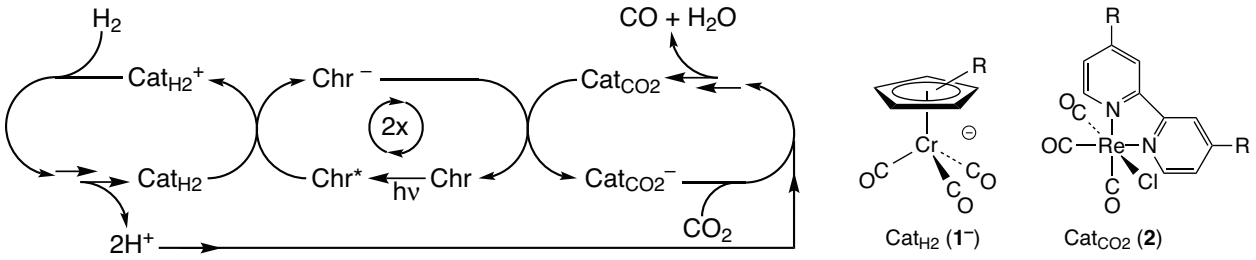

Figure 2.1 Schematic representation of the photodriven reverse water-gas shift reaction.

Among catalysts that accomplish the two-electron reduction of CO_2 to CO, there is extensive precedent that under photochemical conditions rhenium(I) compounds of the form $[Re(bpy\text{-}R)(CO)_3L]^{n+}$ (bpy-R = substituted bipyridine or related diimine ligand; L = anionic (*n* =

0) or neutral (n = 1) ligand) activate CO_2 via one-electron-reduced species.[19] The initial reduced rhenium products are ligand-localized radicals of the type $[Re(bpy\text{-}R\bullet)(CO)_3L]^{(n-1)+}$; these undergo a series of subsequent steps, beginning with dissociation of L, that lead to the activation of a CO_2 molecule by two one-electron-reduced rhenium compounds through substrate-bridged intermediates.[19-24] The catalysts used in the present study ($Re(bpy\text{-}4,4'\text{-}R_2)(CO)_3Cl$: R = H (**2a**), Bu^t (**2c**), CO_2Me (**2b**), OMe (**2d**))[5,25-27] were selected because their one-electron reduction potentials span a range where sensitization by the reduced chromophore will be thermodynamically downhill or uphill, facilitating mechanistic interpretation.

Molecular catalysts for H_2 oxidation may be divided into two mechanistic classes: those with metalloradical active states that homolytically cleave H_2 via a termolecular process;[28] and hydrogenase-inspired catalysts that heterolytically activate H_2 at a closed-shell metal center with assistance of a second-coordination-sphere Brønsted base.[29] Although the hydrogenase-inspired catalysts exhibit faster rates for H_2 activation, their catalytic cycles involve three metal oxidation states. In contrast, catalysts with metalloradical active states cycle through two oxidation states and, thus, can potentially be activated by a single photoinduced electron-transfer reaction. The most extensively studied of these catalysts are of the form $[Cp^RCr(CO)_3]^-$, which participate in the following set of the cycle of reactions:

$$[Cp^RCr(CO)_3]^- (\mathbf{1}^-) \rightarrow [Cp^RCr(CO)_3]\bullet (\mathbf{1}\bullet) + e^- \qquad (4)$$

$$[Cp^RCr(CO)_3]\bullet + \tfrac{1}{2}\, H_2 \rightarrow Cp^RCr(CO)_3H (\mathbf{1H}) \qquad (5)$$

$$Cp^RCr(CO)_3H + \text{base (B:)} \rightarrow [Cp^RCr(CO)_3]^- + BH^+ \qquad (6)$$

where Reaction 5 is a composite of two steps ($\mathbf{1}\bullet + H_2 \rightarrow \mathbf{1}(H_2)$; $\mathbf{1}(H_2) + \mathbf{1}\bullet \rightarrow 2\ \mathbf{1H}$).[28] The derivatives $[Cp^*Cr(CO)_3]^-$ ($\mathbf{1a}^-$) and $[CpCr(CO)_3]^-$ ($\mathbf{1b}^-$) were selected for this study because the Cp^R substituents provide suitable oxidation potentials and pK_as for the relevant

intermediates.[30] Further, the deprotonation step that completes the H_2 activation cycle (Reaction 6) can be accomplished with alkoxide bases such as $^tBuO^-$;[4] the alcohol conjugate-acid products of this step are known to be suitable proton sources for the reduction of CO_2 to CO by rhenium catalysts of type **2**.[31]

In their d^6 configurations, the $[Cp^RCr(CO)_3]^-$ ($\mathbf{1}^-$) ions and Re(bpy-4,4′-R_2)$(CO)_3Cl$ (**2**) compounds are unreactive with each other and toward their respective H_2 and CO_2 substrates; this constitutes the resting state of the system (Figure 2.1). A chromophore that meets the thermodynamic criteria for photosensitized electron transfer between these catalysts ($\mathbf{1}^- + \mathbf{2} \rightarrow \mathbf{1}\bullet + \mathbf{2}^-$), producing their substrate-active forms, is zinc tetraphenylporphyrin (ZnTPP). The electronic-absorption spectra of ZnTPP, $\mathbf{1a}^-$, and **2a** (Figure 2.2) show that their bands are arrayed in energy such that in mixtures of the compounds excitation into the porphyrin Q bands (λ_{ex} = 500−625 nm) will selectively produce the S_1 excited state of ZnTPP; further, their relative excited-state energies exclude the possibility of energy-transfer processes. The typically employed S_1 excited state of ZnTPP is too short lived ($\tau \cong 2$ ns) to allow efficient bimolecular photochemistry at typical catalyst concentrations, but the lower-energy T_1 state is very long lived (E = 1.59 eV, $\tau \cong 1.5$ ms)[32,33] and is thermodynamically capable of being reductive quenched by $\mathbf{1}^-$ ions but not of being oxidatively quenched by **2** (Table 2.1). Thus, ZnTPP meets the criteria of photosensitizing the electron-transfer reaction $\mathbf{1}^- + \mathbf{2} \rightarrow \mathbf{1}\bullet + \mathbf{2}^-$ by a single mechanism without short-circuiting or energy-transfer reactions. Additionally, the fact that ZnTPP is neutral eliminates ion pairing of transient redox species that could accelerate unproductive back electron transfer reactions.

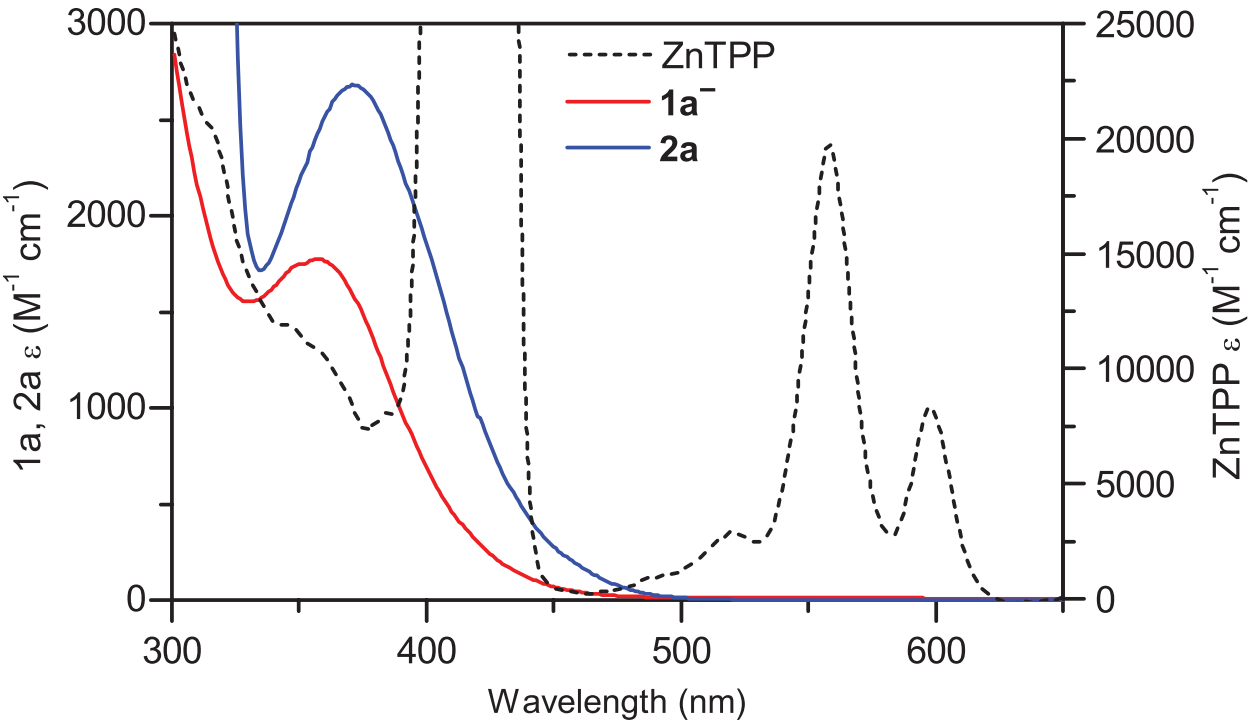

Figure 2.2 Electronic-absorption spectra of [NEt_4]**1a**, **2a**, and ZnTPP in DMF solution at room temperature.

The relative energies of the ZnTPP excited states and the chromophore/catalyst redox states are shown in Figure 2.3. In this figure, the possible reaction pathways following excitation of the S_1 excited state are labeled *a* through *g*. These processes are discussed in order below.

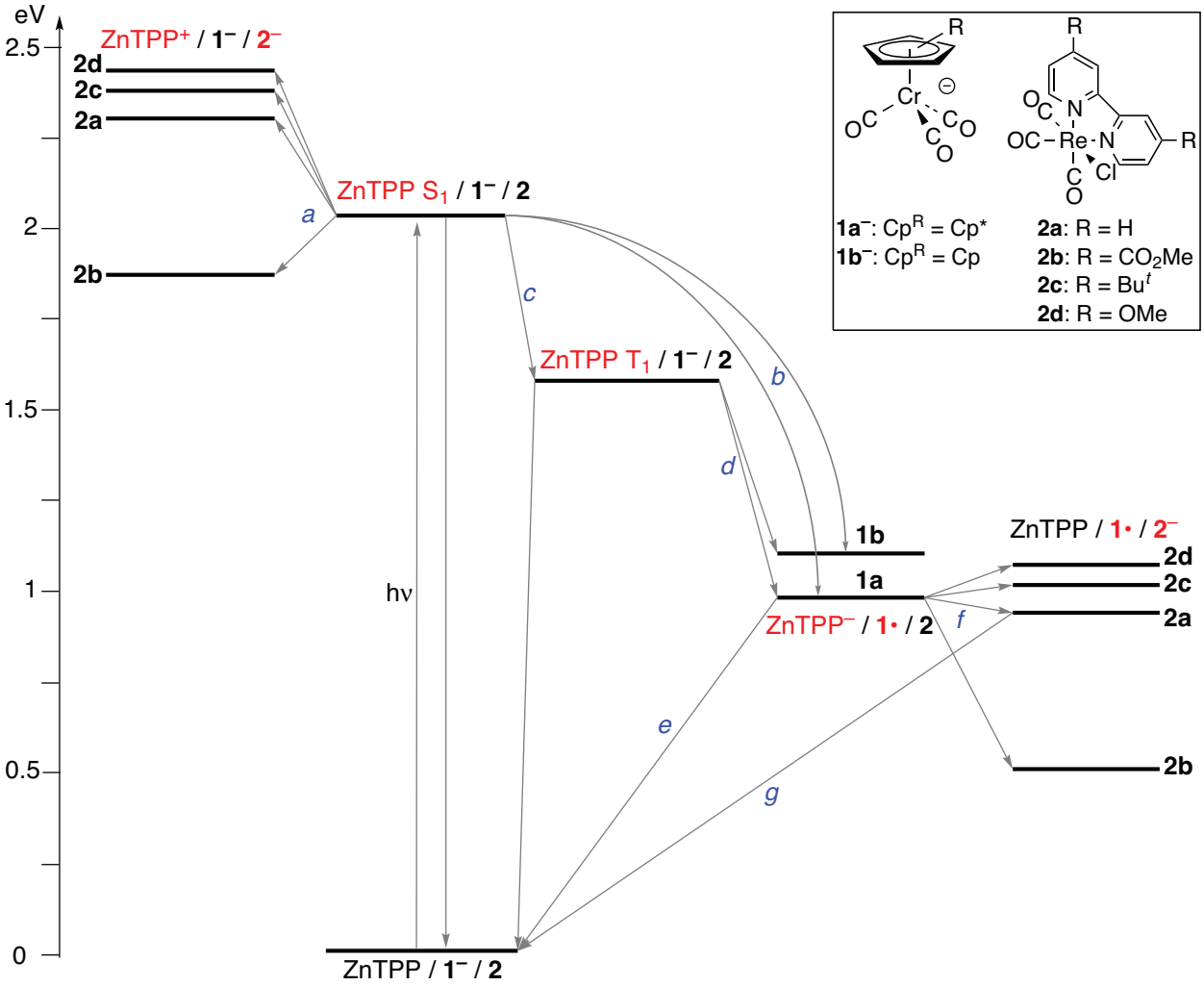

Figure 2.3 Jablonski diagram showing intermolecular electron-transfer processes among ZnTPP, $\mathbf{1}^{-}$, and **2** initiated by excitation of the S_1 state of ZnTPP in DMF. Relative energies of redox states are determined from electrochemical data shown in **Table 2.1**.

Table 2.1 Ground-State and Excited-State Redox Potentials and Electron-Transfer Reaction Free Energies for $\mathbf{1}^-$, **2**, and ZnTPP[a]

			ΔG_{eT}, eV						
			Reductive Quenching		Oxidative Quenching		Electron Transfer		
compound	$E_{1/2}^{-/0}$, V[a]	$E_{1/2}^{0/-}$, V[a]	ZnTPP (S_1)	ZnTPP (T_1)	ZnTPP (S_1)	ZnTPP (T_1)	$ZnTPP^-$	$\mathbf{1a}^-$	$\mathbf{1b}^-$
$\mathbf{1a}^-$	−0.83	–	−1.07	−0.61	–	–	–	–	–
	−1.03[b]	–	−1.14[b]	−0.68[b]	–	–	–	–	–
$\mathbf{1b}^-$	−0.68	–	−0.92	−0.46	–	–	–	–	–
2a	–	−1.75	–	–	0.09	0.55	−0.05	0.92	1.07
2b	–	−1.34	–	–	−0.32	0.14	−0.46	0.51	0.66
2c	–	−1.85	–	–	0.19	0.65	0.05	1.02	1.17
2d	–	−1.89	–	–	0.23	0.69	0.09	1.06	1.21

[a] DMF solution (except as noted), 0.1 M $[NBu^n_4][PF_6]$, room temperature, potentials referenced to $FeCp_2^{0/+}$. [b] THF solution.

2.3.2 Photochemistry of the ZnTPP S_1 Excited State with $\mathbf{1}^-$ and 2.

Excitation of solutions of ZnTPP containing compounds of types $\mathbf{1}^-$ and/or **2** in the porphyrin Q band region (λ_{ex} = 500−625 nm) selectively produces the ZnTPP S_1 excited state (Figure 2.2). The photochemical processes of the S_1 state in these mixtures were probed by measuring the effect on the ZnTPP fluorescence lifetime of added **2b**, the only rhenium compound of this study for which oxidative quenching of the S_1 state is thermodynamically downhill (ΔG = −0.32 eV; Figure 2.2, pathway *a*), and of $\mathbf{1a}^-$ and $\mathbf{1b}^-$, which are capable of reductively quenching the S_1 state (Figure 2.2, pathway *b*). Due to the short lifetime of the S_1 state (τ = 1.9 ns in THF and DMF), even fast (diffusion-limited) bimolecular quenching processes will be characterized by small quantum yields at millimolar concentrations of $\mathbf{1}^-$ and **2**,

such as those employed throughout this study. In accord with this expectation, quenching of the ZnTPP S_1 state by **2b** in DMF was not detected at concentrations of the latter up to 3.5 mM, which is the concentration employed in termolecular photoreactions described later in this report. In the presence of $\mathbf{1a}^-$ and $\mathbf{1b}^-$ (0−8 mM in THF or DMF), the ZnTPP fluorescence lifetime and intensity were observed to decrease only slightly (e.g., from 1.90 ns to 1.64 ns for $\mathbf{1a}^-$ at 8 mM). Stern-Volmer analyses of the data for the $\mathbf{1}^-$ ions (Figure 2.4) provide reductive quenching rate constants ($k_q(S_1)$) of $1.05 \pm 0.03 \times 10^{10}$ M^{-1} s^{-1} for $\mathbf{1a}^-$ and $9.2 \pm 0.2 \times 10^9$ M^{-1} s^{-1} for $\mathbf{1b}^-$, with the faster rate for $\mathbf{1a}^-$ being in accord with the 0.22 V larger driving force (Table 2.1). The products of these reductive quenching reactions are $ZnTPP^-$ and **1**•.

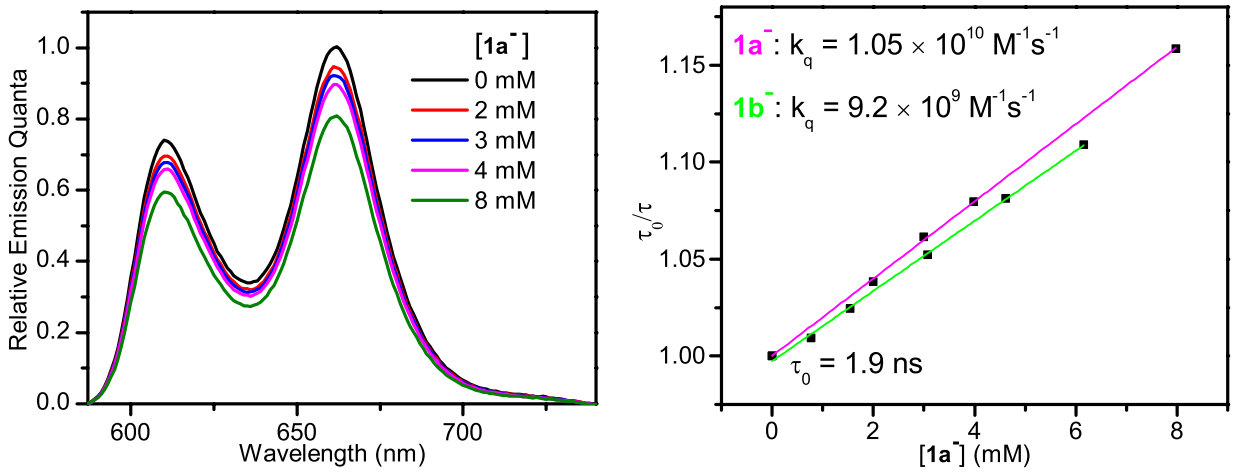

Figure 2.4 Left: Fluorescence intensity of ZnTPP in THF as a function of the concentration of $\mathbf{1a}^-$ (λ_{ex} = 567 nm). Right: Stern-Volmer analyses of the fluorescence lifetime of ZnTPP as a function of the concentration of $\mathbf{1}^-$ ($\mathbf{1a}^-$, THF, λ_{ex} = 595 nm; $\mathbf{1b}^-$, DMF, λ_{ex} = 558 nm). The lines are fits of the data to the equation $\tau_0/\tau = 1 + k_q\tau_0[\mathbf{1}^-]$.

Based on these observations and the kinetics of the intrinsic excited-state decay processes of ZnTPP (fluorescence, $k_r = 1.4 \times 10^7$ s^{-1}; internal conversion, $k_{ic} = 6.3 \times 10^7$ s^{-1}; intersystem crossing, $k_{isc} = 4.0 \times 10^8$ s^{-1}),[34] the ZnTPP S_1 state will decay principally via intersystem crossing to form the T_1 excited state (ϕ_{isc} = 0.78, Figure 2.3, pathway *c*) when in the presence of any combination of compounds of types $\mathbf{1}^-$ and **2** at the highest concentrations employed in the

photochemical experiments described below; the quantum yield for formation of $ZnTPP^-$ and **1a•** via reductive quenching of the S_1 state at these concentrations is $\phi_q(S_1) = 0.08$ (Figure 2.3, pathway *b*). The $ZnTPP^-$ and **1•** products formed from reductive quenching of the S_1 state are also produced via reductive quenching of the T_1 state (see below); thus, their presence does not complicate subsequent analyses.

2.3.3 Reductive Quenching of the ZnTPP T_1 State by 1^-.

In mixtures of ZnTPP, $\mathbf{1}^-$, and **2**, the only thermodynamically downhill bimolecular process for the ZnTPP T_1 excited state is reductive quenching by $\mathbf{1}^-$ (Figure 2.3, pathway *d*). The decay of the T_1 state in the presence of $\mathbf{1a}^-$ and $\mathbf{1b}^-$ in DMF solution was probed using nanosecond time-scale transient-absorption (TA) spectroscopy, with monitoring in the $\lambda \geq 670$ nm wavelength region to avoid excitation of transient **1•**. In the absence of $\mathbf{1}^-$, the TA spectrum observed following ZnTPP S_1 excitation (Figure 2.5) exhibits the characteristic features of the T_1 state: a band at 710 nm, and an absorption edge at ~815 nm associated with a band at 840 nm.[33,35,36] Although the intrinsic T_1 lifetime is 1.5 ms, under the experimental conditions the TA signals of this state are detectable for only ~200 μs and decay via non-first-order kinetics due to triplet−triplet annihilation.[33] Addition of a 50-fold excess of $\mathbf{1a}^-$ ($[\mathbf{1a}^-] = 3.5$ mM, [ZnTPP] = 0.07 mM) results in marked changes to the appearance and kinetics of the TA spectrum (Figure 2.5 and Figure 2.6): the T_1 features at 710 and 815 nm are not detected and, instead, a sharper band at 705 nm with a pronounced shoulder at 720 nm is observed. The position and shape of this band are identical to those of a prominent electronic-absorption band of $ZnTPP^-$, as measured by spectroelectrochemistry.[17] This demonstrates that the T_1 state of ZnTPP is reductively quenched by $\mathbf{1a}^-$ (Figure 2.3, pathway *d*). A similar result is obtained when ZnTPP is excited in the presence of $\mathbf{1b}^-$. By inference, the oxidation products **1a•** and **1b•** are also present

in the samples, but they are not detected because the TA probe beam is blocked in the wavelength region in which they absorb ($\lambda \leq 650$ nm) due to their photosensitivity.[15] To our knowledge, this is the first example of reductive quenching of the T_1 state of ZnTPP.

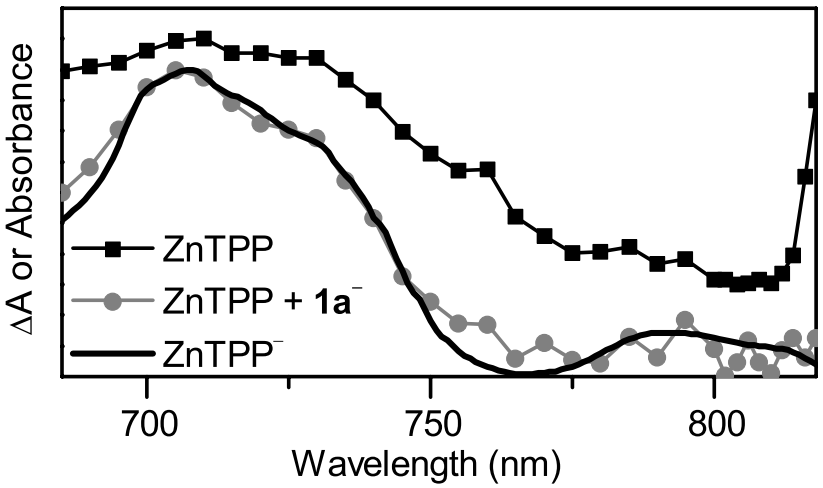

Figure 2.5 Temporally integrated transient-absorption spectra of ZnTPP (0.07 mM; λ_{ex} = 558 nm) in the absence (Δt = 1−100 μs) and presence of **1a**$^-$ (3.5 mM, Δt = 1−200 μs) in DMF solution. The smooth curve is the ground-state absorption spectrum of ZnTPP$^-$ (adapted from ref. [17]).

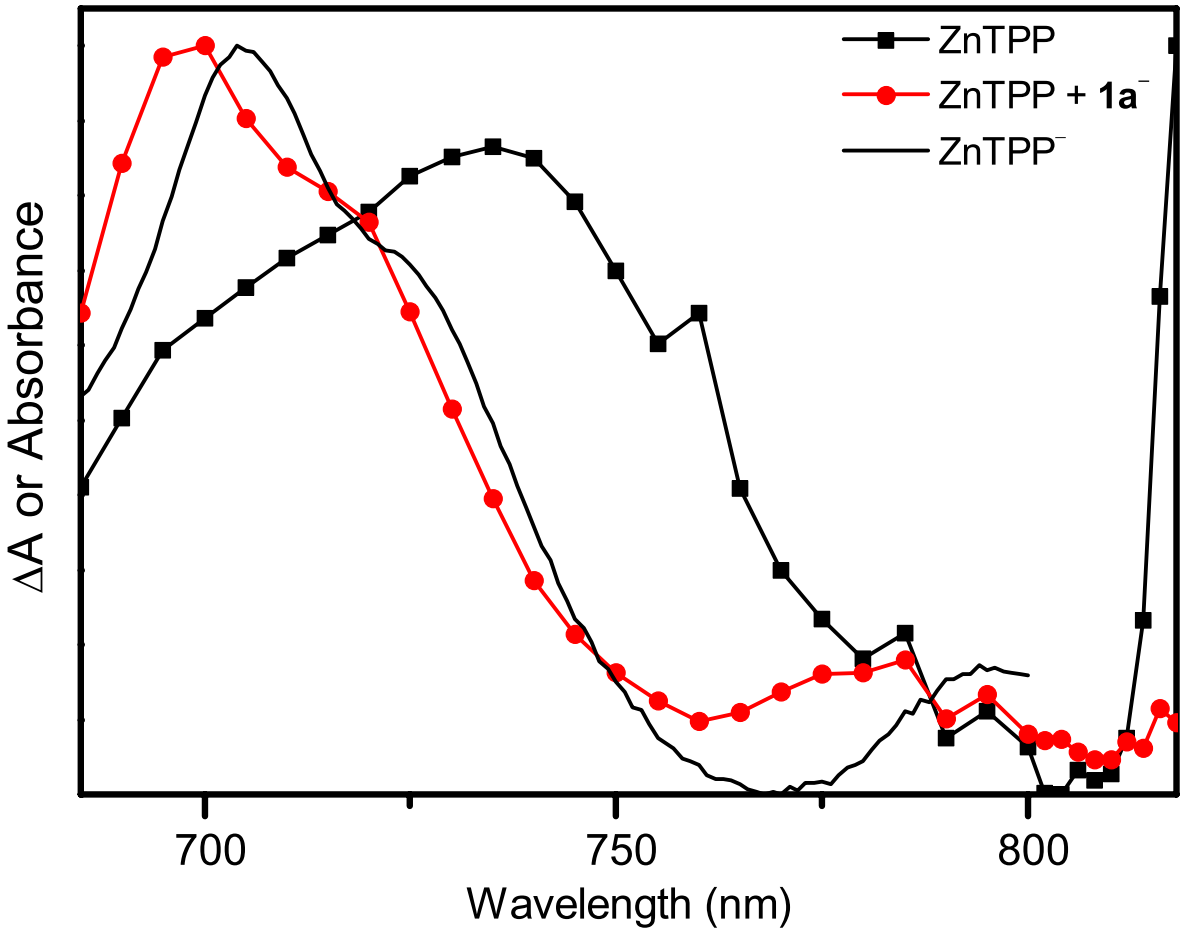

Figure 2.6 Temporally integrated transient-absorption spectra of ZnTPP (0.07 mM; λ_{ex} = 555 nm) in the absence (Δt = 1−100 μs) and presence of **1a**$^-$ (4.6 mM, Δt = 1−200 μs) in THF solution. Also shown is the ground-state absorption spectrum of ZnTPP$^-$ in THF (determined by spectroelectrochemistry).

The rate constants for photoinitiated electron transfer between ZnTPP and **1a**$^-$ and **1b**$^-$ were determined by measuring the dependence of the ZnTPP T_1 lifetime on the concentration of the **1**$^-$ ions ([**1a**$^-$] = 0.056−0.46 mM, [**1b**$^-$] = 0.065−0.54 mM). These measurements employed concentrations of **1**$^-$ that are ~5−50 times lower than those used in the preceding spectroscopic experiments (e.g., Figure 2.5) so that the T_1 bands were still observable in the TA spectra. Under these conditions, the yield for formation of ZnTPP$^-$ and **1•** by the reductive quenching of the S_1 state is $\phi_q(S_1) < 0.01$. A representative kinetic trace from these measurements (Figure 2.7) illustrates the dramatic acceleration of the T_1 decay by sub-millimolar concentrations of **1a**$^-$. Due

to the greatly reduced lifetime of the T_1 state, the contribution to its decay from triplet−triplet annihilation is negligible and the profiles exhibit first-order kinetics. Stern-Volmer analyses of these data (Figure 2.7) provide rate constants for reductive quenching of the T_1 state by **1a**$^-$ of $k_q(T_1) = 4.4 \times 10^9$ M^{-1} s^{-1} ($\Delta G = -0.61$ eV) and by **1b**$^-$ of 2.8×10^9 M^{-1} s^{-1} ($\Delta G = -0.46$ eV). The ordering of these rates and those for reductive quenching of the S_1 state by **1a**$^-$ and **1b**$^-$ (**1a**$^-$: $k_q(S_1) = 1.05 \times 10^{10}$ M^{-1} s^{-1}, $\Delta G = -1.14$ eV, **1b**$^-$: $k_q(S_1) = 9.2 \times 10^9$ M^{-1} s^{-1}, $\Delta G = -0.92$ eV) are entirely consistent with their relative driving forces. Based on these data and the intramolecular decay kinetics of the T_1 state of ZnTPP, the quantum yields for formation of ZnTPP$^-$ and **1•** from the T_1 state exceed 99% for [**1a**$^-$] ≥ 20 μM and [**1b**$^-$] ≥ 30 μM.

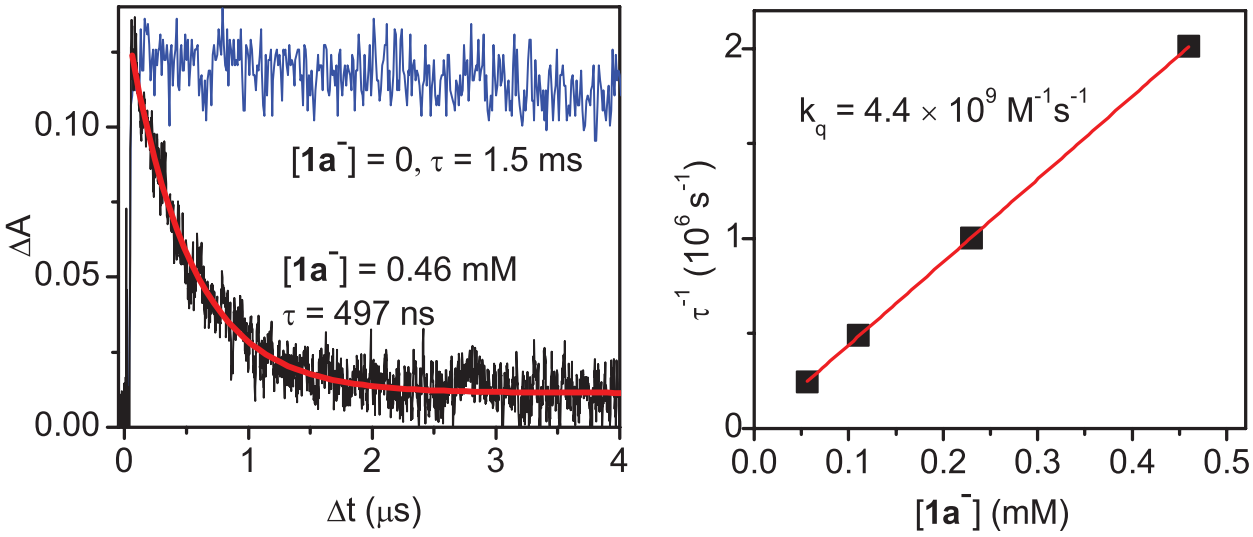

Figure 2.7 Quenching of the ZnTPP T_1 state by **1a**$^-$ in DMF. Left: Transient-absorption kinetic profiles of the ZnTPP T_1 state (λ = 818 nm) with [**1a**$^-$] = 0 and [**1a**$^-$] = 0.46 mM. Right: Stern-Volmer analysis.

2.3.4 Thermal Back Electron Transfer between ZnTPP$^-$ and 1•.

Photogenerated ZnTPP$^-$ and **1•** are expected to undergo back electron transfer to fully reform the ground state (Figure 2.3, pathway *e*), in the absence of other reaction pathways. The only competing pathway under the conditions of the preceding experiments is the dimerization of **1•** to form the Cr−Cr bonded dimers $[Cp^*Cr(CO)_3]_2$ (k_{dimer}(**1a**) ≅ 7×10^6 M^{-1} s^{-1}) and

$[CpCr(CO)_3]_2$ (k_{dimer}(**1b**) ≅ 3 × 10^8 M^{-1} s^{-1}).[37] Under conditions where dimerization of **1•** is negligible, the concentrations of $ZnTPP^-$ and **1•** are identical and the kinetics for the decay of $ZnTPP^-$, which is the observable species in the TA spectra, are described by the second-order expression $d[ZnTPP^-]/dt = k_{BET}[ZnTPP^-]^2$, where k_{BET} is the back-electron-transfer rate. The concentration of $ZnTPP^-$ as a function of time was calculated from the absorbance of the transient-absorption band at 705 nm (Figure 2.5; ε = 12000 M^{-1} cm^{-1})[17] because it does not overlap with other transient features. The temporal decay of the 705-nm band was found to be linear with $[ZnTPP^-]^{-1}$, as shown in Figure 2.8 for **1a•**. This is consistent with the expected second-order kinetics for electron transfer between $ZnTPP^-$ and **1•** without kinetically competitive dimerization (i.e., k_{BET} >> k_{dimer}). Linear fits to these data (Figure 2.8 and Figure 2.9) provide k_{BET} = 7 ± 1 × 10^9 M^{-1} s^{-1} for **1a•** (ΔG = −0.97 eV) and k_{BET} = 7 ± 1 × 10^9 M^{-1} s^{-1} for **1b•** (ΔG = −1.12 eV); these rates are larger than those for dimerization of **1b•** and **1a•** by one and three orders of magnitude, respectively.

Under the experimental conditions, the initial concentrations of photogenerated $ZnTPP^-$ and **1a•** are each ~0.008 mM (ΔA(705 nm) = 0.1 at Δt = 0, Figure 2.8). Thus, the second-order half-life of $ZnTPP^-$ is approximately 15 μs, and it is present in spectroscopically detectable concentrations for approximately 200 μs. This is sufficient to allow the strongly reducing $ZnTPP^-$ radical to be oxidized by CO_2 reduction catalysts of type **2** (Figure 2.3, pathway *f*). For this reaction to occur its electron-transfer kinetics must out-compete back electron transfer between $ZnTPP^-$ and **1•**, as could be the case under diffusion control when **2** is present in greater concentration than transient **1•**.

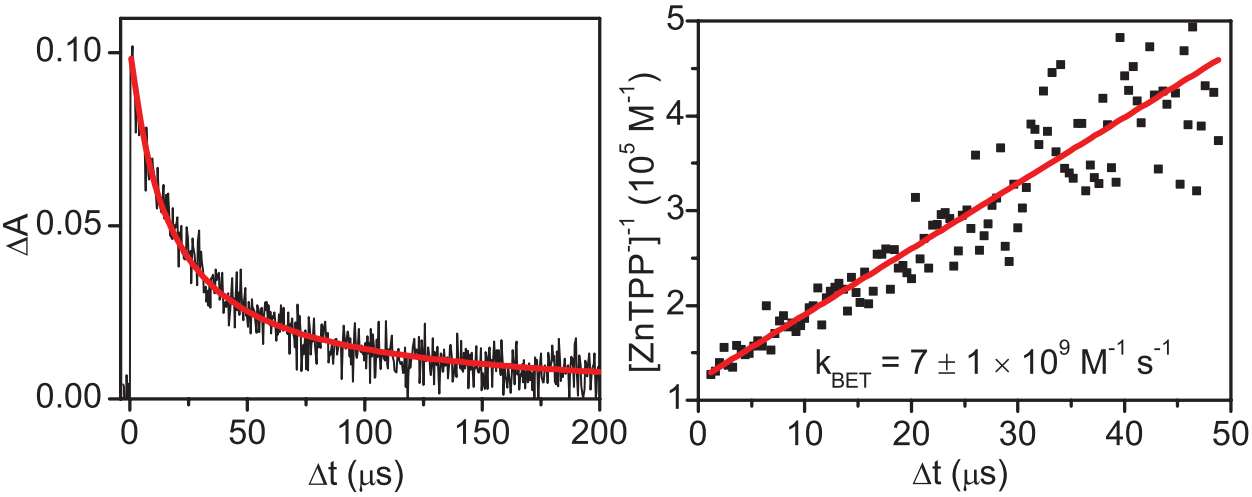

Figure 2.8 Left: Transient-absorption kinetic profile showing decay of photo-generated $ZnTPP^{-}$ (λ = 705 nm) via back electron transfer to **1a•** in DMF (λ_{ex} = 558 nm). Right: Second-order rate plot for these data.

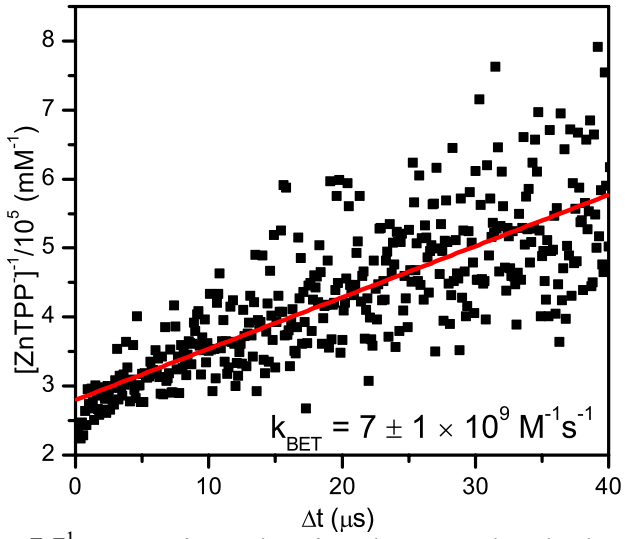

Figure 2.9 Plot of $[ZnTPP^{-}]^{-1}$ versus time, showing the second-order back electron transfer between photogenerated **1b•** and $ZnTPP^{-}$.

2.3.5 Electron-Transfer Sensitization of 2 by Photogenerated $ZnTPP^{-}$.

The oxidation of photogenerated $ZnTPP^{-}$ by catalysts of type **2** produces ZnTPP and the ligand-centered radical $\mathbf{2}^{-}$ (Figure 2.3, pathway *f*); also present is **1•** from the initial quenching reaction. This product state is thermodynamically competent to accomplish the substrate-activation steps of the reverse water-gas shift reaction: $\mathbf{2}^{-}$ undergoes subsequent reactions that, under CO_2 atmosphere, lead ultimately to the reduction of CO_2 to CO,[19] while **1•** reacts with and

cleaves H_2.[28] In order to understand and develop the conditions under which sensitization of **2** by $ZnTPP^-$ is favored over back electron transfer to **1•**, the photochemistry of mixtures of ZnTPP, $\mathbf{1a}^-$, and **2a−2d** were probed using transient-absorption spectroscopy.

The nanosecond time-scale transient-absorption spectra of a mixture of ZnTPP (0.070 mM), $\mathbf{1a}^-$ (3.5 mM), and **2a** (2.4 mM) observed following ZnTPP S_1 excitation are markedly different from those described above for a mixture of ZnTPP and $\mathbf{1a}^-$ without **2a**. In the 670−820 nm region, the spectra in the presence and absence of **2a** are similar in that they exhibit the band at 705 nm due to $ZnTPP^-$ (Figure 2.10); this indicates, as expected, that the presence of **2a** does not interfere with reductive quenching of the ZnTPP T_1 state by $\mathbf{1a}^-$ (Figure 2.3, pathway *d*). However, the $ZnTPP^-$ is consumed in < 5 μs in the presence of **2a** (Figure 2.10), whereas in the absence of **2a** it remains detectable for ~200 μs. Examination of the spectrum in the 450−550 nm region in the time window after the $ZnTPP^-$ has fully decayed (Figure 2.11) shows the presence of an unsymmetrical band maximizing at 505 nm that closely matches the position and shape of an absorption band of electrochemically prepared $\mathbf{2a}^-$.[18] This demonstrates that the accelerated decay of $ZnTPP^-$ is due to oxidation by **2a** to produce $\mathbf{2a}^-$ and ZnTPP (Figure 2.3, pathway *f*); presumably, this occurs with conservation of the initial **1a•** photoproduct.

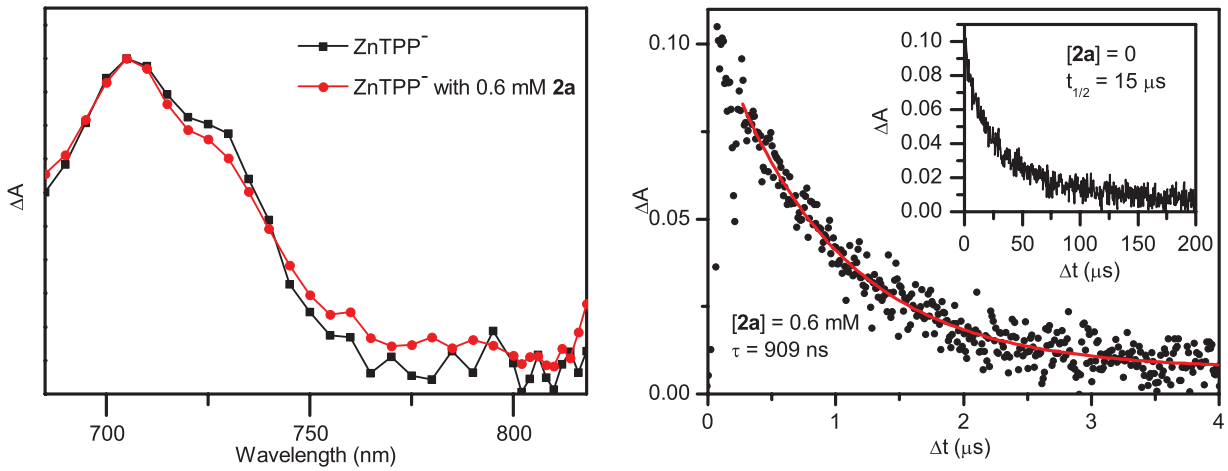

Figure 2.10 Left: Temporally integrated transient-absorption spectra of $ZnTPP^-$ (λ_{ex} = 558 nm) in the absence (black, Δt = 1−100 μs) and presence of **2a** (red, [**2a**] = 0.6 mM, Δt = 80−7500 ns) in DMF solution. Right: Transient-absorption kinetic profile showing decay of photo-generated $ZnTPP^-$ (λ = 705 nm) via electron transfer to **2a** ([**2a**] = 0.6 mM) in DMF; the red curve is a single-exponential fit. Inset: Transient-absorption kinetic profile showing decay of photo-generated $ZnTPP^-$ (λ = 705 nm) via back electron transfer to **1a•** in DMF in the absence of **2a** (data from **Figure 2.8**).

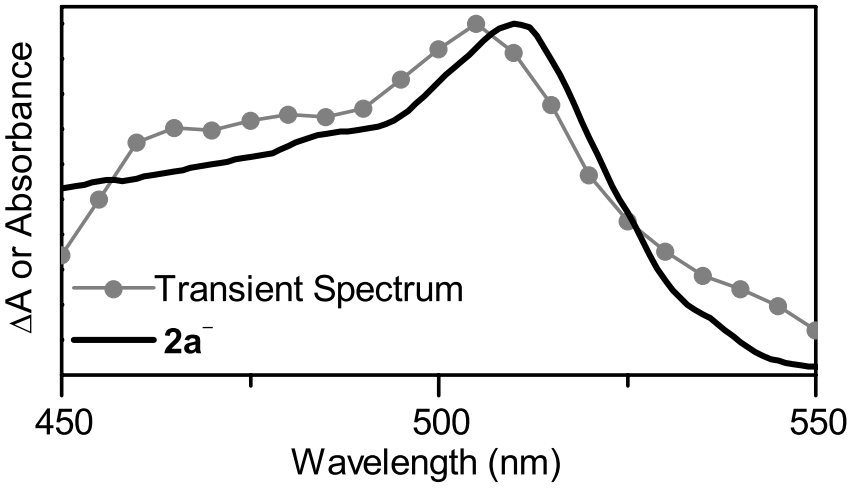

Figure 2.11 Temporally integrated (Δt = 6−400 μs) transient-absorption spectrum of a mixture of ZnTPP (0.070 mM; λ_{ex} = 558 nm), $\mathbf{1a}^-$ (3.5 mM), and **2a** (2.4 mM) in DMF. The transient-absorption bands of photogenerated $ZnTPP^-$ have completely decayed prior to this time window. The spectrum of $\mathbf{2a}^-$ (adapted from ref. [18]) is overlaid.

The kinetics of the thermal electron-transfer reactions between photogenerated $ZnTPP^-$ and **2a**−**2d** were determined by measuring the dependence of the $ZnTPP^-$ lifetime on the concentration of **2** (see above). The concentrations of ZnTPP and $\mathbf{1a}^-$ in these samples were

chosen to be sufficient to produce $ZnTPP^-$ in quantitative yield from the T_1 state ([ZnTPP] = 0.070 mM, [**1a**$^-$] = 3.7 mM (**2a**−**c**) or 3.5 mM (**2d**)); the concentration ranges for **2a**−**2d** differed for each derivative, based on the driving force for the electron-transfer reaction. In the presence of **2a**−**2c**, photogenerated $ZnTPP^-$ decays with first-order kinetics, rather than the second-order kinetics observed for the back electron transfer reaction between $ZnTPP^-$ and **1•** when **2** is absent, because even though the ground-state concentrations of **2** and **1**$^-$ are similar the concentration of **2** is two to three orders of magnitude greater than those of transient $ZnTPP^-$ and **1a**$^{\bullet}$. The measured lifetime of $ZnTPP^-$ varies linearly with the concentration of **2** (Figure 2.12). These data provide rate constants for electron transfer from $ZnTPP^-$ to **2a**−**c** that vary according to the driving force for the reaction: the fastest rate is observed for **2b** ($k_{ET} = 4.0 \times 10^9\ M^{-1}\ s^{-1}$, $\Delta G = -0.46$ eV) and slower rates are found for the approximately thermoneutral reactions with **2a** ($k_{ET} = 1.8 \times 10^9\ M^{-1}\ s^{-1}$, $\Delta G = -0.05$ eV) and **2c** ($k_{ET} = 1.7 \times 10^8\ M^{-1}\ s^{-1}$, $\Delta G = 0.05$ eV). For **2d**, ($k_{ET} = 4.8 \times 10^7\ M^{-1}\ s^{-1}$, $\Delta G = 0.09$ eV), the electron-transfer rate is sufficiently slow that the decay of the $ZnTPP^-$ anion cannot be fit by a single-exponential function, indicating that back electron transfer between $ZnTPP^-$ and **1a•** is kinetically competitive with reduction of **2d**. The electron-transfer rates for these processes are depicted in the Rehm-Weller plot shown in Figure 2.13.

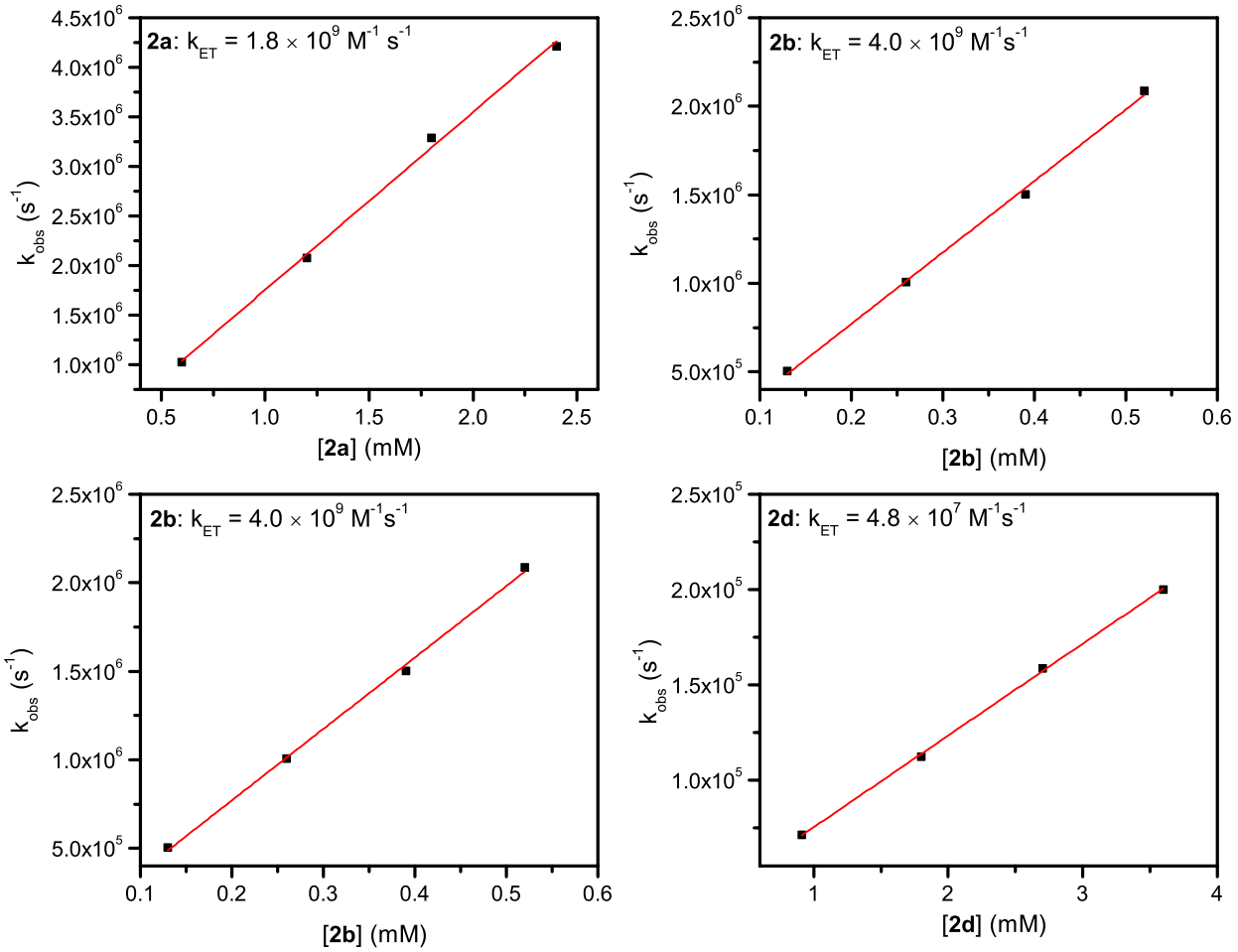

Figure 2.12 Decay rate of photogenerated $ZnTPP^-$ as a function of the concentration of **2** (see **Figure 2.13**); [ZnTPP] = 0.070 mM (**2a**, **2c**) and 0.140 mM (**2b**, **2d**), [$\mathbf{1a}^-$] = 3.7 mM (**2a**–**c**) and 3.5 mM (**2d**). The lines are fits of the data to the equation $1/\tau = A + k_{ET}[\mathbf{2}]$.

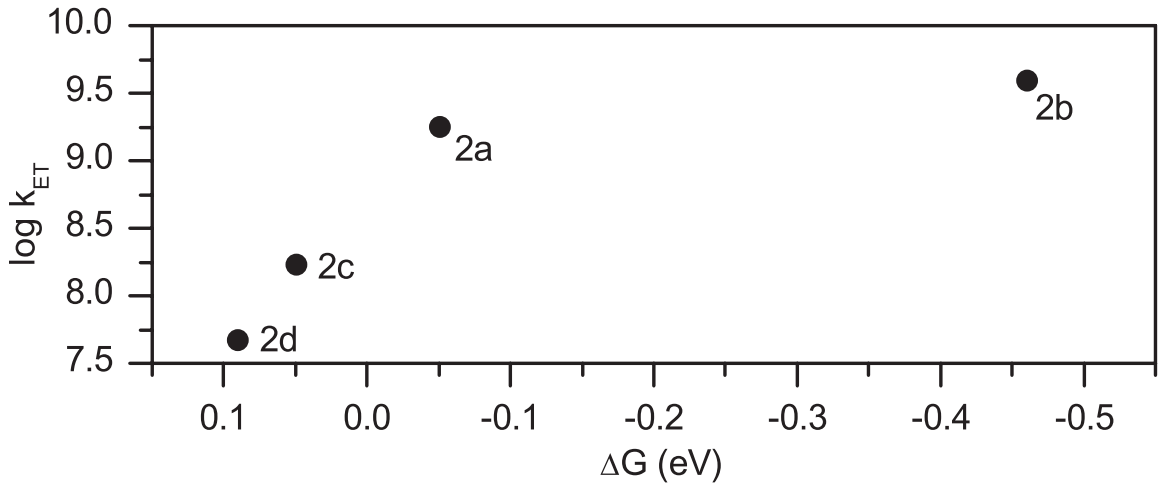

Figure 2.13 Plot of log k_{ET} vs ΔG for electron transfer from photogenerated $ZnTPP^-$ to **2a**–**d** in DMF.

In the absence of reactive substrates, photochemically generated **1•** and $\mathbf{2}^{-}$ will react by electron transfer to reform the ground state mixture of ZnTPP, $\mathbf{1a}^{-}$, and **2** (Figure 2.3, pathway *g*). The rate of this reaction was measured for $\mathbf{2a}^{-}$ and **1a•** ($\Delta G = -0.92$ eV) in a transient-absorption spectroscopic experiment that broadened the probe wavelength window to 450−550 nm, so that the kinetic profile of the TA band of $\mathbf{2a}^{-}$ at 505 nm (Figure 2.11) could be measured. Although these conditions have the potential to trigger photochemical reactions of **1a•**,[15] the decay of $\mathbf{2a}^{-}$ was found to obey the expected second-order kinetics (Figure 2.14) and provided a rate constant of $k_{BET} = 8 \pm 1 \times 10^{9}\ M^{-1}s^{-1}$. This rate is within experimental error of that measured for electron transfer from $ZnTPP^{-}$ to **1a•** ($k_{BET} = 7 \pm 1 \times 10^{9}\ M^{-1}s^{-1}$), for which the driving force is approximately the same ($\Delta G = -0.97$ eV).

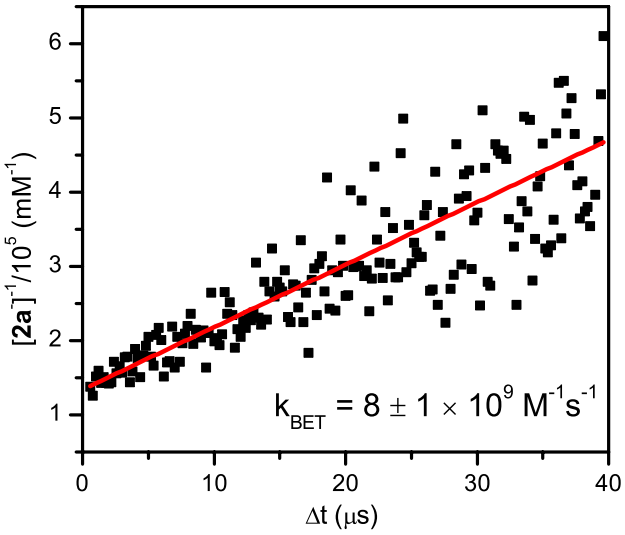

Figure 2.14 Plot of $[\mathbf{2a}^{-}]^{-1}$ versus time, showing the second-order back electron transfer between photogenerated **1a•** and $\mathbf{2a}^{-}$. The red line is a linear fit to the data.

2.4 Conclusion

Using time-resolved spectroscopic methods, a comprehensive mechanistic and kinetic picture of the photoinitiated reactions of ZnTPP, $[Cp^{R}Cr(CO)_3]^{-}$, and $Re(bpy\text{-}4,4'\text{-}R_2)(CO)_3Cl$

has been developed. These results demonstrate the feasibility of sensitizing an H_2 oxidation catalyst and a CO_2 reduction catalyst through sequential electron-transfer steps initiated by the absorption of a single photon by a broadly absorbing chromophore. Although the rates of competing productive (pathway *f*, Figure 2.3) and unproductive pathways (*e*) are of similar magnitude and the precatalysts $\mathbf{1}^-$ and **2** are present in similar ground-state concentrations, the pseudo-first-order conditions of the photochemical experiment bias the system to produce the desired state in which both catalysts are activated. It is noteworthy that photosensitization of this system can be accomplished with the low-energy T_1 state of ZnTPP, which participates via heretofore unobserved reductive quenching; this raises the prospect of capturing light across the full visible spectrum to drive these reactions. Under the experimental conditions, the catalytically competent state decays with a second-order half-life of approximately 15 μs, which is of the right magnitude for substrate-trapping of sensitized catalyst intermediates. Such trapping experiments are the subject of the following chapter.

Note: A portion of this work was previously published in an alternative format as N. T. La Porte D. B. Moravec, and M. D. Hopkins, *PNAS* **111**(27), 9745 (2014)

2.5 References

(1) Xiaoding, X.; Moulijn, J. A. *Energy Fuels* **1996**, *10*, 305.

(2) Ettedgui, J.; Diskin-Posner, Y.; Weiner, L.; Neumann, R. *J. Am. Chem. Soc.* **2010**, *133*, 188.

(3) Pangborn, A. B.; Giardello, M. A.; Grubbs, R. H.; Rosen, R. K.; Timmers, F. J. *Organometallics* **1996**, *15*, 1518.

(4) Tilset, M.; Zlota, A. A.; Folting, K.; Caulton, K. G. *J. Am. Chem. Soc.* **1993**, *115*, 4113.

(5) Smieja, J. M.; Kubiak, C. P. *Inorg. Chem.* **2010**, *49*, 9283.

(6) Cattaneo, M.; Fagalde, F.; Katz, N. E.; Borsarelli, C. D.; Parella, T. *Chem. Ber.* **2007**, *2007*, 5323.

(7) Li, F.; Yang, K.; Tyhonas, J. S.; MacCrum, K. A.; Lindsey, J. S. *Tetrahedron* **1997**, *53*, 12339.

(8) Lindsey, J. S.; Prathapan, S.; Johnson, T. E.; Wagner, R. W. *Tetrahedron* **1994**, *50*, 8941.

(9) Lindsey, J. S.; Hsu, H. C.; Schreiman, I. C. *Tetrahedron Lett.* **1986**, *27*, 4969.

(10) Herrmann, W. In *Synthetic methods of organometallic and inorganic chemistry*; Georg Thieme Verlag: 1997; Vol. 8: Transition Metals Part 2.

(11) van der Eide, E. F.; Hou, G.-L.; Deng, S. H. M.; Wen, H.; Yang, P.; Bullock, R. M.; Wang, X.-B. *Organometallics* **2013**, *32*, 2084.

(12) Behrens, U.; Edelmann, F. *C. R. Chim.* **1984**, *263*, 179.

(13) Gritzner, G.; Kuta, J. *Pure Appl. Chem.* **1984**, *56*, 461.

(14) Connelly, N. G.; Geiger, W. E. *Chem. Rev.* **1996**, *96*, 877.

(15) Jaeger, T. J.; Baird, M. C. *Organometallics* **1988**, *7*, 2074.

(16) Krejčik, M.; Daněk, M.; Hartl, F. *J. Electroanal. Chem. Interfac. Electrochem.* **1991**, *317*, 179.

(17) Lanese, J. G.; Wilson, G. S. *J. Electrochem. Soc.* **1972**, *119*, 1039.

(18) Lee, Y. F.; Kirchhoff, J. R.; Berger, R. M.; Gosztola, D. *J. Chem. Soc., Dalton Trans.* **1995**, 3677.

(19) Morris, A.; Meyer, G.; Fujita, E. *Acc. Chem. Res.* **2009**, *42*, 1983.

(20) Morimoto, T.; Tanabe, J.; Sakamoto, K.; Koike, K.; Ishitani, O. *Res. Chem. Intermed.* **2012**, *39*, 437.

(21) Tamaki, Y.; Watanabe, K.; Koike, K.; Inoue, H.; Morimoto, T.; Ishitani, O. *Faraday Discuss.* **2012**, *155*, 115.

(22) Schneider, J.; Jia, H.; Muckerman, J. T.; Fujita, E. *Chem. Soc. Rev.* **2011**, *41*, 2036.

(23) Agarwal, J.; Fujita, E.; Schaefer III, H. F.; Muckerman, J. T. *J. Am. Chem. Soc.* **2012**, *134*, 5180.

(24) Agarwal, J.; Sanders, B. C.; Fujita, E.; Schaefer, H. F.; Harrop, T. C.; Muckerman, J. T. *Chem. Comm.* **2012**, *48*, 6797.

(25) Sacksteder, L.; Zipp, A. P.; Brown, E. A.; Streich, J.; Demas, J. N.; DeGraff, B. A. *Inorg. Chem.* **1990**, *29*, 4335.

(26) Worl, L. A.; Duesing, R.; Chen, P.; Ciana, L. D.; Meyer, T. J. *J. Chem. Soc., Dalton Trans.* **1991**, 849.

(27) Doherty, M. D.; Grills, D. C.; Fujita, E. *Inorg. Chem.* **2009**, *48*, 1796.

(28) Capps, K.; Bauer, A.; Kiss, G.; Hoff, C. *J. Organomet. Chem.* **1999**, *586*, 23.

(29) Shaw, W. J.; Helm, M. L.; Dubois, D. L. *Biochim. Biophys. Acta, Bioenerg.* **2013**, *1827*, 1123.

(30) Tilset, M. In *Comprehensive Organometallic Chemistry III*; Parkin, G., Ed.; Elsevier: Oxford, 2006, p 280.

(31) Smieja, J. M.; Sampson, M. D.; Grice, K. A.; Benson, E. E.; Froehlich, J. D.; Kubiak, C. P. *Inorg. Chem.* **2013**, *52*, 2484.

(32) Harriman, A.; Porter, G.; Searle, N. *J Chem. Soc, Faraday Trans. 2: Mol. Chem. Phys.* **1979**, *75*, 1515.

(33) Pekkarinen, L.; Linschitz, H. *J. Am. Chem. Soc.* **1960**, *82*, 2407.

(34) Kee, H. L.; Bhaumik, J.; Diers, J. R.; Mroz, P.; Hamblin, M. R.; Bocian, D. F.; Lindsey, J. S.; Holten, D. *J. Photochem. Photobio. A* **2008**, *200*, 346.

(35) Rodriguez, J.; Kirmaier, C.; Holten, D. *J. Am. Chem. Soc.* **1989**, *111*, 6500.

(36) The full 840 nm band is not observed due to the loss of PMT sensitivity and probe beam intensity in this region.

(37) Yao, Q.; Bakac, A.; Espenson, J. H. *Organometallics* **1993**, *12*, 2010.

Chapter 3 Photoinduced reductive trapping of carbon dioxide without a sacrificial electron donor

3.1 Introduction

The steady increase in global energy consumption and the concern regarding the increased concentration of atmospheric carbon dioxide resulting from the burning of fossil fuels have energized considerable research into the production of renewable energy, in particular the use of solar energy to power the synthesis of liquid fuels. Among potential feedstocks for solar fuel production, carbon dioxide is one of the most attractive owing to its abundance as the end product of the combustion of carbon-based fuels. Accordingly, a solar-driven mechanism for capturing CO_2 and reducing it to an energy-rich fuel holds much promise for the recycling of the CO_2 emitted by combustion, leading to a carbon-neutral energy source.[1-6]

Over the past thirty years, considerable research has been done on the photocatalysis of carbon dioxide reduction.[7-12] In the set of reactions that comprise this process, the initial electron-transfer events are that the excited chromophore accepts an electron from some reductant, and the reduced chromophore transfers that electron to a catalyst, activating it towards binding of CO_2.[1] Depending on the nature of the product derived from CO_2, additional electron transfer and/or proton transfer reactions complete the reduction and release of a reduced-carbon product. An example, in which CO_2 is reduced to CO, is shown in Figure 3.1.

[1] In principle, a different pathway is possible, in which the chromophore is quenched oxidatively by the reduction catalyst, and the oxidized chromophore then oxidizes the sacrificial donor. In practice, sacrificial donors are chosen so that oxidative quenching and decomposition of the donor are fast, thereby quickly shutting off back-electron transfer.

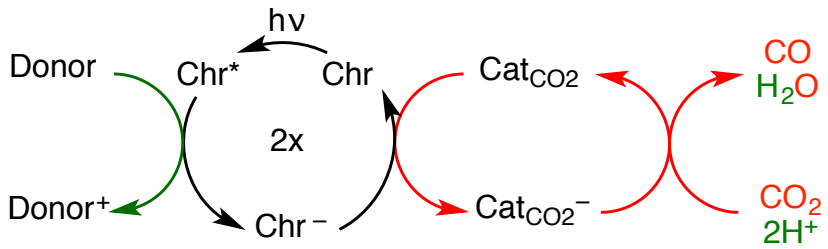

Figure 3.1 Photoreduction of CO_2 to CO, shown proceeding through a reductive quenching mechanism.

With very few exceptions,[13,14] the reducing equivalents for the photochemical reduction of CO_2 have come from a sacrificial species whose decomposition or deprotonation prevents unproductive back-electron transfer and allows the reduced chromophore to persist long enough to undergo further electron-transfer sensitization of the catalyst. Although these reagents are extremely valuable for facilitating fundamental studies, their use is problematic as regards development of functional artificial photosynthetic systems. Some of these donors have also been shown to promote stabilization of the CO_2-bound catalyst, through a combination of assisted precoordination of CO_2 to the catalytic center[15] and further electron- or proton-transfer chemistry to the CO_2-bound reduced catalyst. This non-innocence of the sacrificial electron donor is evident from research showing large differences in the observed reaction rate and composition of reduced products (CO, HCOOH/$HCOO^-$, H_2) when the same catalyst is photolyzed in the presence of different electron donors.[16-18] Furthermore, the stoichiometric decomposition of a sacrificial donor negates the energy-storing potential of the CO_2 reduction reaction.

In the previous chapter, it was shown that it is possible to co-sensitize in high yield a H_2 oxidation catalyst and a CO_2 reduction catalyst following the single-photon excitation of a ZnTPP chromophore, and to maintain this doubly sensitized state with a lifetime of greater than 10 μs, which should be suitable for active catalysts to initiate substrate transformation. This

system is thermodynamically competent to drive the energy-storing reverse water-gas shift reaction (RWGS: $H_2 + CO_2 \rightarrow H_2O + CO$) shown schematically in Figure 3.2. However, the catalysts employed in that study do not bind their substrates fast relative to back-electron transfer, and so are not kinetically competent to drive RWGS photochemically.

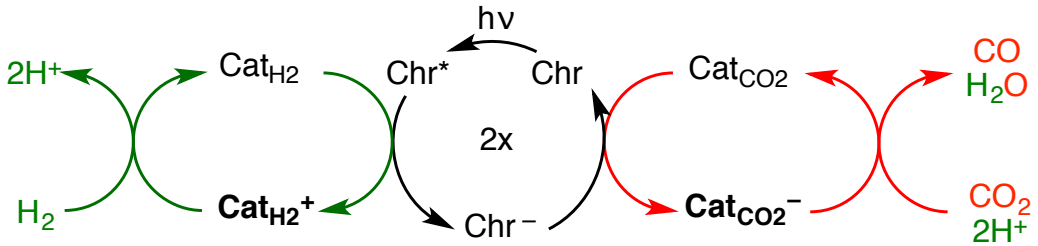

Figure 3.2 Schematic representation of the photocatalysed reverse water-gas shift reaction.

To address this problem, a parallel research project in our group was initiated and led to the discovery that a photo-electrochemical system employing a catalyst of the class $Ni(P^R_2N^{R'}_2)_2^{n+}$ could photo-electrocatalytically oxidize H_2, producing two equivalents of reduced chromophore per H_2 molecule oxidized.[19] This system is comprised of the photosensitizer $Ru(bpy)_3^{2+}$, the H_2-oxidation catalyst $Ni(P^{Cy}_2N^{tBu}_2)^+$ (**Ni**$^+$, Scheme 3.1), the Brønsted base pyrrolidine, and an electrode set at a potential appropriate to remove the electrons produced by H_2 oxidation yet insufficient for direct electrocatalysis.[19] In the catalytic resting state, the Ni catalyst is present as the Ni(I) species **Ni**$^+$ (Scheme 3.2). The system operates by reductive quenching of the excited chromophore, generating $Ru(bpy)_3^+$ and the Ni(II) species **Ni**$^{2+}$. That species has a strong driving force ($\Delta G = -7.9$ kcal/mol) for binding H_2 to form **Ni**$-$**H**$_2^{2+}$, which is rapidly deprotonated by pyrrolidine to produce the hydride **Ni-H**$^+$. The trapping of the Ni(II) species with hydrogen, a strongly exothermic reaction, outcompetes back-electron transfer from the reduced chromophore. A similar sequence of steps occurs starting from **Ni-H**$^+$, for which the driving force for reductive quenching is almost the same as for **Ni**$^+$; the **Ni-H**$^{2+}$ generated by reductive quenching is rapidly deprotonated by intramolecular proton transfer to the pendant

base (and subsequently to pyrrolidine) to regenerate $\mathbf{Ni^+}$, again outcompeting back-electron transfer. Through this sequence of steps, H_2 is oxidized to produce two equivalents of protonated base, which accumulate, and two equivalents of reduced chromophore, which is regenerated by oxidation at the electrode. The energy for the oxidation of H_2 is provided by light.

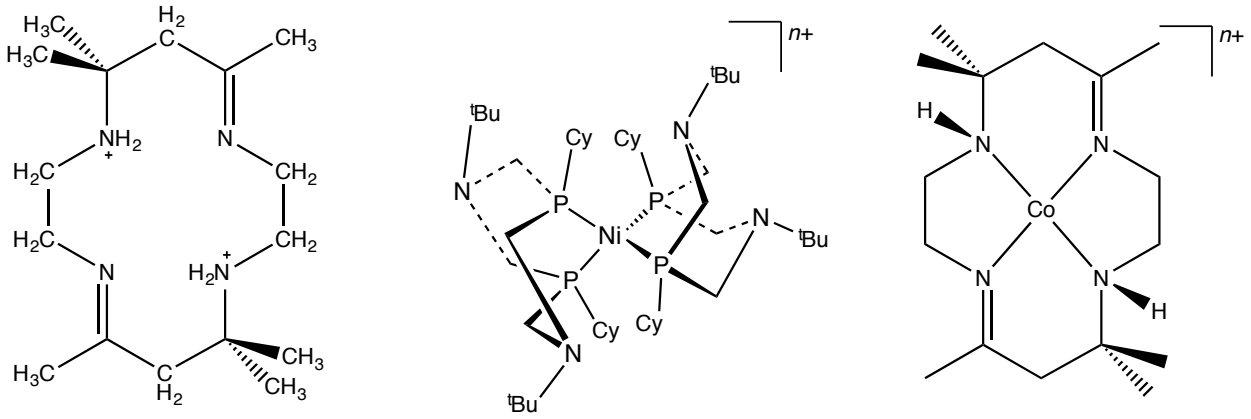

H_2HMD^{2+} **Ni^{n+}** **Co^{n+}**

Scheme 3.1 Structures of the **HMD** ligand (as the diprotonated **H_2HMD^{2+}**) and compounds **Ni^{n+}** and **Co^{n+}**.

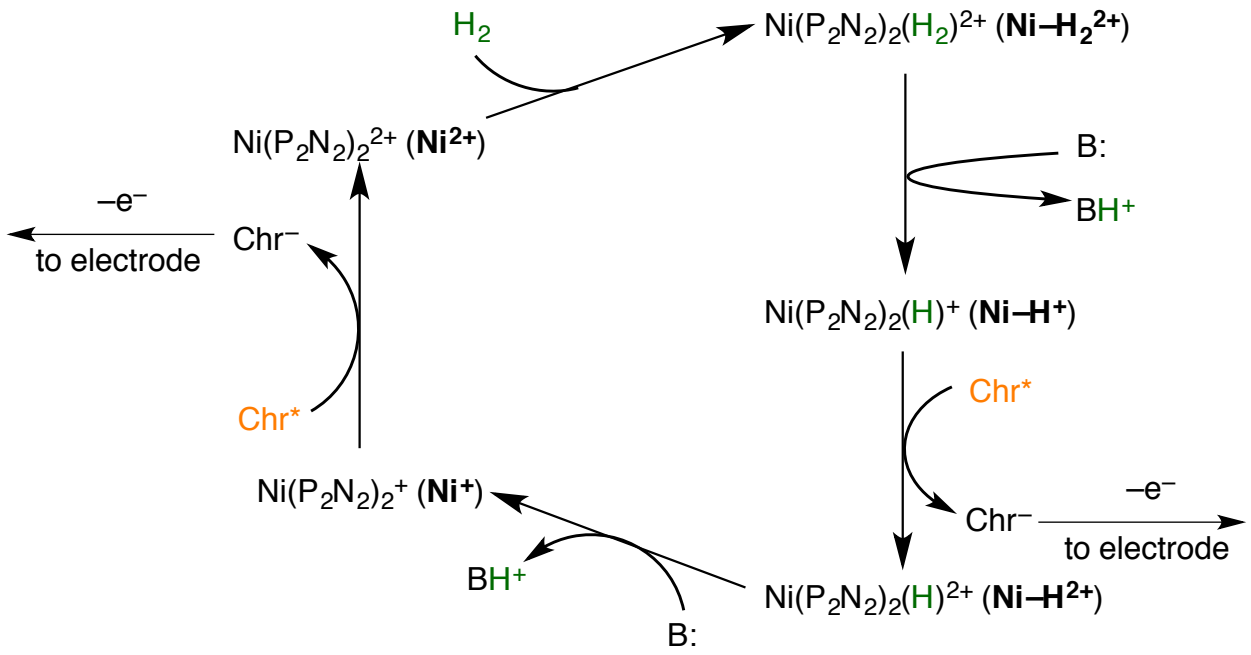

Scheme 3.2 Photoelectrochemical oxidation of H_2 by **Ni$^+$**. Adapted from ref [19].

The goal of the present set of experiments is to build on the observed photooxidation of H_2 by $\mathbf{Ni^+}$ by replacing the electrode with a CO_2 reduction catalyst that could be sensitized by the reduced chromophore. The catalytic H_2 oxidation cycle will take the place of conventional sacrificial electron donors, meeting a key requirement for energy storage, while the protonated base (pyrrolidinium) generated will serve as the proton source in the proton-coupled electron-transfer reduction of CO_2. The CO_2 reduction catalyst chosen for this study is $Co(HMD)^{2+}$ ($\mathbf{Co^{2+}}$; see $\mathbf{H_2HMD^{2+}}$ and $\mathbf{Co^{n+}}$, Scheme 3.1) The redox chemistry of $\mathbf{Co^{2+}}$ with CO_2 has been extensively studied using electrochemical and spectroscopic methods. Lewis and co-workers studied the binding of CO_2 to $\mathbf{Co^+}$, prepared in situ during cyclic voltammetric measurements from $\mathbf{Co^{2+}}$, in a variety of solvents and found a binding constant of $1.8 \pm 0.6 \times 10^4$ M^{-1} in DMF.[20] Flash photolysis studies of $\mathbf{Co^{2+}}$ under CO_2 using *p*-terphenyl as a chromophore and triethylamine as a sacrificial electron donor in acetonitrile:water solution led to determination of the binding rate constant for CO_2 to $\mathbf{Co^+}$ of 1.7×10^8 M^{-1} s^{-1}.[21] This should be sufficient to outcompete diffusion-controlled back-electron transfer between photogenerated substrate-binding catalysts because the concentration of CO_2 in saturated organic solution (0.2−0.28 M at 1 atm and room temperature; solubility varies slightly by solvent)[20] is several orders of magnitude higher than the expected concentrations of the photogenerated catalysts.

Fujita and co-workers prepared solutions of $\mathbf{Co^+}$ using chemical and electrochemical reduction methods. In the course of these studies, they observed a temperature-dependent equilibrium in solutions of $\mathbf{Co^+}$ under CO_2 between five-coordinate $\mathbf{Co(CO_2)^+}$ and six coordinate $\mathbf{(L)Co(CO_2)^+}$, where L is a solvent molecule (Scheme 3.3).[22] Studies of the five- and six-coordinate species using XANES techniques indicated that coordination of CO_2 in $\mathbf{Co(CO_2)^+}$ involves the transfer of approximately 0.71 electrons from the Co d_{z^2} orbital, and coordination of

the sixth ligand in **(L)Co(CO$_2$)$^+$** results in a further transfer of 1.2 electrons, resulting in a complex that is described as Co^{3+}(CO$_2^{2-}$).[23] Electronic absorption and FTIR spectra were reported for **Co^{2+}**, **Co(CO$_2$)$^+$**, **(L)Co(CO$_2$)$^+$** and **Co(CO)$^+$**, and those species were reported to be readily distinguishable,[22,24-26] suggesting that the system can be probed mechanistically by transient absorption spectroscopy.

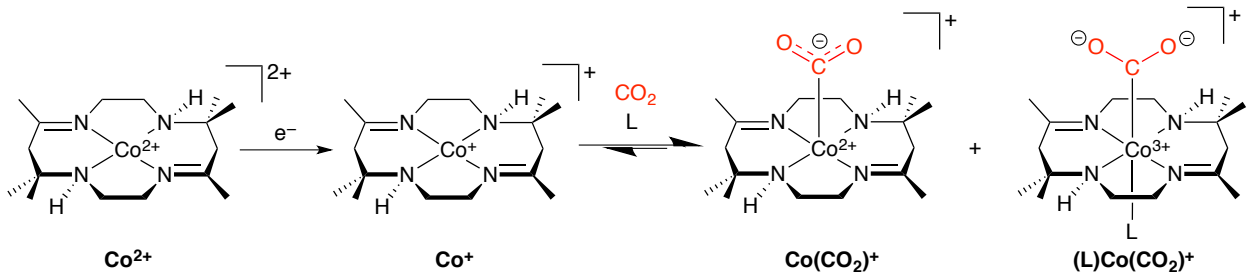

Scheme 3.3 Reduction of **Co^{2+}** in the presence of L and CO$_2$.

The suitability of **Co^{2+}** for the photocatalytic system studied here is further supported by the fact that it reduces CO$_2$ to CO. Solutions of **Co(CO$_2$)$^+$** were found to decompose slowly in the absence of air and water, producing substoichiometric CO (30% yield based on initial **Co^{2+}**) and NaHCO$_3$ (80% yield based on initial **Co^{2+}**).[24] In the presence of MeOH, decomposition to produce CO was reported to be rapid.[27] In addition, it has also been reported that **Co^{2+}** is an electrocatalyst for reduction of CO$_2$ to CO in solutions of acetonitrile with added H$_2$O.[28] Finally, bulk photolysis of solutions of **Co^{3+}** and *p*-terphenyl in acetonitrile:methanol solutions containing triethylamine or triethanolamine as a sacrificial electron donor led to production of reduced carbon products CO and HCO$_2^-$, as well as some H$_2$. The amount and ratio of the reduced products varied depending on the choice of donor.[17]

In this chapter, we report the thermal electron-transfer sensitization of **Co^{2+}** under conditions that are catalytic for H$_2$ oxidation, and the reductive trapping of CO$_2$ by **Co$^+$**. This study demonstrates the closure of the oxidative half of the photosynthetic cycle shown in Figure

3.2, while bringing the reductive half of the cycle one step closer to closure than previously reported. A sequence of reactions that would drive the RWGS, initiated by photoexcitation of the chromophore, is as follows:

(1) $\mathbf{Ni}^{+} + H_2 + B + Chr + h\nu \rightarrow \mathbf{Ni{-}H}^{+} + HB^{+} + Chr^{-}$
(2) $\mathbf{Ni{-}H}^{+} + B + Chr + h\nu \rightarrow \mathbf{Ni}^{+} + HB^{+} + Chr^{-}$
(3) $\mathbf{Co}^{2+} + Chr^{-} \rightarrow \mathbf{Co}^{+} + Chr$
(4) $\mathbf{Co}^{+} + CO_2 + B \rightarrow \mathbf{(B)Co(CO_2)}^{+}$
(5) $\mathbf{(B)Co(CO_2)}^{+} + Chr^{-} + 2BH^{+} \rightarrow \mathbf{Co}^{2+} + CO + H_2O + Chr + 3B$
(6) Net: $H_2 + CO_2 \rightarrow CO + H_2O$

The mechanism for reduction of CO_2 by $\mathbf{Co}^{n+}$ has not been studied in detail. As a consequence, reaction 5 is consistent with the reported chemistry but speculative. However, upon the conclusion of this set of reactions, one equivalent of H_2 has been oxidized to two protons (1 and 2) and two electrons, which are used to reduce one equivalent of CO_2 to bound CO (3−5). We are not able to demonstrate catalytic turnover of CO_2 reduction, which requires release of CO from $\mathbf{Co(CO)}^{+}$ to complete reaction (6); nevertheless we have demonstrated that reducing equivalents can be extracted from H_2 and used to reduce CO_2.

3.2 Experimental

3.2.1 General

All experiments were performed at room temperature under a nitrogen atmosphere using standard Schlenk and glovebox techniques, unless otherwise specified. DMF (Acros, peptide synthesis grade, free amine content < 0.001%) was dried over activated 4A molecular sieves and stored under N_2. Anhydrous methanol (Acros, >99.8 %, Extra Dry) was used as received. $[NBu^{n}_4]PF_6$ (Sigma-Aldrich, 98%) was recrystallized from ethanol and dried under vacuum at 100 °C. Ferrocene was recrystallized from 95% ethanol and then sublimed under vacuum. H_2 (research grade, 99.9999%), CO_2 (research grade, 99.999%), and 28% CO_2 in H_2 were purchased from Airgas. NMR solvents were purchased from Cambridge Isotope Laboratories and stored

over activated 4A sieves under N_2. $[Ni(P^{Cy}_2N^{tBu}_2][BF_4]$ was synthesized as previously described.[29,30] ZnTPP was synthesized by a literature procedure.[31] All other reagents and solvents were obtained from commercial sources and used as received.

3.2.2 Electrochemical Measurements.

Cyclic voltammetry and differential pulse voltammetry experiments were performed at room temperature under a nitrogen atmosphere in a glovebox using a Bioanalytical Systems (BAS) 100 B/W Electrochemical Workstation, except as noted below. A three-electrode configuration was used, consisting of a glassy carbon working electrode (area = 0.07 cm^2), glassy carbon auxiliary electrode (area = 0.07 cm^2), and Ag-wire quasi-reference electrode. The electrodes were polished prior to each experiment. Samples consisted of 1.0−2.0 × 10^{-3} M analyte in 5−10 mL DMF containing 0.1 M $[NBu^n_4][PF_6]$ with other auxiliary compounds in solution as described. Cyclic-voltammetric experiments were conducted over a range of scan rates (0.05−0.40 V s^{-1}). Decamethylferrocene was used as an internal electrode-potential standard for all compounds. Relative to $FeCp_2^{0/+}$, the $FeCp^*_2{}^{+/0}$ couple has been determined to lie at −0.458 V in DMF.[32] Experiments under CO were performed in a nitrogen-purged glovebag using a BAS Epsilon potentiostat. For experiments under CO or CO_2, gas was bubbled through the solution for several minutes before the start of each scan. All experiments under N_2 were performed prior to introduction of CO or CO_2 into the glovebox or glovebag in order to avoid contamination of the nitrogen atmosphere. After introduction of CO_2, the glovebox was purged for at least one hour before experiments under N_2 were performed again. Electrochemical data were analyzed using BAS 100W version 2.0 software or BAS Epsilon EC software.

3.2.3 Nanosecond Transient Absorption Spectroscopy.

Excitation was provided by an integrated Nd:YAG−optical-parametric-oscillator pulsed laser (Opotek Vibrant 355 LD; 10 Hz, 10 ns pulse width, 0.5−1.5 mJ/pulse energy at the sample) that produced tunable output between 410−710 nm. The laser beam sent to the sample was not focused. The white-light probe was provided by a 75 W xenon lamp (PTI model A1010) that was passed through a 1000 nm short-pass filter (to remove much of the infrared radiation) and a 355 nm long-pass filter. The toroidal-shaped probe beam was focused onto the sample with a concave mirror; the transmitted light was focused onto the input slit of a monochromator (Horiba Scientific model iHR320) with a second concave mirror. Laser excitation was collinear with and counter-propagating to the probe beam, passing through holes in the centers of the concave mirrors (where the probe lamp intensity was zero); this allowed overlap of the laser and focused probe beams in the sample. The monochromator output was detected by a thermoelectrically cooled 9-stage Hamamatsu 5108 PMT driven at 1200 V and processed with a digital oscilloscope (Tektronix model TDS 3032C). Transient decay traces at each wavelength were averaged for 512 laser pulses and individually analyzed to determine the transient lifetime and Δ(Absorbance) value. Automated data acquisition was controlled by LabView software.

Solutions for optical experiments were prepared on a vacuum line in sealable cuvettes and were degassed by three freeze-pump-thaw cycles before being backfilled with the appropriate gas. Data were processed and fit using Igor Pro.

3.2.4 ZnTPP T_1 quenching and $ZnTPP^-$ oxidation kinetic measurements.

The kinetics of the quenching of the ZnTPP T_1 state and the oxidation of $ZnTPP^-$ were investigated by transient-absorption spectroscopy in the wavelength range 825−925 nm. Kinetic profiles for ZnTPP T_1 were measured at 825 nm, the maximum of an intense ZnTPP T_1 band.[33]

Kinetic profiles of $ZnTPP^-$ were measured at 900 nm, near the maximum of an intense $ZnTPP^-$ band.[34] Samples contained constant concentrations of ZnTPP (0.070 mM) and, when applicable, pyrrolidine (70 mM). The lifetime of each transient species was monitored as a function of the concentration of $\mathbf{Ni}^+$. Concentrations of $\mathbf{Ni}^+$ were chosen so as to attenuate the lifetime of the ZnTPP T_1 state to less than 10% of the unquenched lifetime in order to minimize the effects of triplet-triplet annihilation and make the observed decay traces fit to a single-exponential function. The samples were excited at the maximum of the ZnTPP Q(1,0) band (λ_{ex} = 558 nm in pure DMF, λ_{ex} = 565 nm in DMF with 70 mM pyrrolidine).

The rate constants for ZnTPP T_1 quenching and $ZnTPP^-$ oxidation were determined using a Stern-Volmer analysis of the dependence of the lifetime on $\mathbf{Ni}^+$. Because the ZnTPP T_1 state does not decay according to single-exponential kinetics in the absence of $\mathbf{Ni}^+$ and the $ZnTPP^-$ state is stable in the absence of an oxidant, a modified Stern-Volmer fitting equation was used that removes the dependence of the rate term k_q on the intrinsic lifetime (τ_0). The derivation of this expression follows. In a traditional Stern-Volmer quenching experiment, k_{obs} (which is equal to τ_0/τ) is plotted versus [Q], and the slope of the plot corresponds to $\tau_0 k_q$:

$$\frac{\tau_0}{\tau} = 1 + \tau_0 k_q [Ni^+] \text{ (Stern-Volmer Equation)} \qquad \text{Equation 3.1}$$

In this case, τ_0 is undefined, so dividing each side through by τ_0 gives an equation that can be used to determine k_q:

$$\frac{1}{\tau} = C + k_q [Ni^+] \qquad \text{Equation 3.2}$$

This equation was used to fit plots of $1/\tau$ versus $[Ni^+]$.

3.2.5 Synthesis of 5,7,7,12.14,14-hexamethyl-1,4,8,11-tetraazacyclotetradeca-4,11-diene bis(tetrafluoroborate) ([H_2**HMD**][BF_4]$_2$).

[H_2**HMD**][BF_4]$_2$ was synthesized by a modification of the procedure reported for the perchlorate salt of the ligand.[35] This synthesis was first reported by Warner[36] but never published in the open literature. To a stirred solution of 50 mL acetone and 11 mL ethylenediamine was slowly added 22 g of 48% aqueous HBF_4. The resultant orange solution was cooled to −20 °C overnight, whereupon colorless crystals formed and were filtered off, washed with diethyl ether and ethanol and vacuum dried. Letting the supernatant solution stand at -20 °C overnight produced a second crop of crystals, which were also filtered off, washed and dried. This process was repeated two more times for a total yield of 10.0 g (28%). ^{1}H NMR: δ_H(400 MHz; dmso-d_6; Me_4Si) 8.56 (t, 4 H, N**H**$_2$), 3.47 (t, 4 H, CH_2C**H**$_2$N=C), 3.24 (q, 4 H, NH_2C**H**$_2$), 2.64 (s, 4 H, N=CC**H**$_2$C=N), 1.92 (s, 6 H, N=CC**H**$_3$), 1.32 (s, 12 H, NH_2C(C**H**$_3$)$_2$).

3.2.6 Synthesis of [*rac*-Co(HMD)][BF_4]$_2$ (Co^{2+}).

[Co(**HMD**)(CH_3OH)][BF_4]$_2$ (**Co**$^{2+}$(CH_3OH)) was synthesized by a modification of the procedure described for the perchlorate salt of the complex.[37] Methanol (50 mL, HPLC grade, not dried) was deoxygenated by sparging with nitrogen for 15 minutes and then added to $Co(CH_3CO_2)_2{\cdot}xH_2O$ (513 mg, 2.1−2.9 mmol depending on extent of hydration) and [H_2**HMD**][BF_4]$_2$ (897 mg, 2.0 mmol) in a nitrogen-purged flask. The mixture was refluxed for two hours and then cooled to room temperature. The volatile components (solvent and acetic acid) were removed by vacuum evaporation and the solids recrystallized twice from anhydrous methanol under nitrogen at −50 °C. The resultant orange crystals were suitable for single-crystal X-ray diffraction experiments if not allowed to dry. Material used for electrochemical and photochemical experiments was collected by vacuum filtration, washed with −50 °C anhydrous ethanol (Acros, 99.5%), room temperature diethyl ether, and dried overnight under vacuum to

produce **Co**$^{2+}$. MS: 338.2 (M^+−H), theory 338.19. Production of the isomer with both H atoms on the same face of the molecule (the N-*rac* isomer) was confirmed by comparison of the FTIR spectrum (KBr pellet) with a literature spectrum of the N-*rac* isomer.[25] The

3.2.7 Bulk photolysis methods.

Various amounts (Section 3.3.4 below) of **Ni**$^{+}$, **Co**$^{2+}$, pyrrolidine, methanol, and $Mg(ClO_4)_2$ were dissolved in DMF in volumetric glassware under an atmosphere of N_2 in a glovebox. ZnTPP was added to make a solution with approximate absorbance 1.0 at the maximum of the Q(0,0) band. Solutions were volumetrically pipetted into conical-bottomed 5 mL vials, which were sealed with Mininert septum caps. The vials were removed from the glovebox and sparged for 30 seconds with the appropriate gas by inserting a needle through the Mininert cap, turning on the gas flow, and then slightly loosening the cap to allow excess pressure to escape. The solutions were photolyzed for 20-24 hours on a merry-go-round photolysis apparatus under illumination from a 590 nm LED (SuperBrightLEDs). After photolysis, 100−200 μL samples were taken using a gas-tight syringe (Hamilton) and analyzed by gas chromatography.

NMR samples for bulk photolysis were prepared under N_2 atmosphere in a glovebox and sealed in NMR tubes with J. Young closures. Samples were removed from the glovebox and degassed on a vacuum line with three freeze-pump-thaw cycles. Samples photolyzed under N_2 were subsequently backfilled with N_2. Samples photolyzed under $^{13}CO_2$ were warmed to room temperature under vacuum and backfilled with $^{13}CO_2$ (Sigma-Aldrich, 99% isotopic enrichment). Samples photolyzed under a mixture of $^{13}CO_2$ and H_2 were warmed to room temperature under vacuum, backfilled with $^{13}CO_2$, and then frozen in liquid nitrogen. The samples were then backfilled with H_2 before being warmed carefully to room temperature.

3.2.8 Gas chromatography methods.

The headspace of the photolysis samples was analyzed and quantitated on an Agilent 7890B GC system equipped with flame ionization (FID) and thermal conductivity (TCD) detectors using N_2 as a carrier gas. In front of the FID was a nickel methanizing catalyst that converted CO and CO_2 into CH_4. Gases were injected using a Hamilton 500 µL gastight syringe into a split:splitless injection port running at a 10:1 split ratio. The gases were separated on a Supelco Carboxen 1010 PLOT column at 35°. Quantitation was performed by the Agilent software using a calibration curve generated by injecting different volumes of standard mixtures (Supelco SCOTTY Specialty Gas; 1.0% H_2, O_2, CH_4, CO, and CO_2 in N_2 or 15.0 % CO_2, 6.99% CO, 4.50% CH_4 and 4.01% O_2 in N_2).

3.2.9 X-ray crystallography of $Co^{2+}(CH_3OH)$.

The X-ray crystallographic experiments and determination of the crystal structure were performed by Dr. Alexander Filatov. Crystals were grown from a methanol solution as described above. All crystal manipulations were carried out under nitrogen atmosphere in a glove bag. A brown small plate (0.06 x 0.09 x 0.16 mm) was mounted on a Dual-Thickness MicroMount^{tm} (MiTeGen) with 30 µm sample aperture with Fluorolube™ oil. The diffraction data were measured at 100 K on a Bruker D8 VENTURE with PHOTON 100 CMOS detector system equipped with a Mo-target X-ray tube (λ = 0.71073 Å). Data were collected using ϕ and ω scans to survey a hemisphere of reciprocal space. Data reduction and integration were performed with the Bruker APEX2 software package (Bruker AXS, version 2014.9-0, 2014). Data were corrected for absorption effects using the multi-scan procedure as implemented in SADABS (Bruker AXS, version 2014/4, 2014, part of Bruker APEX2 software package). The structure was solved by SHELXT[38] and refined by full-matrix least-squares procedure using Bruker

SHELXTL (version 6.14) software package (XL refinement program version 2014/7.[39,40] A full report on the crystal structure is included in this dissertation as Appendix B. The structure is shown below in Figure 3.3.

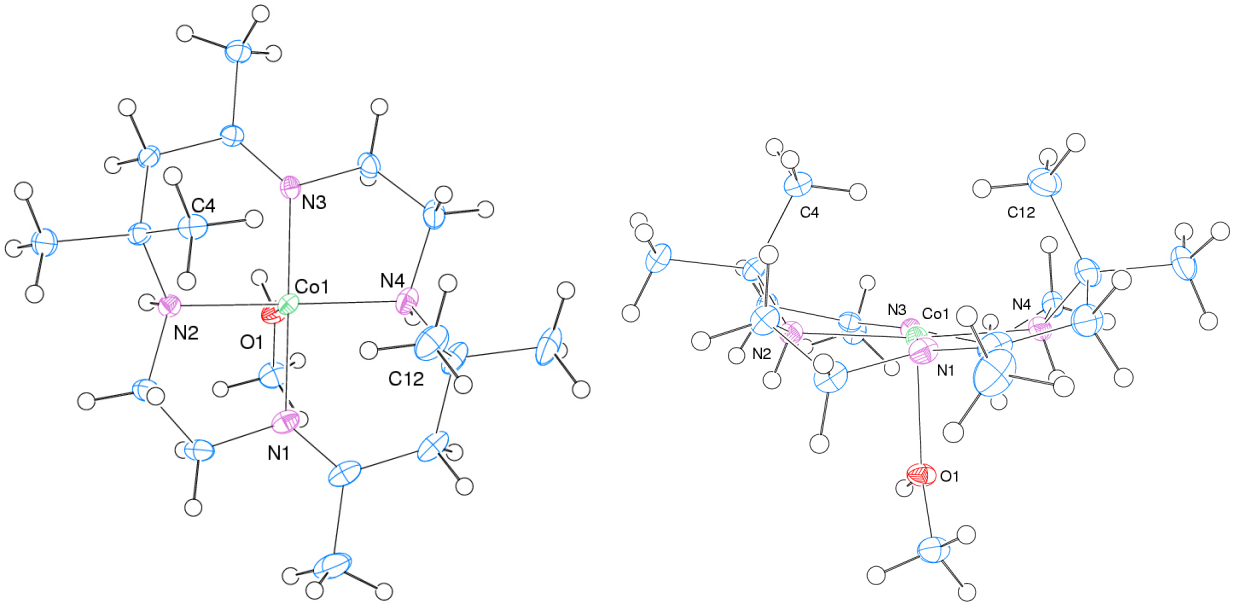

Figure 3.3 ORTEP drawings of crystal structure of $\mathbf{Co^{2+}}(CH_3OH)$. Structures are drawn with thermal ellipsoids at 40% probability.

3.3 Results and discussion

The goal of the research presented in this chapter is to carry out the following series of reactions, in which photoinitiated electron transfer reactions first prepare the substrate-active states of each catalyst, and the sensitized catalysts then bind and transform H_2 and CO_2 into oxidized and reduced products, respectively. For these experiments, ZnTPP was used as the chromophore and pyrrolidine (abbreviated as pyrr) was used as the base. The set of reactions is as follows:

(1) $\mathbf{Ni^{+}} + H_2 + pyrr + ZnTPP + h\nu \rightarrow \mathbf{Ni{-}H^{+}} + pyrrH^{+} + ZnTPP^{-}$

(2) $\mathbf{Ni{-}H^{+}} + pyrr + ZnTPP + h\nu \rightarrow \mathbf{Ni^{+}} + pyrrH^{+} + ZnTPP^{-}$

(3) $\mathbf{Co^{2+}} + ZnTPP^{-} \rightarrow \mathbf{Co^{+}} + ZnTPP$

(4) $\mathbf{Co^{+}} + CO_2 + pyrr \rightarrow \mathbf{(pyrr)Co(CO_2)^{+}}$

In order to investigate the conditions under which $\mathbf{Ni^{+}}$ and $\mathbf{Co^{2+}}$ could be photosensitized to their substrate-active states $\mathbf{Ni^{2+}}$ and $\mathbf{Co^{+}}$, we first performed electrochemical experiments to determine the thermodynamics of electron transfer. Having determined the driving force for each electron transfer step, we then carried out transient-absorption experiments to investigate the kinetics and yield of these processes. Finally, we investigated conditions under which it might be possible to achieve reduction of bound CO_2 to CO, and to release the bound CO to achieve catalysis:

(5) $\mathbf{(pyrr)Co(CO_2)^{+}} + ZnTPP^{-} + 2pyrrH^{+} \rightarrow \mathbf{Co(CO)^{2+}} + H_2O + ZnTPP + 3\ pyrr$

Accomplishing this set of reactions would result in photochemically driving the reverse water-gas shift reaction:

(6) $H_2 + CO_2 \rightarrow CO + H_2O$

3.3.1 Electrochemistry of ZnTPP, Ni^{+}, and Co^{2+}.

The ground-state redox potentials for ZnTPP, $\mathbf{Ni^{+}}$, and $\mathbf{Co^{2+}}$ in DMF solution were measured using cyclic and differential pulse voltammetry under various conditions in order to determine the driving force for electron transfer among these components and to determine the conditions under which CO_2 reduction might occur. From these potentials and the known energy of the ZnTPP T_1 excited state, we can calculate the driving forces for electron transfer from $\mathbf{Ni^{+}}$ to the ZnTPP T_1 state, and for thermal electron transfer from $ZnTPP^{-}$ to $\mathbf{Ni^{2+}}$ (back-electron transfer), to another equivalent of $\mathbf{Ni^{+}}$ (unproductive forward-electron transfer), and to $\mathbf{Co^{2+}}$ (productive forward-electron transfer). The potentials are shown in Table 3.1. Addition of pyrrolidine, which is used as both as a base to deprotonate $\mathbf{Ni{-}H_2^{2+}}$ and as a ligand to effect

intramolecular electron transfer from Co to CO_2 in **(L)Co(CO_2)$^+$**, results in a small change (20-30 mV) in the redox potentials of **Ni$^+$** under N_2. Under CO_2 and in the presence of pyrrolidine, the redox potentials of ZnTPP and **Ni$^+$** do not shift markedly. However, as originally reported by Lewis and co-workers, the reduction potential for **Co^{2+}** shifts positive under CO_2 by 220 mV, from −1.77 V to −1.55 V, reflective of the high binding constant for CO_2 binding to **Co$^+$**.[20] Under CO_2, addition of pyrrolidine shifts the reduction potential of **Co^{2+}** more negative by 110 mV, while under N_2, addition of pyrrolidine has no effect on this potential.

Table 3.1 Redox potentials of ZnTPP, **Ni$^+$**, and **Co^{2+}** in DMF with 0.1 M [^{n}Bu$_4$N][PF_6], referenced to the $Fc^{0/+}$ couple. Redox couples are reversible unless specified.

	without pyrrolidine		with pyrrolidine	
	N_2	CO_2	N_2	CO_2
Ni$^{+/2+}$	−0.88	−0.88	−0.85	−0.85
Ni$^{+/0}$	−1.39 [a]	−1.39 [a]	−1.37 [a]	−1.37 [a]
Co$^{2+/+}$	−1.77	−1.55 [b]	−1.77	−1.66 [b]
ZnTPP$^{0/-}$	−1.80	−1.80	−1.82	−1.82
ZnTPP$^{*(T1)/-}$	−0.21	−0.21	−0.23	−0.23

[a] Partially reversible due to precipitation of **Ni^0**. [b] Irreversible.

In order to investigate the source of the dramatic effect addition of pyrrolidine has on the reduction potential of **Co^{2+}** when measured under CO_2, we studied mixtures of Co^+, CO_2, and pyrrolidine by electronic-absorption spectroscopy. Solutions of **Co$^+$** were prepared in situ from acetonitrile by reduction using Na/Hg amalgam.[24] This dark blue complex exhibits a strong band centered at 678 nm, as shown in Figure 3.4. As originally reported by Fujita and co-workers, addition of CO_2 to a solution of **Co$^+$** results in a pronounced change in the spectrum as the result of CO_2 coordination to the metal center.[23] The 678 nm band disappears, and in its place a band at 530 nm forms, assigned by Fujita and co-workers to the five-coordinate complex **Co(CO_2)$^+$**. Addition of pyrrolidine to a solution of **Co$^+$** does not perturb the band at 680 nm. However, the band at 530 nm in **Co(CO_2)$^+$** is dramatically affected by addition of pyrrolidine, with the 530 nm band disappearing completely and a weaker band at 445 nm forming. This shift is analogous to

the behavior reported by Fujita and co-workers upon cooling of solutions of **Co(CO₂)⁺**, allowing acetonitrile or propionitrile (the solvent) to coordinate *trans* to the CO_2 ligand to form **(S)Co(CO₂)⁺**. This coordination is hypothesized on the basis of XANES evidence to result in the net transfer of another electron from the metal center to the CO_2 ligand, resulting in a complex **(S)Co(CO₂)⁺** in which the Co center is formally Co^{III} and the CO_2 is formally CO_2^{2-}.[23] We hypothesize that the much greater Lewis basicity of pyrrolidine compared to acetonitrile allows this six-coordinate complex to form at room temperature, instead of only at low temperature, resulting in the spectrum observed.

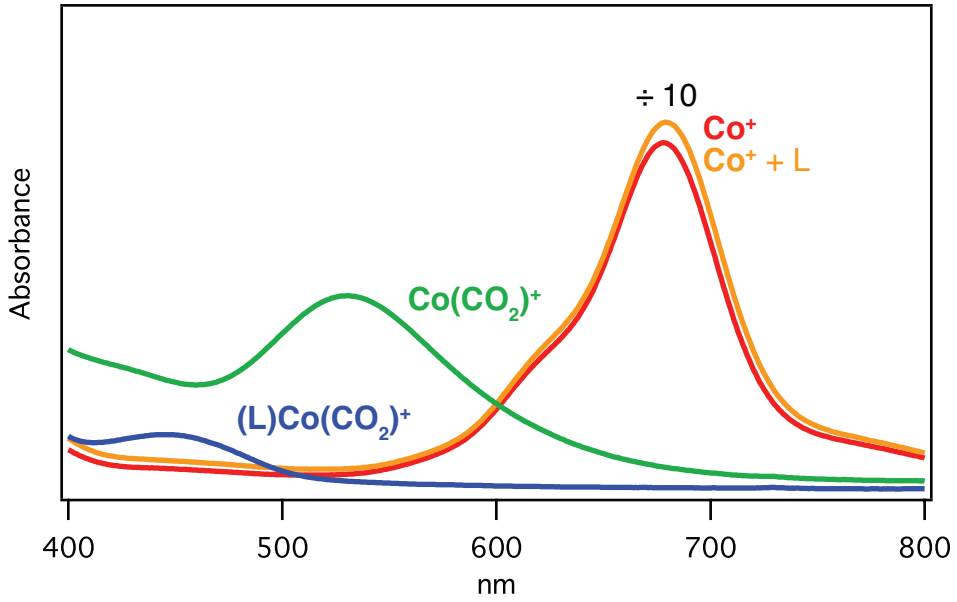

Figure 3.4 Electronic absorption spectra of **Co⁺** (prepared in situ by Na/Hg reduction of **Co²⁺**) in acetonitrile under various conditions.

The observation that pyrrolidine binds to **Co(CO₂)⁺** at room temperature explains the observed negative shift of the reduction of **Co²⁺** under CO_2 in the presence of pyrrolidine. In our hypothesis, the extra electron density transferred to the CO_2 in the formation of **(L)Co(CO₂)⁺** electrostatically destabilizes the molecule by forming a zwitterion, and this destabilization makes the reduction potential more negative. Based on this observation, we hypothesized that an added

Lewis acid might coordinate to the **(L)Co(CO$_2$)$^+$** zwitterion, potentially activating it for C–O bond cleavage upon further reduction, as depicted in Scheme 3.4. Precedent for this comes from work by Savéant and co-workers on the electrocatalyzed reduction of CO_2 using Fe(0) tetraarylporphyrins.[41] In that work, it was found that addition of alkali or alkaline-earth metal cations was able to stabilize the CO_2 molecule bound to the Fe center, and improve both the catalytic activity and the lifetime of the catalyst, with Mg^{2+} being among the most effective Lewis acids for this purpose. In this vein, Lewis investigated the effect of Li^+ addition on the redox potentials of **Co^{2+}** in acetonitrile under N_2 and CO_2 and reported no significant effect of Li^+ addition.[20] However, that report did not include any alkaline earth dications, which were found by Savéant to be much more effective than alkali metal monocations.[41]

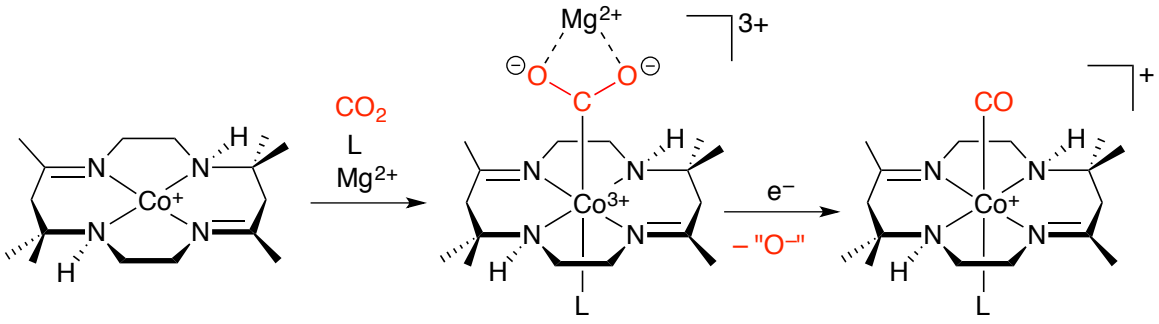

Scheme 3.4 Hypothesized stabilization of **(L)Co(CO$_2$)$^+$** by Mg^{2+}.

In Scheme 3.4, the nature of the species associated with the loss of O^- is not known. In their studies of Mg^{2+}-assisted reduction of CO_2 by Fe^0(TPP), Savéant and co-workers describe the species as "CO_3Mg^{+}", formed by reductive disproportionation of bound CO_2 by a second equivalent of CO_2. In our system, the nature of this species has not been investigated, and is likely to vary under conditions of differing proton availability, and so we represent it merely as "O^-".

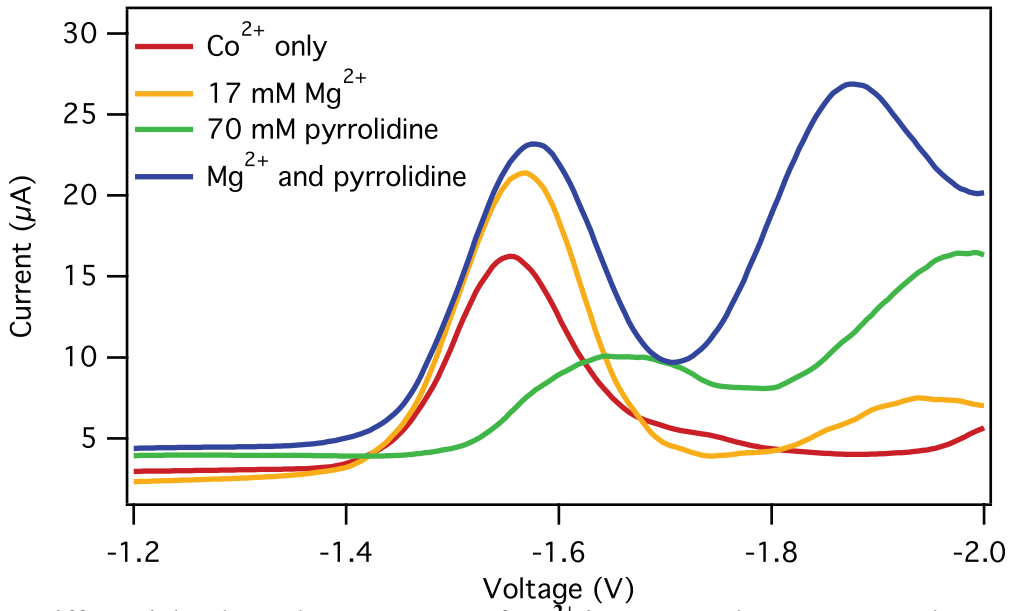

Figure 3.5 Differential pulse voltammograms of $\mathbf{Co^{2+}}$ in DMF under CO_2 atmosphere, with 0.1 M [^{n}Bu$_4$N][PF_6] and other reagents as listed, referenced to the $Fc^{0/+}$ couple.

In order to investigate the effect of adding Mg^{2+} to solutions of $\mathbf{Co^{2+}}$ under CO_2, we first performed differential pulse voltammery (DPV) to determine the reduction potentials under different conditions. As shown in Figure 3.5 and summarized in Table 3.2, addition of 17 mM $Mg(ClO_4)_2$ to a solution of $\mathbf{Co^{2+}}$ has a minimal effect on the first reduction of $\mathbf{Co^{2+}}$ under CO_2, shifting the first reduction negative by only 20 mV (reduction of $\mathbf{Co^{2+}}$ under N_2 is completely unaffected, just as it is when pyrrolidine is added under N_2). However, addition of 17 mM $Mg(ClO_4)_2$ to a solution of $\mathbf{Co^{2+}}$ containing 70 mM pyrrolidine shifts the reduction potential positive by 80 mV. This suggests that Mg^{2+} is able to react with $\mathbf{(L)Co(CO_2)^+}$ to form a stabilized Mg^{2+} adduct $\mathbf{(L)Co(CO_2Mg)^{3+}}$.

Addition of Mg^{2+} also had an effect on the second reduction of $\mathbf{Co^{2+}}$ under CO_2. This reduction is barely accessible within the potential window in the absence of pyrrolidine or Mg^{2+} [42]. Addition of either Lewis base or Lewis acid shifts this potential positive, and the combination of pyrrolidine and Mg^{2+} shifts it to −1.87 V.

Table 3.2 Reduction potentials of $\mathbf{Co^{2+}}$ in DMF under CO_2 atmosphere unless otherwise specified, with 0.1 M [$^nBu_4N$][PF_6], referenced to the $Fc^{0/+}$ couple.

Conditions	first reduction	second reduction
pure DMF, N_2	−1.77	not observed
pure DMF	−1.55	not observed
+ 70 mM pyrrolidine	−1.66	−1.99
+ 17 mM $Mg(ClO_4)_2$	−1.57	−1.94
+ 70 mM pyrrolidine and 17 mM $Mg(ClO_4)_2$	−1.58	−1.87

Having determined the reduction potentials using DPV, we then sought to investigate the reversibility of each reduction using cyclic voltammetry (CV). CV scans of $\mathbf{Co^{2+}}$ in the absence of pyrrolidine and Mg^{2+} shows only one reversible reduction under CO_2 ($E_{1/2}$ = −1.55 V). Cyclic voltammograms of $\mathbf{Co^{2+}}$ (Figure 3.6) in the presence of pyrrolidine and Mg^{2+} under atmospheres of different gases showed that the first reduction is reversible under N_2 (red trace), while under CO_2 (blue traces) it is shifted positive and becomes irreversible at scan rates ≤ 400 mV/s. This suggests that $\mathbf{(L)Co(CO_2Mg)^{2+}}$, the product of reduction of $\mathbf{(L)Co(CO_2Mg)^{3+}}$, is unstable toward a chemical reaction of the CO_2 ligand. The second reduction is not observed under N_2 at potentials as negative as −2.0 V; under CO_2, it is observed at −1.87 V (irreversible) and paired with a return wave at −1.14 V. These results are interpreted as being consistent with the production of $\mathbf{Co(CO)^+}$, based on the following additional observations. The cyclic voltammogram of $\mathbf{Co^{2+}}$ under a CO atmosphere (green trace) shows a single reduction wave at a potential very close to that of the first reduction of $\mathbf{Co^{2+}}$ under CO_2, and a corresponding oxidative wave at −1.14 V. This behavior was originally reported by Fujita and co-workers and explained by a E_rC_i mechanism in which reduction of $\mathbf{Co^{2+}}$ is followed by rapid binding of CO to form $\mathbf{Co(CO)^+}$, and oxidation of $\mathbf{Co(CO)^+}$ at −1.14 V is followed by loss of CO. We posit that the second reduction of $\mathbf{Co^{2+}}$ observed under CO_2 in the presence of pyrrolidine and Mg^{2+}, with its corresponding oxidative wave at −1.14V, indicates the operation of a similar mechanism, in

which CO_2 is bound at the first reduction, transformed into **Co(CO)**$^{+}$ at the second reduction, and released as CO upon oxidation.

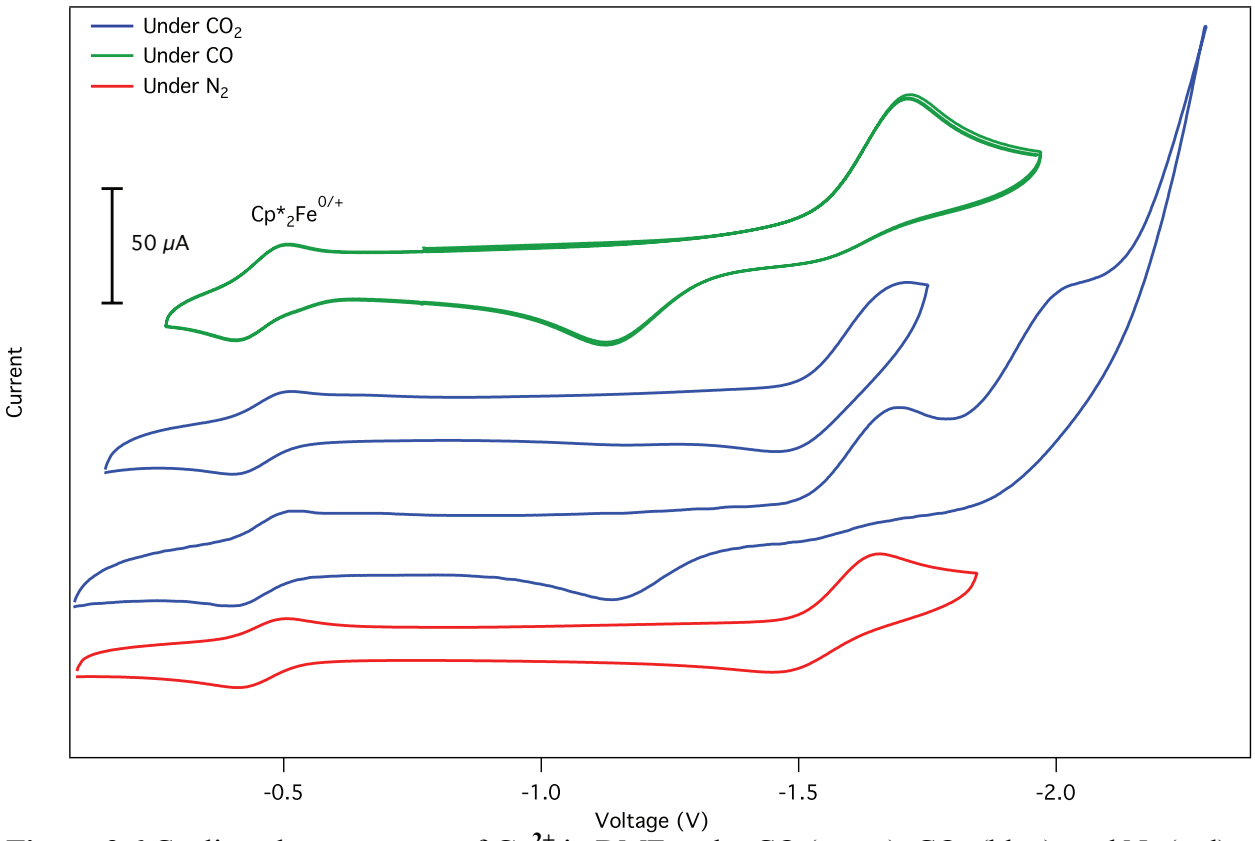

Figure 3.6 Cyclic voltammagrams of **Co**$^{2+}$ in DMF under CO (green), CO_2 (blue), and N_2 (red) with 0.1 M [$^{n}Bu_4N$][PF_6], 70 mM pyrrolidine, 200 mM MeOH and 17 mM $Mg(ClO_4)_2$, with internal $FeCp^*_2$ (potential adjusted for reference to the $Fc^{0/+}$ couple). All CVs were acquired at a scan rate of 400 mV/s.

The second reduction of **Co**$^{2+}$ under CO_2 in the presence of both Mg^{2+} and pyrrolidine occurs at −1.87 V, making the reaction **(L)Co(CO$_2$Mg)**$^{3+}$ + $ZnTPP^-$ → **(L)Co(CO$_2$Mg)**$^{2+}$ + ZnTPP close to thermoneutral (ΔG = +0.07 V). We hypothesized that it might be possible, under carefully chosen circumstances, to effect this second reduction photochemically and thereby achieve reduction of CO_2 to CO.

3.3.2 Photoredox sensitization of Ni^+ and Co^{2+} by the ZnTPP T_1 state.

In order to investigate the photoprocesses of mixtures of ZnTPP, $\mathbf{Ni^+}$, and $\mathbf{Co^{2+}}$ under different conditions, we carried out transient-absorption experiments to determine the kinetics and yield of each electron transfer step, both productive and unproductive, as follows:

Productive reactions:

(1) $\mathbf{Ni^+} + \text{ZnTPP*} \rightarrow \mathbf{Ni^{2+}} + \text{ZnTPP}^-$

(2) $\mathbf{Co^{2+}} + \text{ZnTPP}^- \rightarrow \mathbf{Co^+} + \text{ZnTPP}$

Substrate trapping and transformation reactions:

(3) $\mathbf{Ni^{2+}} + H_2 \rightarrow \mathbf{Ni{-}H_2^{2+}}$

(4) $\mathbf{Ni{-}H_2^{2+}} + \text{pyrr} \rightarrow \mathbf{Ni{-}H^+} + \text{pyrrH}^+$

(5) $\mathbf{Ni{-}H^+} + \text{ZnTPP*} \rightarrow \mathbf{Ni{-}H^{2+}} + \text{ZnTPP}^-$

(6) $\mathbf{Ni{-}H^{2+}} + \text{pyrr} \rightarrow \mathbf{Ni^+} + \text{pyrrH}^+$

(7) $\mathbf{Co^+} + CO_2 \rightarrow \mathbf{Co(CO_2)^+}$

Deactivation or unproductive reactions:

(8) $\mathbf{Ni^{2+}} + \text{ZnTPP}^- \rightarrow \mathbf{Ni^+} + \text{ZnTPP}$

(9) $\mathbf{Ni^+} + \text{ZnTPP}^- \rightarrow \mathbf{Ni^0} + \text{ZnTPP}$

(10) $\mathbf{Ni^{2+}} + \mathbf{Co^+} \rightarrow \mathbf{Ni^+} + \mathbf{Co^{2+}}$

(11) $\mathbf{Ni^+} + \mathbf{Co^+} \rightarrow \mathbf{Ni^0} + \mathbf{Co^{2+}}$

(12) $\mathbf{Ni^{2+}} + \mathbf{Ni^0} \rightarrow 2\mathbf{Ni^+}$

All photophysical experiments, including quenching experiments investigating the quenching rate of $\text{ZnTPP*}^{(T1)}$ by $\mathbf{Ni^+}$ (in which $\mathbf{Co^{2+}}$ is not expected to participate) were performed on solutions containing $\mathbf{Co^{2+}}$. This was done for several reasons. First, owing to the extreme reactivity of ZnTPP^- with trace air or water present in solution, solutions not containing $\mathbf{Co^{2+}}$ were observed to contain porphryin degradation products (detectable at very low concentration by their strong Soret and Q bands that are redshifted from those of ZnTPP). When $\mathbf{Co^{2+}}$ is present in solution, these degradation products are not observed by UV/Vis spectroscopy. Second, ZnTPP^- can reduce $\mathbf{Ni^+}$ to $\mathbf{Ni^0}$ (Reaction 9), which will precipitate and make the solution unsuitable for further optical experiments. We therefore sought to slow the formation of $\mathbf{Ni^0}$ by oxidizing ZnTPP^- with $\mathbf{Co^{2+}}$ (Reaction 2), producing $\mathbf{Co^+}$, which reacts slowly with $\mathbf{Ni^+}$ (reaction 11), thereby prolonging the useful experimental lifetime of the solution.

Addition of millimolar concentrations of **Ni**$^{+}$ to a DMF solution of ZnTPP and **Co**$^{2+}$ results in a marked shortening of the ZnTPP T_1 lifetime, as observed by nanosecond transient absorption spectroscopy. Using the Stern-Volmer relationship (see Figure 3.7) the quenching rate was determined to be 1.8×10^8 M^{-1} s^{-1} in DMF with 70 mM pyrrolidine (a similar concentration to that used in photochemical H_2 oxidation experiments).[19] This value is consistent with the quenching rate observed by Westwood for **Ni**$^{+}$ with $Ru(bpy)_3^{2+}$ (4.8×10^8 M^{-1} s^{-1} in PhCN).

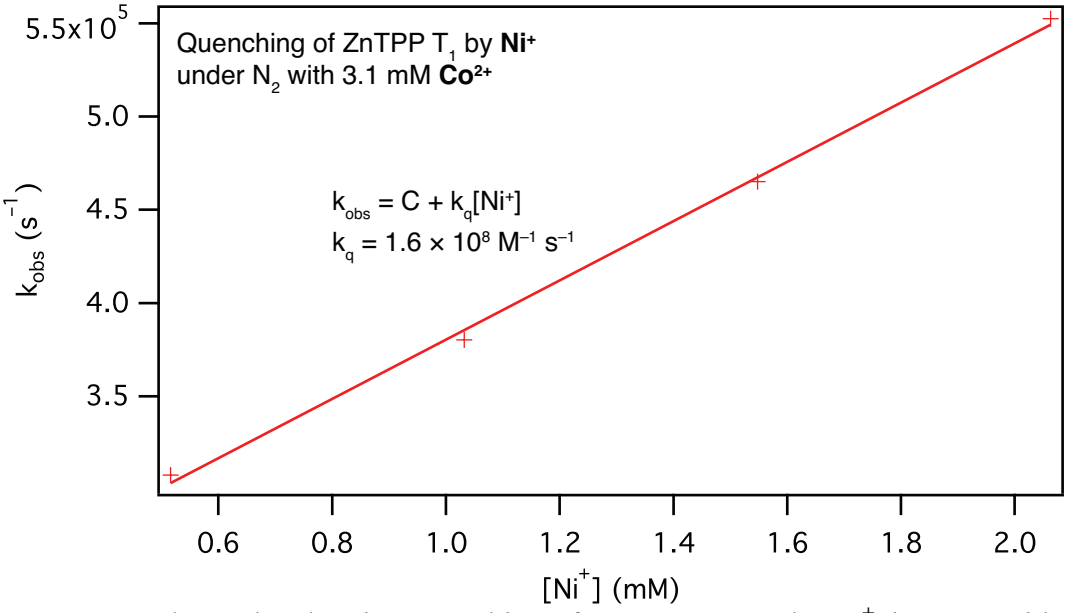

Figure 3.7 Stern-Volmer plot showing quenching of ZnTPP T_1 state by **Ni**$^{+}$, in DMF with 3.1 mM **Co**$^{2+}$.

The photochemical processes that take place in a DMF solution of ZnTPP, **Ni**$^{+}$, **Co**$^{2+}$, and pyrrolidine were probed by transient-absorption spectroscopy. Under an atmosphere of nitrogen, a DMF solution containing 1.1 mM **Ni**$^{+}$, 3.1 mM **Co**$^{2+}$, 70 µM ZnTPP and 70 mM pyrrolidine excited at 547 nm exhibits transient features corresponding to the ZnTPP S_1 and T_1 states.[43] As shown in Figure 3.8, in the first 250 ns after excitation, the spectrum exhibits negative features at 605 and 650 nm (not visible in Figure 3.8 because the features are off-scale), corresponding to a combination of bleaching of the Q(0,0) band and S_1 fluorescence (Q(0,0) and Q(0,1)), and absorptions at 740 nm (broad) and 825 nm (sharp) corresponding to the ZnTPP T_1 state. By 1 µs,

the emission features have disappeared and the spectrum exhibits only the T_1 absorption and S_0 bleach features. Over the next tens of microseconds, those features also decay, leaving behind a very weak absorption at 700 nm. This band is likely due to production of a small amount of $\mathbf{Co^{+}}$, which is reported to absorb at 695 nm in DMF.[24,44] While weak, that band persists, not weakening in intensity, for the duration of the TA experiment (80 μs). We thus conclude that the following series of reactions have taken place:

Productive reactions:

(1) $\mathbf{Ni^{+}} + \text{ZnTPP*} \rightarrow \mathbf{Ni^{2+}} + \text{ZnTPP}^{-}$

(2) $\mathbf{Co^{2+}} + \text{ZnTPP}^{-} \rightarrow \mathbf{Co^{+}} + \text{ZnTPP}$ (minor pathway)

Deactivation or unproductive reactions:

(3) $\mathbf{Ni^{2+}} + \text{ZnTPP}^{-} \rightarrow \mathbf{Ni^{+}} + \text{ZnTPP}$

(4) $\mathbf{Ni^{+}} + \text{ZnTPP}^{-} \rightarrow \mathbf{Ni^{0}} + \text{ZnTPP}$

(5) $\mathbf{Ni^{2+}} + \mathbf{Co^{+}} \rightarrow \mathbf{Ni^{+}} + \mathbf{Co^{2+}}$

(6) $\mathbf{Ni^{+}} + \mathbf{Co^{+}} \rightarrow \mathbf{Ni^{0}} + \mathbf{Co^{2+}}$

(7) $\mathbf{Ni^{2+}} + \mathbf{Ni^{0}} \rightarrow 2\mathbf{Ni^{+}}$

Reactions 1 and 3 occur in high yield, producing and subsequently consuming ZnTPP^{-}. Some of the ZnTPP^{-} produced can react with a second equivalent of $\mathbf{Ni^{+}}$ to produce $\mathbf{Ni^{0}}$ (Reaction 4), which recombines with $\mathbf{Ni^{2+}}$ to produce two equivalents of $\mathbf{Ni^{+}}$ (Reaction 7). A small amount of ZnTPP^{-} produced by reaction 1 is able to react with $\mathbf{Co^{2+}}$ (Reaction 2) to produce $\mathbf{Co^{+}}$, which we observe in low yield, and which decays either through back-electron transfer to $\mathbf{Ni^{2+}}$ (Reaction 5) or forward electron transfer to a second equivalent of $\mathbf{Ni^{+}}$ (Reaction 6). These reactions are inferred to be slow, based on the observation that the weak $\mathbf{Co^{+}}$ signal is long-lived (>80 μs).

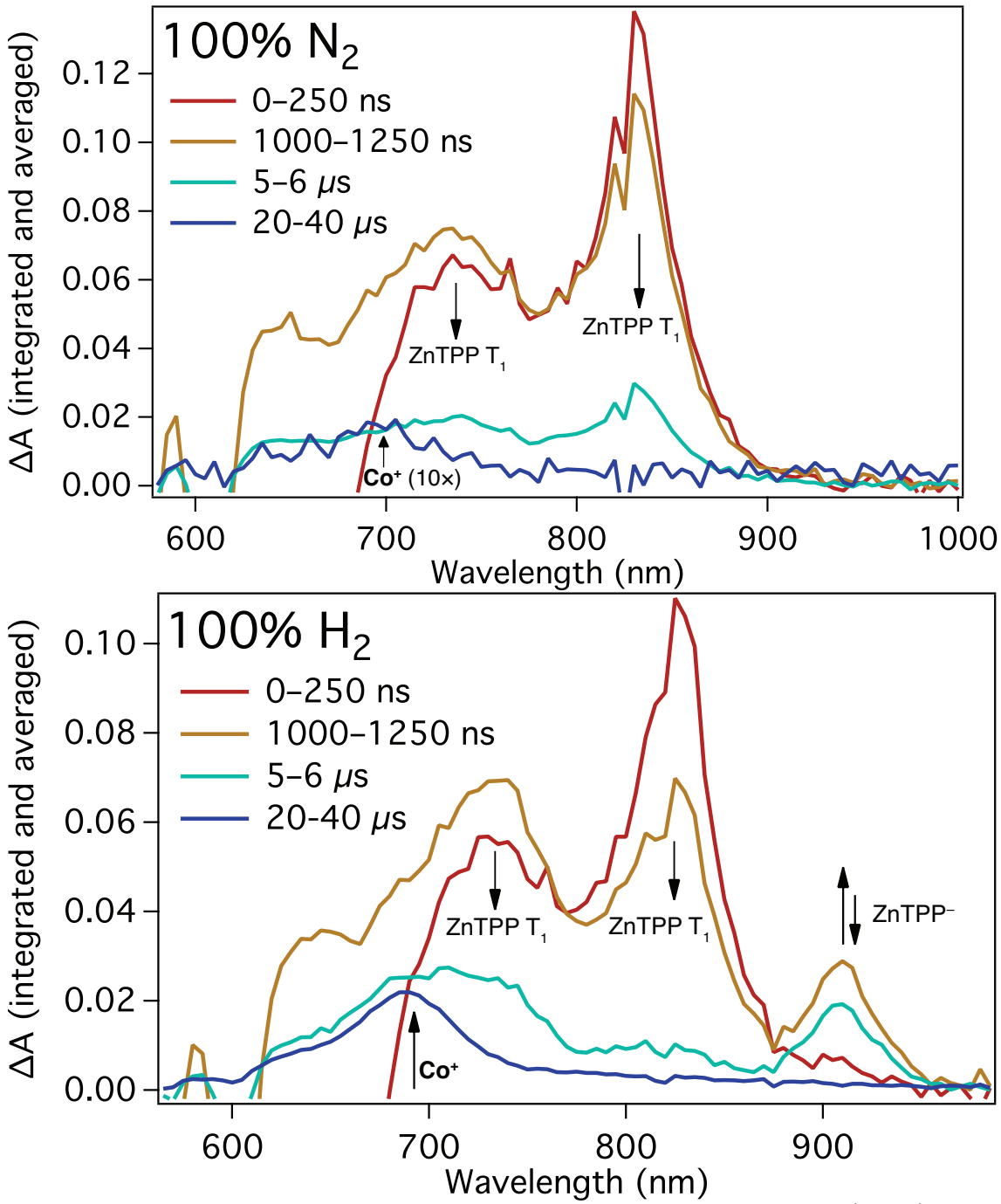

Figure 3.8 *Top*: Transient-absorption spectrum (λ_{ex} = 547 nm) of solution of $\mathbf{Ni^+}$ ([$\mathbf{Ni^+}$] = 1.1 mM), $\mathbf{Co^{2+}}$ ([$\mathbf{Co^{2+}}$] = 3.1 mM), and ZnTPP in DMF containing 70 mM pyrrolidine under N_2 atmosphere. Spectra are integrated and averaged over the time ranges shown to allow intensities to be compared over different time windows. Spectrum from 20−40 μs magnified 10× to show faint band of $\mathbf{Co^+}$. *Bottom*: Transient-absorption spectrum (λ_{ex} = 551 nm) of solution of $\mathbf{Ni^+}$ ([$\mathbf{Ni^+}$] = 1.2 mM), $\mathbf{Co^{2+}}$ ([$\mathbf{Co^{2+}}$] = 3.1 mM), and ZnTPP in DMF containing 70 mM pyrrolidine under 100% H_2 atmosphere. Spectra are integrated and averaged over the time ranges shown to allow intensities to be compared over different time windows.

Under an atmosphere of 100% H_2, the TA spectra differ from those observed under N_2 in several notable respects, as shown in Figure 3.8. At short times (0−250 ns), the spectrum is nearly identical to that seen under N_2, displaying bands that correspond to the ZnTPP T_1 state: the strong, sharp band at 825 nm, broader band at 740 nm, and negative features corresponding to S_0 bleaching and fluorescence (Q(0,1) and Q(0,0)) at 650 nm and 605 nm. Over the next 1 μs the spectrum evolves, with the emission features disappearing, the ZnTPP T_1 feature at 825 nm weakening but the absorbance in the region of the T_1 band at 740 nm increasing, and a band at 905 nm growing in. This band corresponds to the $ZnTPP^-$ radical (reported at 905 nm in DMF);[34] it is not observed in the spectrum measured under N_2. The $ZnTPP^-$ anion also exhibits a band at 710 nm with intensity roughly equal to the intensity of the 905 nm band, and a band at 800 nm which is roughly half as intense,[34] but these are hidden by the stronger ZnTPP T_1 features that persist. By 5 μs, the bands from the ZnTPP T_1 state have diminished significantly, leaving behind the $ZnTPP^-$ feature at 905 nm, as well as a weaker feature at 815 nm and a broad, unsymmetrical band from 690−740 nm. The weak 815 nm band is assigned to overlapping absorption from ZnTPP T_1 and $ZnTPP^-$, while the broad band at from 690−740 nm is assigned to overlapped absorptions from ZnTPP T_1, $ZnTPP^-$ at 710 nm and from $\mathbf{Co}^+$, which is reported in DMF at 695 nm (a redshift of 17 nm relative to the same band in acetonitrile).[24,44] Over the course of the following 10 μs, the porphyrin-based absorptions are all observed to decay, leaving behind only a band at 690 nm, corresponding to $\mathbf{Co}^+$. In contrast to the spectrum under N_2, this band is strong, indicating that $\mathbf{Co}^+$ is being produced in much higher yield than under N_2. Owing to its strength, the decay kinetics of this band can be measured and were fit to a single-exponential with a lifetime of 12.0 ± 0.2 ms (Figure 3.9).

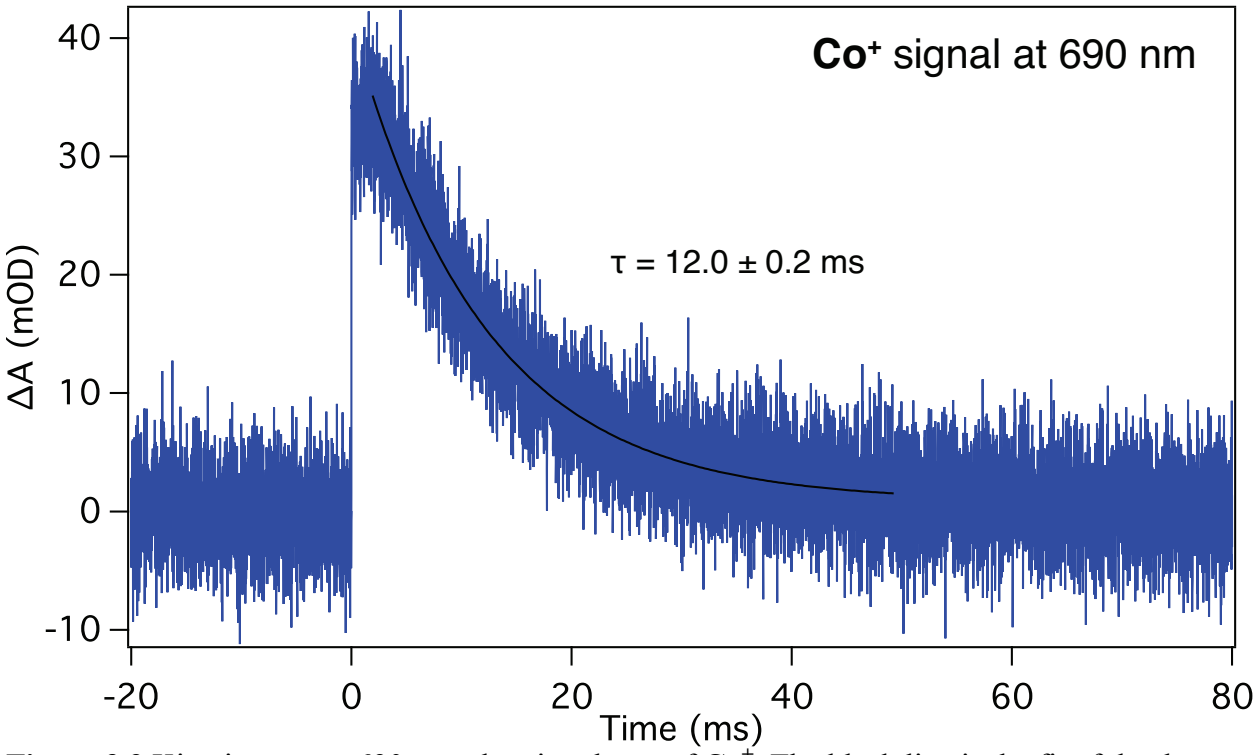

Figure 3.9 Kinetic trace at 690 nm, showing decay of $\mathbf{Co}^{+}$. The black line is the fit of the data to a single exponential decay.

Thus, comparing the photochemistry of ZnTPP with $\mathbf{Co}^{2+}$ and $\mathbf{Ni}^{+}$ under N_2 and H_2, it is evident that addition of the substrate H_2 results in increases to the concentrations of both of $ZnTPP^{-}$ and $\mathbf{Co}^{+}$. This is presumably because the rapid binding of H_2 to photogenerated $\mathbf{Ni}^{2+}$ reduces the efficiency of back electron transfer from $ZnTPP^{-}$ and $\mathbf{Co}^{+}$. The set of reactions occurring under H_2 is thus:

H_2 oxidation reactions:

(1) $\mathbf{Ni}^{+} + \text{ZnTPP}^{*} \rightarrow \mathbf{Ni}^{2+} + \text{ZnTPP}^{-}$

(2) $\mathbf{Ni}^{2+} + H_2 \rightarrow \mathbf{Ni{-}H_2}^{2+}$

(3) $\mathbf{Ni{-}H_2}^{2+} + \text{pyrr} \rightarrow \mathbf{Ni{-}H}^{+} + \text{pyrrH}^{+}$

(4) $\mathbf{Ni{-}H}^{+} + \text{ZnTPP}^{*} \rightarrow \mathbf{Ni{-}H}^{2+} + \text{ZnTPP}^{-}$

(5) $\mathbf{Ni{-}H}^{2+} + \text{pyrr} \rightarrow \mathbf{Ni}^{+} + \text{pyrrH}^{+}$

Productive reactions:

(6) $\mathbf{Co}^{2+} + \text{ZnTPP}^{-} \rightarrow \mathbf{Co}^{+} + \text{ZnTPP}$

Deactivation or unproductive reactions:

(7) $\mathbf{Ni}^{2+} + \text{ZnTPP}^{-} \rightarrow \mathbf{Ni}^{+} + \text{ZnTPP}$

(8) $\mathbf{Ni}^{+} + \text{ZnTPP}^{-} \rightarrow \mathbf{Ni}^{0} + \text{ZnTPP}$

(9) $\mathbf{Ni}^{2+} + \mathbf{Co}^{+} \rightarrow \mathbf{Ni}^{+} + \mathbf{Co}^{2+}$

(10) $\mathbf{Ni}^{+} + \mathbf{Co}^{+} \rightarrow \mathbf{Ni}^{0} + \mathbf{Co}^{2+}$

(11) $\mathbf{Ni}^{0} + \mathbf{Ni}^{2+} \rightarrow 2\mathbf{Ni}^{+}$

Just as was the case above under N_2, reaction 1 takes place in high yield to produce $\mathbf{Ni}^{2+}$ and ZnTPP^{-}. Unlike under N_2, however, reactions 2 and 3 consume $\mathbf{Ni}^{2+}$, suppressing back-electron transfer reaction 7. Additional ZnTPP^{-} is produced by reactions 4 and 5. Together, these processes increase the yield of productive reaction 6, leading to a higher observed concentration of $\mathbf{Co}^{+}$. Consumption of $\mathbf{Ni}^{2+}$ also suppresses back-electron transfer reaction 10. Unproductive forward electron transfer from ZnTPP^{-} or $\mathbf{Co}^{+}$ to a second equivalent of $\mathbf{Ni}^{+}$, producing $\mathbf{Ni}^{0}$, is still able to occur (reactions 8 and 9). $\mathbf{Ni}^{0}$ thus produced is able to recombine with an equivalent of $\mathbf{Ni}^{2+}$ to produce two equivalents of $\mathbf{Ni}^{+}$ (reaction 11). Based on the extremely long observed lifetime of $\mathbf{Co}^{+}$, we conclude that electron transfer from $\mathbf{Co}^{+}$ to $\mathbf{Ni}^{+}$ (reaction 10), the only decay pathway available in the absence of $\mathbf{Ni}^{2+}$, must be extremely slow.

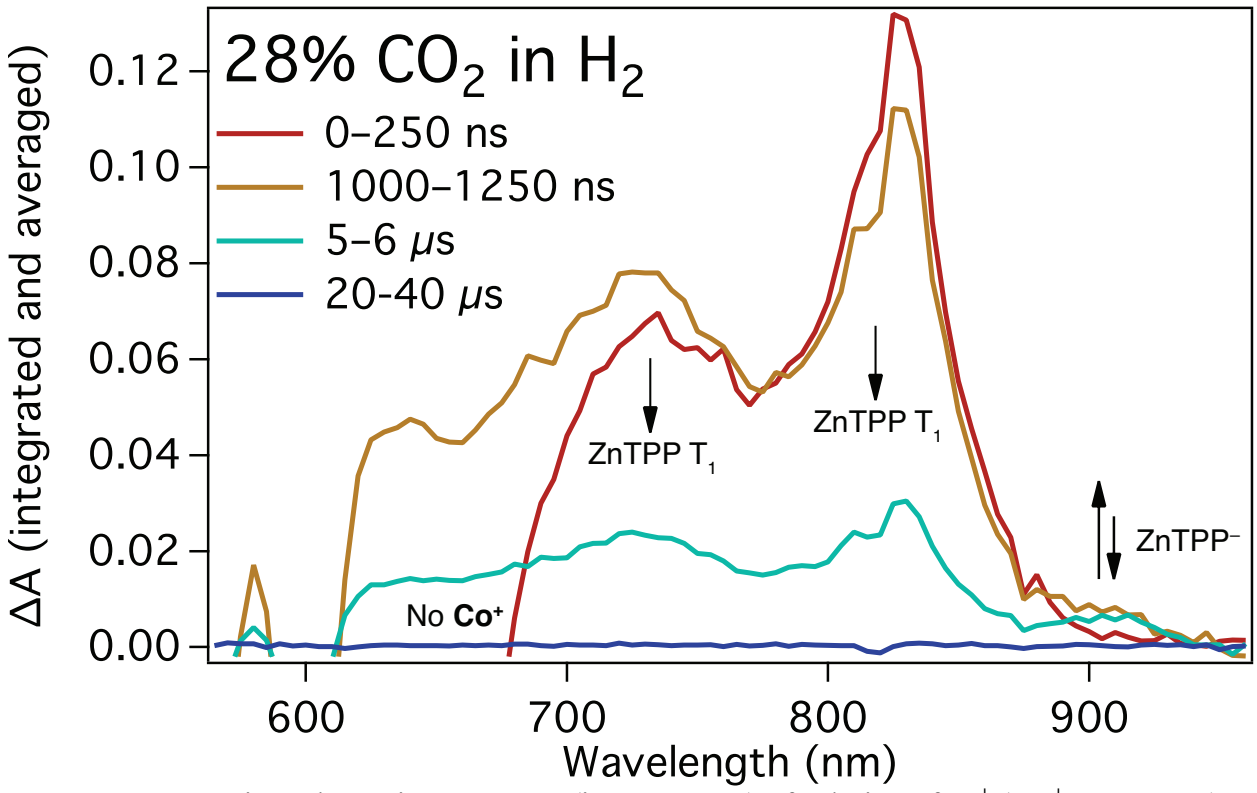

Figure 3.10 Transient-absorption spectrum (λ_{ex} = 551 nm) of solution of $\mathbf{Ni^+}$ ([$\mathbf{Ni^+}$] = 1.2 mM), $\mathbf{Co^{2+}}$ ([$\mathbf{Co^{2+}}$] = 3.1 mM), and ZnTPP in DMF containing 70 mM pyrrolidine under 28% CO_2 in H_2 atmosphere. Spectra are integrated and averaged over the time ranges shown to allow intensities to be compared over different time windows.

The TA spectra acquired under a mixture of H_2 with 28% CO_2 (Figure 3.10) differ from those obtained under pure H_2, and instead resemble those seen under N_2. As with the other samples, the spectra observed at short times (up to ~250 ns) display only features corresponding to the ZnTPP T_1 state. At long times, however, these signals simply decay. The band at 690 nm seen under pure H_2, corresponding to $\mathbf{Co^+}$, is not observed, and the signal in the region of the 905 nm band due to $ZnTPP^-$ seen under H_2 is very weak. Thus, compared with the sample under H_2, the added CO_2 either interferes with the trapping of $\mathbf{Ni^{2+}}$ by H_2 or rapidly consumes $\mathbf{Co^+}$ and/or $ZnTPP^-$. Therefore, we conclude that the sequence of reactions that take place in the presence of both H_2 and CO_2 are the following:

H_2 oxidation reactions:

(1) $\mathbf{Ni^{+}} + \text{ZnTPP*} \rightarrow \mathbf{Ni^{2+}} + \text{ZnTPP}^{-}$

(2) $\mathbf{Ni^{2+}} + H_2 \rightarrow \mathbf{Ni{-}H_2^{2+}}$

(3) $\mathbf{Ni{-}H_2^{2+}} + \text{pyrr} \rightarrow \mathbf{Ni{-}H^{+}} + \text{pyrrH}^{+}$

(4) $\mathbf{Ni{-}H^{+}} + \text{ZnTPP*} \rightarrow \mathbf{Ni{-}H^{2+}} + \text{ZnTPP}^{-}$

(5) $\mathbf{Ni{-}H^{2+}} + \text{pyrr} \rightarrow \mathbf{Ni^{+}} + \text{pyrrH}^{+}$

CO_2 reduction reactions:

(6) $\mathbf{Co^{2+}} + CO_2 + \text{ZnTPP}^{-} \rightarrow \mathbf{Co(CO_2)^{+}} + \text{ZnTPP}$

Deactivation or unproductive reactions:

(7) $\mathbf{Ni^{2+}} + \text{ZnTPP}^{-} \rightarrow \mathbf{Ni^{+}} + \text{ZnTPP}$

(8) $\mathbf{Ni^{+}} + \text{ZnTPP}^{-} \rightarrow \mathbf{Ni^{0}} + \text{ZnTPP}$

(9) $\mathbf{Ni^{2+}} + \mathbf{Co(CO_2)^{+}} \rightarrow \mathbf{Ni^{+}} + \mathbf{Co^{2+}} + CO_2$

(10) $\mathbf{Ni^{+}} + \mathbf{Co(CO_2)^{+}} \rightarrow \mathbf{Ni^{0}} + \mathbf{Co^{2+}} + CO_2$

(11) $\mathbf{Ni^{0}} + \mathbf{Ni^{2+}} \rightarrow 2\mathbf{Ni^{+}}$

This sequence is extremely similar to the sequence postulated under pure H_2, with the chief difference being that the rapid binding of CO_2 to $\mathbf{Co^{+}}$ changes the product of reaction 6 to $\mathbf{Co(CO_2)^{+}}$, which we are not able to observe on our equipment. In addition, the stabilization of $\mathbf{Co(CO_2)^{+}}$ relative to $\mathbf{Co^{+}}$ lowers the driving force (see below), and hence the rate, of unproductive reactions 9 and 10.

3.3.3 Analysis of TA results

Several factors come into play when analyzing these transient absorption results. The first consideration for analyzing the transient-absorption spectroscopic results is the driving forces for the various electron transfer reactions that proceed from the ZnTPP T_1 state. The second consideration is the rate at which photogenerated $\mathbf{Ni^{2+}}$ and $\mathbf{Co^{+}}$ trap and transform H_2 and CO_2, respectively. The driving forces for electron transfer are given in Table 3.3 below, and are displayed as an energy-level diagram in Figure 3.11.

Table 3.3 Driving forces in DMF (given in eV) for the electron transfer reactions shown.

	without pyrrolidine		with pyrrolidine	
	N_2/H_2 [a]	CO_2	N_2/H_2	CO_2
$\mathbf{Ni^+} \rightarrow ZnTPP(T_1)$ [b]	−0.67	−0.67	−0.62	−0.62
$ZnTPP^- \rightarrow \mathbf{Co^{2+}}$	−0.03	−0.23	−0.05	−0.23
$ZnTPP^- \rightarrow \mathbf{Ni^+}$	−0.41	−0.41	−0.45	−0.45
$\mathbf{Co^+} \rightarrow \mathbf{Ni^+}$	−0.38	−0.16	−0.40	−0.29
$\mathbf{Co^+} \rightarrow \mathbf{Ni^{2+}}$	−0.89	−0.67	−0.92	−0.81

[a] The redox potentials of ZnTPP and $\mathbf{Co^{2+}}$ were observed to be identical under N_2 and H_2; those for $\mathbf{Ni^+}$ under H_2 have not been reported. [b] Based on E_{00} = 1.59 eV for ZnTPP T_1.[45]

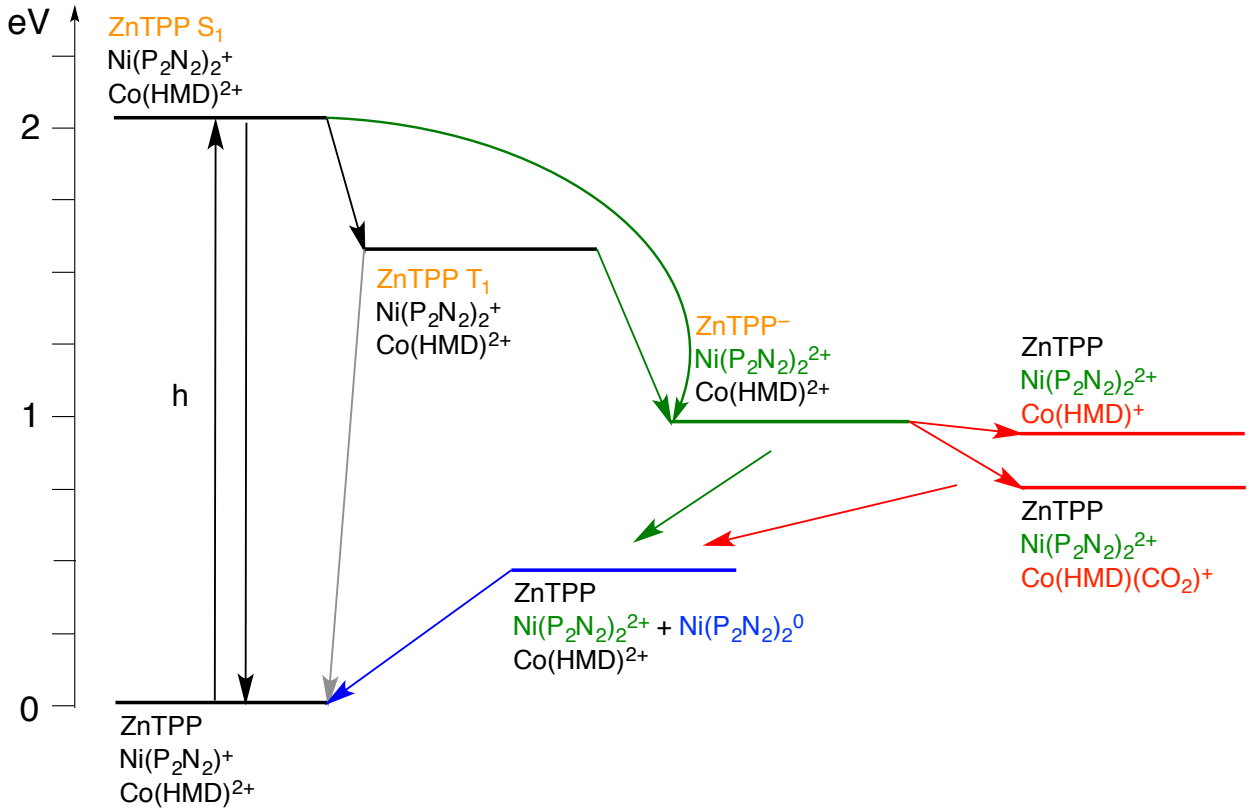

Figure 3.11 Energy-level diagram showing the possible decay pathways following S_1 excitation of ZnTPP in solution containing $\mathbf{Ni^+}$ and $\mathbf{Co^{2+}}$, with and without CO_2 present in the reaction atmosphere.

Reductive quenching of the ZnTPP T_1 state by $\mathbf{Ni^+}$, producing $\mathbf{Ni^{2+}}$ and $ZnTPP^-$ ($\mathbf{Ni^+}$ + ZnTPP* → $\mathbf{Ni^{2+}}$ + $ZnTPP^-$), is extremely energetically favorable. Under N_2, there is no mechanism for trapping the $\mathbf{Ni^{2+}}$ produced by reductive quenching, and so back-electron transfer to reform $\mathbf{Ni^+}$ and ZnTPP ($\mathbf{Ni^{2+}}$ + $ZnTPP^-$ → $\mathbf{Ni^+}$ + ZnTPP) is not suppressed. Oxidation of $ZnTPP^-$ by $\mathbf{Co^{2+}}$ ($\mathbf{Co^{2+}}$ + $ZnTPP^-$ → $\mathbf{Co^+}$ + ZnTPP) is also thermodynamically favorable, but

given that the signal observed for $\mathbf{Co^{+}}$ is very weak this is either a low-yield process or the $\mathbf{Co^{+}}$ is rapidly oxidized by $\mathbf{Ni^{+}}$ to form $\mathbf{Ni^{0}}$ ($\mathbf{Ni^{+}} + \mathbf{Co^{+}} \rightarrow \mathbf{Ni^{0}} + \mathbf{Co^{2+}}$), which reforms $\mathbf{Ni^{+}}$ via comproportionation with $\mathbf{Ni^{2+}}$ ($\mathbf{Ni^{2+}} + \mathbf{Ni^{0}} \rightarrow 2\mathbf{Ni^{+}}$). The weak signal due to $\mathbf{Co^{+}}$ is observed to persist for a long time, suggesting this latter possibility is less likely (see below). Under H_2, $\mathbf{Ni^{2+}}$ reacts exothermically with H_2 to produce $\mathbf{Ni{-}H_2^{2+}}$ ($\mathbf{Ni^{2+}} + H_2 \rightarrow \mathbf{Ni{-}H_2^{2+}}$), which is exothermically deprotonated by pyrrolidine to produce $\mathbf{Ni{-}H^{+}}$ ($\mathbf{Ni{-}H_2^{2+}}$ + pyrr $\rightarrow \mathbf{Ni{-}H^{+}}$ + $pyrrH^{+}$), suppressing back-electron transfer from $ZnTPP^{-}$ ($\mathbf{Ni^{2+}} + ZnTPP^{-} \rightarrow \mathbf{Ni^{+}}$ + ZnTPP). While the kinetics of H_2 binding to $\mathbf{Ni^{2+}}$ to form $\mathbf{Ni{-}H_2^{2+}}$ ($\mathbf{Ni^{2+}} + H_2 \rightarrow \mathbf{Ni{-}H_2^{2+}}$) and deprotonation of $\mathbf{Ni{-}H_2^{2+}}$ to form $\mathbf{Ni{-}H^{+}}$ ($\mathbf{Ni{-}H_2^{2+}}$ + pyrr $\rightarrow \mathbf{Ni{-}H^{+}}$ + $pyrrH^{+}$) have not been measured, it is evident from the observed buildup of $ZnTPP^{-}$ that these reactions are fast. Forward electron transfer from $ZnTPP^{-}$ to $\mathbf{Co^{2+}}$ to produce $\mathbf{Co^{+}}$ ($\mathbf{Co^{2+}} + ZnTPP^{-} \rightarrow \mathbf{Co^{+}}$ + ZnTPP) is only slightly energetically favorable in the absence of CO_2 ($\Delta G = -0.05$ eV), accounting for the observed buildup and decay of $ZnTPP^{-}$, and resulting in the buildup of $\mathbf{Co^{+}}$. In the presence of CO_2, however, the driving force for forward electron transfer from $ZnTPP^{-}$ to $\mathbf{Co^{2+}}$ ($\mathbf{Co^{2+}} + CO_2 + ZnTPP^{-} \rightarrow \mathbf{Co(CO_2)^{+}}$ + ZnTPP) is increased dramatically ($\Delta G = -0.23$ eV). The resultant increase in electron transfer rate leads to $ZnTPP^{-}$ never building up to observable concentrations. The species produced by this reduction under CO_2, $\mathbf{Co(CO_2)^{+}}$, does not exhibit signals within the range we are able to monitor (see Figure 3.10 above). We are therefore not able to observe that species directly, although we infer its presence from the absence of signals due to unligated $\mathbf{Co^{2+}}$ at long times.

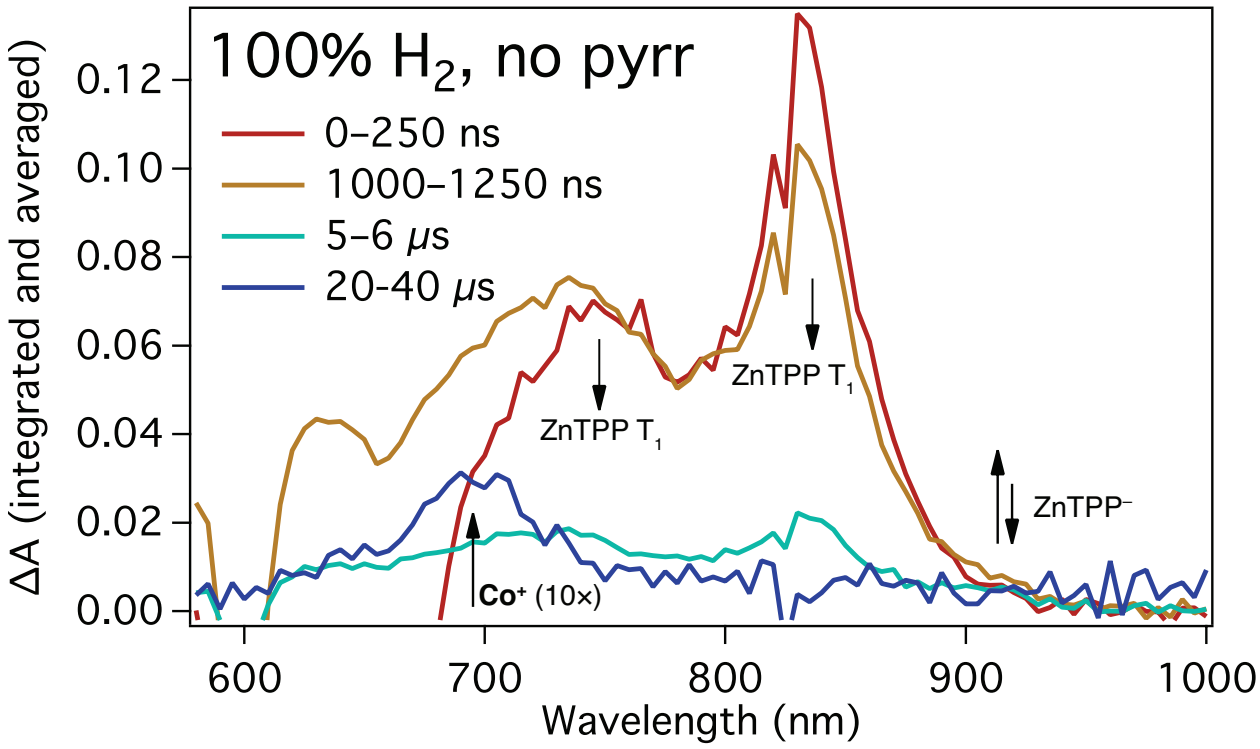

Figure 3.12 Transient-absorption spectrum (λ_{ex} = 547 nm) of solution of $\mathbf{Ni^{+}}$ ([$\mathbf{Ni^{+}}$] = 1.1 mM), $\mathbf{Co^{2+}}$ ([$\mathbf{Co^{2+}}$] = 3.1 mM), and ZnTPP in DMF under H_2 atmosphere. Spectra are integrated and averaged over the time ranges shown to allow intensities to be compared over different time windows. Spectrum from 20–40 μs magnified 10× to show faint band of $\mathbf{Co^{+}}$.

The reaction of $\mathbf{Ni^{2+}}$ with H_2 ($\mathbf{Ni^{2+}} + H_2 \rightarrow \mathbf{Ni{-}H_2^{2+}}$) and the subsequent deprotonation of $\mathbf{Ni{-}H_2^{2+}}$ to produce $\mathbf{Ni{-}H^{+}}$ ($\mathbf{Ni{-}H_2^{2+}}$ + pyrr → $\mathbf{Ni{-}H^{+}}$ + pyrrH^{+}) are crucial to the high yield of $\mathbf{Co^{+}}$ observed under H_2. When transient-absorption measurements are carried out under H_2 in the absence of pyrrolidine, spectral features corresponding to ZnTPP^{-} are observed to be extremely faint (Figure 3.12). Under those conditions, a long-lived signal consistent with the spectrum of $\mathbf{Co^{+}}$ is observed. This signal is several times stronger than the signal observed under N_2, indicating that back-electron transfer from ZnTPP^{-} to $\mathbf{Ni^{2+}}$ ($\mathbf{Ni^{2+}}$ + ZnTPP^{-} → $\mathbf{Ni^{+}}$ + ZnTPP) is slightly suppressed.

In addition to back-electron transfer, there is another pathway by which either ZnTPP^{-} or $\mathbf{Co^{+}}$ can decay. As shown in Table 3.3 and Figure 3.11, the driving force for unproductive electron transfer from ZnTPP^{-} or $\mathbf{Co^{+}}$ to a second equivalent of $\mathbf{Ni^{+}}$, producing $\mathbf{Ni^{0}}$ ($\mathbf{Ni^{+}}$ +

$ZnTPP^- \rightarrow \mathbf{Ni^0} + ZnTPP$) or ($\mathbf{Ni^+} + \mathbf{Co^+} \rightarrow \mathbf{Ni^0} + \mathbf{Co^{2+}}$) is equal to or greater than the driving force for productive electron transfer from $ZnTPP^-$ to $\mathbf{Co^{2+}}$. The formation of $\mathbf{Ni^0}$ was observed by Westwood et al. in their studies of $Ru(bpy)_3^{2+}$-sensitized oxidation of H_2 with $\mathbf{Ni^+}$; in that case, the $\mathbf{Ni^0}$ formed via oxidation of photogenerated $Ru(bpy)_3^+$ ($\mathbf{Ni^+} + Ru(bpy)_3^+ \rightarrow \mathbf{Ni^0} + Ru(bpy)_3^{2+}$) and subsequently deprotonated transient $\mathbf{Ni{-}H_2^{2+}}$, resulting in formation of two equivalents of $\mathbf{Ni{-}H^+}$ ($\mathbf{Ni^0} + \mathbf{Ni{-}H_2^{2+}} \rightarrow 2\mathbf{Ni{-}H^+}$). Due to the lack of distinctive UV-Vis bands of $\mathbf{Ni^0}$, $\mathbf{Ni^+}$, and $\mathbf{Ni^{2+}}$ it has not been possible to measure the rates of their individual reactions following photoexcitation of ZnTPP. However, the long lifetime of $\mathbf{Co^+}$ measured under H_2 in the presence of pyrrolidine (where back-electron transfer from $\mathbf{Co^+}$ to $\mathbf{Ni^{2+}}$ ($\mathbf{Ni^{2+}} + \mathbf{Co^+} \rightarrow \mathbf{Ni^+} + \mathbf{Co^{2+}}$) is suppressed) suggests that, despite the large driving force for this reaction ($\Delta G = -0.40$ V), the reaction is relatively quite slow. Under the conditions of the transient-absorption experiment, we can use the known extinction coefficient for $\mathbf{Co^+}$ ($\varepsilon = 18000\ M^{-1}\ cm^{-1}$)[24] to determine the maximum concentration of $\mathbf{Co^+}$ and conclude that the decay of $\mathbf{Co^+}$ is pseudo-first-order ($[\mathbf{Ni^+}] = 1.2$ mM, $[\mathbf{Co^+}] = 0.002$ mM). Given that electron transfer to $\mathbf{Ni^+}$ is the only decay pathway available for $\mathbf{Co^+}$ in the absence of substrate, this gives an electron transfer rate of $6 \times 10^{-2}\ M^{-1}\ s^{-1}$. This low rate, given the driving force, indicates that other factors (reorganization energy or coulombic repulsion between $\mathbf{Co^+}$ and $\mathbf{Ni^+}$) must play a role in decreasing the electron transfer rate.

3.3.4 Bulk Photolysis Experiments Directed Toward the RWGS Reaction.

Having established that production of $\mathbf{Co^+}$ is possible, and that under an atmosphere of CO_2 $\mathbf{Co^+}$ reacts to form $\mathbf{Co(CO_2)^+}$ or $\mathbf{(L)Co(CO_2)^+}$, we turn our attention to the possibility of further reducing $\mathbf{(L)Co(CO_2)^+}$ in order to produce CO (bound or free). Because the second reduction of $\mathbf{Co^{2+}}$ in the presence of pyrrolidine and Mg^{2+} is thermodynamically accessible from

$ZnTPP^-$, albeit with an expected slow electron transfer rate (ΔG = +0.08 eV), we hypothesized that bulk photolysis of solutions of ZnTPP, $\mathbf{Ni^+}$, and $\mathbf{Co^{2+}}$ in DMF with pyrrolidine and $Mg(ClO_4)_2$ might result in the buildup of a meaningful amount of the product of reduction of $\mathbf{(L)Co(CO_2Mg)^{3+}}$, which could subsequently be oxidized by electron transfer to a second equivalent of T_1 excited ZnTPP, potentially releasing CO, as shown in the following set of reactions:

(1) $\mathbf{Ni^+} + \mathbf{Co^{2+}} + ZnTPP(T_1) + H_2 + CO_2 + pyrr + Mg^{2+} \rightarrow \mathbf{Ni{-}H^+} + \mathbf{(L)Co(CO_2Mg)^{3+}} + ZnTPP + pyrrH^+$

(2) $\mathbf{Ni{-}H^+} + \mathbf{Co^{2+}} + ZnTPP(T_1) + CO_2 + pyrr + Mg^{2+} \rightarrow \mathbf{Ni^+} + \mathbf{(L)Co(CO_2Mg)^{3+}} + ZnTPP + pyrrH^+$

(3) $\mathbf{(L)Co(CO_2Mg)^{3+}} + ZnTPP^- \rightarrow \mathbf{(L)Co(CO_2Mg)^{2+}} + ZnTPP \rightarrow \mathbf{Co(CO)^+} + ZnTPP$ + other products

(4) $\mathbf{Co(CO)^+} + ZnTPP(T_1) \rightarrow \mathbf{Co^{2+}} + CO + ZnTPP^-$

We recognize in these reactions, release of CO comes at the end of a number of low-yield electron transfer steps. Reduction of $\mathbf{(L)Co(CO_2Mg)^{3+}}$ by $ZnTPP^-$ (reaction 3) has ΔG = +0.08 eV, so the reaction is expected to be slow relative to other electron transfer reactions from $ZnTPP^-$. Furthermore, the kinetics of decomposition of the reduced product $\mathbf{(L)Co(CO_2Mg)^{2+}}$ are not known, and it is possible that before decomposition it could undergo the deactivating reaction

(5) $\mathbf{(L)Co(CO_2Mg)^{2+}} + \mathbf{Ni^+} \rightarrow \mathbf{(L)Co(CO_2Mg)^{3+}} + \mathbf{Ni^0}$

for which ΔG is expected to be extremely favorable (~0.4 eV), further limiting the potential yield of $\mathbf{Co(CO)^+}$.

The parameter space of possible conditions for these photochemical reactions is quite large; variables include the concentrations of $\mathbf{Ni^+}$ and $\mathbf{Co^{2+}}$ relative to each other and ZnTPP, the nature and concentration of the proton source, and the concentration of Mg^{2+} (or other Lewis acids, yet to be screened). Systematically exploring the parameter space and identifying possible hits is a research project of greater scope than was possible for this dissertation; the results

described here are, therefore, a first step. Bulk photolysis using a 590 nm LED was performed both on solutions in septum-capped vials sparged with 28% CO_2 in H_2 as well as on NMR samples which had been degassed and backfilled with $^{13}CO_2$, and subsequently frozen in liquid nitrogen and backfilled with H_2. A summary of conditions and products is shown below:

Table 3.4 Summary of bulk photolysis experiments using GC detection. Concentrations are given in mM, CO produced is given in μmols per 3.0 mL of headspace gas. Volume of solution photolyzed is 2.0 mL.

Sample	Gas	[**Ni**$^+$]	[**Co**$^{2+}$]	[pyrr]	proton source	[Mg^{2+}]	CO produced
1	N_2	0.4	1.9	57	324 mM MeOH	17	0
2	H_2	0.4	1.9	57	324 mM MeOH	17	0
3	CO_2	0.4	1.9	57	324 mM MeOH	17	0
4	28% CO_2 in H_2	0.4	1.9	57	324 mM MeOH	17	trace
5	28% CO_2 in H_2	0	1.9	72	194 mM MeOH	17	0
6	28% CO_2 in H_2	0.17	1.9	72	194 mM MeOH	17	trace
7	28% CO_2 in H_2	0.43	1.9	72	194 mM MeOH	17	trace
8	28% CO_2 in H_2	0.68	1.9	72	194 mM MeOH	17	0
9	28% CO_2 in H_2	0.94	1.9	72	194 mM MeOH	17	0
10	28% CO_2 in H_2	1.2	1.9	72	194 mM MeOH	17	0
11	28% CO_2 in H_2	1.4	1.9	72	194 mM MeOH	17	0
12	28% CO_2 in H_2	1.7	1.9	72	194 mM MeOH	17	0
13	28% CO_2 in H_2	0.4	2.3	250	323 mM MeOH	17	trace
14	28% CO_2 in H_2	0.4	2.3	480	323 mM MeOH	17	trace
15	28% CO_2 in H_2	0.4	2.3	480	1.4 M 2,2,2-trifluoroethanol	18	trace
16	28% CO_2 in H_2	0.4	2.3	480	none	18	trace
17	28% CO_2 in H_2	0.4	2.3	480	none	18	trace

Under pure N_2, H_2, or $^{13}CO_2$, a solution of 0.6 mM **Ni**$^+$, 2.7 mM **Co**$^{2+}$, 16 mM $Mg(ClO_4)_2$, 202 mM MeOH and 72 mM pyrrolidine did not produce CO or $HCOO^-$, as monitored by ^{13}C NMR. In addition, samples photolyzed under N_2 or CO_2 without H_2 did not exhibit formation of any oxidized H_2 products, as determined by ^{31}P NMR analysis of the Ni species.

Samples photolyzed under 28% CO_2 in H_2 exhibited formation of **Ni-H**$^+$, identical to the observation of **Ni-H**$^+$ by Westwood et al. in samples of **Ni**$^+$ and $Ru(bpy)_3^{2+}$ photolyzed under H_2 in the presence of pyrrolidine. Formation of a product with a broad ^{13}C NMR signal centered at

162 ppm, consistent with the formation of a CO_2–pyrrolidine carbamate,[46] was observed. When the headspace of these reactions was analyzed by gas chromatography, a trace amount of CO was observed which was not present in the headspace before the photolysis reactions. The amount of CO produced was too small to quantify using the calibration curve that it was possible to generate using our equipment. The lower limit of quantification for this curve is 0.15 μmol CO per 3.0 mL of headspace. Omission of $\mathbf{Ni}^{+}$ from the reaction mixture resulted in no production of CO, as did addition of 0.68 mM or more of $\mathbf{Ni}^{+}$. Addition of different proton sources to the reaction mixture (MeOH, 2,2,2-trifluoroethanol) did not affect the amount of CO detected.

3.4 Conclusion

In this chapter, we have investigated the intercatalyst electron transfer dynamics of a hydrogen oxidation catalyst and a carbon dioxide reduction catalyst upon excitation of a chromophore. We have demonstrated using time-resolved spectroscopy that under conditions that are catalytic for the oxidation of H_2 we can sensitize a carbon dioxide reduction catalyst $\mathbf{Co}^{2+}$, and observe the trapping of the reduced catalyst $\mathbf{Co}^{+}$ by CO_2. We have further demonstrated electrochemically that the addition of pyrrolidine and Mg^{2+} to a solution of $\mathbf{Co}^{2+}$ in DMF stabilizes the product of multiple electron reduction of $\mathbf{Co}^{2+}$ under CO_2, producing a product which has identical electrochemical behavior to the product of CO binding to $\mathbf{Co}^{+}$.

This result suggests that it is possible to photocatalyze the reduction of carbon dioxide without the use of a conventional sacrificial electron donor. Elimination of the sacrificial donor, however, has a profound effect on the proton-transfer dynamics necessary for closing the reductive catalytic cycle. Further study will need to investigate how the reductive cycle can be closed, either by replacing $\mathbf{Ni}^{+}$ with a catalyst which cannot be reduced by $\mathbf{Co(CO_2)}^{+}$, or by finding conditions under which $\mathbf{Co(CO_2)}^{+}$ can be more rapidly reduced to release CO or $HCOO^{-}$.

3.5 References

(1) Alstrum-Acevedo, J.; Brennaman, M.; Meyer, T. *Inorg Chem* **2005**, *44*, 6802.

(2) Balzani, V.; Credi, A.; Venturi, M. *ChemSusChem* **2008**, *1*, 26.

(3) Benniston, A. C.; Harriman, A. *Materials Today* **2008**, *11*, 26.

(4) Concepcion, J. J.; House, R. L.; Papanikolas, J. M.; Meyer, T. J. *Proc. Nat. Acad. Sci. USA* **2012**, *109*, 15560.

(5) Gust, D.; Moore, T. A.; Moore, A. L. *Acc. Chem. Res.* **2009**, *42*, 1890.

(6) Magnuson, A.; Styring, S. R. *Aus. J Chem.* **2012**, *65*, 564.

(7) Appel, A. M.; Bercaw, J. E.; Bocarsly, A. B.; Dobbek, H.; Dubois, D. L.; Dupuis, M.; Ferry, J. G.; Fujita, E.; Hille, R.; Kenis, P. J.; Kerfeld, C. A.; Morris, R. H.; Peden, C. H.; Portis, A. R.; Ragsdale, S. W.; Rauchfuss, T. B.; Reek, J. N.; Seefeldt, L. C.; Thauer, R. K.; Waldrop, G. L. *Chem. Rev.* **2013**, *113*, 6621.

(8) Benson, E.; Kubiak, C.; Sathrum, A.; Smieja, J. *Chem. Soc. Rev.* **2009**, *38*, 89.

(9) Cokoja, M.; Bruckmeier, C.; Rieger, B.; Herrmann, W. A.; Kühn, F. E. *Angew. Chem., Int. Ed.* **2011**, *50*, 8511.

(10) Kumar, B.; Llorente, M.; Froehlich, J.; Dang, T.; Sathrum, A.; Kubiak, C. P. *Ann. Rev. Phys. Chem.* **2012**, *63*, 541.

(11) Morris, A.; Meyer, G.; Fujita, E. *Acc. Chem. Res/* **2009**, *42*, 1983.

(12) Windle, C. D.; Perutz, R. N. *Coord. Chem. Rev.* **2012**, *256*, 2562.

(13) La Porte, N.; Moravec, D. B.; Hopkins, M. D. *Proc. Nat. Acad. Sci. USA* **2014**, *111*, 9745.

(14) Ettedgui, J.; Diskin-Posner, Y.; Weiner, L.; Neumann, R. *J Am. Chem. Soc.* **2010**, *133*, 188.

(15) Morimoto, T.; Nakajima, T.; Sawa, S.; Nakanishi, R.; Imori, D.; Ishitani, O. *J Am. Chem. Soc.* **2013**, *135*, 16825.

(16) Takeda, H.; Ishitani, O. *Coord. Chem. Rev.* **2010**, *254*, 346.

(17) Matsuoka, S.; Yamamoto, K.; Ogata, T.; Kusaba, M.; Nakashima, N.; Fujita, E.; Yanagida, S. *J Am. Chem. Soc.* **1993**, *115*, 601.

(18) Ziessel, R.; Hawecker, J.; Lehn, J.-M. *Helv. Chim. Acta* **1986**, *69*, 1065.

(19) Westwood, M.; Hopkins, M. D. *in preparation* **2015**.

(20) Schmidt, M. H.; Miskelly, G. M.; Lewis, N. S. *J Am. Chem. Soc.* **1990**, *112*, 3420.

(21) Ogata, T.; Yanagida, S.; Brunschwig, B. S.; Fujita, E. *J Am. Chem. Soc.***1995**, *117*, 6708.

(22) Fujita, E.; Creutz, C.; Sutin, N.; Szalda, D. J. *J Am. Chem. Soc.***1991**, *113*, 343.

(23) Fujita, E.; Furenlid, L. R.; Renner, M. W. *J Am. Chem. Soc.* **1997**, *119*, 4549.

(24) Fujita, E.; Szalda, D. J.; Creutz, C.; Sutin, N. *J Am. Chem. Soc.* **1988**, *110*, 4870.

(25) Szalda, D. J.; Fujita, E.; Creutz, C. *Inorg. Chem.* **1989**, *28*, 1446.

(26) Fujita, E.; Creutz, C.; Sutin, N.; Brunschwig, B. S. *Inorg. Chem.* **1993**, *32*, 2657.

(27) Schneider, J.; Jia, H.; Muckerman, J. T.; Fujita, E. *Chem. Soc. Rev.* **2011**, *41*, 2036.

(28) Tinnemans, A. H. A.; Koster, T. P. M.; Thewissen, D. H. M. W.; Mackor, A. *Recueil des Travaux Chimiques des Pays-Bas* **1984**, *103*, 288.

(29) Niklas, J.; Westwood, M.; Mardis, K. L.; Brown, T. L.; Pitts-McCoy, A. M.; Hopkins, M. D.; Poluektov, O. G. *Inorg. Chem.* **2015**, *54*, 6226.

(30) Yang, J. Y.; Smith, S. E.; Liu, T.; Dougherty, W. G.; Hoffert, W. A.; Kassel, W. S.; Rakowski DuBois, M.; Dubois, D. L.; Bullock, R. M. *J Am. Chem. Soc.* **2013**, *135*, 9700.

(31) Lindsey, J. S.; Hsu, H. C.; Schreiman, I. C. *Tet. Lett.* **1986**, *27*, 4969.

(32) Noviandri, I.; Brown, K. N.; Fleming, D. S. *J Phys. Chem. B* **1999**.

(33) Harriman, A. *J Chem. Soc., Faraday Trans. 2* **1981**, *77*, 1281.

(34) Lanese, J. G.; Wilson, G. S. *J Electrochem. Soc.* **1972**, *119*, 1039.

(35) Tait, A. M.; Busch, D. H.; Curtis, N. F. *Inorg. Synth.* **1978**, *18*, 1.

(36) Warner, L. G., Thesis, The Ohio State University, 1968.

(37) Goedken, V. L.; Kildahl, N. K.; Busch, D. H. *J Coord. Chem.* **1977**, *7*, 89.

(38) Sheldrick, G. M. *Acta Cryst.* **2015**, *A71*, 3.

(39) Sheldrick, G. M. *Acta Cryst.* **2008**, *A64*, 112.

(40) Sheldrick, G. M. *Acta Cryst.* **2015**, *C71*, 3.

(41) Bhugun, I.; Lexa, D.; Savéant, J.-M. *J Am. Chem. Soc.* **1996**, *118*, 1769.

(42) Direct reduction of CO2, independent of catalyst, begins to occur at potentials negative of –2.0 V

(43) Pekkarinen, L.; Linschitz, H. *J Am. Chem. Soc.***1960**, *82*, 2407.

(44) Creutz, C.; Schwarz, H. A.; Wishart, J. F.; Fujita, E.; Sutin, N. *J Am. Chem. Soc.***1991**, *113*, 3361.

(45) Harriman, A.; Porter, G.; Searle, N. *J Chem. Soc., Faraday Trans 2* **1979**, *75*, 1515.

(46) Sigma-Aldrich; *The Aldrich Spectral Viewer with FT-NMR Library*; Sigma-Aldrich: Milwaukee, WI, 2002.

Chapter 4 Dual photoredox sensitization of CO_2 and H_2 activating complexes in a self-assembled triad

4.1 Introduction

The previous chapters have focused on the development of catalytic systems in which the catalyts and chromophore are freely diffusing in solution. However, in natural photosynthetic systems, the chromophoric and electron transfer components are precisely spatially arranged in order to promote optimally efficient energy and electron transfer.[1] Many researchers have investigated synthetic mimics of the natural photosynthetic apparatus, attempting to achieve the end product of the natural light-harvesting apparatus—high quantum yield of a long-lived charge-separated state produced by the absorption of a broad spectrum of photons. In the context of supramolecular systems of this nature, much attention has been focused on developing design criteria for architectures capable of achieving long-lived charge-separated states. Various techniques have been developed for covalent assembly of systems that undergo photoinduced charge separation.[2-8] Other systems have been developed in which the oxidized and reduced moieties self-assemble in solution, a technique that offers the promise of a simpler synthetic route to supramolecules with defined intraunit spacing.[9-12] Common electron donor moieties have included phenothiazines, ferrocenes,[13,14] perylene diimides, subporphyrins[5] and free-base porphyrins[5] while common electron acceptor moieties have included boron dipyrrins (BODIPYs),[13] naphthalene mono- or diimides,[15] fullerenes,[5] subphthalocyanines and phthalocyanines.[5]

Less attention has been focused on the problem of achieving long-lived photoinduced charge separation in supramolecular systems where the electron and hole reside on reactive metal centers that are thereby sensitized to activate substrates, rather than on chemically stable redox sites that facilitate fundamental physical studies. A supramolecular system containing a

chromophore and two catalysts, one each for the oxidative and reductive transformation of separate substrates, could accomplish productive chemistry if the charge-separated state resulting from photoinduced intercatalyst electron transfer is sufficiently long lived for at least one center to irreversibly consume the redox equivalent. Even with the many advances in the design of supramolecular systems with long-lived charge-separated states, this condition is generally not met and charge recombination must be suppressed using a sacrificial reductant or oxidant in order to achieve product formation. Many chromophore/single-catalyst assemblies for the photochemical reduction of CO_2 to CO and other products[7,16-18] have been studied using this approach, which has allowed elucidation of fundamental relationships among structures, mechanisms, kinetics, and yields. However, the fact that the reducing equivalents are supplied by a sacrificial donor rather than by catalytic oxidation of a sustainable feedstock means these systems are not functional in an artificial-photosynthetic sense.

In Chapter 2, we reported a homogeneous chromophore/two-catalyst non-supramolecular system in which a chromophore (ZnTPP, zinc tetraphenylporphyrin) photosensitizes electron transfer between a H_2 oxidation catalyst ($Cp^RCr(CO)_3^-$) and CO_2 reduction catalyst (Re(bpy-R_2)$(CO)_3Cl$), producing with a single photon the substrate-active redox state of both catalysts in high quantum yield and with a lifetime potentially suitable for accomplishing net chemistry.[19] A functioning system of this type would accomplish photocatalysis of the reverse water-gas shift reaction (RWGS: $H_2 + CO_2 = CO + H_2O$) and store solar energy ($\Delta H_f = +41.7$ kJ/mol).[20] In this vein, Neumann and co-workers reported that a supramolecular assembly consisting of a Re(diimine)$(CO)_3L^{n+}$ chromophore/CO_2-catalyst and polyoxotungstate electron-storage reservoir, produced CO from H_2 and CO_2 under UV irradiation in the presence of a heterogeneous H_2 oxidation catalyst (Pt/C).[21] In view of these results we wondered whether an

all-molecular assembly could be designed for the RWGS reaction, because of the possible advantages it would provide in independently controlling and tuning the properties of each component. In this report, we describe the photophysical properties of one such assembly.

The basis for the supramolecular architecture described here is an interesting and well-studied class of dyads for photochemically driven CO_2 reduction that contain a porphyrin or metalloporphyrin chromophore linked with a CO_2 reduction catalyst of form $Re^{I}(diimine)(CO)_3L^{n+}$ (diimine = bpy, phen, etc.). The development of these systems has been motivated by the fact that porphyrins are strongly absorbing and tunable chromophores that possess useful photophysical and photoredox properties, and that these rhenium-diimine complexes are among the best and selective molecular catalysts for CO_2 reduction. One class of dyads of this type, reported by Perutz and coworkers, connects the bpy ligand of $Re(bpy)(CO)_3L$ with a tetraphenylporphyrin phenyl group via an amide linker.[22] This dyad, in the presence of a sacrificial electron donor, was able to photocatalyze the reduction of CO_2 to CO.[23,24] Ishitani and co-workers developed a very similar dyad that also incorporated an amide linkage, only with the amide bridge reversed.[25] By modifying the porphyrin to adsorb to a *p*-type semiconducting electrode composed of NiO, they were able to induce photoelectrochemical reduction of CO_2 to CO.[26] A subsequent dyad incorporating a chlorophyll derivative in place of the porphyrin and using an ester linkage was able reduce CO_2 in the presence of a sacrificial electron donor.[27] In a recent report by Indelli, Iengo, and co-workers the Perutz amide-linked dyad is elaborated to incorporate a fullerene as the terminal electron acceptor.[28] Finally, Iengo and co-workers have reported several variations on a dyad that links a porphyrin chromophore with a $Re(bpy)(CO)_3$ catalyst through an equatorial pyridine on the porphyrin that coordinates directly to the Re

center.[29-31] One example of this latter class, containing a zinc porphyrin, is shown in Scheme 4.1, where it is denoted **ZnP–Re**$^+$.

In the present report, we describe a system that accomplishes the same sensitization in a self-assembled catalyst-chromophore-catalyst triad. The H_2 oxidation complex chosen for study is the metalloligand W(≡C-4,4′-$C_6H_4CCC_5H_4N$)$(dppe)_2Cl$ (**W**, Scheme 4.1) from the family of tungsten−benzylidyne compounds, which is known to undergo an H_2 oxidation cycle,[32] and which has already been shown to axially coordinate to Zn tetraarylporphyrins and participate in photoinduced electron- and energy-transfer reactions with these chromophores (**W–ZnTPP,** Scheme 4.1).[10,11] This compound self-assembles in solution with **ZnP–Re**$^+$ to form triad **1** (**W–ZnP–Re**$^+$, Scheme 4.1).

It is found that upon excitation of the porphyrinic subunit of **1**, the excited state is oxidatively quenched by the **Re**$^+$ subunit to give the state **W–ZnP**$^+$**–Re•**. Subsequent thermal reduction of the porphyrin by **W** produces the final charge-separated state **W**$^+$**–ZnP–Re•** in which the **W**$^+$ and **Re•** centers are the active forms to initiate substrate transformation. This series of photoinduced electron transfer reactions was monitored by transient-absorption spectroscopy. Due to the presence of many overlapping transient signals in the visible region, TA spectroscopy in the near-IR and mid-IR was crucial for resolving the sequence of processes and determining the overall mechanism of reaction, as well as determining the lifetime of the final charge-separated state. The charge-separated state is found to persist for the entire window of the experiment, at least 3.5 ns. This is several orders of magnitude longer than the observed charge-separated lifetime in similar systems.[22]

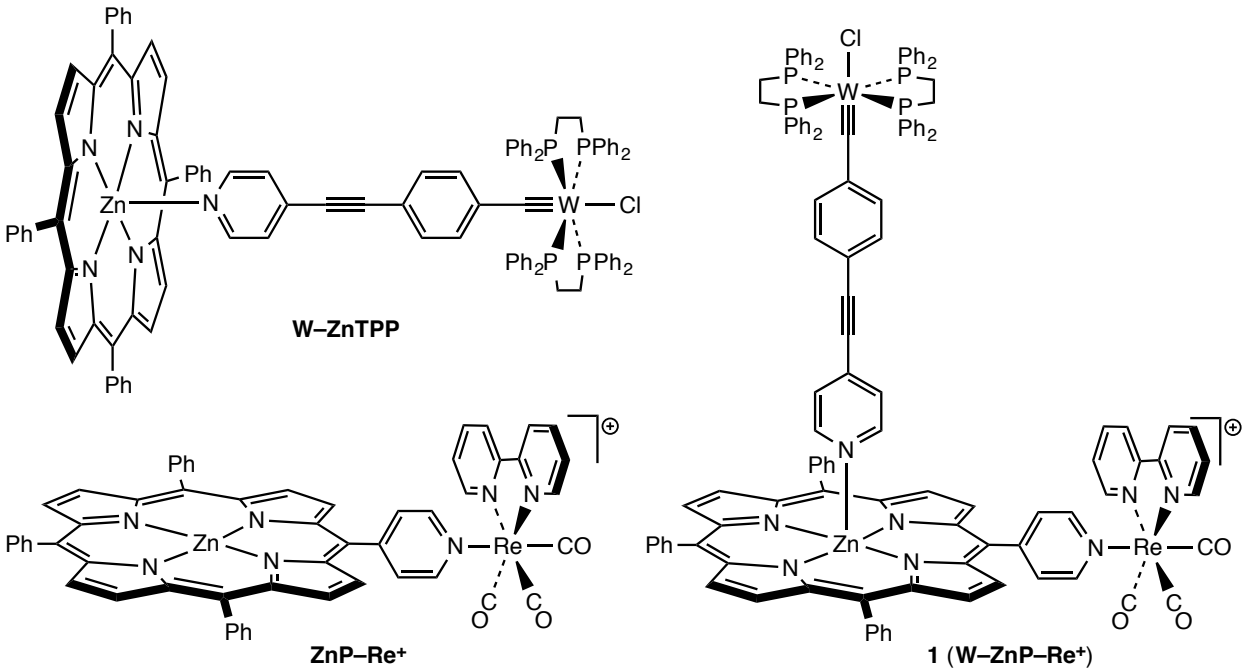

Scheme 4.1 Triad **1** and its components **W** and **ZnP−Re**$^{+}$.

4.2 Experimental

4.2.1 General Procedures

All syntheses were performed in air, all optical experiments were performed under a nitrogen atmosphere using standard Schlenk and glovebox techniques. CH_2Cl_2, toluene, MeOH and diethyl ether for synthesis were HPLC grade (Fisher). CH_2Cl_2 for photophysical experiments (Fisher, HPLC grade stored under nitrogen) was passed through two 4.5 in × 24 in. (1 gal) columns of activated A2 aluminum under nitrogen pressure.[33] Anhydrous methanol (Acros, >99.8 %, Extra Dry) was used as received. Solution samples for UV/vis/NIR experiments were prepared on a vacuum line in sealable cuvettes of path length 1 cm (absorption/emission) or 2 mm (transient absorption), degassed with five freeze−pump−thaw cycles, and sealed under purified nitrogen. Solution samples for IR experiments were prepared in a glovebox in a demountable IR cell (Specac) equipped with CaF_2 windows and a 500 μm PTFE spacer.

Compound **ZnP−Re**$^{+}$ was assembled by a modification of the literature procedure (see below).[30] In order to avoid porphyrin-porphyrin coordination and aggregation, the free-base

pyridyl porphyrin (**H_2P**) was used to assemble the **H_2P–Re^+** dyad, which was subsequently metallated under mild conditions. The compounds W(C-4,4′-$C_6H_4CCC_5H_4N$)(dppe)$_2$Cl (**W**; dppe = 1,2-bis(diphenylphosphino)ethane),[11] 5,10,15-triphenyl-20-(*p*-pyridyl)porphyrin (**H_2P**),[34] W(CC_6H_4-4-CCPh)(dppe)$_2$Cl (**WPh**),[35] and [Re(bpy)(CO)$_3$(dmso-O)][CF_3SO_3][36] were prepared according to standard procedures. Electronic absorption spectra were recorded on a Cary 300 spectrometer. FTIR spectra were recorded on a Nicolet 6700 FTIR spectrometer. All other reagents were obtained from commercial sources and used as received.

4.2.2 Preparation of [H_2P−Re][CF_3SO_3].

The dyad was prepared by a modification of a previously reported procedure.[29] A solution of [Re(bpy)(CO)$_3$(dmso-O)][CF_3SO_3] (0.1516 g, 0.232 mmol) and **H_2P** (0.160 g, 0.256 mmol) in CH_2Cl_2 (50 mL) was refluxed in the dark for 7 d, at which point unreacted [Re(bpy)(CO)$_3$(dmso)][CF_3SO_3] was not detectable by ^{1}H NMR spectroscopy. It was found that use of a slight excess of porphyrin was necessary for all [Re(bpy)(CO)$_3$(dmso)][CF_3SO_3] to be consumed; unreacted **H_2P** is much easier to separate from the reaction mixture than unreacted [Re(bpy)(CO)$_3$(dmso)][CF_3SO_3]. The reaction mixture was reduced to dryness on a rotary evaporator and the remaining purple solid dissolved in a minimum volume of CH_2Cl_2 (6 mL), to which was then added toluene (500 mL). The mixture was allowed to stand in an open beaker for 4 h until purple microcrystals formed. These were isolated by filtration, washed with toluene and Et_2O, and dried under vacuum. Yield: 0.204 g (71% yield). Use of THF instead of CH_2Cl_2 as the solvent for the initial reaction was found to lead to decomposition. The ^{1}H NMR of the product is consistent with the formation of the product. δ (400 MHz, CD_2Cl_2): 9.35 (δ, 2 H, 6,6′-bpy), 8.88 (m, 8 H, porphyrin β), 8.65 (d, 2 H, 3,3′-bpy), 8.60 (d, 2 H, 2,6-pyridyl), 8.45 (t, 2 H, 4,4′-bpy),

8.20 (m, 8 H, *ortho*-phenyl, 3,5-pyridyl), 7.89 (t, 2 H, 5,5′-bpy), 7.79 (m, 9 H, *meta/para* phenyl), –2.19 (s, 2H, NH).

4.2.3 Preparation of ZnP−Re$^+$.

[**ZnP−Re**][CF_3SO_3] was prepared by a modification of the literature procedure.[30] A solution of [**H_2P−Re**][CF_3SO_3] (0.100 g, 0.081 mmol) in CH_2Cl_2 (30 mL) was combined with a solution of $Zn(OAc)_2{\cdot}2H_2O$ (0.075 g, 342 mmol; Sigma-Aldrich, 99.999% trace metals basis) in MeOH (10 mL) and stirred for 5 d at room temperature (heating at reflux was found to degrade the compounds). The reaction mixture was reduced to dryness by rotary evaporation, and the remaining red-purple solid was dissolved in CH_2Cl_2 (50 mL). The solution was washed with H_2O (6 × 150 mL), dried over K_2CO_3, gravity filtered and evaporated to dryness by rotary evaporation. The solid was dissolved in 10 mL CH_2Cl_2 and layered with 30 mL pentane. After a week, purple crystals formed which were filtered off, washed with pentane and dried. Yield: 0.049 g (43% yield). The ^{1}H NMR of the product is consistent with the formation of the product. δ (400 MHz, CD_2Cl_2): 9.37 (δ, 2 H, 6,6′-bpy), 8.98–8.93 (m, 6 H, porphyrin β), 8.82 (d, 2H, 3,3′-bpy), 8.72 (d, 2 H, porphyrin β), 8.57 (d, 2 H, 3,5-pyridyl), 8.45 (t, 2 H, 4,4′-bpy), 8.19 (m, 8 H, *ortho*-phenyl, 2,6-pyridyl), 7.90 (t, 2 H, 5,5′-bpy), 7.78 (m, 9 H, *meta*+*para* phenyl). IR (CH_2Cl_2): ν(CO), 2041 (sharp), 1936 (broad) cm^{-1}.

4.2.4 Visible and Near-IR Transient Absorption Spectroscopy.

Experiments were performed at the Center for Nanoscale Materials, Argonne National Laboratory. The instrument employed a femtosecond Ti:sapphire oscillator regeneratively amplified at 1.7 kHz. The white-light continuum probe was generated using 5% of the output (sapphire crystal in the visible region, sapphire-containing proprietary material in the near-infrared region). The remaining output was used to drive an optical parametric amplifier that

produced a tunable 35-femtosecond excitation (pump) pulses. The pump and probe output entered a transient-absorption spectrometer (Helios, Ultrafast Systems), where the delay of the probe relative to the pump was varied using a mechanical delay line. The pump beam was chopped at one-half the repetition rate of the laser so that an absorption change ($\Delta A = -[\log(I_p/I_0)]$) could be measured as a function of delay, where I_p and I_0 are the intensities of the transmitted probe with the pump on and off. Spectral content of the probe in the regions 440−700 nm and 830−1400 nm was collected as a function of delay using separate spectrographs. Second-order diffractions were removed from the near-infrared by passing the probe through an 850 nm long-pass filter before entering the detector. The data were chirp-corrected to within 200 fs over the spectral range by fitting the solvent response of a pure-solvent standard (under identical conditions) to a polynomial function. The photochemical stability of samples was established by comparing electronic absorption spectra obtained before and after transient-absorption measurements. Global kinetic analyses of spectra were performed using OriginPro.

4.2.5 Time-resolved IR (TR-IR) Spectroscopy.

Experiments were performed at the Center for Nanoscale Materials, Argonne National Laboratory. The instrument employed a femtosecond Ti:sapphire oscillator regeneratively amplified at 2 kHz. The 35 fs, 2 mJ, 800 nm output of the titanium:sapphire laser was beamsplit 50:50 and used to pump two optical parametric amplifiers (OPA). Mid-infrared probe pulses, generated via difference frequency mixing of signal and idler beams in a $AgGaS_2$ crystal, were focused to a 250 micron-diameter spot on the sample, directed to a 190-mm imaging spectrograph, dispersed with a 150 groove/mm grating, and detected with a HgCdTe array detector and boxcar integrator. Pump pulses, produced via either second harmonic generation of the laser fundamental or OPA signal beam, were mechanically delayed relative to the probe

pulse, mechanically chopped at 1 kHz, and overlapped with the probe pulse on the sample. Global kinetic analyses of spectra were performed using OriginPro. The wavelength of the detector was calibrated by comparison to an FTIR absorbance scan of $Re(bpy)(CO)_3Cl$ in CH_3CN. Kinetic traces were first corrected by setting the average of all points at $t < 0$ to zero. Next, the baseline drift was determined by measuring the kinetic trace in regions containing no transient signal, averaging those traces, and subtracting the result from all the kinetic traces analyzed. Baseline drift was measured at several wavelengths to ensure the uniformity of baseline drift. The sample was moved back and forth across the laser beams to reduce the risk of sample degradation due to overexposure.

4.2.6 Time-Resolved Photoluminescence (TRPL) Spectroscopy.

Experiments were performed at the Center for Nanoscale Materials, Argonne National Laboratory. The instrument employed a femtosecond Ti:sapphire oscillator regeneratively amplified at 2 kHz. The 35 fs, 800 nm output of the titanium:sapphire laser was used to pump a white-light seeded optical parametric amplifier to generate the tunable pump beam. Photons emitted by the sample were collected with a lens and directed to a 150 mm spectrograph and single-photon sensitive streak camera. Samples were excited at 565 nm, the maximum absorption wavelength of the Q(1,0) band of $\mathbf{Zn_{py}P{-}Re^{+}}$, and the output was filtered using a long-pass filter to exclude the bulk of the pump beam from the detector. An instrument response function was measured using scattered laser light. The data were fit using OriginPro. The instrument response function was fit to a Gaussian curve, and the fluorescence decay was fit at times greater than 5σ from the maximum of the IRF. For **3**, TRPL data were fit only at the red edge of the spectrum ($\lambda > 710$ nm), to avoid background luminescence or fluorescence from unligated **W** and unligated $\mathbf{ZnP{-}Re^{+}}$, respectively.

4.2.7 Determination of the extent of formation of 1 in solution.

The extent of coordination of **ZnP−Re**$^+$ by **W** to form **1** in TA samples was determined by fitting their electronic-absorption spectra to a linear combination of the spectra of **W**, **ZnP−Re**$^+$, and **Zn$_{py}$P−Re**$^+$ (which was assumed to be identical to the porphyrinic chromophore of **1**). A known volume of a solution of **ZnP−Re**$^+$ was diluted with 1% pyridine, and a spectrum acquired and scaled appropriately to produce a hypothetical spectrum of **Zn$_{py}$P−Re**$^+$, which was assumed to be equivalent to the spectrum of the porphyrinic component of **1**. These spectra were then used as basis spectra for a linear combination fit in Igor Pro. The equation for the best-fit spectrum F is:

$$F(\lambda) = A\mathbf{1}(\lambda) + B\mathbf{2}(\lambda) + C\mathbf{3}(\lambda) \qquad \text{Equation 4.1}$$

Values of *A, B,* and *C* from the fit then represented the concentrations of **W**, **ZnP−Re**$^+$, and **1** in solution. The extent of selective excitation of **1** at 565 nm was then determined by comparing the absorbance at that wavelength by a solution of **1** at the concentration C to the total sample absorbance. The residual from the fit represents the unaccounted-for extent to which the spectrum of ligated **W** differs from that of ligated **W**.

As described previously for **W−ZnTPP**,[10,11] it is possible to identify conditions under which the complex may be selectively excited. At the concentrations used for TA experiments, the porphyrin species present are approximately 78−91% **1** and the balance **ZnP−Re**$^+$. Owing to the Q band red shift and the loss of Q(1,0) intensity in **1** relative to **ZnP−Re**$^+$, excitation at 565 nm, the wavelength used in our TA experiments, produces 89−96% excited **1**.

Shown below in Figure 4.1 are example fits to representative visible/NIR and mid-IR TA samples, showing the extent of ligation as well as the selectivity of excitation at 565 nm.

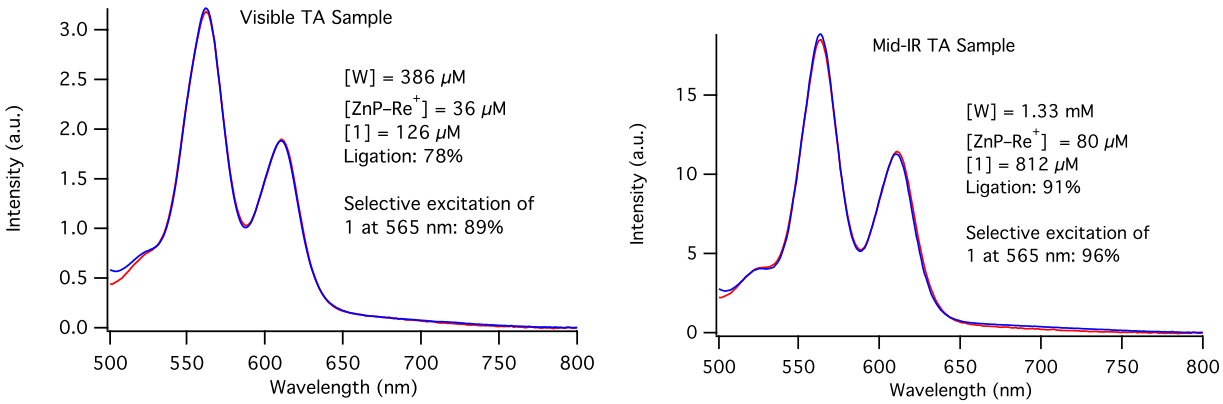

Figure 4.1 Spectra (blue) and fits (red) for representative TA samples, corrected to 1 cm pathlengths, showing extent of ligation of **ZnP−Re**$^{+}$ by **W**.

4.2.8 Kinetic Analysis of the TR-IR spectra of ZnP−Re^{+}.

The intensities of the bleaches at 2041 cm^{-1} and 1945 cm^{-1} and S_1 absorption bands at 2035 cm^{-1} were fit to a single exponential, with the kinetic parameter shared across all three wavelengths. The duration of the experiment (1.6 ns) was too short to accurately determine the S_1 lifetime. The kinetic data with the best fit line obtained from the fit, where τ = 776 ± 26 ps, is shown in Figure 4.6b.

The intensity of the band at 2014 cm^{-1} attributable to the **Re•** fragment of **ZnP^{+}−Re•** was fit to a biexponential expression to model its growth and decay:

$$\Delta A(t) = A_{rise}(e^{-t/\tau_{rise}}) + A_{decay}(e^{-t/\tau_{decay}}) + A_0 \qquad \text{Equation 4.2}$$

Forcing τ_{rise} and τ_{decay} to lie anywhere within the range τ_{rise} = 40 ± 30 ps and τ_{decay} = 600 ± 200 ps did not markedly decrease the observed quality of the fit. The data and the best fit as determined, with τ_{rise} = 20 ± 3 ps and τ_{decay} = 601 ± 76 ps, is shown in Figure 4.6c.

4.2.9 Kinetic Analysis of S_1 Transient-Absorption Data of 1.

The kinetic analysis of **1** was performed on the data in the wavelength regions of the S_1 absorption features. The features were fit to a biexponential expression:

$$\Delta A(t) = A_{S_1,background}(e^{-t/\tau_{S_1}}) + A_{S_1}(e^{-t/\tau_{decay}}) + A_0 \qquad \text{Equation 4.3}$$

where the term with the $_{S1,\ background}$ subscript is a fixed background process with a lifetime of 1700 ps, and the term with the $_{S1}$ subscript corresponds to the decay of the S_1 transient features The data were fit using an unweighted global analysis in OrginPro at six different wavelengths covering both transient absorption features (~590-594 nm and 1259-1325 nm[37]). The time constant τ_{S1} was shared between all kinetic profiles; the other variables were unconstrained. A representative fit is shown in Figure 4.2.

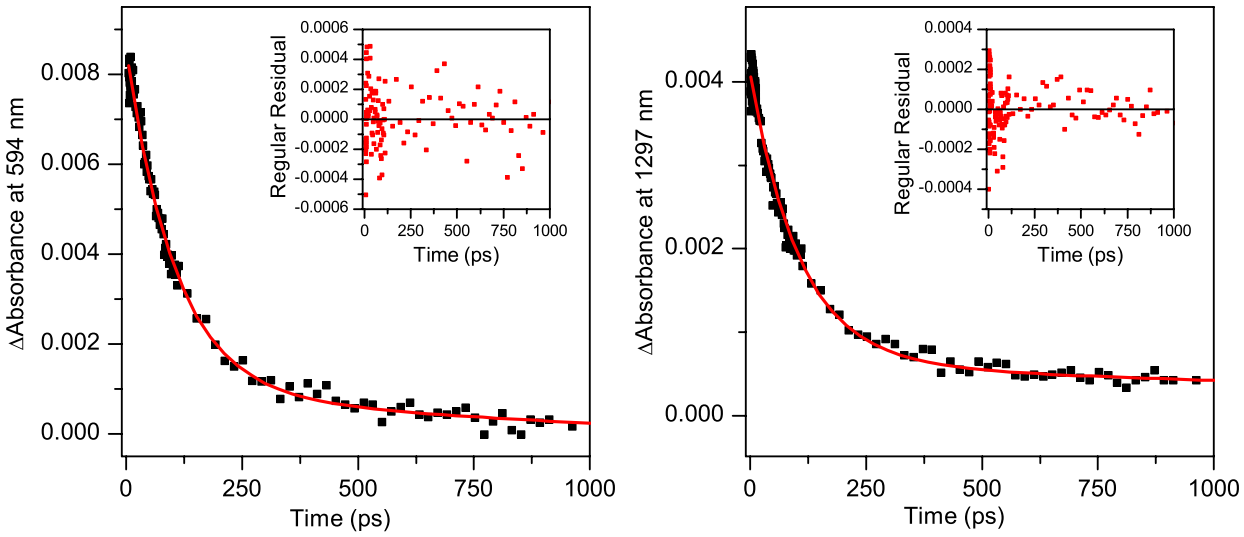

Figure 4.2 Fits to the transient-absorption band of **1** at 594 nm (left) and 1297 nm (right) provided by global kinetic analysis of the spectrum (τ_{S1} = 106 ± 1 ps). Inset: Residuals from global fit.

4.2.10 Kinetic Analysis of the TR-IR spectra of 1.

The kinetic traces of the induced absorption features at 2012, 1901, 1898 and 1881 cm^{-1} were fit to a single exponential, with the kinetic parameter shared across all three wavelengths. Kinetic data and the fit obtained with τ = 102 ± 4 ps are shown in Figure 4.9. The kinetic traces of the bleach feature at 2035 cm^{-1} was fit to a single exponential. Kinetic data and the fit obtained with τ = 114 ± 6 ps is shown in Figure 4.9bc.

4.2.11 Excited-State Energy Levels

The energy levels presented in Figure 4.4 and Figure 4.10 and shown below in Table 4.1 were determined as follows. For unligated **ZnP−Re**$^+$, the S_1 energy level is taken from the report by Casanova et al.[30] For ligated **Zn$_{py}$P−Re**$^+$ and **1**, the energy shift of the S_1 state upon coordination is estimated from the redshift of the Q(0,0) absorption band from 592 nm to 611 nm. The T_1 energy for unligated **ZnP−Re**$^+$ is assumed to be equal to the T_1 energy for ZnTPP, and the drop in T_1 energy upon pyridine coordination in ZnTPP(py) is used to compute the T_1 energy for **Zn$_{py}$P−Re**$^+$ and **1**.[38]

Table 4.1 Excited-state energy levels for **ZnP−Re**$^+$ with various ligands.

Ligand	S_1 (eV)	T_1 (eV)	ZnPor$^+$−Re(bpy•−) (eV)
none	2.04	1.61	1.99
pyridine	1.98	1.57	1.88
W	1.98	1.57	1.88 (see below for further discussion)

The energy of the charge-shift state **W−ZnP**$^+$**−Re•** is taken from the literature report on the model pyridine adduct, **Zn$_{py}$P−Re**$^+$.[30] This report relies on the observation by Gust and co-workers that coordination of pyridine to ZnTPP lowers the oxidation potential of ZnTPP by 0.11 V in the absence of a coordinating electrolyte.[39] The energy of the **ZnP**$^+$**−Re•** state in **3** is assumed to be identical (see discussion below).

The energy of the **W**$^+$**−ZnP**$^-$**−Re** charge-separated state and the **W**$^+$**−ZnP−Re•** charge-shift state are taken from Table 4.3 (see discussion below). The excited-state energies of the $^{1,3}[(d_{xy})^1(\pi^*)^1]$ ($^{1,3}[d\pi^*]$) states of **W** are taken from our report on the photophysics of **W−ZnTPP** in toluene and fluorobenzene.[10,11]

4.2.12 Gibbs' Free Energy Change for Electron Transfer Events

In **3** there are three distinct non-ground redox states that are potentially accessible from the porphyrin S_1 state: (i) oxidized porphyrin/reduced rhenium, (ii) oxidized tungsten/reduced

porphyrin, and (iii) oxidized tungsten/reduced rhenium. States (i) and (iii) are charge shift processes and (ii) is a charge separation process. The Gibbs free energy change for an excited-state charge shift is estimated by the following equation:[40]

$$\Delta G_{CS} = e[E_{ox} - E_{red}] - E_{00} \qquad \text{Equation 4.4}$$

where e is the elementary charge, E_{ox} and E_{red} are the oxidation potential of the donor and the reduction potential of the donor, respectively, and E_{00} is the excited-state energy (2.02 eV).[30]

In the relevant charge-separation process in this dyad we need to account for three electrostatic interactions. Two of these are attractive stabilization terms (oxidized tungsten/reduced porphyrin and reduced porphyrin/cationic rhenium) and the third is a repulsive destabilizing term (oxidized tungsten/cationic rhenium). The Gibbs free energy change for an excited-state charge separation in this system is estimated by the following equation:[40]

$$\Delta G_{CS} = e[E_{ox} - E_{red}] - \frac{e^2}{4\pi\varepsilon_0\varepsilon R_{WZn}} - \frac{e^2}{4\pi\varepsilon_0\varepsilon R_{ZnRe}} + \frac{e^2}{4\pi\varepsilon_0\varepsilon R_{WRe}} - E_{00} \qquad \text{Equation 4.5}$$

where e is the elementary charge, E_{ox} and E_{red} are the oxidation potential of the donor and the reduction potential of the donor, respectively, E_{00} is the excited-state energy (2.02 eV),[30] ε_s is the solvent dielectric constant (CH_2Cl_2 ε_S = 8.93),[41] and R_{WZn}, R_{ZnRe}, and R_{WRe} are the distances between the three metal centers. The relevant oxidation and reduction potentials of the dyads and respective model compounds are laid out in Table 4.2. Because compound **W** was found to adsorb to the electrodes and produce erratic electrochemical data, model compound **WPh** (shown in Scheme 4.2) was used in its place. This substitution is not predicted to result in a change in oxidation or reduction potentials, as described by O'Hanlon et al. in a study of tungsten−benzylidyne compounds with different length oligo-phenylene-ethynylene substituents.[42]

Table 4.2 Redox Potentials for Triad Compounds and Model Complexes[a]

compound	$E_{1/2}^{0/-}$, V	$E_{1/2}^{0/+}$, V
WPh	−2.95[b]	−0.59[c]
$Re(bpy)(CO)_3(py)^{+}$ [d]	−1.59	+1.28
ZnP−Re^{+}[d]	−1.62	+0.26[e]

[a] CH_2Cl_2 solution (except as noted), room temperature, V vs. $FeCp_2^{0/+}$. [b] THF solution (ref. [42])[c] Ref. [43d] Values from ref.[30], converted from SCE to $FeCp_2^{0/+}$ using ref. [44]. [e] $E_{1/2}^{0/+}$ adjusted by −0.11 V to account for stabilization of the $ZnPor^{+}$ state upon pyridine coordination. [38]

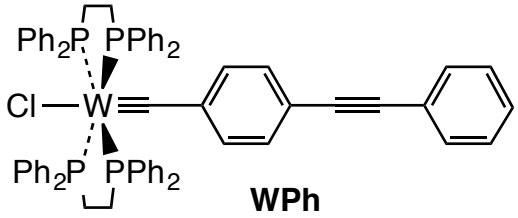

WPh

Scheme 4.2 Model compound **WPh**, used to determine redox potentials of compound **W**.

The donor-acceptor distance between the tungsten and porphyrin is taken from DFT calculations (R_{WZn} = 15.2 Å).[11] In order to determine the donor-acceptor distances for the other two relevant charge-separated state we present the DFT model for **ZnP−Re**$^{+}$ in Figure 4.3. Since the first rhenium reduction is bipyridine based,[45] the average zinc-bipyridine carbon distance is used for the zinc-rhenium donor-acceptor distance (R_{ZnRe} = 10.5 Å). The oxidized tungsten/reduced rhenium distance was determined geometrically (R_{WRe} = 19.6 Å) using the law of cosines $c^2 = a^2 + b^2 - 2ab \cos \gamma$, with the system considered a triangle with the three nodes located at the tungsten center, zinc center in **ZnP−Re**$^{+}$, and one of the 1,1′ bpy carbons in **ZnP−Re**$^{+}$. The parameters were a = 15.2 Å, b = 10.5 Å, and γ = 98°. Presented in Table 4.3 are the Gibbs free energy change for photochemical charge separation for the relevant charge-shifted and charge-separated states in **3**, determined from Equations 4.4 and 4.5.

Table 4.3 Gibbs Free Energy for Photochemical Charge Separation and State Energy for Relevant Charge-Separated States.

charge-separated state	ΔG_{CS} (ZnPor S_1), eV[a]	$-\Delta G_{CR}$, eV[b]	Process
W−ZnP$^+$−Re•	−0.10	1.88	Charge Shift
W$^+$−ZnP$^-$−Re	−0.88	1.14	Charge Separation
W$^+$−ZnP−Re•	−0.98	1.00	Charge Shift

[a] Equations 4.4 (Charge Shift) and 4.5 (Charge Separation). [b] $-\Delta G_{CR} = E_{00} + \Delta G_{CS}$.

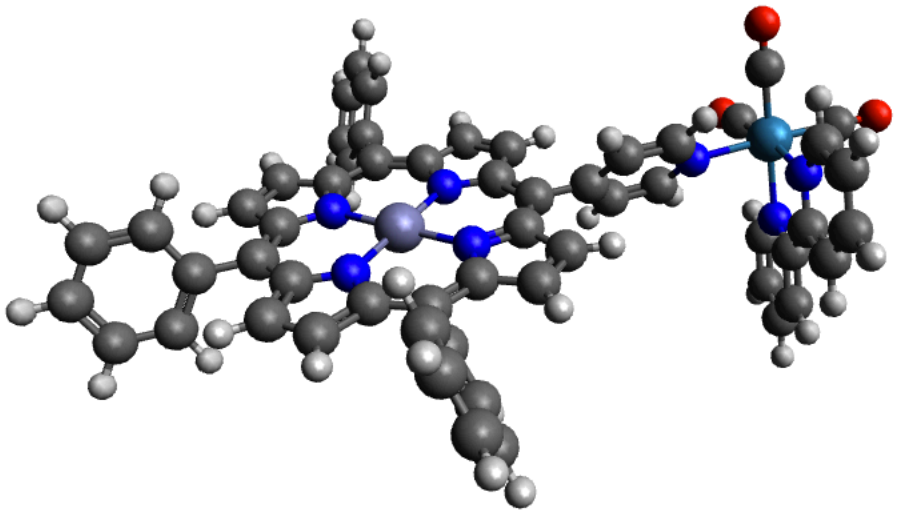

Figure 4.3 Calculated (DFT) model structure of **ZnP−Re$^+$**. The average Zn−bpy(C) distance is 10.5 Å. Calculations performed in Gaussian 09[46] with the B3P86 functional and 6-31G* (H, C, N, O)[47,48] and LANL2DZ (Zn, Re)[49,50] basis sets. LANL2DZ effective-core potentials were used for Zn and Re.[49,50]

4.2.13 Solvent correction for rates of FRET and reductive quenching

The rates of FRET and reductive quenching were measured for **W−ZnTPP** in toluene (FRET) and C_6H_5F (reductive quenching). In order to use the measured values to estimate the rates of FRET and reductive quenching in **3** in CH_2Cl_2, it is necessary to apply a correction.

The rate of FRET in different solvents depends almost entirely on the refractive index η of each solvent. The rate of FRET is determined by the following equation:

$$k_{FRET} = \frac{9000\ln(10)\kappa^2\Phi_D J_F}{128\pi^5\eta^4 N_A \tau_D R_{DA}^6}$$

Equation 4.6

In this equation, the porphyrin radiative lifetime (φ_D/τ_D), dyad geometry (which determines R_{DA}, the donor-acceptor distance, and κ^2, the dipole orientation factor), and spectral-overlap integral (J_F) are nearly or completely solvent-independent. Consequently, the FRET rate constant in dichloromethane ($k_{FRET,\,DCM}$) can be related to the rate constant measured in toluene by the following equation:

$$k_{FRET,DCM} = k_{FRET,tol}\frac{\eta_{tol}^4}{\eta_{DCM}^4} \qquad \text{Equation 4.7}$$

where $k_{FRET,\,tol} = 1.63 \times 10^9$ s^{-1},[11] $\eta_{tol} = 1.4941$,[41] and $\eta_{DCM} = 1.4242$.[41] This provides an energy-transfer rate of $k_{FRET,DCM} = 1.97 \times 10^9$ s^{-1}.

To estimate the rate of reductive quenching, we must first consider the factors that influence the observed electron transfer rate in C_6H_5F, and how changing those parameters when switching to CH_2Cl_2 will affect the rate. We begin with the equation from Marcus theory for the rate of electron transfer:

$$k_{ET} = \sqrt{\frac{\pi}{\hbar^2 \lambda k_b T}}\left|V\right|^2 e^{\frac{-(\Delta G^\circ + \lambda)^2}{4\lambda k_B}} \qquad \text{Equation 4.8}$$

where V is the donor-acceptor electronic coupling, λ is the total reorganization energy, T is the temperature, k_B is the Boltzmann constant, and $\hbar$ is the Planck constant ($\hbar = h/2\pi$). The driving force, ΔG°, is −0.71 eV in C_6H_5F[10] and −0.88 in CH_2Cl_2 (see above). The total reorganization energy λ can be divided into two terms, the solvent-independent inner-sphere reorganization energy λ_i and the solvent-dependent outer-sphere reorganization energy λ_o, which can be estimated using the dielectric continuum model

$$\lambda = \lambda_i + \lambda_o = \lambda_i + \frac{e^2}{4\pi\varepsilon_0}\left(\frac{1}{r} - \frac{1}{R_{CC}}\right)\left(\frac{1}{\eta^2} - \frac{1}{\varepsilon_s}\right) \qquad \text{Equation 4.9}$$

where r is the average radius of the donor and acceptor (5.0 Å, taken from DFT models)[11], R_{CC} is the center-to-center distance between the donor and acceptor (15.4 Å, see above), η is the solvent refractive index (see above), and ε_s is the solvent dielectric constant (PhF: ε_s = 5.465, DCM: ε_s = 8.93).[41] The inner-sphere reorganization energy has not been measured for W≡CR−ZnTPP donor-acceptor pairs, but is assumed to be roughly 0.2 eV by analogy with ZnP/AuP$^+$ donor-acceptor pairs (varying this value in the range 0.1−0.5 eV has a negligible effect on the final estimate of k_{RedQ} in CH_2Cl_2). With the exception of Δit and λ_o, none of the parameters are expected to change between C_6H_5F and CH_2Cl_2. For C_6H_5F, λ_o = 0.55 eV, and for CH_2Cl_2, λ_o = 0.74 eV. Using the Marcus equation above, we find that $k_{ET,\,DCM} = k_{ET,\,PhF} \times 0.91 = 1.1 \times 10^9\ s^{-1}$.

4.3 Results

4.3.1 TR-IR Spectroscopy of ZnP−Re$^+$.

The excited-state properties of **ZnP−Re**$^+$ were probed using picosecond TR-IR spectroscopy to complement the luminescence and visible-wavelength transient-absorption spectroscopic studies reported by Casanova, et al.,[30] and to establish IR spectroscopic signatures for the excited-state processes of **1**. The results from Casanova et al. provide the framework for interpreting the TR-IR spectra, and thus are briefly summarized here (Figure 4.4). They reported that the lowest-lying electronic excited states of **ZnP−Re**$^+$ are the **ZnP**-centered S_1 and T_1 states, with the ^{1}MLCT and ^{3}MLCT excited states of the **Re**$^+$ unit being substantially higher in energy. Excitation of **ZnP−Re**$^+$ in CH_2Cl_2 solution results in fluorescence from the ^{1}**ZnP*−Re**$^+$ S_1 excited state. Compared to the model chromophore ZnTPP, the fluorescence lifetime of **ZnP−Re**$^+$ (900 ps) is shorter by a factor of 2 and the quantum yield is smaller by a factor of 1.6. The accelerated decay of the S_1 state was attributed to enhancement of the $S_1 \rightarrow T_1$ intersystem

crossing rate by the appended Re center ("heavy-atom effect").[1] Quenching of the S_1 state via photoinduced electron transfer, ^{1}**ZnP*−Re**$^+$ → **ZnP**$^+$**−Re•** (where **Re•** symbolizes the one-electron reduced subunit (pyridyl)Re(bpy•)$(CO)_3$, which is a bpy-centered radical) is thermodynamically feasible ($\Delta G \sim -0.05$ V), but was excluded from contributing to the shortened lifetime because the visible-wavelength transient-absorption spectrum did not exhibit bands attributable to **ZnP**$^+$. Instead, the spectrum showed features characteristic of the S_1 state evolving to those of the T_1 state on the same time scale as fluorescence decay.[30]

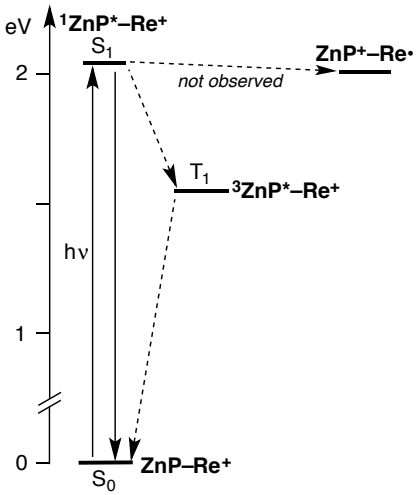

Figure 4.4 Jablonski diagram for **ZnP−Re**$^+$ (adapted from ref. [30])

The TR-IR spectra of **ZnP−Re**$^+$ obtained upon excitation of the **ZnP**-centered S_1 state is shown in Figure 4.6a, and the frequencies of the bands it displays are set out in Table 4.4. Immediately following excitation, the spectra exhibit prominent bleaches at 2041 and 1940 cm^{-1} (ν_{CO}(ground state) = 2041 and 1936 cm^{-1}, Figure 4.5) and excited-state absorption bands at 2035 cm^{-1} (strong) and ~1920 cm^{-1} (weak). The sharpness of the 2041 cm^{-1} bleach and 2035 cm^{-1}

[1] An alternative explanation has been proposed by Sampaio and coworkers, based on studies of free-base tetrapyridyl porphyrins coordinated to single $Ru^{II}L_5$ moeity: the shortened S_1 lifetime arises from an increase in the number of vibrational modes that facilitate internal conversion and/or energy transfer processes.[51] They also state that the appended Ru center, in fact, decreases the rate of intersystem crossing.

absorption is partly a result of their mutual overlap. These features do not fully decay within the 2 ns time window of the experiment (Figure 4.6b), which precludes accurate kinetic analysis, but approximate fitting indicates they decay according to single-exponential kinetics with a lifetime of ~800 ps. This is consistent with the reported 900 ps fluorescence lifetime of **ZnP−Re**$^+$.[30] Casanova, et al. reported that excited-state decay of **ZnP−Re**$^+$ from the S_1 state to the T_1 state has a lifetime of approximately 1 ns, based on visible wavelength transient-absorption spectra.

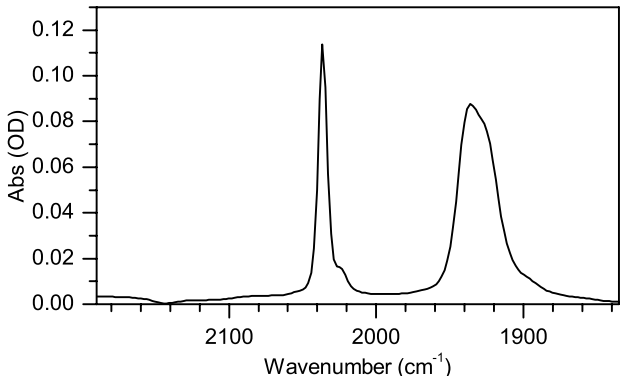

Figure 4.5 IR absorption spectrum of **ZnP−Re**$^+$ in CH_2Cl_2.

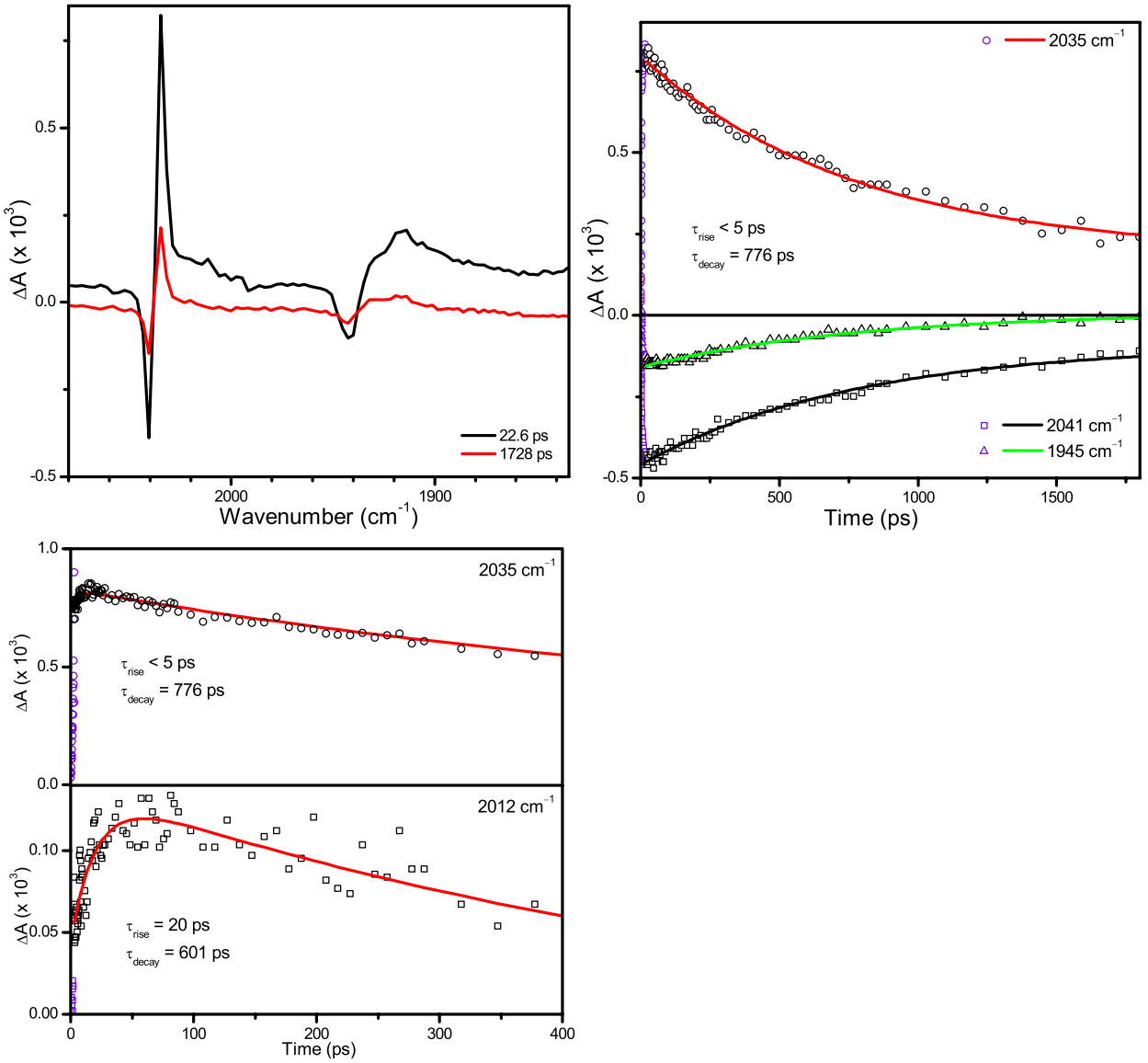

Figure 4.6 (a) TR-IR spectra of **ZnP−Re**$^{+}$ in CH_2Cl_2 solution (λ_{ex} = 565 nm, Q(0,0)). (b) Kinetic analyses of the bands at 2035 cm^{-1}, 2041 cm^{-1}, and 1945 cm^{-1}; the solid lines are fits to the data (open markers) (c) Kinetic analyses of the bands at 2035 cm^{-1} and 2012 cm^{-1}; the red lines are fits to the data (open markers). Data in purple is masked from the fit.

Table 4.4 CO Stretching Frequencies of $[Re(bpy)(CO)_3L]^{n+}$ Compounds.

	CO stretching frequency (cm^{-1})			
compound	ground state	excited state	$Re^I(bpy•)(CO)_3L$	ref
ZnP−Re$^+$	2041, 1936	2035, ~1920[a]	~2012	this work
1	2041, 1936	2035[a]	2012, 1898	this work
$[Re(bpy)(CO)_3(4\text{-Etpy})]^+$	2035, 1937	2074, 2010, 1971[b]		52
$[Re(bpy)(CO)_3(CH_3CN)]^+$	2040, 1937	2070, 2017, 1987[b]	2017, 1902[c]	53
ZnTPP−[(NHC(O)−bpy) $Re(CO)_3(3\text{-Mepy})]^+$	2035, 1933	2026[a]	2012, 1902[d] 2007, 1896[e]	22

[a] Zn(Por) S_1 state. [b] ^{3}MLCT state. [c] Determined by reductively quenching excited state with triethylamine. [d] Determined via spectroelectrochemistry. [e] Measured by TR-IR spectroscopy.

The fact that the CO stretching frequencies of **ZnP−Re$^+$** in the S_1 state (2035 and ~1920 cm^{-1}) differ only slightly from those of the ground state (by −6 and −16 cm^{-1}, respectively) indicates that the **Re$^+$** unit they correspond to neither is in an electronic excited state nor has undergone reduction. Specifically, studies of the compounds $[Re(bpy)(CO)_3(4\text{-Etpy})]^+$ [52] and $[Re(bpy)(CO)_3(CH_3CN)]^+$ [53] (Table 4.4) demonstrated that the CO stretching frequencies are higher in the ^{3}MLCT excited state than in the ground state, which is opposite to the frequency shifts observed for **ZnP−Re$^+$**, whereas upon reduction to the **Re•** bpy-centered radical state the CO frequencies decrease by substantially more than observed for **ZnP−Re$^+$**. The small change in CO stretching frequency for **ZnP−Re$^+$** instead indicates that the ground-state electronic structure of the $[Re(bpy)(CO)_3(pyridyl)]^+$ subunit is weakly perturbed by the adjacent Zn(Por)-localized S_1 excited state. This conclusion is consistent with that of Casanova, et al., who described the

electronic coupling between the **ZnP** and $\mathbf{Re}^{+}$ units of $\mathbf{ZnP{-}Re}^{+}$ as weak based on the fact that its **ZnP**-derived Soret and Q electronic-absorption bands differ only slightly in wavelength and intensity from those of ZnTPP. The small CO frequency shifts observed for $\mathbf{ZnP{-}Re}^{+}$ are of similar magnitude to that reported for the dyad ZnTPP−[(NHC(O)−bpy)Re(CO)$_3$(3-Mepy)]$^+$ upon Zn(TPP) S_1 excitation (−9 cm^{-1}, Table 4.4),[22] which those authors describe as a $\pi\rightarrow\pi^*$ state without assigning the multiplicity of the porphyrin excited state.

In addition to the prominent TR-IR bands of $\mathbf{ZnP{-}Re}^{+}$ at 2035 and ~1920 cm^{-1}, a weak absorption band is observed at ~2012 cm^{-1} (Figure 4.6a). The temporal behavior of this band differs from that of S_1 bleaches and absorptions described above; while the accuracy of the fit is limited by the low signal strength, the band rises more slowly than the S_1 features (τ_{rise} = 40 ± 30 ps) and decays more quickly (τ_{decay} = 600 ± 200 ps, Figure 4.6c). The frequency of this band and its shift relative to that of the ground state are similar to those observed for the one-electron reduced compound Re(bpy•)(CO)$_3$(CH$_3$CN)[53] and the dyad ZnTPP−(NHC(O)−bpy•)Re(CO)$_3$(3-Mepy) (Table 4.4),[22] suggesting that it arises from oxidative quenching of the S_1 state: $\mathbf{^1ZnP^*{-}Re^{+}\rightarrow ZnP^{+}{-}Re\bullet}$. This transient species is expected to exhibit a second, broader CO stretching band near 1900 cm^{-1}; this band is not observed, presumably due to overlap with the comparatively strong S_1 band at ~1920 cm^{-1}. Based on the low relative intensity of the 2012-cm^{-1} band, the quantum yield for formation of this product is relatively small; this may account for the fact that a band attributable to $\mathbf{ZnP}^{+}$ was not detected in the visible transient-absorption spectrum of $\mathbf{ZnP{-}Re}^{+}$.[30,31]

The electron-transfer rate associated with oxidative quenching of the S_1 state cannot be determined because the native lifetime of the **ZnP** S_1 state in the absence of quenching is

unknown. Assuming a native lifetime for ZnTPP of $\tau_0 = 1.7$ ns in CH_2Cl_2,[31] Equation 4.10 can be used to provide the combined rate of the processes that accelerate S_1 decay (k_q):

$$k_q = \tau_{S_1}^{-1} - \tau_0^{-1} \qquad \text{Equation 4.10}$$

This provides $k_q = 5.2 \times 10^8$ s^{-1}, which contains contributions from the heavy-atom effect[30] (or other non-radiative processes facilitated by the Re center)[51] and oxidative quenching. The fact that the 2012 cm^{-1} band is very weak compared to the analogous band in **1** (for which the overall quantum yield of formation of $Re(bpy\bullet)(CO)_3$ is close to unity, see below) indicates that the oxidative quenching process is extremely low yield in **ZnP−Re$^+$**. The magnitude of this band above the baseline is no more than 2×10^{-5} absorbance units, compared to 8.9×10^{-3} absorbance units for the analogous band in **1**. From the ratio of these two peak heights we estimate that the quantum yield of oxidative quenching in **ZnP−Re$^+$** is approximately 0.002, corresponding to a rate of approximately 1×10^6 s^{-1}. A slow rate is not inconsistent with the fact that the reaction is roughly thermoneutral ($\Delta G \sim -0.05$ V), and occurs between weakly coupled redox orbitals (ZnPor and bpy).

4.3.2 Formation of Triad 1 in Solution.

Triad **1** forms in CH_2Cl_2 solutions that contain a mixture of **W** and **ZnP−Re$^+$**, as evidenced by electronic-absorption spectroscopy. Addition of excess **W** to a solution of **ZnP−Re$^+$** results in redshifts of the Q(1,0) and Q(0,0) bands from 550 to 564 nm and 592 to 611 nm, respectively, and changes in their relative intensities (Figure 4.7). The resulting spectrum is identical to that observed for **Zn_{py}P−Re$^+$** (the species formed when pyridine coordinates to the Zn center of **ZnP−Re$^+$**)[30] (Figure 4.7 and Table 4.5), and characteristic of axial coordination to zinc−tetraarylporphyrins by pyridine.[11,54]

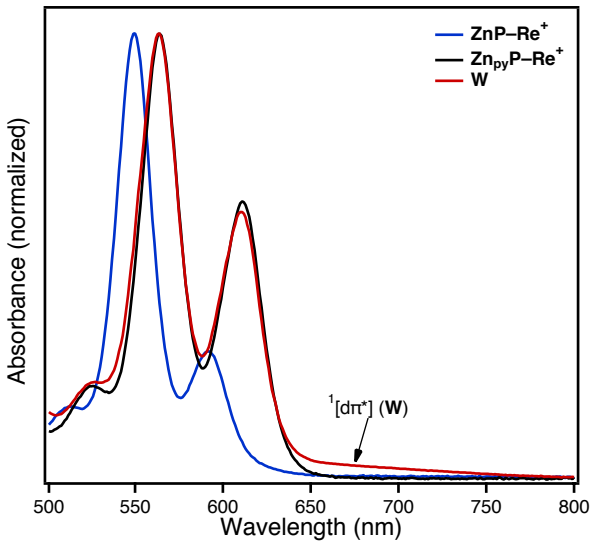

Figure 4.7 Electronic-absorption spectra of **ZnP−Re**$^+$ and its mixtures with 1% pyridine (quantitatively forming **Zn$_{py}$P−Re**$^+$) and 1.33 mM **W** (forming a 91:9 mixture of **1** and **ZnP−Re**$^+$) in CH_2Cl_2. Intensities are normalized to the peak of the Q(1,0) band.

Table 4.5 Electronic Absorption Spectroscopic Data for **ZnP−Re**$^+$, **Zn$_{py}$P−Re**$^+$, and **1**[a]

	λ_{max}, nm		
Compound	Q(1,0)	Q(0,0)	A(Q(1,0))/A(Q(0,0))[b]
ZnTPP	547	585	5.9
ZnP−Re$^+$	550	592	3.29
Zn$_{py}$P−Re^{+c}	564	611	1.64
1[d]	564	611	1.7[e]

[a] CH_2Cl_2 solution; room temperature. [b] Relative intensity at λ_{max}. [c] Solution contains 1% v/v pyridine. [d] Solution contains 1 mM **W**. [e] Estimated by subtracting the absorbance due to unligated **W**.

It was found previously that the equilibrium binding constant for the complex formed between **W** and ZnTPP is 7700 M^{-1} in toluene,[11] which is similar to the value for ZnTPP with pyridine (6000 M^{-1}).[54] Given a binding constant of this magnitude, **W** must be present in appreciable excess relative to **ZnP−Re**$^+$ in order to ensure substantial formation of **1** (as is necessary for photophysical measurements). As a result, electronic-absorption spectra of **1** (Figure 4.7) generally show a broad absorption tail in the 650−800 nm region attributable to the ^{1}[d→π*] transition of unligated (excess) **W** (λ_{max} = 630 nm, ε = 360 M^{-1} cm^{-1}),[11] which overlaps the Q bands of **1**. Due to the low extinction coefficient of the ^{1}[d→π*] band compared to the

Zn(Por) Q bands (ε ~10^4 M^{-1} cm^{-1}) and the magnitude of the Q band shift from **ZnP−Re$^+$** to **1**, it is possible to excite **1** with high selectivity (>85%, with the balance **ZnP−Re$^+$**).

4.3.3 Transient-Absorption Spectroscopy of 1.

Triad **1** was studied using visible and near-IR transient-absorption spectroscopy, which probes features that report on **ZnP** processes, and by TR-IR spectroscopy, which provides CO stretching frequencies that are fingerprints of the state of the **Re$^+$** unit. The visible and near-IR transient-absorption spectra of **1** are shown in Figure 4.8, and the TR-IR spectra are shown in Figure 4.9a. The spectra are described below in three time windows: (1) immediately following excitation; (2) the time period centered ~300 ps following excitation; and (3) the end of the experimental window (~3 ns). Promptly following excitation, the spectra in all three wavelength ranges display features characteristic of the **ZnP** S_1 state. Specifically, the visible and near-IR spectra (Figure 4.8) exhibit dips in the absorption profile at 618 nm and 672 nm that are due to Q(0,0) bleach/stimulated emission and Q(0,1) stimulated emission, respectively, and strong S_1 absorptions at 468, 1170, and 1300 nm. The absorption band at 468 nm is coincident with a band reported for **Zn$_{py}$P−Re$^+$** immediately following excitation[30] and similar to a strong S_1 band of ZnTPP,[55] while the 1300-nm band is analogous to prominent S_1 bands observed for ZnTPP and ZnTPP(L) in the 1250−1300 nm region.[37] The TR-IR spectra of **1** (Figure 4.9a) shows bleaches at 2041 and 1943 cm^{-1} (cf. 2041 and 1936 cm^{-1} for **ZnP−Re$^+$**), and a strong absorption at 2035 cm^{-1} that matches the frequency of the S_1 CO-stretching band observed for **ZnP−Re$^+$** (Table 4.4). The TR-IR spectrum of **1** does not display an obvious analogue of the weak ~1920 cm^{-1} S_1 absorption band seen for **ZnP−Re$^+$**, but there is nonzero differential absorbance in this region; there is evidence its intensity is suppressed by the overlapping bleach at 1943 cm^{-1} (see above).

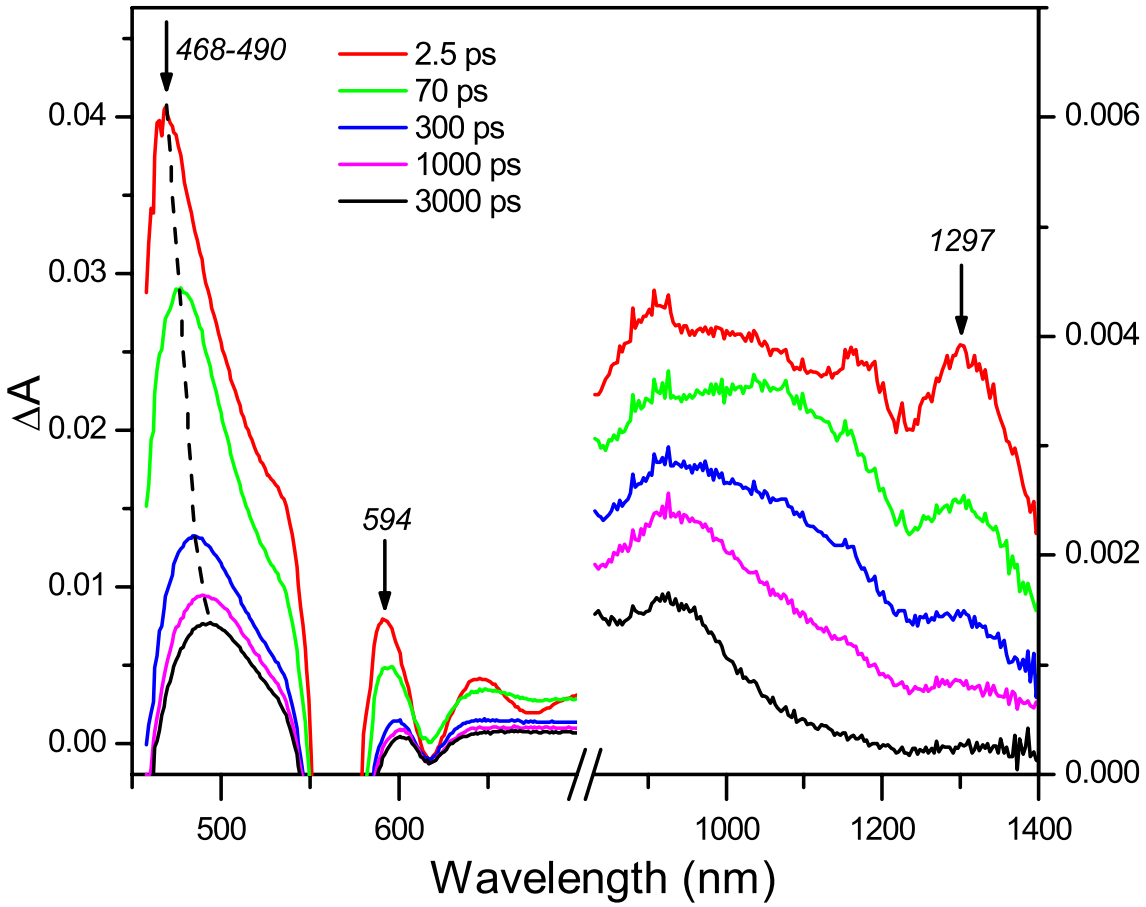

Figure 4.8 Visible and near-IR transient-absorption spectrum of **1** in CH_2Cl_2 (λ_{ex} = 565 nm, Q(1,0), 89% selective excitation of **1** based on [**1**]:[**ZnP**−**Re**$^+$] = 78:22). Values of ΔA cannot be compared between spectra since they were recorded on different instruments with different laser powers.

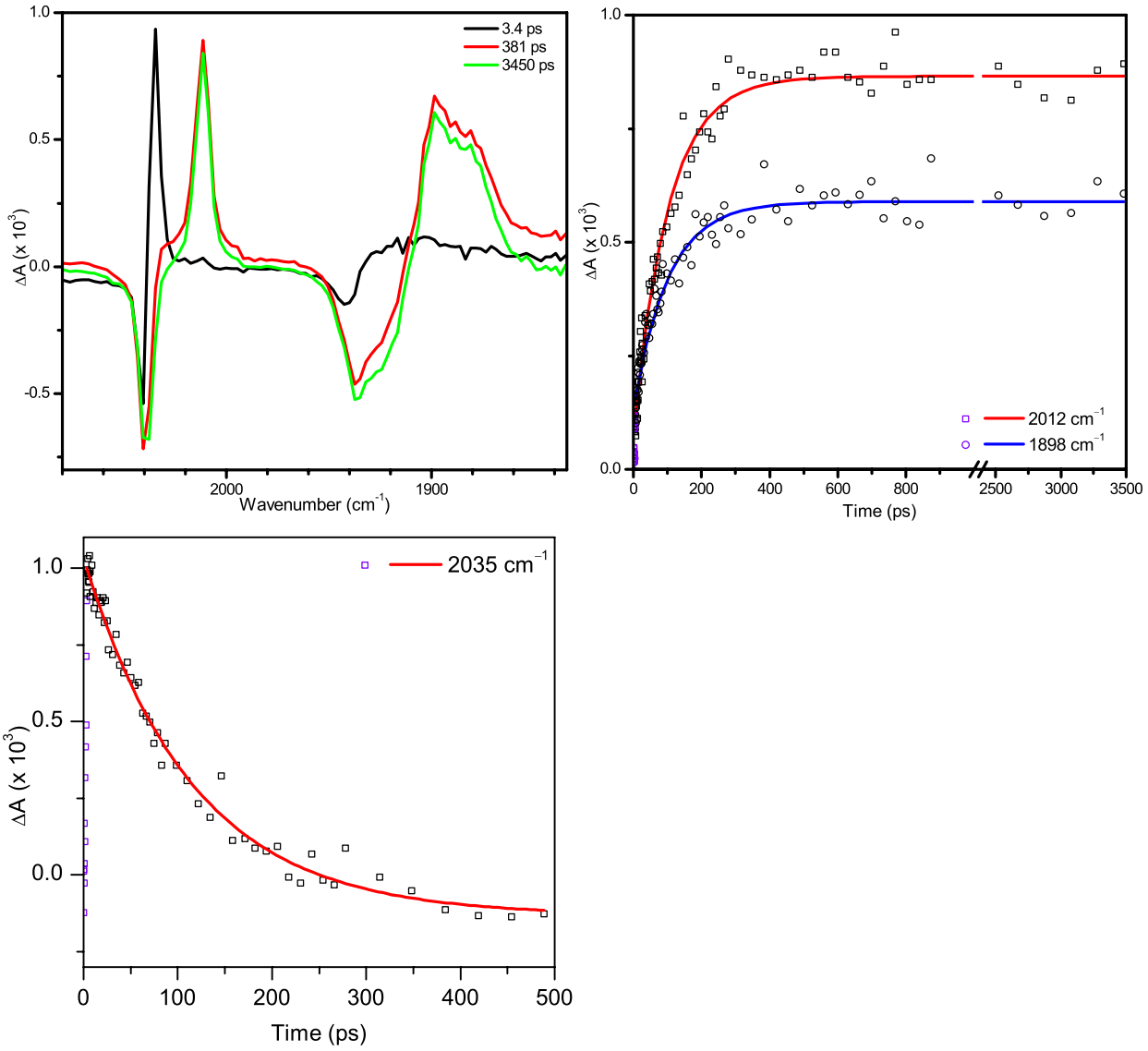

Figure 4.9 (a) TR-IR spectrum of **1** in CH_2Cl_2 with 2 mM **W** (λ_{ex} = 565 nm, Q(1,0)). (b) Kinetic analyses of bands attributable to the **Re•** moiety. (c) Kinetic analysis of S_1 induced absorption feature in TRIR spectrum of **1**. Data points go below $\Delta A = 0$ due to overlap of this induced absorption and the ground state bleach.

Over the next ~300 ps the S_1 features centered at 672 nm, 1170 nm, and 1300 nm are observed to decay almost completely (Figure 4.8). (A negative feature is still observed at 618 nm due to the Q(0,0) absorbance bleach.) Concurrently, the strong S_1 absorption at 468 nm decreases in intensity and redshifts to 477 nm, indicating it corresponds to a new state of the **ZnP** unit (described below). The lifetime of the S_1 state, determined from a global fit of the visible and near-IR absorption features (Figure 4.2), is τ_{S1} = 106 ± 1 ps. The TR-IR spectra evolve on the

same time scale (Figure 4.9bc). The S_1 absorption band at 2035 cm^{-1} decays and the overlapping bleach at 2041 cm^{-1} correspondingly broadens, intensifies, and shifts to 2037 cm^{-1}. The bleach at 1943 cm^{-1} behaves similarly to the 2041 cm^{-1} bleach, shifting to 1937 cm^{-1}, presumably due to decay of the expected, but not observed, S_1 absorption band (~1920 cm^{-1} for **ZnP−Re$^+$**; Table 4.4). In addition, new bands appear at 2012 cm^{-1} and 1898 cm^{-1}. The kinetic profiles of the TR-IR S_1 and new bands (Figure 4.9bc) can be described by single-exponential functions that provide essentially the same lifetimes; τ_{S1}(2035 cm^{-1}) = 114 ± 6 ps and τ_{rise}(2012 and 1898 cm^{-1}) = 102 ± 4 ps. These lifetimes are in good agreement with the S_1 lifetime provided by the visible and near-IR transient absorption spectra (106 ± 1 ps).

The new bands of **1** that emerge as the S_1 state decays may be assigned to redox states of its **ZnP** and **Re$^+$** subunits. In the visible transient-absorption spectrum (Figure 4.8), the evolution of the 468 nm S_1 band to a weaker band at 477 nm is assigned to formation of **ZnP$^+$** in **1**. The assignment is based on the observation that the spectroscopic changes mirror those evident in the transient-absorption spectra for **Zn$_{py}$P−Re$^+$** in the time window corresponding to maximum concentration of the oxidative-quenching product **Zn$_{py}$P$^+$−Re•**.[30] It is also consistent with the fact that the electronic absorption spectrum of ZnTPP$^+$ displays a prominent shoulder ($\varepsilon \sim 10^4$ M^{-1} cm^{-1}) between 450−500 nm, where ZnTPP exhibits only weak absorption. It is not possible to estimate the quantum yield for formation of the **ZnP$^+$**-containing transient from the spectroscopic data due to the overlap of the 477 nm band with the stronger Soret bleach, the **ZnP** T_1 state of unligated **ZnP−Re$^+$** (see below) and the absence of other distinct **ZnP$^+$** absorption bands.[56]

The TR-IR bands of **1** that appear at 2012 and 1898 cm^{-1} are assigned to CO stretches of the one-electron-reduced **Re•** subunit. These frequencies are very similar to those of

$Re(bpy•)(CO)_3(NCCH_3)$ (2017 and 1902 cm^{-1}),[53] and of the dyad ZnTPP−(NHC(O)bpy•)$Re(CO)_3$(3-Mepy) (2012 and 1902 cm^{-1}; Table 1).[22] The facts that the bleaches at 2037 and 1937 cm^{-1} do not decay during the rise of the bands 2012 and 1898 cm^{-1}, and that no other CO stretching bands are observed, indicates that the yield for forming transients containing a reduced **Re•** unit approaches unity.

Over the remaining time window of the TR-IR experiment (to 3.5 ns), the bands at 2012 and 1898 cm^{-1} and bleaches at 2037 and 1937 cm^{-1} exhibit very small changes to their intensities and no new bands emerge (Figure 4.9a). This indicates that the reduced **Re•** subunit of **1** persists during this time. In contrast, the visible and near-IR transient-absorption spectra, which report on the **ZnP** subunit, continue to decay in intensity and change. The final spectrum (Figure 4.8) exhibits the ground state bleaches, a band at 490 nm that will be discussed below, and a weak band at ~930 nm that does not correspond to a known zinc−porphyrin feature. Vestiges of the 930 nm band are also evident at earlier times; it is assigned to free **W**, which exhibits a similar transient absorption band assigned to ^{3}**W*** in this region (915 nm in toluene).[10] The corresponding band of **W−ZnTPP** is strongly shifted from that of free **W** (1077 nm in toluene, 1110 nm in C_6H_5F),[10] indicating that the 930 nm band in **1** is not attributable to coordinated **W**.

The 490 nm band overlaps with the reported spectra of $Re(bpy•)(CO)_3(L)$ (L = neutral ligand) complexes, which exhibit a maximum at approximately 490 nm.[57] The extinction coefficient for this band is not reported, but the corresponding band of $[Re(bpy•)(CO)_3Cl]^-$ (509 nm) has an extinction coefficient of 5700 M^{-1} cm^{-1} Additional spectral density in this region is likely due to background production of the **ZnP** T_1 state of unligated **ZnP−Re**$^+$. A band at 475 nm was observed by Casanova, et al., at 1000 ps in their ultrafast transient-absorption studies of unligated **ZnP−Re**$^+$, and was observed by nanosecond transient-absorption spectroscopy to

persist for more than 20 ns. This band was assigned to the T_1 state of **ZnP−Re**$^+$ generated by intersystem crossing from the S_1 state. Uncoordinated **ZnP−Re**$^+$ is expected to account for 11% of the total sample excitation (see above), and is therefore the **ZnP** T_1 state is expected to begin contributing to the observed spectrum by 300 ps.[55,58] The extinction coefficient of this band is not reported either, but by comparison, that of the ZnTPP T_1 band, which is expected to be similar to the T_1 band of the **ZnP** subunit of unligated **ZnP−Re**$^+$, is 87000 M^{-1} cm^{-1}.[55,59]We therefore assign this band at 490 nm to overlapping features from the **Re•** subunit of **1** and the **ZnP** T_1 subunit of **ZnP−Re**$^+$.

4.4 Discussion

4.4.1 Excited-State Processes of 1.

The excited state processes of triad **1** are best analyzed within the framework of the previously reported photophysical processes of the dyads **W−ZnTPP** [10] and **Zn$_{py}$P−Re**$^+$ **2**(py),[30] which model the two pairwise subunits of **1**. In studies of these dyads, it was concluded that the electronic coupling between their **ZnP**, **W**, and **Re**$^+$ components is weak and that they possess component-localized redox and excited states. For **1**, therefore, it is reasonable to describe the nature and energies of its photophysically relevant states on the basis of those previously reported for **Zn$_{py}$P−Re**$^+$ and **W−ZnTPP**. These states are shown in Figure 4.10; full details about the energy calculations are set out in Section 4.2.11. The photophysically relevant states are the **ZnP**-centered S_1 and T_1 excited states; the **W**-centered $^1[(d_{xy})^1(\pi^*(WCAr))^1]$ and $^3[(d_{xy})^1(\pi^*(WCAr))^1]$ excited states (denoted $^1[d\pi^*]$ and $^3[d\pi^*]$), where d_{xy} is the HOMO and π^*(WCAr) is the LUMO of **1**;[2] the redox states **W−ZnP**$^+$**−Re•**, and **W**$^+$**−ZnP**$^-$**−Re**$^+$, which are

[2] The π^*(WCAr) orbital is principally W≡C π-antibonding but delocalized over the C_6H_4CCpy (Ar) alkylidyne substituent. Its energy, and those of the $d\pi^*$ excited states, is perturbed by an uncertain degree upon coordination to Zn(Por), as reflected by the energy ranges in Figure 4.10.

analogous, respectively, to the $\mathbf{Zn_{py}P^{+}}$**–Re•** and $\mathbf{W^{+}}$**–ZnTPP**$^{-}$ states of the model dyads; and the charge-shift state $\mathbf{W^{+}}$**–ZnP–Re•**, in which an electron is transferred from **W** to the $\mathbf{Re^{+}}$ unit. This state lies to lower energy of all of the states described above, and could, in principle, be the product of decay of any of them. Electronic excited states of the $\mathbf{Re^{+}}$ unit lie much higher in energy than S_1 [30], and are not shown.

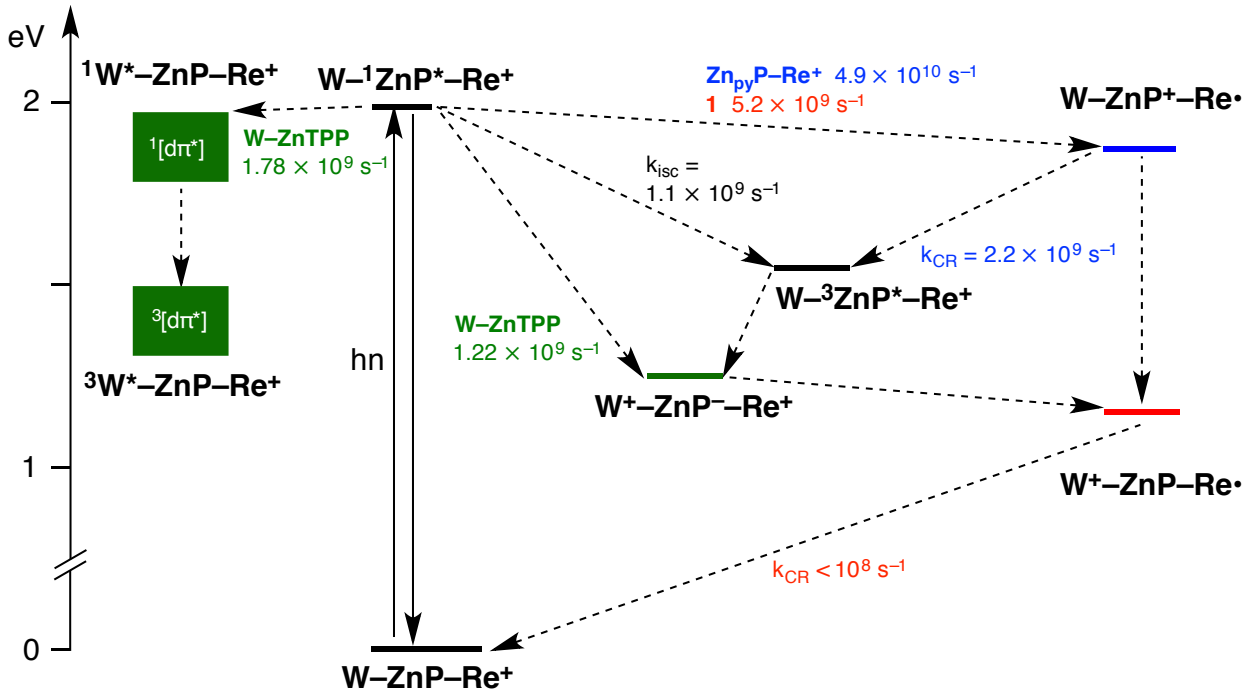

Figure 4.10 Jablonski diagram for **1**, based on excited-state energies deduced from **W–ZnTPP** and $\mathbf{Zn_{py}P–Re^{+}}$,[10,30] color coded as follows: (black) states common to **W–ZnTPP** and $\mathbf{Zn_{py}P–Re^{+}}$; (blue) state of $\mathbf{Zn_{py}P–Re^{+}}$; (dark green) states of **W–ZnTPP**; (red) terminal photoproduct of **1**. Rate constants measured in studies of **W–ZnTPP** and $\mathbf{Zn_{py}P–Re^{+}}$ are similarly color coded. Energies and rates were determined from experiments conducted in CH_2Cl_2 ($\mathbf{Zn_{py}P–Re^{+}}$, **1**) and fluorobenzene (**W–ZnTPP**). Shaded boxes indicate ranges of dπ* excited-state energies for coordinated **W**, as deduced previously.[42] Rates shown in red are calculated for **1** based on TA observations.

The intra-component decay pathways of the initial S_1 excited state of **1** are considered first. The observation in the transient-absorption spectrum of a band attributable to $\mathbf{ZnP^{+}}$ (λ =

These ranges were determined on the basis of spectroscopic studies of model compounds, as described by O'Hanlon et al.[42]

477 nm) indicates that product is the charge-shift state **W−ZnP$^+$−Re•**, which lies slightly below S_1 in energy (ΔG = −0.10 V). In **Zn$_{py}$P−Re$^+$**, the principal S_1 decay process is **Zn$_{py}$P→Re$^+$** oxidative quenching to form the analogous state **Zn$_{py}$P$^+$−Re•**.[30] Two energetically feasible S_1 decay pathways of **1**, associated with the **W−ZnP** subunit, that are not directly observed are **ZnP→W** ($S_1 \rightarrow {}^1[d\pi^*]$) Förster resonance energy transfer (FRET), which in **W−ZnTPP** gives rise to a strong transient-absorption band at 1110 nm attributable to the $^3[d\pi^*]$ state (for **W−ZnTPP** in C_6H_5F: $k_{FRET} = 1.78 \times 10^9$ s^{-1}, $\phi_{EnT} = 0.51$);[10] and **W→ZnP** reductive quenching, which in **W−ZnTPP** is manifested by the appearance of sharp transient-absorption bands near 700 nm and 900 nm due to the ZnTPP$^-$ subunit of **W$^+$−ZnTPP$^-$** (for **W−ZnTPP** in C_6H_5F: $k_{RedQ} = 1.22 \times 10^9$ s^{-1}, $\phi_{RedQ} = 0.35$),[10,56,60] The signature transient-absorption bands of these two processes are not observed for **1**, indicating either that they are formed in low quantum yield or that the product states decay rapidly to the **W$^+$−ZnP−Re•** state. The TR-IR bands at 2012 and 1898 cm^{-1} due to the reduced **Re•** subunit, which appear concomitant with S_1 decay, could be attributable to **W−ZnP$^+$−Re•** and/or **W$^+$−ZnP−Re•**, and therefore do not allow these mechanistic possibilities to be distinguished.

The quantum yields of the S_1 decay processes for **1** can be estimated if reasonable assumptions can be made as to the decay rates along each channel. Assuming for **1** that the S_1 radiative and nonradiative decay rates leading to ZnP T_1 and S_0 are the same as those of **ZnP−Re$^+$**, and that the rates of **ZnP→W** ($S_1 \rightarrow {}^1[d\pi^*]$) FRET and **W→ZnP** reductive quenching are comparable to those observed for **W−ZnTPP** (see Section 4.2.13 for details), the rates of each S_1 decay process may be estimated from the following equation:

$$\tau_{obs}^{-1} = \tau_{s_1}^{-1} - (k_{OxQ} + k_{FRET} + k_{RedQ}) \qquad \text{Equation 4.11}$$

In Equation 1, τ_{obs} is the observed S_1 lifetime of **3 1** (106 ps), τ_{S1} is the S_1 lifetime of **2 ZnP−Re$^+$** (900 ps),[30] k_{FRET} is the rate of FRET for **W−ZnTPP** (1.97×10^9 s^{-1}, determined in toluene and adjusted for CH_2Cl_2, see section 4.2.13 above),[10] and k_{RedQ} is the rate of reductive quenching for **W−ZnTPP** (1.1×10^9 s^{-1}, determined in C_6H_5F and estimated for CH_2Cl_2, see section 4.2.13 above).[10] Using these rates for the processes that are not observed provides the rate of **W−ZnP−Re$^+$** → **W−ZnP$^+$−Re•** oxidative quenching as $k_{OxQ} = 5.02 \times 10^9$ s^{-1}. From these rates, the quantum yields of the various decay processes are $\varphi_{OxQ} = k_{OxQ} \times \tau_{obs} = 0.56$, $\varphi_{FRET} = k_{FRET} \times \tau_{obs} = 0.21$, $\varphi_{RedQ} = k_{RedQ} \times \tau_{obs} = 0.12$. The relatively low estimated quantum yields for FRET and reductive quenching are consistent with the absence of signatures for these processes in the transient absorption spectrum, particularly if the **^{3}W*−ZnP−Re$^+$** and **W$^+$−ZnP−Re$^+$** states decay rapidly to the **W$^+$−ZnP−Re•** state. Alternatively, if the signatures of FRET and reductive quenching are not observed because these processes are much slower than the above estimates, the oxidative quenching rate increases to an upper bound of 8.2×10^9 s^{-1}.

In **Zn$_{py}$P−Re$^+$**, Casanova et al. observed a lifetime of 300 ps for the equilibrium between the **ZnP** S_1 and **ZnP$^+$−Re•** states.[30] Assuming that this state decays through a combination of charge recombination and the S_1 radiative and nonradiative decay pathways, we can calculate the rate of charge recombination in the absence of **1** as $k_{CR} = \tau_{obs}^{-1} - \tau_{S1}^{-1} = 2.2 \times 10^9$ s^{-1}. We assume that in **1**, the **W$^+$−ZnP−Re•** state decays through a combination of charge recombination and thermal electron transfer from **W** to **ZnP$^+$**, but since we cannot observe the kinetics of **ZnP$^+$** decay independently of other species, due to spectral overlap, we cannot calculate the rate of thermal electron transfer from **W** to **ZnP$^+$**. Although the present data do not allow the S_1 decay mechanism and kinetics to be elucidated in greater detail, it may be concluded that S_1 excitation

ultimately produces the **W$^+$−ZnP−Re•** state with high efficiency, based on the fact that the TR-IR spectrum shows that **Re•** is formed with a quantum yield approaching unity.

These results demonstrate that the excited-state properties of **1** (**W−ZnP−Re$^+$**) and **Zn$_{py}$P−Re$^+$** [30] differ in several ways. First, the intrinsic lifetime observed for the S_1 state of **Zn$_{py}$P−Re$^+$** (20 ps) is considerably shorter than that for **1** (106 ps), even though oxidative quenching is the only quenching pathway for **Zn$_{py}$P−Re$^+$** while for **1** FRET and reductive quenching pathways may also be operative. The origin of the comparatively long lifetime of **1** is unknown. Second, for **Zn$_{py}$P−Re$^+$** the product state **Zn$_{py}$P$^+$−Re•** is reported to form an equilibrium with the S_1 excited state state, which lies close to it in energy (~0.1 eV), based on the observation that the fluorescence lifetime (300 ps) is much longer than that measured for initial decay of the S_1 state. There is no evidence of this equilibrium for **1**, indicating either that the energy gap between the S_1 and **W−ZnP$^+$−Re•** states is larger, or that decay to the **W$^+$−ZnP−Re•** outcompetes repopulation of the S_1 state. The most important difference, due to its implications for photochemical reactivity, concerns the decay of the transient redox states. For **Zn$_{py}$P−Re$^+$**, as noted above, the **Zn$_{py}$P$^+$−Re•** state has a lifetime of 300 ps. In contrast, the **W$^+$−ZnP−Re•** state of **1** is not observed to decay across the 3.5 ns time window of the TR-IR, demonstrating that its lifetime is, most likely, on the ten(s) of nanoseconds time scale. Moreover, this charge-separated state is thermodynamically activated for the binding and redox transformation of CO_2 and H_2.

4.5 Conclusion

We report here on a system that efficiently produces a charge-separated state in which the oxidized and reduced species are both catalysts for energy-storing reactions. The strongly reducing tungsten−alkylidyne moiety **W**, a catalyst for H_2 oxidation, axially coordinates to dyad **ZnP−Re$^+$** composed of a zinc tetraphenylporphyrin chromophore (**ZnP**) and a rhenium-bipyridyl

CO_2 reduction catalyst (**Re**$^+$). Because the system self-assembles, each moiety can be tuned independently without extensive modification to the synthetic procedures. Once assembled, the triad can undergo a series of photoinduced electron transfer steps on the ultrafast timescale, resulting in a long-lived charge-separated state.

Upon excitation of the porphyrin moiety, the initial charge-separated state is formed within 300 ps through oxidative quenching by the **Re**$^+$ moiety. The kinetics of charge separation were monitored by visible, near-IR, and mid-IR transient absorption spectroscopy. Mid-IR TA in particular proved to be essential for verifying the reduction of the **Re**$^+$ moiety. After oxidative quenching, the **ZnP**$^+$ is reduced rapidly back to the ground state, while the reduced **Re•** lives past the timescale of our experiments (>3.5 ns). This is attributable to the coordination of strongly reducing **W** to the **ZnP**$^+$. This result stands in stark contrast to the situation in the analogous system $\mathbf{Zn_{py}P{-}Re^+}$, in which **ZnP** is ligated by pyridine. In that system, there is nothing to prevent back-electron transfer from **Re•** to **ZnP**$^+$, either to set up an equilibrium between the **ZnP** S_1 and the charge-separated state, to recombine to the **ZnP** T_1 state, or to recombine back to the ground state. Without appended **W**, the charge-separated state decays with a lifetime of 300 ps.

This system demonstrates the feasibility of producing catalytic assemblies capable of charge separation without the use of a sacrificial electron donor. Further work on this system would include the use of more active catalyst species that are capable of binding their substrates within the lifetime of the final charge-separated state.

4.6 References

(1) Barber, J.; Tran, P. D. *J Royal Soc. Interfac.* **2013**, *10*, 20120984.

(2) Albinsson, B.; Mårtensson, J. *J Photochem. Photobio. C: Photochem. Rev.* **2008**, *9*, 138.

(3) Artero, V.; Fontecave, M. *Chem. Soc. Rev.* **2013**, *42*, 2338.

(4) Balzani, V.; Credi, A.; Venturi, M. *Chem. Eur. J.* **2008**, *14*, 26.

(5) de la Torre, G.; Bottari, G.; Sekita, M.; Hausmann, A.; Guldi, D. M.; Torres, T. *Chem. Soc. Rev.* **2013**, *42*, 8049.

(6) Falkenström, M.; Johansson, O.; Hammarström, L. *Inorg. Chim. Acta* **2007**, *360*, 741.

(7) Takeda, H.; Ishitani, O. *Coord. Chem. Rev.* **2010**, *254*, 346.

(8) El-Khouly, M. E.; Wijesinghe, C. A.; Nesterov, V. N.; Zandler, M. E.; Fukuzumi, S.; D'Souza, F. *Chem. Eur. J.* **2012**, *18*, 13844.

(9) Wasielewski, M. R. *Acc. Chem. Res.* **2009**, *42*, 1910.

(10) Moravec, D. B.; Hopkins, M. D. *Chem. Eur. J* .**2013**, *19*, 17082.

(11) Moravec, D. B.; Hopkins, M. D. *J. Phys. Chem. A* **2013**, *117*, 1744.

(12) Bottari, G.; Trukhina, O.; Ince, M.; Torres, T. *Coord. Chem. Rev.* **2012**, *256*, 2453.

(13) Lifschitz, A. M.; Young, R. M.; Mendez-Arroyo, J.; Stern, C. L.; McGuirk, C. M.; Wasielewski, M. R.; Mirkin, C. A. *Nat. Comm.* **2015**, *6*, 1.

(14) Poddutoori, P.; Co, D. T.; Samuel, A. P. S.; Kim, C. H.; Vagnini, M. T.; Wasielewski, M. R. *Energy Environ. Sci.* **2011**, *4*, 2441.

(15) Veldkamp, B. S.; Han, W.-S.; Dyar, S. M.; Eaton, S. W.; Ratner, M. A.; Wasielewski, M. R. *Energy Environ. Sci.* **2013**, *6*, 1917.

(16) Tamaki, Y.; Watanabe, K.; Koike, K.; Inoue, H.; Morimoto, T.; Ishitani, O. *Faraday Discussions* **2012**, *155*, 115.

(17) Sahara, G.; Ishitani, O. *Inorg. Chem.* **2015**, *54*, 150128111221006.

(18) Windle, C. D.; Perutz, R. N. *Coord. Chem. Rev.* **2012**, *256*, 2562.

(19) La Porte, N.; Moravec, D. B.; Hopkins, M. D. *Proc. Nat. Acad. Sci. USA* **2014**, *111*, 9745.

(20) Xiaoding, X.; Moulijn, J. A. *Energ. Fuels* **1996**, *10*, 305.

(21) Ettedgui, J.; Diskin-Posner, Y.; Weiner, L.; Neumann, R. *J. Am. Chem. Soc.* **2011**, *133*, 188.

(22) Gabrielsson, A.; Hartl, F.; Zhang, H.; Smith, J. R. L.; Towrie, M.; Antonín Vlček Jr, a.; Perutz, R. N. *J. Am. Chem. Soc* .**2006**, *128*, 4253.

(23) Perutz, R.; Windle, C.; Câmpian, M. *Chem. Comm.* **2012**, *48*, 8189.

(24) Schneider, J.; Vuong, K. Q.; Calladine, J. A.; Sun, X.-Z.; Whitwood, A. C.; George, M. W.; Perutz, R. N. *Inorg. Chem.* **2013**, *50*, 11877.

(25) Kiyosawa, K.; Shiraishi, N.; Shimada, T.; Masui, D.; Tachibana, H.; Takagi, S.; Ishitani, O.; Tryk, D. A.; Inoue, H. *J. Phys. Chem. C* **2009**, *113*, 11667.

(26) Kou, Y.; Nakatani, S.; Sunagawa, G.; Tachikawa, Y.; Masui, D.; Shimada, T.; Takagi, S.; Tryk, D. A.; Nabetani, Y.; Tachibana, H.; Inoue, H. *J. Catal*. **2013**, *310*, 57.

(27) Kitagawa, Y.; Takeda, H.; Ohashi, K.; Asatani, T.; Kosumi, D.; Hashimoto, H.; Ishitani, O.; Tamiaki, H. *Chem. Lett.* **2014**, *43*, 1383.

(28) Cavigli, P.; Da Ros, T.; Kahnt, A.; Gamberoni, M.; Indelli, M. T.; Iengo, E. *Inorg. Chem.* **2014**, *54*, 280.

(29) Ghirotti, M.; Chiorboli, C.; Indelli, M. T.; Scandola, F.; Casanova, M.; Iengo, E.; Alessio, E. *Inorg. Chim. Acta* **2007**, *360*, 1121.

(30) Casanova, M.; Zangrando, E.; Iengo, E.; Alessio, E.; Indelli, M. T.; Scandola, F.; Orlandi, M. *Inorg. Chem.* **2008**, *47*, 10407.

(31) Gatti, T.; Cavigli, P.; Zangrando, E.; Iengo, E.; Chiorboli, C.; Indelli, M. T. *Inorg. Chem.* **2013**, *52*, 3190.

(32) Morales-Verdejo, C. A.; Newsom, M. I.; Cohen, B. W.; Vibbert, H. B.; Hopkins, M. D. *Chem. Comm*. **2013**, *49*, 10566.

(33) Pangborn, A. B.; Giardello, M. A.; Grubbs, R. H.; Rosen, R. K.; Timmers, F. J. *Organomet.* **1996**, *15*, 1518.

(34) Fleischer, E. B.; Shachter, A. M. *Inorg. Chem.* **1991**, *30*, 3763.

(35) Cohen, B. W.; Lovaasen, B. M.; Simpson, C. K.; Cummings, S. D.; Dallinger, R. F.; Hopkins, M. D. *Inorg. Chem.* **2010**, *49*, 5777.

(36) Casanova, M.; Zangrando, E.; Munini, F.; Iengo, E.; Alessio, E. *J. Chem. Soc. Dalton Trans.* **2006**, 5033.

(37) Moravec, D. B.; Lovaasen, B. M.; Hopkins, M. D. *J Photochem. Photobio. A* **2013**, *254*, 20.

(38) Walters, V. A.; de Paula, J. C.; Jackson, B.; Nutaitis, C.; Hall, K.; Lind, J.; Cardozo, K.; Chandran, K.; Raible, D.; Phillips, C. M. *J. Phys. Chem.* **1995**, *99*, 1166.

(39) Gust, D.; Moore, T. A.; Moore, A. L.; Kang, H. K.; DeGraziano, J. M.; Liddell, P. A.; Seely, G. R. *J. Phys. Chem.* **1993**, *97*, 13637.

(40) Braslavsky, S. E. *Pure. Appl. Chem.* **2007**, *79*, 293.

(41) *CRC Handbook of Chemistry and Physics*; Haynes, W. M., Ed.; CRC Press/Taylor and Francis: Boca Raton, FL, 2013.

(42) O'Hanlon, D. C.; Cohen, B. W.; Moravec, D. B.; Dallinger, R. F.; Hopkins, M. D. *J. Am. Chem. Soc.* **2014**, *136*, 3127.

(43) Lovaasen, B., 2011.

(44) Connelly, N. G.; Geiger, W. E. *Chem. Rev.* **1996**, *96*, 877.

(45) Kalyanasundaram, K. *Photochemistry of Polypyridine and Porphyrin Complexes*; Academic Press, 1992.

(46) Frisch, M. J.; Trucks, G. W.; Schlegel, H. B.; Scuseria, G. E.; Robb, M. A.; Cheeseman, J. R.; Scalmani, G.; Barone, V.; Mennucci, B.; Petersson, G. A.; Nakatsuji, H.; Caricato, M.; Li, X.; Hratchian, H. P.; Izmaylov, A. F.; Bloino, J.; Zheng, G.; Sonnenberg, J. L.; Hada, M.; Ehara, M.; Toyota, K.; Fukuda, R.; Hasegawa, J.; Ishida, M.; Nakajima, T.; Honda, Y.; Kitao, O.; Nakai, H.; Vreven, T.; Montgomery, J. A.; Peralta, J. E.; Ogliaro, F.; Bearpark, M.; Heyd, J. J.; Brothers, E.; Kudin, K. N.; Staroverov, V. N.; Kobayashi, R.; Normand, J.; Raghavachari, K.; Rendell, A.; Burant, J. C.; Iyengar, S. S.; Tomasi, J.; Cossi, M.; Rega, N.; Millam, J. M.; Klene, M.; Knox, J. E.; Cross, J. B.; Bakken, V.; Adamo, C.; Jaramillo, J.; Gomperts, R.; Stratmann, R. E.; Yazyev, O.; Austin, A. J.; Cammi, R.; Pomelli, C.; Ochterski, J. W.; Martin, R. L.; Morokuma, K.; Zakrzewski, V. G.; Voth, G. A.; Salvador, P.; Dannenberg, J. J.; Dapprich, S.; Daniels, A. D.; Farkas; Foresman, J. B.; Ortiz, J. V.; Cioslowski, J.; Fox, D. J. Wallingford CT, 2009.

(47) Hehre, W. J.; Ditchfield, R.; Pople, J. A. *J. Chem. Phys.* **1972**, *56*, 2257.

(48) Hariharan, P. C.; Pople, J. A. *Theoretica chimica acta* **1973**, *28*, 213.

(49) Hay, P. J.; Wadt, W. R. *J. Chem. Phys.* **1985**, *82*, 270.

(50) Wadt, W. R.; Hay, P. J. *J. Chem. Phys.* **1985**, *82*, 284.

(51) Sampaio, R. N.; Gomes, W. R.; Araujo, D. M. S.; Machado, A. E. H.; Silva, R. A.; Marletta, A.; Borissevitch, I. E.; Ito, A. S.; Dinelli, L. R.; Batista, A. A.; Zílio, S. C.; Gonçalves, P. J.; Barbosa Neto, N. M. *J. Phys. Chem. A* **2012**, *116*, 18.

(52) Dattelbaum, D. M.; Omberg, K. M.; Schoonover, J. R.; Richard L Martin, a.; Meyer, T. J. *Inorg. Chem.* **2002**, *41*, 6071.

(53) Hayashi, Y.; Kita, S.; Brunschwig, B. S.; Fujita, E. *J. Am. Chem. Soc.* **2003**, *125*, 11976.

(54) Bhyrappa, P.; Krishnan, V.; Nethaji, M. *J. Chem. Soc. Dalton. Trans.* **1993**, 1901.

(55) Rodriguez, J.; Kirmaier, C.; Holten, D. *J. Am. Chem. Soc.* **1989**, *111*, 6500.

(56) Fajer, J.; Borg, D. C.; Forman, A.; Dolphin, D.; Felton, R. H. *J. Am. Chem. Soc.* **1970**, *92*, 3451.

(57) Fujita, E.; Muckerman, J. T. *Inorg. Chem.* **2004**, *43*, 7636.

(58) Pekkarinen, L.; Linschitz, H. *J. Am. Chem. Soc.* **1960**, *82*, 2407.

(59) Lee, Y. F.; Kirchhoff, J. R.; Berger, R. M.; Gosztola, D. *J. Chem. Soc. Dalton. Trans* . **1995**, 3677.

(60) Lanese, J. G.; Wilson, G. S. *J. Electrochem. Soc*. **1972**, *119*, 1039.

Appendix A Crystal Structure of $[NEt_4][CpCr(CO)_3]$

A.1 Experimental

The complex was synthesized and crystallized as described in Chapter 2. An irregular broken fragment (0.40 x 0.20 x 0.16 mm) was selected under a stereo-microscope while immersed in Fluorolube oil to avoid possible reaction with air. The crystal was removed from the oil using a tapered glass fiber that also served to hold the crystal for data collection. The crystal was mounted and centered on a Bruker SMART APEX system at 100 K. Still images showed the diffractions to be sharp. Frames separated in reciprocal space were obtained and provided an orientation matrix and initial cell parameters. Final cell parameters were obtained from the full data set.

A "full sphere" data set was obtained which samples approximately all of reciprocal space to a resolution of 0.84 Å using 0.3^{o} steps in w using 20 second integration times for each frame. Data collection was performed at 100 K. Data were corrected for absorption effects using the multi-scan procedure as implemented in SADABS (Bruker AXS, version 2014/4, 2014, part of Bruker APEX2 software package). The structure was solved by SHELXT[1] and refined by a full-matrix least-squares procedure using Bruker SHELXTL (version 6.14) software package (XL refinement program version 2014/7).[2,3] Crystallographic data and details of the data collection and structure refinement are listed in Table A.1.

A.2 Structure solution and refinement

The space group was determined as $P2_1/c$ based on cell parameters, systematic absences and intensity statistics. Final refinement was anisotropic for non-H atoms and isotropic-riding for H atoms. The displacement parameters for the Cp groups are slightly elongated suggesting

libration about the rotation axis. No other anomalous bond lengths or thermal parameters were noted. All ORTEP diagrams have been drawn with 35% probability ellipsoids.

Table A.1 Crystal data and structure refinement for $[NEt_4][Cp^*Cr(CO)_3]$

Empirical formula	$C_{16}H_{25}CrNO_3$	
Formula weight	331.37	
Temperature	100(2) K	
Wavelength	0.71073 Å	
Crystal system	Monoclinic	
Space group	$P2_1/n$	
Unit cell dimensions	a = 17.711(7) Å	α= 90°.
	b = 8.600(3) Å	β= 107.446(6)°.
	c = 21.619(8) Å	γ = 90°.
Volume	3142(2) Å3	
Z	8	
Density (calculated)	1.401 Mg/m3	
Absorption coefficient	0.738 mm-1	
F(000)	1408	
Crystal size	0.400 x 0.200 x 0.160 mm3	
Theta range for data collection	1.309 to 25.597°.	
Index ranges	$-21 \le h \le 21, -10 \le k \le 10, -26 \le l \le 25$	
Reflections collected	23194	
Independent reflections	5803 [R(int) = 0.0608]	
Completeness to theta = 25.242°	99.90%	
Absorption correction	Semi-empirical from equivalents	
Max. and min. transmission	0.745 and 0.618	
Refinement method	Full-matrix least-squares on F^2	
Data / restraints / parameters	5803 / 0 / 387	
Goodness-of-fit on F^2	1.045	
Final R indices [$I > 2\sigma(I)$]	R1 = 0.0494, wR2 = 0.1158	
R indices (all data)	R1 = 0.0782, wR2 = 0.1298	
Extinction coefficient	n/a	
Largest diff. peak and hole	0.533 and -0.426 e.Å^{-3}	

$R_{int} = \Sigma | F_o^2 - \langle F_o^2 \rangle | / \Sigma | F_o^2 |$

$R1 = \Sigma || F_o | - | F_c || / \Sigma | F_o |$

$wR2 = [\Sigma [w (F_o^2 - F_c^2)^2] / \Sigma [w (F_o^2)^2]]^{1/2}$

Goodness-of-fit = $[\Sigma [w (F_o^2 - F_c^2)^2] / (n-p)]^{1/2}$

n: number of independent reflections; p: number of refined parameters

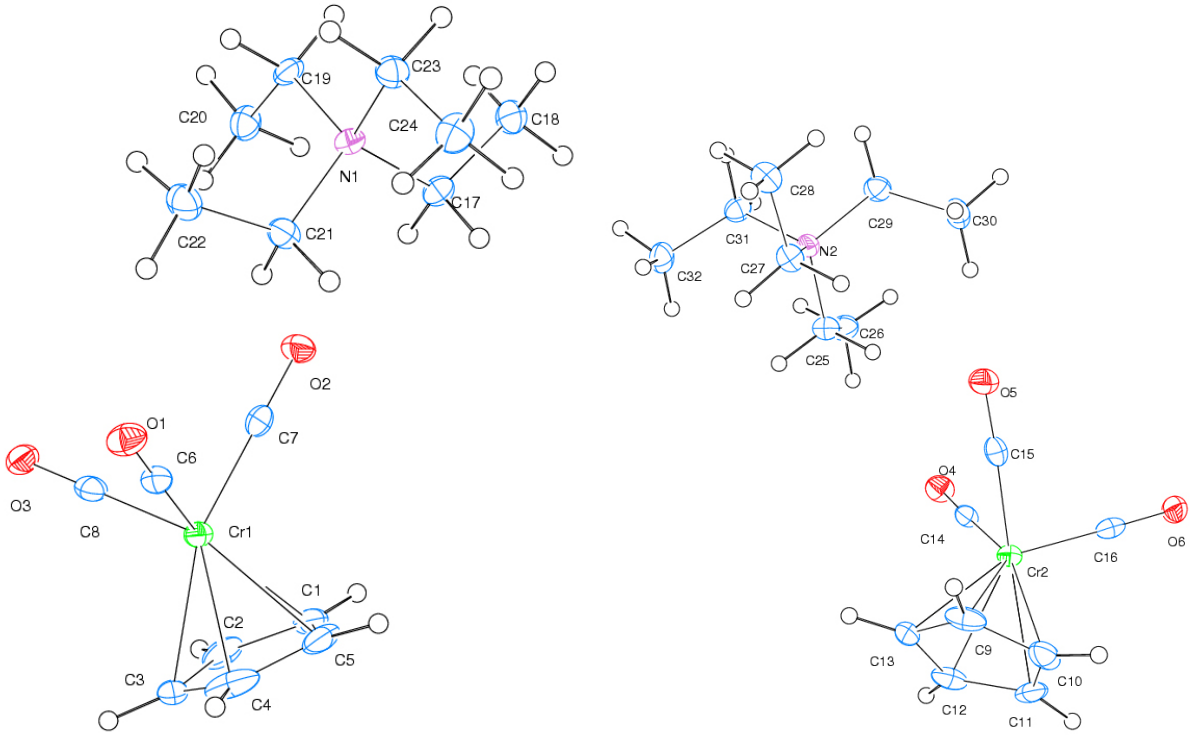

Figure A.1 ORTEP views of the two repeating subunits of the $[NEt_4][Cp^*Cr(CO)_3]$ crystal. Thermal ellipsoids are drawn at 35% probability.

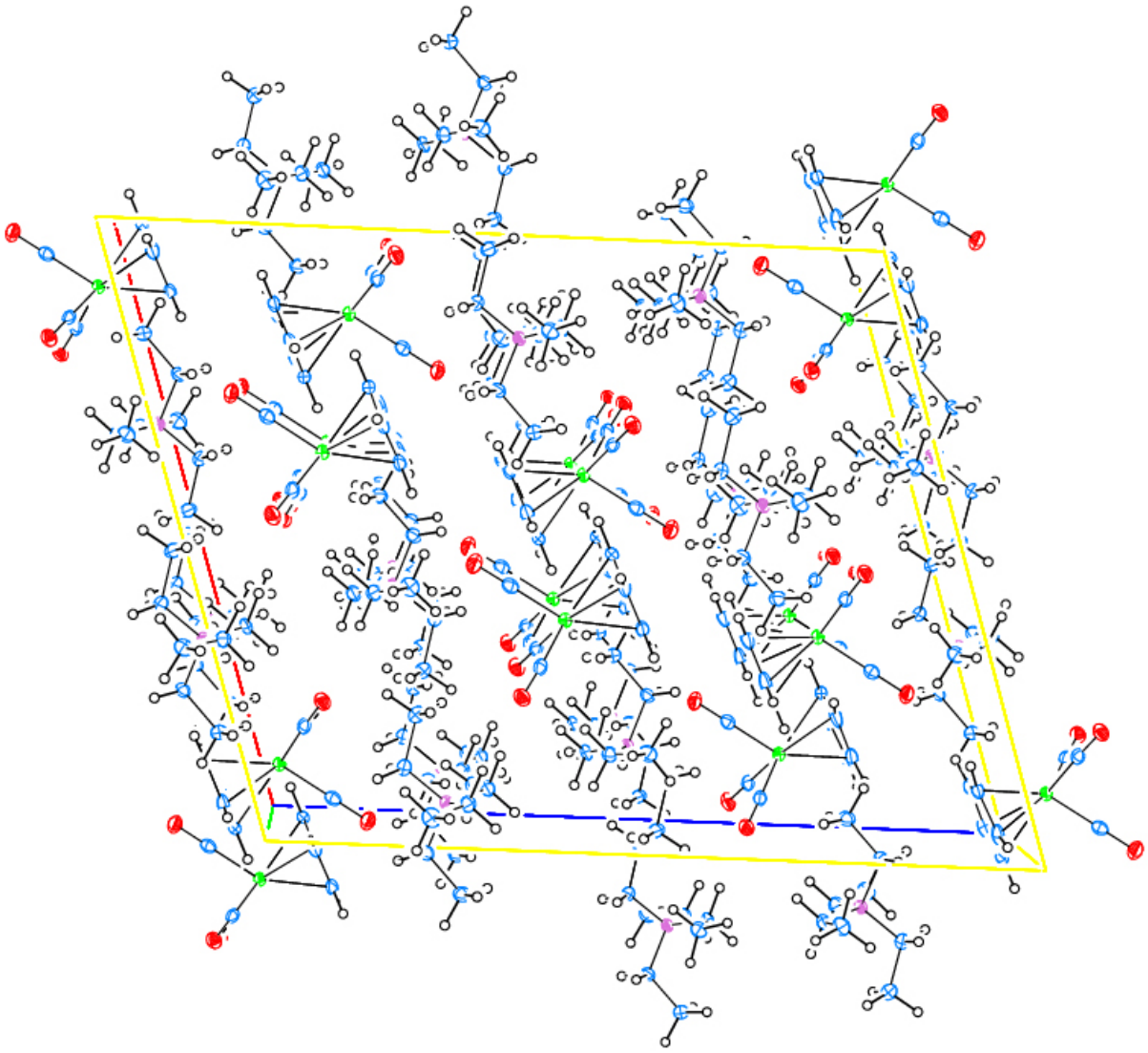

Figure A.2 Depiction of the unit cell of $[NEt_4][Cp^*Cr(CO)_3]$.

Table A.2 Bond lengths [Å] and angles [°] for $[NEt_4][Cp^*Cr(CO)_3]$.

Cr(1)-C(6)	1.784(3)
Cr(1)-C(8)	1.786(4)
Cr(1)-C(7)	1.793(3)
Cr(1)-C(2)	2.167(3)
Cr(1)-C(1)	2.178(4)
Cr(1)-C(3)	2.184(3)
Cr(1)-C(4)	2.184(3)
Cr(1)-C(5)	2.195(3)
Cr(2)-C(14)	1.779(3)
Cr(2)-C(15)	1.786(3)
Cr(2)-C(16)	1.786(4)
Cr(2)-C(13)	2.179(3)
Cr(2)-C(12)	2.183(3)
Cr(2)-C(9)	2.186(3)
Cr(2)-C(10)	2.189(3)
Cr(2)-C(11)	2.194(3)
O(1)-C(6)	1.171(4)
O(2)-C(7)	1.160(3)
O(3)-C(8)	1.167(4)
O(4)-C(14)	1.174(4)
O(5)-C(15)	1.167(4)
O(6)-C(16)	1.169(4)
N(1)-C(19)	1.493(4)
N(1)-C(23)	1.495(4)
N(1)-C(21)	1.506(4)
N(1)-C(17)	1.521(4)
N(2)-C(31)	1.488(4)
N(2)-C(29)	1.496(4)
N(2)-C(25)	1.507(4)
N(2)-C(27)	1.512(4)
C(1)-C(2)	1.361(5)
C(1)-C(5)	1.387(5)
C(1)-H(1)	0.9500
C(2)-C(3)	1.371(5)
C(2)-H(2)	0.9500
C(3)-C(4)	1.369(5)
C(3)-H(3)	0.9500
C(4)-C(5)	1.385(5)
C(4)-H(4)	0.9500
C(5)-H(5)	0.9500
C(9)-C(10)	1.378(5)
C(9)-C(13)	1.387(5)
C(9)-H(9)	0.9500
C(10)-C(11)	1.387(5)
C(10)-H(10)	0.9500
C(11)-C(12)	1.372(5)
C(11)-H(11)	0.9500
C(12)-C(13)	1.383(5)
C(12)-H(12)	0.9500
C(13)-H(13)	0.9500
C(17)-C(18)	1.500(4)
C(17)-H(17A)	0.9900
C(17)-H(17B)	0.9900
C(18)-H(18A)	0.9800
C(18)-H(18B)	0.9800
C(18)-H(18C)	0.9800
C(19)-C(20)	1.496(4)
C(19)-H(19A)	0.9900
C(19)-H(19B)	0.9900
C(20)-H(20A)	0.9800
C(20)-H(20B)	0.9800
C(20)-H(20C)	0.9800
C(21)-C(22)	1.500(4)
C(21)-H(21A)	0.9900
C(21)-H(21B)	0.9900
C(22)-H(22A)	0.9800
C(22)-H(22B)	0.9800
C(22)-H(22C)	0.9800
C(23)-C(24)	1.505(4)
C(23)-H(23A)	0.9900
C(23)-H(23B)	0.9900
C(24)-H(24A)	0.9800
C(24)-H(24B)	0.9800
C(24)-H(24C)	0.9800
C(25)-C(26)	1.509(4)
C(25)-H(25A)	0.9900
C(25)-H(25B)	0.9900
C(26)-H(26A)	0.9800
C(26)-H(26B)	0.9800
C(26)-H(26C)	0.9800
C(27)-C(28)	1.497(4)
C(27)-H(27A)	0.9900
C(27)-H(27B)	0.9900
C(28)-H(28A)	0.9800
C(28)-H(28B)	0.9800
C(28)-H(28C)	0.9800
C(29)-C(30)	1.500(4)
C(29)-H(29A)	0.9900
C(29)-H(29B)	0.9900
C(30)-H(30A)	0.9800
C(30)-H(30B)	0.9800
C(30)-H(30C)	0.9800
C(31)-C(32)	1.500(4)
C(31)-H(31A)	0.9900
C(31)-H(31B)	0.9900
C(32)-H(32A)	0.9800
C(32)-H(32B)	0.9800
C(32)-H(32C)	0.9800
C(6)-Cr(1)-C(8)	88.93(15)
C(6)-Cr(1)-C(7)	88.30(14)
C(8)-Cr(1)-C(7)	89.67(13)
C(6)-Cr(1)-C(2)	153.54(14)
C(8)-Cr(1)-C(2)	97.20(14)
C(7)-Cr(1)-C(2)	117.32(14)
C(6)-Cr(1)-C(1)	144.27(15)
C(8)-Cr(1)-C(1)	126.74(15)
C(7)-Cr(1)-C(1)	93.35(14)
C(2)-Cr(1)-C(1)	36.52(13)
C(6)-Cr(1)-C(3)	116.92(14)

Table A.2, continued

C(8)-Cr(1)-C(3)	99.03(14)
C(7)-Cr(1)-C(3)	153.25(14)
C(2)-Cr(1)-C(3)	36.74(13)
C(1)-Cr(1)-C(3)	61.20(13)
C(6)-Cr(1)-C(4)	95.60(13)
C(8)-Cr(1)-C(4)	130.64(15)
C(7)-Cr(1)-C(4)	139.46(16)
C(2)-Cr(1)-C(4)	61.08(13)
C(1)-Cr(1)-C(4)	61.21(13)
C(3)-Cr(1)-C(4)	36.53(14)
C(6)-Cr(1)-C(5)	108.20(15)
C(8)-Cr(1)-C(5)	158.20(14)
C(7)-Cr(1)-C(5)	103.87(15)
C(2)-Cr(1)-C(5)	61.49(14)
C(1)-Cr(1)-C(5)	37.00(14)
C(3)-Cr(1)-C(5)	61.52(13)
C(4)-Cr(1)-C(5)	36.86(14)
C(14)-Cr(2)-C(15)	86.30(14)
C(14)-Cr(2)-C(16)	89.84(14)
C(15)-Cr(2)-C(16)	90.15(13)
C(14)-Cr(2)-C(13)	103.96(14)
C(15)-Cr(2)-C(13)	106.05(14)
C(16)-Cr(2)-C(13)	159.15(13)
C(14)-Cr(2)-C(12)	95.91(13)
C(15)-Cr(2)-C(12)	142.38(14)
C(16)-Cr(2)-C(12)	127.32(13)
C(13)-Cr(2)-C(12)	36.97(12)
C(14)-Cr(2)-C(9)	138.54(14)
C(15)-Cr(2)-C(9)	92.44(14)
C(16)-Cr(2)-C(9)	131.62(14)
C(13)-Cr(2)-C(9)	37.06(12)
C(12)-Cr(2)-C(9)	61.63(13)
C(14)-Cr(2)-C(10)	156.93(13)
C(15)-Cr(2)-C(10)	114.24(14)
C(16)-Cr(2)-C(10)	100.02(14)
C(13)-Cr(2)-C(10)	61.63(13)
C(12)-Cr(2)-C(10)	61.54(13)
C(9)-Cr(2)-C(10)	36.71(13)
C(14)-Cr(2)-C(11)	121.35(14)
C(15)-Cr(2)-C(11)	150.89(14)
C(16)-Cr(2)-C(11)	98.20(13)
C(13)-Cr(2)-C(11)	61.33(13)
C(12)-Cr(2)-C(11)	36.54(13)
C(9)-Cr(2)-C(11)	61.31(13)
C(10)-Cr(2)-C(11)	36.90(12)
C(19)-N(1)-C(23)	106.7(2)
C(19)-N(1)-C(21)	111.9(2)
C(23)-N(1)-C(21)	111.3(2)
C(19)-N(1)-C(17)	110.7(2)
C(23)-N(1)-C(17)	110.8(2)
C(21)-N(1)-C(17)	105.5(2)
C(31)-N(2)-C(29)	106.7(2)
C(31)-N(2)-C(25)	110.9(2)
C(29)-N(2)-C(25)	111.9(2)
C(31)-N(2)-C(27)	111.2(2)
C(29)-N(2)-C(27)	110.9(2)
C(25)-N(2)-C(27)	105.4(2)
C(2)-C(1)-C(5)	108.4(3)
C(2)-C(1)-Cr(1)	71.3(2)
C(5)-C(1)-Cr(1)	72.2(2)
C(2)-C(1)-H(1)	125.8
C(5)-C(1)-H(1)	125.8
Cr(1)-C(1)-H(1)	122.4
C(1)-C(2)-C(3)	108.7(3)
C(1)-C(2)-Cr(1)	72.2(2)
C(3)-C(2)-Cr(1)	72.3(2)
C(1)-C(2)-H(2)	125.7
C(3)-C(2)-H(2)	125.7
Cr(1)-C(2)-H(2)	121.6
C(4)-C(3)-C(2)	107.6(3)
C(4)-C(3)-Cr(1)	71.77(19)
C(2)-C(3)-Cr(1)	71.0(2)
C(4)-C(3)-H(3)	126.2
C(2)-C(3)-H(3)	126.2
Cr(1)-C(3)-H(3)	122.7
C(3)-C(4)-C(5)	108.8(3)
C(3)-C(4)-Cr(1)	71.70(19)
C(5)-C(4)-Cr(1)	72.0(2)
C(3)-C(4)-H(4)	125.6
C(5)-C(4)-H(4)	125.6
Cr(1)-C(4)-H(4)	122.4
C(4)-C(5)-C(1)	106.5(3)
C(4)-C(5)-Cr(1)	71.2(2)
C(1)-C(5)-Cr(1)	70.8(2)
C(4)-C(5)-H(5)	126.8
C(1)-C(5)-H(5)	126.8
Cr(1)-C(5)-H(5)	123.0
O(1)-C(6)-Cr(1)	178.4(3)
O(2)-C(7)-Cr(1)	179.1(3)
O(3)-C(8)-Cr(1)	179.5(3)
C(10)-C(9)-C(13)	108.1(3)
C(10)-C(9)-Cr(2)	71.8(2)
C(13)-C(9)-Cr(2)	71.22(19)
C(10)-C(9)-H(9)	126.0
C(13)-C(9)-H(9)	126.0
Cr(2)-C(9)-H(9)	122.7
C(9)-C(10)-C(11)	107.7(3)
C(9)-C(10)-Cr(2)	71.5(2)
C(11)-C(10)-Cr(2)	71.74(19)
C(9)-C(10)-H(10)	126.1
C(11)-C(10)-H(10)	126.1
Cr(2)-C(10)-H(10)	122.3
C(12)-C(11)-C(10)	108.3(3)
C(12)-C(11)-Cr(2)	71.32(17)
C(10)-C(11)-Cr(2)	71.35(19)
C(12)-C(11)-H(11)	125.8
C(10)-C(11)-H(11)	125.8
Cr(2)-C(11)-H(11)	123.1
C(11)-C(12)-C(13)	108.1(3)
C(11)-C(12)-Cr(2)	72.15(18)
C(13)-C(12)-Cr(2)	71.35(18)

Table A.2, continued

C(11)-C(12)-H(12)	126.0
C(13)-C(12)-H(12)	126.0
Cr(2)-C(12)-H(12)	122.2
C(12)-C(13)-C(9)	107.8(3)
C(12)-C(13)-Cr(2)	71.69(19)
C(9)-C(13)-Cr(2)	71.72(19)
C(12)-C(13)-H(13)	126.1
C(9)-C(13)-H(13)	126.1
Cr(2)-C(13)-H(13)	122.2
O(4)-C(14)-Cr(2)	177.5(3)
O(5)-C(15)-Cr(2)	177.4(3)
O(6)-C(16)-Cr(2)	179.1(3)
C(18)-C(17)-N(1)	115.7(3)
C(18)-C(17)-H(17A)	108.4
N(1)-C(17)-H(17A)	108.4
C(18)-C(17)-H(17B)	108.4
N(1)-C(17)-H(17B)	108.4
H(17A)-C(17)-H(17B)	107.4
C(17)-C(18)-H(18A)	109.5
C(17)-C(18)-H(18B)	109.5
H(18A)-C(18)-H(18B)	109.5
C(17)-C(18)-H(18C)	109.5
H(18A)-C(18)-H(18C)	109.5
H(18B)-C(18)-H(18C)	109.5
N(1)-C(19)-C(20)	115.3(3)
N(1)-C(19)-H(19A)	108.4
C(20)-C(19)-H(19A)	108.4
N(1)-C(19)-H(19B)	108.4
C(20)-C(19)-H(19B)	108.4
H(19A)-C(19)-H(19B)	107.5
C(19)-C(20)-H(20A)	109.5
C(19)-C(20)-H(20B)	109.5
H(20A)-C(20)-H(20B)	109.5
C(19)-C(20)-H(20C)	109.5
H(20A)-C(20)-H(20C)	109.5
H(20B)-C(20)-H(20C)	109.5
C(22)-C(21)-N(1)	114.6(3)
C(22)-C(21)-H(21A)	108.6
N(1)-C(21)-H(21A)	108.6
C(22)-C(21)-H(21B)	108.6
N(1)-C(21)-H(21B)	108.6
H(21A)-C(21)-H(21B)	107.6
C(21)-C(22)-H(22A)	109.5
C(21)-C(22)-H(22B)	109.5
H(22A)-C(22)-H(22B)	109.5
C(21)-C(22)-H(22C)	109.5
H(22A)-C(22)-H(22C)	109.5
H(22B)-C(22)-H(22C)	109.5
N(1)-C(23)-C(24)	115.0(3)
N(1)-C(23)-H(23A)	108.5
C(24)-C(23)-H(23A)	108.5
N(1)-C(23)-H(23B)	108.5
C(24)-C(23)-H(23B)	108.5
H(23A)-C(23)-H(23B)	107.5
C(23)-C(24)-H(24A)	109.5
C(23)-C(24)-H(24B)	109.5
H(24A)-C(24)-H(24B)	109.5
C(23)-C(24)-H(24C)	109.5
H(24A)-C(24)-H(24C)	109.5
H(24B)-C(24)-H(24C)	109.5
N(2)-C(25)-C(26)	114.4(3)
N(2)-C(25)-H(25A)	108.7
C(26)-C(25)-H(25A)	108.7
N(2)-C(25)-H(25B)	108.7
C(26)-C(25)-H(25B)	108.7
H(25A)-C(25)-H(25B)	107.6
C(25)-C(26)-H(26A)	109.5
C(25)-C(26)-H(26B)	109.5
H(26A)-C(26)-H(26B)	109.5
C(25)-C(26)-H(26C)	109.5
H(26A)-C(26)-H(26C)	109.5
H(26B)-C(26)-H(26C)	109.5
C(28)-C(27)-N(2)	115.0(3)
C(28)-C(27)-H(27A)	108.5
N(2)-C(27)-H(27A)	108.5
C(28)-C(27)-H(27B)	108.5
N(2)-C(27)-H(27B)	108.5
H(27A)-C(27)-H(27B)	107.5
C(27)-C(28)-H(28A)	109.5
C(27)-C(28)-H(28B)	109.5
H(28A)-C(28)-H(28B)	109.5
C(27)-C(28)-H(28C)	109.5
H(28A)-C(28)-H(28C)	109.5
H(28B)-C(28)-H(28C)	109.5
N(2)-C(29)-C(30)	115.3(3)
N(2)-C(29)-H(29A)	108.5
C(30)-C(29)-H(29A)	108.5
N(2)-C(29)-H(29B)	108.5
C(30)-C(29)-H(29B)	108.5
H(29A)-C(29)-H(29B)	107.5
C(29)-C(30)-H(30A)	109.5
C(29)-C(30)-H(30B)	109.5
H(30A)-C(30)-H(30B)	109.5
C(29)-C(30)-H(30C)	109.5
H(30A)-C(30)-H(30C)	109.5
H(30B)-C(30)-H(30C)	109.5
N(2)-C(31)-C(32)	115.4(3)
N(2)-C(31)-H(31A)	108.4
C(32)-C(31)-H(31A)	108.4
N(2)-C(31)-H(31B)	108.4
C(32)-C(31)-H(31B)	108.4
H(31A)-C(31)-H(31B)	107.5
C(31)-C(32)-H(32A)	109.5
C(31)-C(32)-H(32B)	109.5
H(32A)-C(32)-H(32B)	109.5
C(31)-C(32)-H(32C)	109.5

A.3 References

(1) Sheldrick, G. M. *Acta Cryst*. **2015**, *A71*, 3–8

(2) Sheldrick, G. M. *Acta Cryst.* **2008**, *A64*, 112–122

(3) Sheldrick*, G. M. Acta Cryst.* **2015**, *C71*, 3–8

Appendix B Crystal Structure of $[Co(HMD)(CH_3OH)][BF_4]_2 \cdot CH_3OH$

B.1 Experimental

The complex was synthesized and crystallized as described in Chapter 3. Briefly, crystals were grown from a methanol solution at –50 °C. All crystal manipulations were carried out under nitrogen atmosphere in a glove bag. A brown small plate (0.06 x 0.09 x 0.16 mm) was mounted on a Dual-Thickness MicroMount^{tm} (MiTeGen) with 30 μm sample aperture with Fluorolube™ oil. The diffraction data were measured at 100 K on a Bruker D8 VENTURE with PHOTON 100 CMOS detector system equipped with a Mo-target X-ray tube (λ = 0.71073 Å). Data were collected using ϕ and ω scans to survey a hemisphere of reciprocal space. Data reduction and integration were performed with the Bruker APEX2 software package (Bruker AXS, version 2014.9-0, 2014). Data were corrected for absorption effects using the multi-scan procedure as implemented in SADABS (Bruker AXS, version 2014/4, 2014, part of Bruker APEX2 software package). The structure was solved by SHELXT[1] and refined by full-matrix least-squares procedure using Bruker SHELXTL (version 6.14) software package (XL refinement program version 2014/7).[2,3] Crystallographic data and details of the data collection and structure refinement are listed in Table B.1.

B.2 Structure solution and refinement

All elements were refined anisotropically. No disorder of BF_4 groups was observed. Hydrogen atoms on C atoms were included in idealized positions for structure factor calculations. Hydrogen atoms bound to N and O atoms were located on the difference Fourier map and their coordinates were allowed to be freely refined while their thermal parameters were constrained to be 1.2 times of the U_{eq} value of the N or O atoms. After all atoms were found, assigned and refined anisotropically, the refinement still left one relatively large q peak located

far from any heavy atoms while other q peaks were considerably smaller. This electron density peak was assigned to an oxygen atom (water molecule) and refined to 20% occupancy. Its thermal parameter was constrained to be approximately isotropic.

Table B.1 Crystal data and structure refinement for $[Co(HMD)(CH_3OH)][BF_4]_2$.

Empirical formula	$C_{18}H_{40}B_2CoF_8N_4O_{2.10}$	
Formula weight	578.69	
Temperature	100(2) K	
Wavelength	0.71073 Å	
Crystal system	Monoclinic	
Space group	*C*2/*c*	
Unit cell dimensions	a = 41.618(6) Å	α= 90°.
	b = 8.0149(11) Å	β= 99.000(4)°.
	c = 15.884(2) Å	γ = 90°.
Volume	5233.1(13) $Å^3$	
Z	8	
Density (calculated)	1.469 Mg/m^3	
Absorption coefficient	0.736 mm^{-1}	
F(000)	2414	
Crystal size	0.160 x 0.090 x 0.060 mm^3	
Theta range for data collection	2.589 to 27.158°.	
Index ranges	$-53 \le h \le 52$, $-10 \le k \le 10$, $-20 \le l \le 20$	
Reflections collected	53209	
Independent reflections	5793 [R(int) = 0.0425]	
Completeness to theta = 27.16°	99.70%	
Absorption correction	Semi-empirical from equivalents	
Max. and min. transmission	0.746 and 0.682	
Refinement method	Full-matrix least-squares on F^2	
Data / restraints / parameters	5793 / 6 / 341	
Goodness-of-fit on F^2	1.062	
Final R indices [I > 2σ(I)]	R1 = 0.0386, wR2 = 0.0870	
R indices (all data)	R1 = 0.0531, wR2 = 0.0925	
Extinction coefficient	n/a	
Largest diff. peak and hole	1.118 and -0.343 $e.Å^{-3}$	

$R_{int} = \Sigma | F_o^2 - \langle F_o^2 \rangle | / \Sigma | F_o^2 |$

$R1 = \Sigma | |F_o| - |F_c| | / \Sigma |F_o|$

$wR2 = [\Sigma [w (F_o^2 - F_c^2)^2] / \Sigma [w (F_o^2)^2]]^{1/2}$

$Goodness\text{-}of\text{-}fit = [\Sigma [w (F_o^2 - F_c^2)^2] / (n-p)^{1/2}$

n: number of independent reflections; p: number of refined parameters

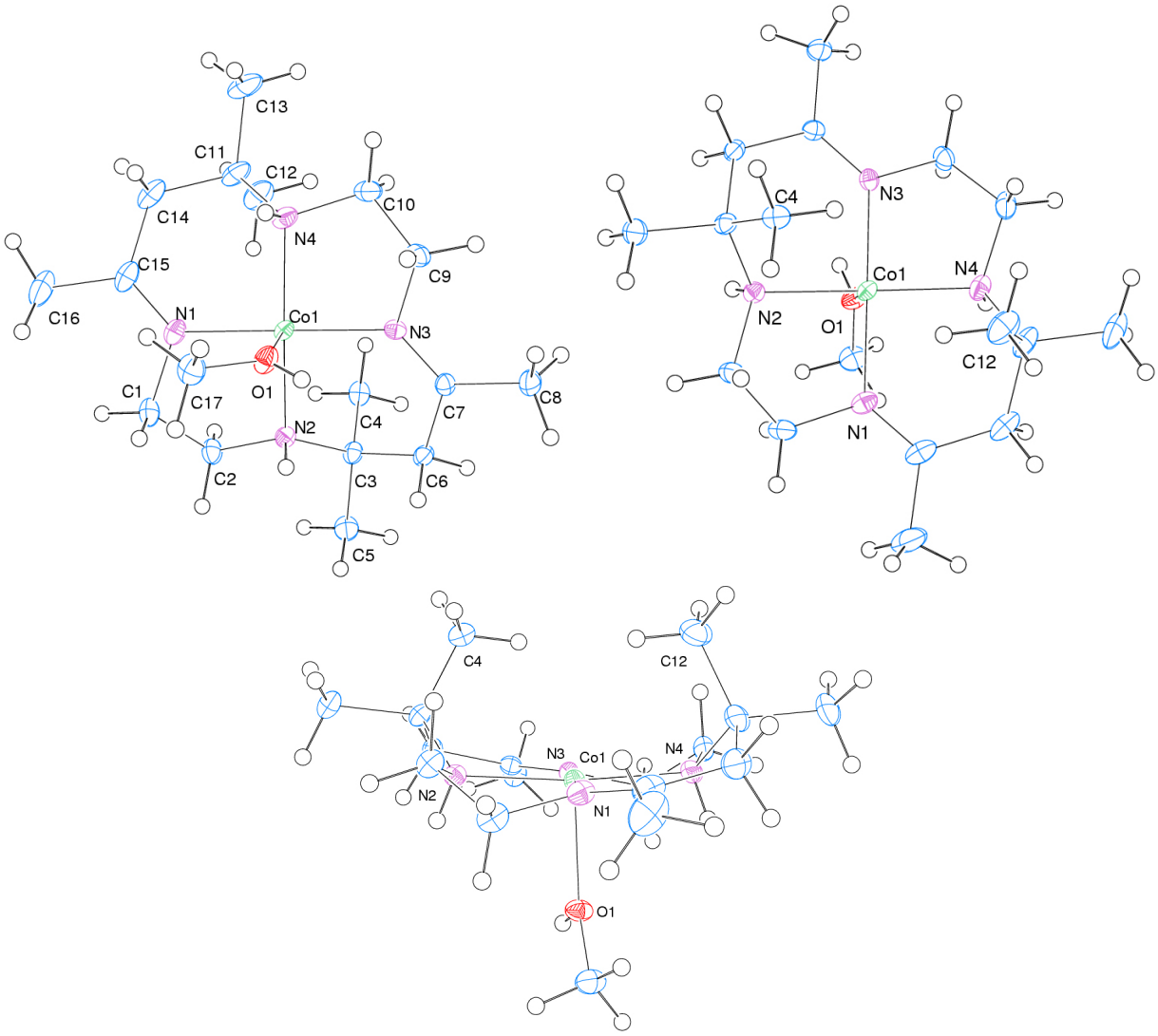

Figure B.1 ORTEP drawings of crystal structure of $[Co(HMD)(CH_3OH)][BF_4]_2$. Structures are drawn with thermal ellipsoids at 40% probability.

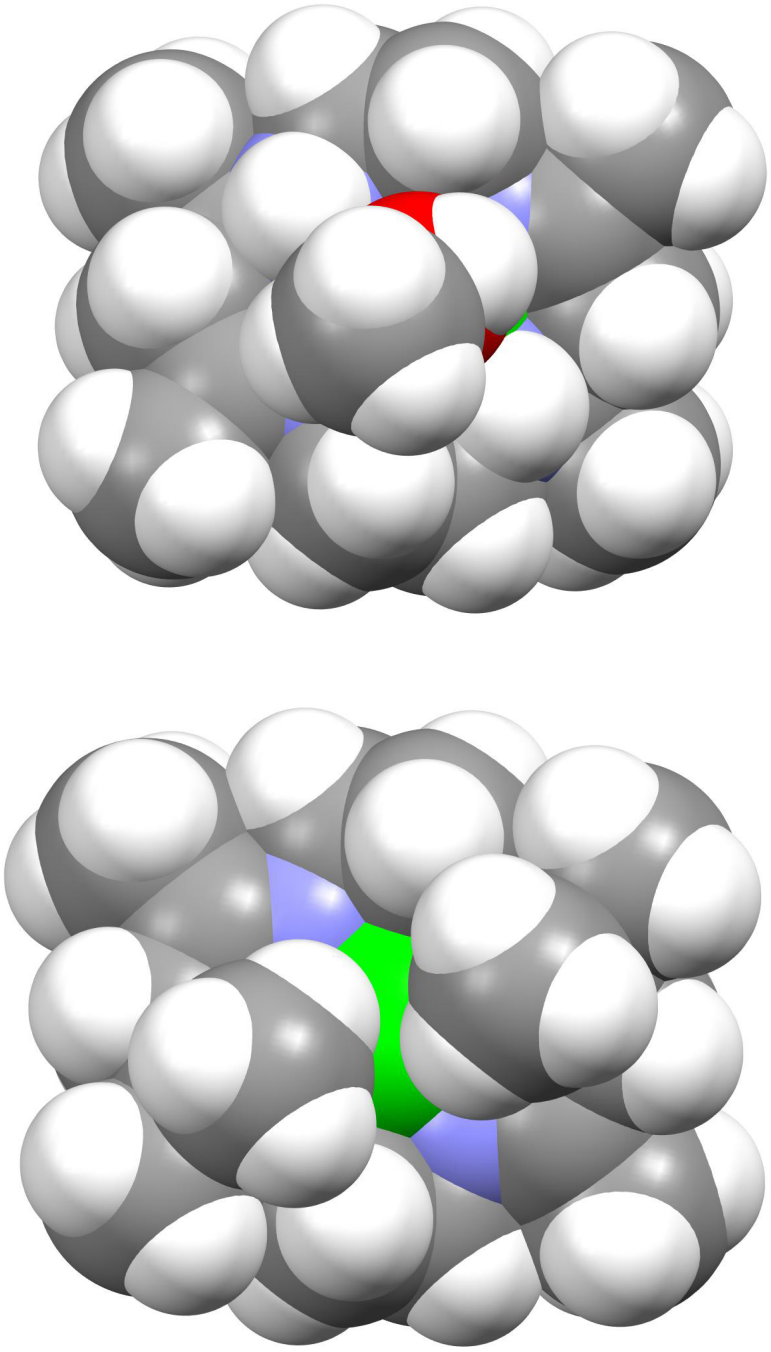

Figure B.2 Two space-filling views at different sides of the $[Co(HMD)(CH_3OH)][BF_4]_2$ molecule: Co green, N blue, O red

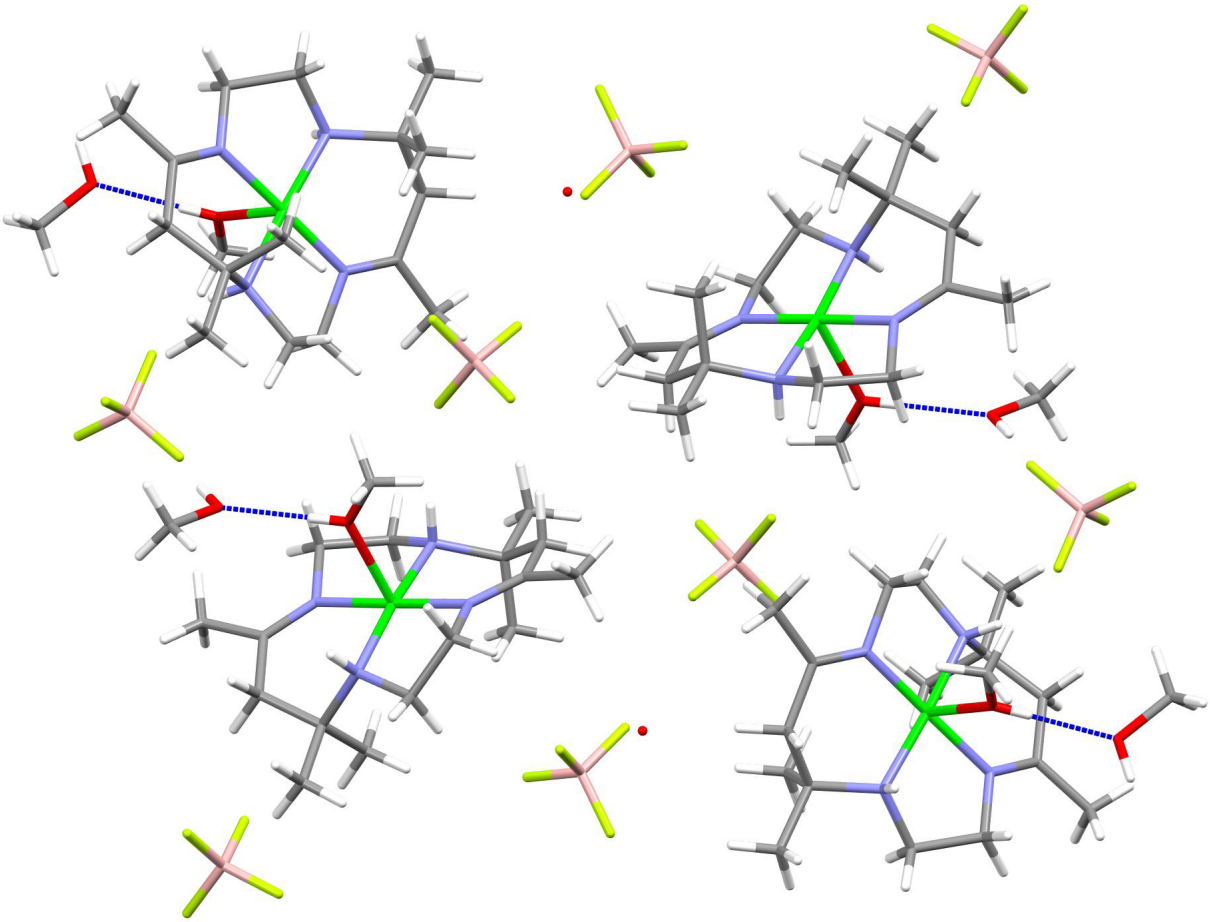

Figure B.3 Methanol molecule attached to a Co atom is also involved in further intermolecular H-bonding with another solvent methanol molecule.

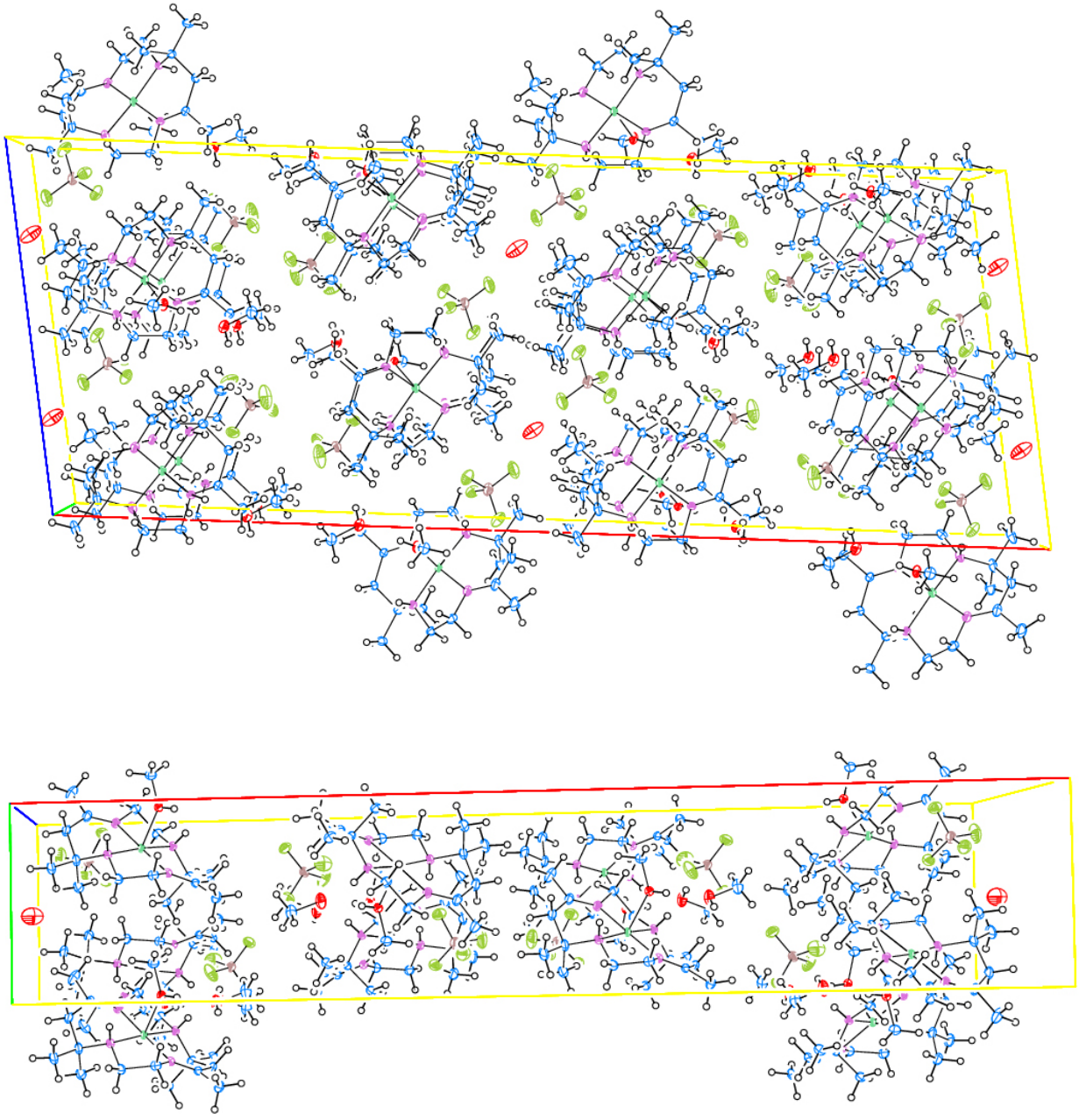

Figure B.4 Depiction of the unit cell of $[Co(HMD)(CH_3OH)][BF_4]_2$.

Table B.2 Bond lengths [Å] and angles [°] for $[Co(HMD)(CH_3OH)][BF_4]_2$.

Co(1)-N(1)	1.9258(17)
Co(1)-N(3)	1.9321(17)
Co(1)-N(4)	1.9569(18)
Co(1)-N(2)	1.9618(17)
Co(1)-O(1)	2.1847(15)
N(1)-C(15)	1.278(3)
N(1)-C(1)	1.479(3)
N(2)-C(2)	1.486(3)
N(2)-C(3)	1.502(3)
N(2)-H(2N)	0.82(3)
N(3)-C(7)	1.280(3)
N(3)-C(9)	1.477(2)
N(4)-C(10)	1.485(3)
N(4)-C(11)	1.506(3)
N(4)-H(4N)	0.83(3)
C(1)-C(2)	1.507(3)
C(1)-H(1A)	0.9900
C(1)-H(1B)	0.9900
C(2)-H(2A)	0.9900
C(2)-H(2B)	0.9900
C(3)-C(4)	1.527(3)
C(3)-C(6)	1.529(3)
C(3)-C(5)	1.530(3)
C(4)-H(4A)	0.9800
C(4)-H(4B)	0.9800
C(4)-H(4C)	0.9800
C(5)-H(5A)	0.9800
C(5)-H(5B)	0.9800
C(5)-H(5C)	0.9800
C(6)-C(7)	1.499(3)
C(6)-H(6A)	0.9900
C(6)-H(6B)	0.9900
C(7)-C(8)	1.498(3)
C(8)-H(8A)	0.9800
C(8)-H(8B)	0.9800
C(8)-H(8C)	0.9800
C(9)-C(10)	1.514(3)
C(9)-H(9A)	0.9900
C(9)-H(9B)	0.9900
C(10)-H(10A)	0.9900
C(10)-H(10B)	0.9900
C(11)-C(12)	1.519(3)
C(11)-C(14)	1.529(3)
C(11)-C(13)	1.535(3)
C(12)-H(12A)	0.9800
C(12)-H(12B)	0.9800
C(12)-H(12C)	0.9800
C(13)-H(13A)	0.9800
C(13)-H(13B)	0.9800
C(13)-H(13C)	0.9800
C(14)-C(15)	1.496(3)
C(14)-H(14A)	0.9900
C(14)-H(14B)	0.9900
C(15)-C(16)	1.511(3)
C(16)-H(16A)	0.9800
C(16)-H(16B)	0.9800
C(16)-H(16C)	0.9800
B(1)-F(4)	1.374(3)
B(1)-F(3)	1.382(3)
B(1)-F(1)	1.392(3)
B(1)-F(2)	1.400(3)
B(2)-F(7)	1.360(3)
B(2)-F(6)	1.369(3)
B(2)-F(8)	1.379(3)
B(2)-F(5)	1.397(3)
O(1)-C(17)	1.420(3)
O(1)-H(1O)	0.75(3)
C(17)-H(17A)	0.9800
C(17)-H(17B)	0.9800
C(17)-H(17C)	0.9800
O(2)-C(18)	1.408(3)
O(2)-H(2O)	0.83(3)
C(18)-H(18A)	0.9800
C(18)-H(18B)	0.9800
C(18)-H(18C)	0.9800
N(1)-Co(1)-N(3)	178.85(7)
N(1)-Co(1)-N(4)	93.35(8)
N(3)-Co(1)-N(4)	86.89(7)
N(1)-Co(1)-N(2)	86.60(7)
N(3)-Co(1)-N(2)	93.29(7)
N(4)-Co(1)-N(2)	173.42(8)
N(1)-Co(1)-O(1)	92.45(7)
N(3)-Co(1)-O(1)	86.42(6)
N(4)-Co(1)-O(1)	91.25(7)
N(2)-Co(1)-O(1)	95.32(7)
C(15)-N(1)-C(1)	120.61(19)
C(15)-N(1)-Co(1)	129.83(17)
C(1)-N(1)-Co(1)	109.38(13)
C(2)-N(2)-C(3)	114.73(16)
C(2)-N(2)-Co(1)	108.14(12)
C(3)-N(2)-Co(1)	112.73(13)
C(2)-N(2)-H(2N)	104.6(16)
C(3)-N(2)-H(2N)	108.1(17)
Co(1)-N(2)-H(2N)	108.0(16)
C(7)-N(3)-C(9)	120.76(17)
C(7)-N(3)-Co(1)	129.24(14)
C(9)-N(3)-Co(1)	109.33(12)
C(10)-N(4)-C(11)	114.50(17)
C(10)-N(4)-Co(1)	108.42(13)
C(11)-N(4)-Co(1)	113.74(14)
C(10)-N(4)-H(4N)	107.3(17)
C(11)-N(4)-H(4N)	108.5(17)
Co(1)-N(4)-H(4N)	103.6(17)
N(1)-C(1)-C(2)	106.52(17)
N(1)-C(1)-H(1A)	110.4
C(2)-C(1)-H(1A)	110.4
N(1)-C(1)-H(1B)	110.4
C(2)-C(1)-H(1B)	110.4
H(1A)-C(1)-H(1B)	108.6
N(2)-C(2)-C(1)	107.43(16)
N(2)-C(2)-H(2A)	110.2
C(1)-C(2)-H(2A)	110.2
N(2)-C(2)-H(2B)	110.2
C(1)-C(2)-H(2B)	110.2
H(2A)-C(2)-H(2B)	108.5
N(2)-C(3)-C(4)	109.83(16)
N(2)-C(3)-C(6)	106.74(15)
C(4)-C(3)-C(6)	111.81(17)
N(2)-C(3)-C(5)	111.30(17)
C(4)-C(3)-C(5)	109.71(17)
C(6)-C(3)-C(5)	107.41(16)
C(3)-C(4)-H(4A)	109.5
C(3)-C(4)-H(4B)	109.5
H(4A)-C(4)-H(4B)	109.5
C(3)-C(4)-H(4C)	109.5
H(4A)-C(4)-H(4C)	109.5
H(4B)-C(4)-H(4C)	109.5
C(3)-C(5)-H(5A)	109.5
C(3)-C(5)-H(5B)	109.5
H(5A)-C(5)-H(5B)	109.5
C(3)-C(5)-H(5C)	109.5
H(5A)-C(5)-H(5C)	109.5
H(5B)-C(5)-H(5C)	109.5
C(7)-C(6)-C(3)	118.75(17)
C(7)-C(6)-H(6A)	107.6
C(3)-C(6)-H(6A)	107.6
C(7)-C(6)-H(6B)	107.6
C(3)-C(6)-H(6B)	107.6
H(6A)-C(6)-H(6B)	107.1
N(3)-C(7)-C(8)	124.08(18)
N(3)-C(7)-C(6)	121.57(18)
C(8)-C(7)-C(6)	114.35(17)
C(7)-C(8)-H(8A)	109.5
C(7)-C(8)-H(8B)	109.5
H(8A)-C(8)-H(8B)	109.5
C(7)-C(8)-H(8C)	109.5
H(8A)-C(8)-H(8C)	109.5
H(8B)-C(8)-H(8C)	109.5
N(3)-C(9)-C(10)	106.76(16)
N(3)-C(9)-H(9A)	110.4
C(10)-C(9)-H(9A)	110.4
N(3)-C(9)-H(9B)	110.4
C(10)-C(9)-H(9B)	110.4
H(9A)-C(9)-H(9B)	108.6
N(4)-C(10)-C(9)	108.12(17)
N(4)-C(10)-H(10A)	110.1
C(9)-C(10)-H(10A)	110.1
N(4)-C(10)-H(10B)	110.1
C(9)-C(10)-H(10B)	110.1
H(10A)-C(10)-H(10B)	108.4
N(4)-C(11)-C(12)	110.30(18)
N(4)-C(11)-C(14)	107.45(18)
C(12)-C(11)-C(14)	111.0(2)
N(4)-C(11)-C(13)	110.1(2)

Table B.2, continued

C(12)-C(11)-C(13)	110.2(2)
C(14)-C(11)-C(13)	107.79(19)
C(11)-C(12)-H(12A)	109.5
C(11)-C(12)-H(12B)	109.5
H(12A)-C(12)-H(12B)	109.5
C(11)-C(12)-H(12C)	109.5
H(12A)-C(12)-H(12C)	109.5
H(12B)-C(12)-H(12C)	109.5
C(11)-C(13)-H(13A)	109.5
C(11)-C(13)-H(13B)	109.5
H(13A)-C(13)-H(13B)	109.5
C(11)-C(13)-H(13C)	109.5
H(13A)-C(13)-H(13C)	109.5
H(13B)-C(13)-H(13C)	109.5
C(15)-C(14)-C(11)	119.80(19)
C(15)-C(14)-H(14A)	107.4
C(11)-C(14)-H(14A)	107.4
C(15)-C(14)-H(14B)	107.4
C(11)-C(14)-H(14B)	107.4
H(14A)-C(14)-H(14B)	106.9
N(1)-C(15)-C(14)	121.6(2)
N(1)-C(15)-C(16)	123.3(2)
C(14)-C(15)-C(16)	115.1(2)
C(15)-C(16)-H(16A)	109.5
C(15)-C(16)-H(16B)	109.5
H(16A)-C(16)-H(16B)	109.5
C(15)-C(16)-H(16C)	109.5
H(16A)-C(16)-H(16C)	109.5
H(16B)-C(16)-H(16C)	109.5
F(4)-B(1)-F(3)	110.3(2)
F(4)-B(1)-F(1)	110.2(2)
F(3)-B(1)-F(1)	109.8(2)
F(4)-B(1)-F(2)	108.4(2)
F(3)-B(1)-F(2)	109.3(2)
F(1)-B(1)-F(2)	108.7(2)
F(7)-B(2)-F(6)	111.39(19)
F(7)-B(2)-F(8)	110.1(2)
F(6)-B(2)-F(8)	110.0(2)
F(7)-B(2)-F(5)	108.3(2)
F(6)-B(2)-F(5)	109.9(2)
F(8)-B(2)-F(5)	107.08(19)
C(17)-O(1)-Co(1)	131.89(14)
C(17)-O(1)-H(1O)	109(2)
Co(1)-O(1)-H(1O)	117(2)
O(1)-C(17)-H(17A)	109.5
O(1)-C(17)-H(17B)	109.5
H(17A)-C(17)-H(17B)	109.5
O(1)-C(17)-H(17C)	109.5
H(17A)-C(17)-H(17C)	109.5
H(17B)-C(17)-H(17C)	109.5
C(18)-O(2)-H(2O)	110(2)
O(2)-C(18)-H(18A)	109.5
O(2)-C(18)-H(18B)	109.5
H(18A)-C(18)-H(18B)	109.5
O(2)-C(18)-H(18C)	109.5
H(18A)-C(18)-H(18C)	109.5
H(18B)-C(18)-H(18C)	109.5

B.3 References

(1) Sheldrick, G. M. *Acta Cryst*. **2015**, *A71*, 3–8

(2) Sheldrick, G. M. *Acta Cryst.* **2008**, *A64*, 112–122

(3) Sheldrick*, G. M. Acta Cryst.* **2015**, *C71*, 3–8

Appendix C Crystal structure of $[Pd(triphos)(CH_3CN)][BF_4]_2$

C.1 Experimental

The complex was synthesized according to the literature procedure.[1] Crystals were grown by recrystallizing twice by dissolving into acetonitrile, filtering through Celite, and layering with diethyl ether. For the final recrystallization, a thin layer of hexanes was layered atop the acetonitrile layer before adding diethyl ether, in order to slow down diffusion of the layers. Large colorless needle-shaped crystals were obtained in this manner. An irregular broken fragment (0.16 x 0.24 x 0.28 mm) was selected under a stereo-microscope while immersed in Fluorolube oil to avoid possible reaction with air. The crystal was removed from the oil using a tapered glass fiber that also served to hold the crystal for data collection. The crystal was mounted and centered on a Bruker D8 Venture system with CMOS detector, Mo microsource radiation, and crystal cooling set at 100K. Frames separated in reciprocal space were obtained and provided an orientation matrix and initial cell parameters. A "full sphere" data set was obtained using a combination of omega and phi scans which sample approximately all of reciprocal space to a resolution of 0.75 Å with an integration time of 10.0 sec/frame. Data reduction and integration were performed with the Bruker APEX3 software package (Bruker AXS, version 2015.5-2, 2015). Data were scaled and corrected for absorption effects using the multi-scan procedure as implemented in SADABS (Bruker AXS, version 2014/5, 2015, part of Bruker APEX3 software package). The structure was solved by SHELXT Version 2014/5[2] and refined by a full-matrix least-squares procedure using Bruker SHELXTL (version 6.14) [3,4] and OLEX2[5] software packages. Crystallographic data and details of the data collection and structure refinement are listed in Table C.1.

C.2 Structure solution and refinement

Following anisotropic refinement of all non-H atoms, ideal H atom positions were calculated. All BF_4 anions were disordered and modelled individually. 2 out of 4 of them were disorders due to rotation over one of the CF bonds. The rest of BF_4 anions showed positional disorder including B atoms. One of the CH_3CN non-coordinated solvent molecules also was positionally disordered. Geometric restraints, such as SAME/SADI, and restraints on thermal parameters, such as RIGU, were utilized for disorder modelling. ADPs of C74/C74X and N3/N3X were constrained to be the same. Solvent accessible voids masks implemented in OLEX2 were utilized for several relatively small voids found in the crystal. See the CIF file for a full list of used restraints/constraints. All ORTEP diagrams have been drawn with 40% probability ellipsoids.

Table C.1 Crystal data and structure refinement for $[Pd(triphos)(CH_3CN)][BF_4]_2$.

Empirical formula	$C_{38}H_{39}B_2F_8N_2P_3Pd$
Formula weight	896.64
Temperature	100.0 K
Wavelength	0.71073 Å
Crystal system	Monoclinic
Space group	$P2_1/n$
Unit cell dimensions	a = 22.3998(13) Å α= 90°.
	b = 9.9421(6) Å β= 102.3760(10)°.
	c = 37.331(2) Å γ = 90°.
Volume	8120.5(8) $Å^3$
Z	8
Density (calculated)	1.467 Mg/m^3
Absorption coefficient	0.642 mm^{-1}
F(000)	3632
Crystal size	0.28 x 0.24 x 0.16 mm3
Theta range for data collection	1.955 to 26.434°.
Index ranges	$-27 \le h \le 28$, $-12 \le k \le 12$, $-44 \le l \le 46$
Reflections collected	96675
Independent reflections	16317 [R(int) = 0.0455]
Completeness to theta = 26.000°	98.90%
Absorption correction	Semi-empirical from equivalents
Max. and min. transmission	0.7454 and 0.6876
Refinement method	Full-matrix least-squares on F^2
Data / restraints / parameters	16317 / 278 / 1142
Goodness-of-fit on F^2	1.076
Final R indices [$I > 2\sigma(I)$]	R1 = 0.0526, wR2 = 0.1094
R indices (all data)	R1 = 0.0724, wR2 = 0.1143
Extinction coefficient	n/a

$R_{int} = \Sigma | F_o^2 - \langle F_o^2 \rangle | / \Sigma | F_o^2 |$

$R1 = \Sigma | |F_o| - |F_c| | / \Sigma |F_o|$

$wR2 = [\Sigma [w (F_o^2 - F_c^2)^2] / \Sigma [w (F_o^2)^2]]^{1/2}$

Goodness-of-fit = $[\Sigma [w (F_o^2 - F_c^2)^2] / (n-p)^{1/2}$

n: number of independent reflections; p: number of refined parameters

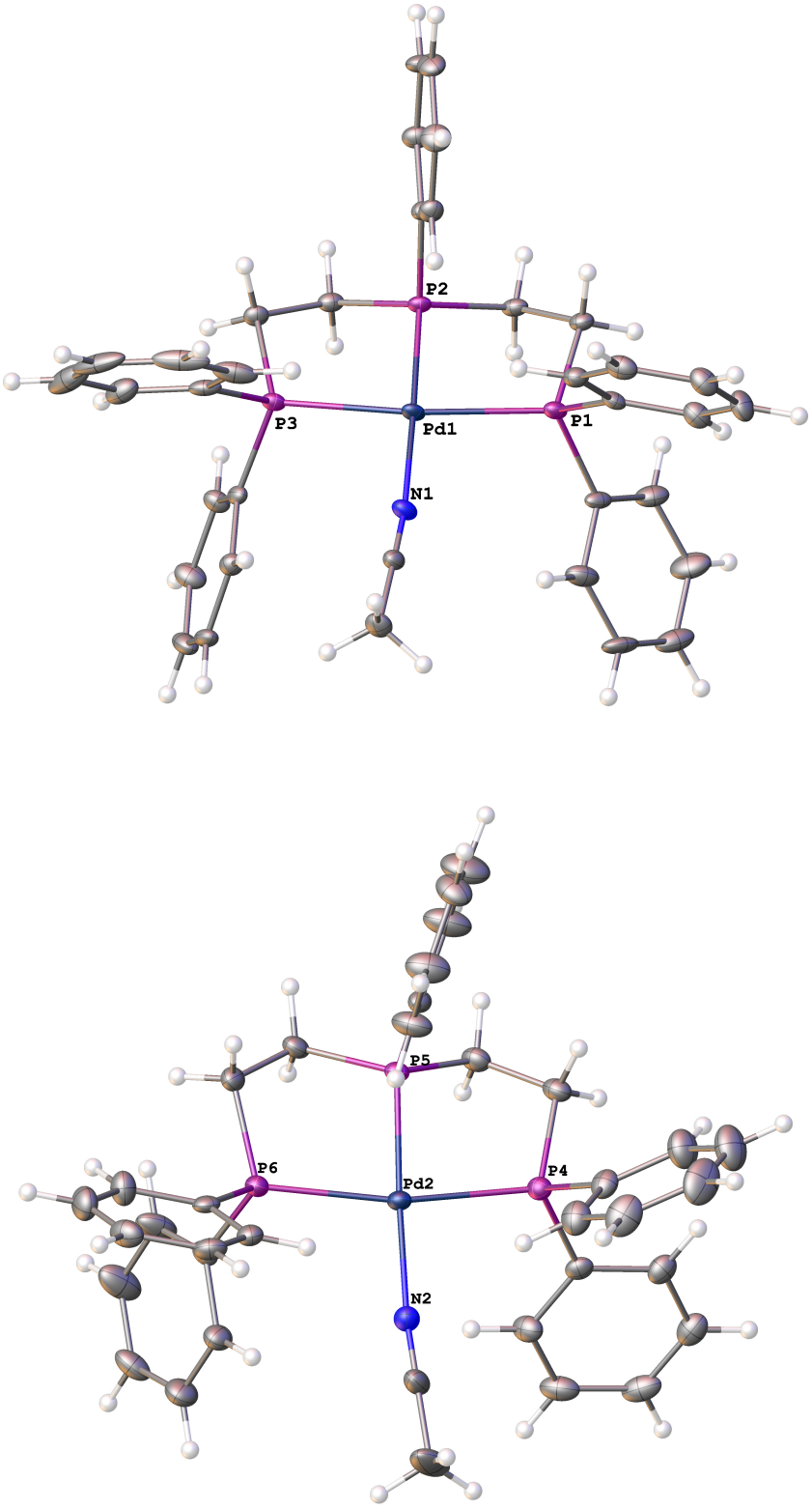

Figure C.1 ORTEP drawings of crystal structure of $[Pd(triphos)(CH_3CN)][BF_4]_2$. Structures are drawn with thermal ellipsoids at 40% probability.

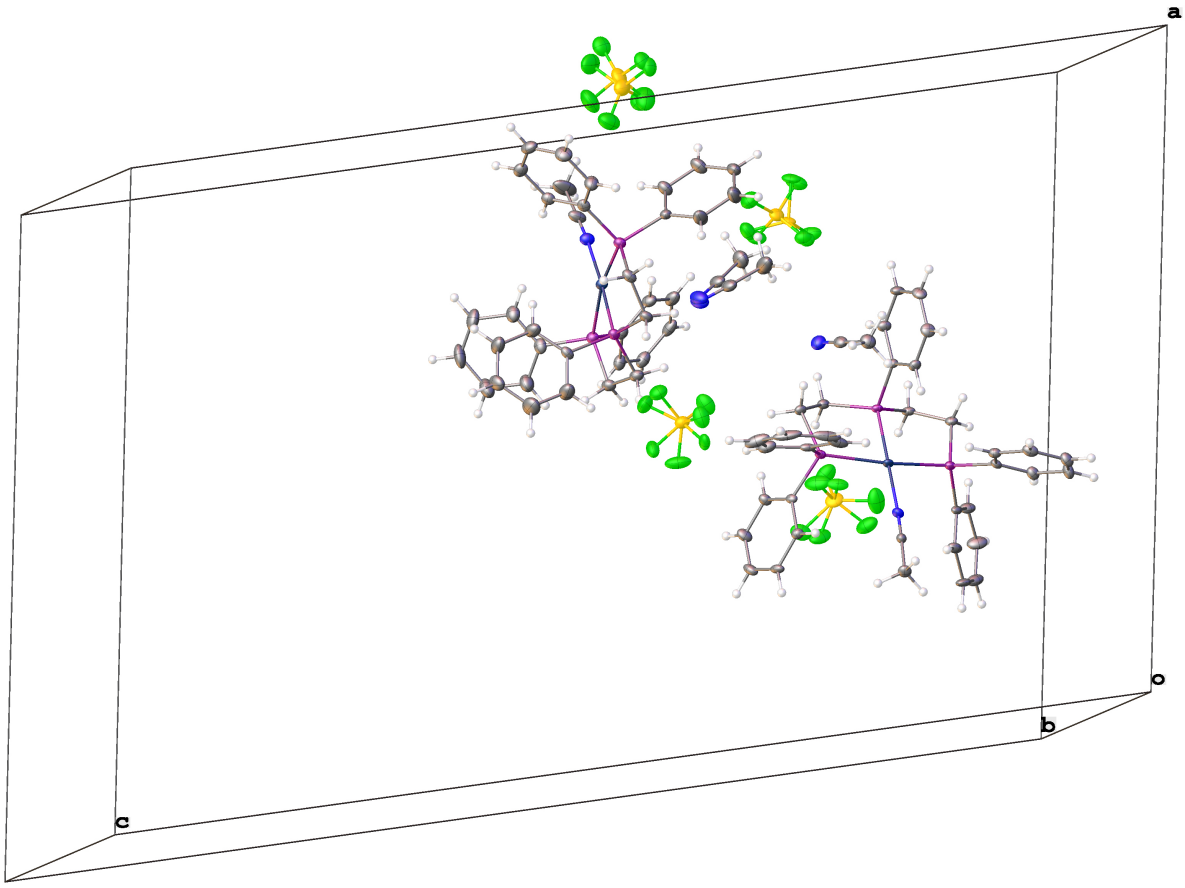

Figure C.2 Depiction of the unit cell of $[Pd(triphos)(CH_3CN)][BF_4]_2$. Two independent Pd-complexes, 4 $[BF_4]^-$ anions and 2 acetonitrile molecules are present in the unit cell. All disordered moieties are shown.

Table C.2 Bond lengths [Å] and angles [°] for $[Pd(triphos)(CH_3CN)][BF_4]_2$.

Pd(1)-P(1)	2.3395(11)
Pd(1)-P(2)	2.2213(11)
Pd(1)-P(3)	2.3344(11)
Pd(1)-N(1)	2.073(4)
P(1)-C(1)	1.813(4)
P(1)-C(7)	1.808(4)
P(1)-C(13)	1.836(4)
P(2)-C(14)	1.820(4)
P(2)-C(15)	1.815(4)
P(2)-C(17)	1.808(4)
P(3)-C(16)	1.842(4)
P(3)-C(23)	1.812(5)
P(3)-C(29)	1.810(4)
N(1)-C(35)	1.134(5)
C(1)-C(2)	1.383(7)
C(1)-C(6)	1.401(6)
C(2)-H(2)	0.9500
C(2)-C(3)	1.381(7)
C(3)-H(3)	0.9500
C(3)-C(4)	1.379(7)
C(4)-H(4)	0.9500
C(4)-C(5)	1.379(8)
C(5)-H(5)	0.9500
C(5)-C(6)	1.380(7)
C(6)-H(6)	0.9500
C(7)-C(8)	1.382(6)
C(7)-C(12)	1.398(6)
C(8)-H(8)	0.9500
C(8)-C(9)	1.388(6)
C(9)-H(9)	0.9500
C(9)-C(10)	1.385(7)
C(10)-H(10)	0.9500
C(10)-C(11)	1.374(7)
C(11)-H(11)	0.9500
C(11)-C(12)	1.379(6)
C(12)-H(12)	0.9500
C(13)-H(13A)	0.9900
C(13)-H(13B)	0.9900
C(13)-C(14)	1.532(6)
C(14)-H(14A)	0.9900
C(14)-H(14B)	0.9900
C(15)-H(15A)	0.9900
C(15)-H(15B)	0.9900
C(15)-C(16)	1.524(6)
C(16)-H(16A)	0.9900
C(16)-H(16B)	0.9900
C(17)-C(18)	1.382(6)
C(17)-C(22)	1.390(6)
C(18)-H(18)	0.9500
C(18)-C(19)	1.380(6)
C(19)-H(19)	0.9500
C(19)-C(20)	1.377(6)
C(20)-H(20)	0.9500
C(20)-C(21)	1.372(7)
C(21)-H(21)	0.9500
C(21)-C(22)	1.398(6)
C(22)-H(22)	0.9500
C(23)-C(24)	1.390(6)
C(23)-C(28)	1.385(7)
C(24)-H(24)	0.9500
C(24)-C(25)	1.380(8)
C(25)-H(25)	0.9500
C(25)-C(26)	1.358(9)
C(26)-H(26)	0.9500
C(26)-C(27)	1.390(9)
C(27)-H(27)	0.9500
C(27)-C(28)	1.394(7)
C(28)-H(28)	0.9500
C(29)-C(30)	1.413(6)
C(29)-C(34)	1.371(6)
C(30)-H(30)	0.9500
C(30)-C(31)	1.375(6)
C(31)-H(31)	0.9500
C(31)-C(32)	1.385(7)
C(32)-H(32)	0.9500
C(32)-C(33)	1.380(7)
C(33)-H(33)	0.9500
C(33)-C(34)	1.391(6)
C(34)-H(34)	0.9500
C(35)-C(36)	1.448(6)
C(36)-H(36A)	0.9800
C(36)-H(36B)	0.9800
C(36)-H(36C)	0.9800
Pd(2)-P(4)	2.3417(12)
Pd(2)-P(5)	2.2145(11)
Pd(2)-P(6)	2.3376(12)
Pd(2)-N(2)	2.067(4)
P(4)-C(37)	1.804(4)
P(4)-C(43)	1.813(5)
P(4)-C(49)	1.856(5)
P(5)-C(50)	1.808(5)
P(5)-C(51)	1.813(5)
P(5)-C(53)	1.803(4)
P(6)-C(52)	1.840(5)
P(6)-C(59)	1.804(5)
P(6)-C(65)	1.813(4)
N(2)-C(71)	1.129(6)
C(37)-C(38)	1.395(6)
C(37)-C(42)	1.397(6)
C(38)-H(38)	0.9500
C(38)-C(39)	1.382(7)
C(39)-H(39)	0.9500
C(39)-C(40)	1.368(7)
C(40)-H(40)	0.9500
C(40)-C(41)	1.378(8)
C(41)-H(41)	0.9500
C(41)-C(42)	1.386(7)
C(42)-H(42)	0.9500
C(43)-C(44)	1.389(7)
C(43)-C(48)	1.396(7)
C(44)-H(44)	0.9500
C(44)-C(45)	1.383(7)
C(45)-H(45)	0.9500
C(45)-C(46)	1.381(9)
C(46)-H(46)	0.9500
C(46)-C(47)	1.388(9)
C(47)-H(47)	0.9500
C(47)-C(48)	1.377(8)
C(48)-H(48)	0.9500
C(49)-H(49A)	0.9900
C(49)-H(49B)	0.9900
C(49)-C(50)	1.536(7)
C(50)-H(50A)	0.9900
C(50)-H(50B)	0.9900
C(51)-H(51A)	0.9900
C(51)-H(51B)	0.9900
C(51)-C(52)	1.527(6)
C(52)-H(52A)	0.9900
C(52)-H(52B)	0.9900
C(53)-C(54)	1.361(7)
C(53)-C(58)	1.401(7)
C(54)-H(54)	0.9500
C(54)-C(55)	1.384(7)
C(55)-H(55)	0.9500
C(55)-C(56)	1.364(7)
C(56)-H(56)	0.9500
C(56)-C(57)	1.371(8)
C(57)-H(57)	0.9500
C(57)-C(58)	1.381(8)
C(58)-H(58)	0.9500
C(59)-C(60)	1.392(6)
C(59)-C(64)	1.383(7)
C(60)-H(60)	0.9500
C(60)-C(61)	1.389(7)
C(61)-H(61)	0.9500
C(61)-C(62)	1.391(7)
C(62)-H(62)	0.9500
C(62)-C(63)	1.345(7)
C(63)-H(63)	0.9500
C(63)-C(64)	1.395(7)
C(64)-H(64)	0.9500
C(65)-C(66)	1.396(6)
C(65)-C(70)	1.362(7)
C(66)-H(66)	0.9500
C(66)-C(67)	1.374(7)
C(67)-H(67)	0.9500
C(67)-C(68)	1.377(8)
C(68)-H(68)	0.9500
C(68)-C(69)	1.367(8)
C(69)-H(69)	0.9500
C(69)-C(70)	1.389(7)
C(70)-H(70)	0.9500
C(71)-C(72)	1.442(7)
C(72)-H(72A)	0.9800

Table C.2, continued

C(72)-H(72B)	0.9800
C(72)-H(72C)	0.9800
F(13)-B(4)	1.385(12)
F(14)-B(4)	1.399(18)
F(15)-B(4)	1.407(13)
F(16)-B(4)	1.379(10)
F(13X)-B(4X)	1.389(12)
F(14X)-B(4X)	1.403(19)
F(15X)-B(4X)	1.403(14)
F(16X)-B(4X)	1.388(12)
F(3)-B(1)	1.387(6)
F(1)-B(1)	1.362(6)
F(2)-B(1)	1.399(7)
F(4)-B(1)	1.363(7)
F(1X)-B(1)	1.425(18)
F(2X)-B(1)	1.307(17)
F(4X)-B(1)	1.40(2)
F(8)-B(2)	1.388(7)
F(5)-B(2)	1.324(7)
F(6)-B(2)	1.364(7)
F(7)-B(2)	1.396(8)
F(5X)-B(2)	1.55(2)
F(6X)-B(2)	1.359(19)
F(7X)-B(2)	1.380(17)
F(9)-B(3)	1.376(16)
F(10)-B(3)	1.358(17)
F(11)-B(3)	1.395(14)
F(12)-B(3)	1.388(15)
F(9X)-B(3X)	1.374(12)
F(10X)-B(3X)	1.357(13)
F(11X)-B(3X)	1.380(11)
F(12X)-B(3X)	1.395(13)
N(3)-C(74)	1.150(6)
C(73)-H(73A)	0.9800
C(73)-H(73B)	0.9800
C(73)-H(73C)	0.9800
C(73)-C(74)	1.452(6)
N(3X)-C(74X)	1.150(6)
C(73X)-H(73D)	0.9800
C(73X)-H(73E)	0.9800
C(73X)-H(73F)	0.9800
C(73X)-C(74X)	1.452(6)
N(4)-C(75)	1.150(6)
C(75)-C(76)	1.452(6)
C(76)-H(76A)	0.9800
C(76)-H(76B)	0.9800
C(76)-H(76C)	0.9800
P(2)-Pd(1)-P(1)	83.99(4)
P(2)-Pd(1)-P(3)	83.42(4)
P(3)-Pd(1)-P(1)	164.84(4)
N(1)-Pd(1)-P(1)	97.48(10)
N(1)-Pd(1)-P(2)	177.44(11)
N(1)-Pd(1)-P(3)	95.43(10)
C(1)-P(1)-Pd(1)	114.34(14)
C(1)-P(1)-C(13)	107.5(2)
C(7)-P(1)-Pd(1)	117.75(14)
C(7)-P(1)-C(1)	103.45(19)
C(7)-P(1)-C(13)	106.22(19)
C(13)-P(1)-Pd(1)	106.93(14)
C(14)-P(2)-Pd(1)	108.94(14)
C(15)-P(2)-Pd(1)	109.73(14)
C(15)-P(2)-C(14)	112.9(2)
C(17)-P(2)-Pd(1)	110.82(14)
C(17)-P(2)-C(14)	106.11(19)
C(17)-P(2)-C(15)	108.29(19)
C(16)-P(3)-Pd(1)	108.31(14)
C(23)-P(3)-Pd(1)	119.30(16)
C(23)-P(3)-C(16)	106.76(19)
C(29)-P(3)-Pd(1)	109.46(13)
C(29)-P(3)-C(16)	109.3(2)
C(29)-P(3)-C(23)	103.33(19)
C(35)-N(1)-Pd(1)	174.0(4)
C(2)-C(1)-P(1)	123.2(3)
C(2)-C(1)-C(6)	119.0(4)
C(6)-C(1)-P(1)	117.5(4)
C(1)-C(2)-H(2)	119.8
C(3)-C(2)-C(1)	120.4(4)
C(3)-C(2)-H(2)	119.8
C(2)-C(3)-H(3)	119.8
C(4)-C(3)-C(2)	120.4(5)
C(4)-C(3)-H(3)	119.8
C(3)-C(4)-H(4)	120.1
C(3)-C(4)-C(5)	119.8(5)
C(5)-C(4)-H(4)	120.1
C(4)-C(5)-H(5)	119.8
C(4)-C(5)-C(6)	120.3(5)
C(6)-C(5)-H(5)	119.8
C(1)-C(6)-H(6)	120.0
C(5)-C(6)-C(1)	120.0(5)
C(5)-C(6)-H(6)	120.0
C(8)-C(7)-P(1)	119.9(3)
C(8)-C(7)-C(12)	120.0(4)
C(12)-C(7)-P(1)	120.1(3)
C(7)-C(8)-H(8)	120.1
C(7)-C(8)-C(9)	119.9(4)
C(9)-C(8)-H(8)	120.1
C(8)-C(9)-H(9)	120.1
C(10)-C(9)-C(8)	119.8(4)
C(10)-C(9)-H(9)	120.1
C(9)-C(10)-H(10)	119.8
C(11)-C(10)-C(9)	120.3(4)
C(11)-C(10)-H(10)	119.8
C(10)-C(11)-H(11)	119.8
C(10)-C(11)-C(12)	120.4(4)
C(12)-C(11)-H(11)	119.8
C(7)-C(12)-H(12)	120.2
C(11)-C(12)-C(7)	119.6(4)
C(11)-C(12)-H(12)	120.2
P(1)-C(13)-H(13A)	109.7
P(1)-C(13)-H(13B)	109.7
H(13A)-C(13)-H(13B)	108.2
C(14)-C(13)-P(1)	109.6(3)
C(14)-C(13)-H(13A)	109.7
C(14)-C(13)-H(13B)	109.7
P(2)-C(14)-H(14A)	110.5
P(2)-C(14)-H(14B)	110.5
C(13)-C(14)-P(2)	106.0(3)
C(13)-C(14)-H(14A)	110.5
C(13)-C(14)-H(14B)	110.5
H(14A)-C(14)-H(14B)	108.7
P(2)-C(15)-H(15A)	110.2
P(2)-C(15)-H(15B)	110.2
H(15A)-C(15)-H(15B)	108.5
C(16)-C(15)-P(2)	107.5(3)
C(16)-C(15)-H(15A)	110.2
C(16)-C(15)-H(15B)	110.2
P(3)-C(16)-H(16A)	109.6
P(3)-C(16)-H(16B)	109.6
C(15)-C(16)-P(3)	110.2(3)
C(15)-C(16)-H(16A)	109.6
C(15)-C(16)-H(16B)	109.6
H(16A)-C(16)-H(16B)	108.1
C(18)-C(17)-P(2)	121.7(3)
C(18)-C(17)-C(22)	120.2(4)
C(22)-C(17)-P(2)	118.1(3)
C(17)-C(18)-H(18)	120.0
C(19)-C(18)-C(17)	120.0(4)
C(19)-C(18)-H(18)	120.0
C(18)-C(19)-H(19)	120.0
C(20)-C(19)-C(18)	120.0(4)
C(20)-C(19)-H(19)	120.0
C(19)-C(20)-H(20)	119.6
C(21)-C(20)-C(19)	120.8(4)
C(21)-C(20)-H(20)	119.6
C(20)-C(21)-H(21)	120.1
C(20)-C(21)-C(22)	119.7(4)
C(22)-C(21)-H(21)	120.1
C(17)-C(22)-C(21)	119.3(4)
C(17)-C(22)-H(22)	120.4
C(21)-C(22)-H(22)	120.4
C(24)-C(23)-P(3)	120.8(4)
C(28)-C(23)-P(3)	118.3(3)
C(28)-C(23)-C(24)	120.9(5)
C(23)-C(24)-H(24)	120.5
C(25)-C(24)-C(23)	119.0(6)
C(25)-C(24)-H(24)	120.5
C(24)-C(25)-H(25)	119.2
C(26)-C(25)-C(24)	121.6(6)
C(26)-C(25)-H(25)	119.2
C(25)-C(26)-H(26)	120.3
C(25)-C(26)-C(27)	119.5(5)
C(27)-C(26)-H(26)	120.3
C(26)-C(27)-H(27)	119.7
C(26)-C(27)-C(28)	120.6(6)
C(28)-C(27)-H(27)	119.7
C(23)-C(28)-C(27)	118.5(5)

Table C.2, continued

C(23)-C(28)-H(28)	120.7
C(27)-C(28)-H(28)	120.7
C(30)-C(29)-P(3)	116.7(3)
C(34)-C(29)-P(3)	123.5(3)
C(34)-C(29)-C(30)	119.8(4)
C(29)-C(30)-H(30)	120.0
C(31)-C(30)-C(29)	120.1(4)
C(31)-C(30)-H(30)	120.0
C(30)-C(31)-H(31)	120.1
C(30)-C(31)-C(32)	119.7(4)
C(32)-C(31)-H(31)	120.1
C(31)-C(32)-H(32)	119.9
C(33)-C(32)-C(31)	120.2(4)
C(33)-C(32)-H(32)	119.9
C(32)-C(33)-H(33)	119.7
C(32)-C(33)-C(34)	120.6(4)
C(34)-C(33)-H(33)	119.7
C(29)-C(34)-C(33)	119.6(4)
C(29)-C(34)-H(34)	120.2
C(33)-C(34)-H(34)	120.2
N(1)-C(35)-C(36)	178.3(5)
C(35)-C(36)-H(36A)	109.5
C(35)-C(36)-H(36B)	109.5
C(35)-C(36)-H(36C)	109.5
H(36A)-C(36)-H(36B)	109.5
H(36A)-C(36)-H(36C)	109.5
H(36B)-C(36)-H(36C)	109.5
P(5)-Pd(2)-P(4)	82.80(4)
P(5)-Pd(2)-P(6)	84.25(4)
P(6)-Pd(2)-P(4)	166.13(4)
N(2)-Pd(2)-P(4)	95.26(11)
N(2)-Pd(2)-P(5)	176.59(11)
N(2)-Pd(2)-P(6)	97.91(11)
C(37)-P(4)-Pd(2)	113.95(15)
C(37)-P(4)-C(43)	107.3(2)
C(37)-P(4)-C(49)	106.3(2)
C(43)-P(4)-Pd(2)	114.74(16)
C(43)-P(4)-C(49)	105.4(2)
C(49)-P(4)-Pd(2)	108.53(16)
C(50)-P(5)-Pd(2)	108.22(16)
C(50)-P(5)-C(51)	112.4(2)
C(51)-P(5)-Pd(2)	109.87(15)
C(53)-P(5)-Pd(2)	110.75(15)
C(53)-P(5)-C(50)	107.3(2)
C(53)-P(5)-C(51)	108.3(2)
C(52)-P(6)-Pd(2)	107.31(15)
C(59)-P(6)-Pd(2)	118.36(15)
C(59)-P(6)-C(52)	105.8(2)
C(59)-P(6)-C(65)	104.7(2)
C(65)-P(6)-Pd(2)	112.08(15)
C(65)-P(6)-C(52)	108.1(2)
C(71)-N(2)-Pd(2)	174.7(4)
C(38)-C(37)-P(4)	120.3(3)
C(38)-C(37)-C(42)	118.7(4)
C(42)-C(37)-P(4)	120.9(4)
C(37)-C(38)-H(38)	119.8
C(39)-C(38)-C(37)	120.4(5)
C(39)-C(38)-H(38)	119.8
C(38)-C(39)-H(39)	119.7
C(40)-C(39)-C(38)	120.7(5)
C(40)-C(39)-H(39)	119.7
C(39)-C(40)-H(40)	120.2
C(39)-C(40)-C(41)	119.6(5)
C(41)-C(40)-H(40)	120.2
C(40)-C(41)-H(41)	119.6
C(40)-C(41)-C(42)	120.9(5)
C(42)-C(41)-H(41)	119.6
C(37)-C(42)-H(42)	120.1
C(41)-C(42)-C(37)	119.7(5)
C(41)-C(42)-H(42)	120.1
C(44)-C(43)-P(4)	118.6(4)
C(44)-C(43)-C(48)	119.0(5)
C(48)-C(43)-P(4)	122.3(4)
C(43)-C(44)-H(44)	119.8
C(45)-C(44)-C(43)	120.3(5)
C(45)-C(44)-H(44)	119.8
C(44)-C(45)-H(45)	119.9
C(46)-C(45)-C(44)	120.3(5)
C(46)-C(45)-H(45)	119.9
C(45)-C(46)-H(46)	120.1
C(45)-C(46)-C(47)	119.7(5)
C(47)-C(46)-H(46)	120.1
C(46)-C(47)-H(47)	119.9
C(48)-C(47)-C(46)	120.3(6)
C(48)-C(47)-H(47)	119.9
C(43)-C(48)-H(48)	119.8
C(47)-C(48)-C(43)	120.3(5)
C(47)-C(48)-H(48)	119.8
P(4)-C(49)-H(49A)	109.7
P(4)-C(49)-H(49B)	109.7
H(49A)-C(49)-H(49B)	108.2
C(50)-C(49)-P(4)	109.6(3)
C(50)-C(49)-H(49A)	109.7
C(50)-C(49)-H(49B)	109.7
P(5)-C(50)-H(50A)	110.1
P(5)-C(50)-H(50B)	110.1
C(49)-C(50)-P(5)	107.9(3)
C(49)-C(50)-H(50A)	110.1
C(49)-C(50)-H(50B)	110.1
H(50A)-C(50)-H(50B)	108.4
P(5)-C(51)-H(51A)	110.2
P(5)-C(51)-H(51B)	110.2
H(51A)-C(51)-H(51B)	108.5
C(52)-C(51)-P(5)	107.7(3)
C(52)-C(51)-H(51A)	110.2
C(52)-C(51)-H(51B)	110.2
P(6)-C(52)-H(52A)	109.7
P(6)-C(52)-H(52B)	109.7
C(51)-C(52)-P(6)	109.9(3)
C(51)-C(52)-H(52A)	109.7
C(51)-C(52)-H(52B)	109.7
H(52A)-C(52)-H(52B)	108.2
C(54)-C(53)-P(5)	121.6(4)
C(54)-C(53)-C(58)	119.9(4)
C(58)-C(53)-P(5)	118.5(4)
C(53)-C(54)-H(54)	120.1
C(53)-C(54)-C(55)	119.7(5)
C(55)-C(54)-H(54)	120.1
C(54)-C(55)-H(55)	119.3
C(56)-C(55)-C(54)	121.3(5)
C(56)-C(55)-H(55)	119.3
C(55)-C(56)-H(56)	120.5
C(55)-C(56)-C(57)	119.0(5)
C(57)-C(56)-H(56)	120.5
C(56)-C(57)-H(57)	119.5
C(56)-C(57)-C(58)	121.1(6)
C(58)-C(57)-H(57)	119.5
C(53)-C(58)-H(58)	120.5
C(57)-C(58)-C(53)	118.9(5)
C(57)-C(58)-H(58)	120.5
C(60)-C(59)-P(6)	120.2(3)
C(64)-C(59)-P(6)	120.2(4)
C(64)-C(59)-C(60)	119.5(4)
C(59)-C(60)-H(60)	120.1
C(61)-C(60)-C(59)	119.8(4)
C(61)-C(60)-H(60)	120.1
C(60)-C(61)-H(61)	120.1
C(60)-C(61)-C(62)	119.7(5)
C(62)-C(61)-H(61)	120.1
C(61)-C(62)-H(62)	119.8
C(63)-C(62)-C(61)	120.3(5)
C(63)-C(62)-H(62)	119.8
C(62)-C(63)-H(63)	119.6
C(62)-C(63)-C(64)	120.9(5)
C(64)-C(63)-H(63)	119.6
C(59)-C(64)-C(63)	119.7(5)
C(59)-C(64)-H(64)	120.2
C(63)-C(64)-H(64)	120.2
C(66)-C(65)-P(6)	116.8(3)
C(70)-C(65)-P(6)	124.2(4)
C(70)-C(65)-C(66)	118.9(4)
C(65)-C(66)-H(66)	119.7
C(67)-C(66)-C(65)	120.5(5)
C(67)-C(66)-H(66)	119.7
C(66)-C(67)-H(67)	119.9
C(66)-C(67)-C(68)	120.3(5)
C(68)-C(67)-H(67)	119.9
C(67)-C(68)-H(68)	120.5
C(69)-C(68)-C(67)	119.1(5)
C(69)-C(68)-H(68)	120.5
C(68)-C(69)-H(69)	119.4
C(68)-C(69)-C(70)	121.1(5)
C(70)-C(69)-H(69)	119.4
C(65)-C(70)-C(69)	120.1(5)
C(65)-C(70)-H(70)	120.0
C(69)-C(70)-H(70)	120.0
N(2)-C(71)-C(72)	179.8(7)

Table C.2, continued

C(71)-C(72)-H(72A)	109.5
C(71)-C(72)-H(72B)	109.5
C(71)-C(72)-H(72C)	109.5
H(72A)-C(72)-H(72B)	109.5
H(72A)-C(72)-H(72C)	109.5
H(72B)-C(72)-H(72C)	109.5
F(13)-B(4)-F(14)	108.9(16)
F(13)-B(4)-F(15)	108.2(11)
F(14)-B(4)-F(15)	108.5(15)
F(16)-B(4)-F(13)	108.6(9)
F(16)-B(4)-F(14)	112.5(19)
F(16)-B(4)-F(15)	110.1(10)
F(13X)-B(4X)-F(14X)	107.7(17)
F(13X)-B(4X)-F(15X)	108.4(13)
F(14X)-B(4X)-F(15X)	106.7(17)
F(16X)-B(4X)-F(13X)	111.2(10)
F(16X)-B(4X)-F(14X)	113(2)
F(16X)-B(4X)-F(15X)	109.9(12)
F(3)-B(1)-F(2)	109.4(4)
F(3)-B(1)-F(1X)	111.6(9)
F(3)-B(1)-F(4X)	108.6(10)
F(1)-B(1)-F(3)	109.6(4)
F(1)-B(1)-F(2)	109.5(5)
F(1)-B(1)-F(4)	110.1(5)
F(4)-B(1)-F(3)	109.5(4)
F(4)-B(1)-F(2)	108.6(5)
F(2X)-B(1)-F(3)	111.8(8)
F(2X)-B(1)-F(1X)	109.3(13)
F(2X)-B(1)-F(4X)	112.2(13)
F(4X)-B(1)-F(1X)	103.0(13)
F(8)-B(2)-F(7)	108.3(5)
F(8)-B(2)-F(5X)	112.7(8)
F(5)-B(2)-F(8)	108.6(5)
F(5)-B(2)-F(6)	113.1(6)
F(5)-B(2)-F(7)	111.5(5)
F(6)-B(2)-F(8)	107.0(5)
F(6)-B(2)-F(7)	108.1(5)
F(6X)-B(2)-F(8)	119.8(11)
F(6X)-B(2)-F(5X)	100.5(12)
F(6X)-B(2)-F(7X)	108.0(13)
F(7X)-B(2)-F(8)	113.8(8)
F(7X)-B(2)-F(5X)	99.4(12)
F(9)-B(3)-F(11)	107.1(17)
F(9)-B(3)-F(12)	111.6(17)
F(10)-B(3)-F(9)	110.7(13)
F(10)-B(3)-F(11)	109.6(16)
F(10)-B(3)-F(12)	110.8(18)
F(12)-B(3)-F(11)	106.8(17)
F(9X)-B(3X)-F(11X)	108.7(12)
F(9X)-B(3X)-F(12X)	110.3(13)
F(10X)-B(3X)-F(9X)	110.9(10)
F(10X)-B(3X)-F(11X)	112.3(11)
F(10X)-B(3X)-F(12X)	107.0(13)
F(11X)-B(3X)-F(12X)	107.6(13)
H(73A)-C(73)-H(73B)	109.5
H(73A)-C(73)-H(73C)	109.5
H(73B)-C(73)-H(73C)	109.5
C(74)-C(73)-H(73A)	109.5
C(74)-C(73)-H(73B)	109.5
C(74)-C(73)-H(73C)	109.5
N(3)-C(74)-C(73)	177(2)
H(73D)-C(73X)-H(73E)	109.5
H(73D)-C(73X)-H(73F)	109.5
H(73E)-C(73X)-H(73F)	109.5
C(74X)-C(73X)-H(73D)	109.5
C(74X)-C(73X)-H(73E)	109.5
C(74X)-C(73X)-H(73F)	109.5
N(3X)-C(74X)-C(73X)	173(3)
N(4)-C(75)-C(76)	179.4(5)
C(75)-C(76)-H(76A)	109.5
C(75)-C(76)-H(76B)	109.5
C(75)-C(76)-H(76C)	109.5
H(76A)-C(76)-H(76B)	109.5
H(76A)-C(76)-H(76C)	109.5
H(76B)-C(76)-H(76C)	109.5

Symmetry transformations used to generate equivalent atoms.

Table C.3 Torsion angles [°] for [Pd(triphos)(CH_3CN)][BF_4]$_2$.

Pd(1)-P(1)-C(1)-C(2)	128.3(4)
Pd(1)-P(1)-C(1)-C(6)	-58.4(4)
Pd(1)-P(1)-C(7)-C(8)	167.2(3)
Pd(1)-P(1)-C(7)-C(12)	-13.4(4)
Pd(1)-P(1)-C(13)-C(14)	-33.0(3)
Pd(1)-P(2)-C(14)-C(13)	-49.6(3)
Pd(1)-P(2)-C(15)-C(16)	47.9(3)
Pd(1)-P(2)-C(17)-C(18)	9.5(4)
Pd(1)-P(2)-C(17)-C(22)	-173.3(3)
Pd(1)-P(3)-C(16)-C(15)	27.4(3)
Pd(1)-P(3)-C(23)-C(24)	8.3(4)
Pd(1)-P(3)-C(23)-C(28)	-172.7(3)
Pd(1)-P(3)-C(29)-C(30)	73.4(3)
Pd(1)-P(3)-C(29)-C(34)	-106.1(4)
P(1)-C(1)-C(2)-C(3)	171.7(4)
P(1)-C(1)-C(6)-C(5)	-173.2(4)
P(1)-C(7)-C(8)-C(9)	178.6(3)
P(1)-C(7)-C(12)-C(11)	-177.9(3)
P(1)-C(13)-C(14)-P(2)	51.7(3)
P(2)-C(15)-C(16)-P(3)	-46.6(3)
P(2)-C(17)-C(18)-C(19)	177.2(3)
P(2)-C(17)-C(22)-C(21)	-177.7(3)
P(3)-C(23)-C(24)-C(25)	178.5(4)
P(3)-C(23)-C(28)-C(27)	-179.0(4)
P(3)-C(29)-C(30)-C(31)	-178.5(3)
P(3)-C(29)-C(34)-C(33)	179.3(3)
C(1)-P(1)-C(7)-C(8)	40.0(4)
C(1)-P(1)-C(7)-C(12)	-140.6(3)
C(1)-P(1)-C(13)-C(14)	90.2(3)
C(1)-C(2)-C(3)-C(4)	1.4(8)
C(2)-C(1)-C(6)-C(5)	0.4(7)
C(2)-C(3)-C(4)-C(5)	-0.3(8)
C(3)-C(4)-C(5)-C(6)	-0.8(8)
C(4)-C(5)-C(6)-C(1)	0.8(7)
C(6)-C(1)-C(2)-C(3)	-1.5(7)
C(7)-P(1)-C(1)-C(2)	-102.4(4)
C(7)-P(1)-C(1)-C(6)	70.9(4)
C(7)-P(1)-C(13)-C(14)	-159.6(3)
C(7)-C(8)-C(9)-C(10)	-0.2(7)
C(8)-C(7)-C(12)-C(11)	1.5(6)
C(8)-C(9)-C(10)-C(11)	0.4(7)
C(9)-C(10)-C(11)-C(12)	0.3(7)
C(10)-C(11)-C(12)-C(7)	-1.2(6)
C(12)-C(7)-C(8)-C(9)	-0.8(6)
C(13)-P(1)-C(1)-C(2)	9.8(4)
C(13)-P(1)-C(1)-C(6)	-177.0(3)
C(13)-P(1)-C(7)-C(8)	-73.1(4)
C(13)-P(1)-C(7)-C(12)	106.3(4)
C(14)-P(2)-C(15)-C(16)	169.6(3)
C(14)-P(2)-C(17)-C(18)	-108.6(4)
C(14)-P(2)-C(17)-C(22)	68.6(4)
C(15)-P(2)-C(14)-C(13)	-171.8(3)
C(15)-P(2)-C(17)-C(18)	129.9(4)
C(15)-P(2)-C(17)-C(22)	-52.9(4)
C(16)-P(3)-C(23)-C(24)	-114.8(4)
C(16)-P(3)-C(23)-C(28)	64.2(4)
C(16)-P(3)-C(29)-C(30)	-168.1(3)
C(16)-P(3)-C(29)-C(34)	12.4(4)
C(17)-P(2)-C(14)-C(13)	69.7(3)
C(17)-P(2)-C(15)-C(16)	-73.2(3)
C(17)-C(18)-C(19)-C(20)	-0.3(7)
C(18)-C(17)-C(22)-C(21)	-0.4(6)
C(18)-C(19)-C(20)-C(21)	1.1(7)
C(19)-C(20)-C(21)-C(22)	-1.5(7)
C(20)-C(21)-C(22)-C(17)	1.2(7)
C(22)-C(17)-C(18)-C(19)	0.0(6)
C(23)-P(3)-C(16)-C(15)	157.0(3)
C(23)-P(3)-C(29)-C(30)	-54.7(4)
C(23)-P(3)-C(29)-C(34)	125.8(4)
C(23)-C(24)-C(25)-C(26)	0.5(7)
C(24)-C(23)-C(28)-C(27)	0.0(7)
C(24)-C(25)-C(26)-C(27)	0.0(8)
C(25)-C(26)-C(27)-C(28)	-0.5(8)
C(26)-C(27)-C(28)-C(23)	0.5(7)
C(28)-C(23)-C(24)-C(25)	-0.4(7)
C(29)-P(3)-C(16)-C(15)	-91.8(3)
C(29)-P(3)-C(23)-C(24)	130.0(4)
C(29)-P(3)-C(23)-C(28)	-51.0(4)
C(29)-C(30)-C(31)-C(32)	-1.3(6)
C(30)-C(29)-C(34)-C(33)	-0.3(6)
C(30)-C(31)-C(32)-C(33)	0.7(7)
C(31)-C(32)-C(33)-C(34)	0.1(7)
C(32)-C(33)-C(34)-C(29)	-0.3(7)
C(34)-C(29)-C(30)-C(31)	1.1(6)
Pd(2)-P(4)-C(37)-C(38)	-179.5(3)
Pd(2)-P(4)-C(37)-C(42)	2.4(4)
Pd(2)-P(4)-C(43)-C(44)	24.1(4)
Pd(2)-P(4)-C(43)-C(48)	-156.9(4)
Pd(2)-P(4)-C(49)-C(50)	-19.4(3)
Pd(2)-P(5)-C(50)-C(49)	-53.0(3)
Pd(2)-P(5)-C(51)-C(52)	45.7(3)
Pd(2)-P(5)-C(53)-C(54)	-19.8(5)
Pd(2)-P(5)-C(53)-C(58)	159.3(4)
Pd(2)-P(6)-C(52)-C(51)	31.7(3)
Pd(2)-P(6)-C(59)-C(60)	-7.3(4)
Pd(2)-P(6)-C(59)-C(64)	173.4(3)
Pd(2)-P(6)-C(65)-C(66)	60.1(4)
Pd(2)-P(6)-C(65)-C(70)	-119.0(4)
P(4)-C(37)-C(38)-C(39)	-178.5(4)
P(4)-C(37)-C(42)-C(41)	178.5(4)
P(4)-C(43)-C(44)-C(45)	-179.8(4)
P(4)-C(43)-C(48)-C(47)	-179.2(5)
P(4)-C(49)-C(50)-P(5)	44.4(4)
P(5)-C(51)-C(52)-P(6)	-48.5(4)
P(5)-C(53)-C(54)-C(55)	-178.0(4)
P(5)-C(53)-C(58)-C(57)	-179.8(5)
P(6)-C(59)-C(60)-C(61)	179.9(3)
P(6)-C(59)-C(64)-C(63)	179.4(4)
P(6)-C(65)-C(66)-C(67)	-179.4(4)

Table C.3, continued

P(6)-C(65)-C(70)-C(69)	179.4(5)
C(37)-P(4)-C(43)-C(44)	-103.6(4)
C(37)-P(4)-C(43)-C(48)	75.4(5)
C(37)-P(4)-C(49)-C(50)	103.6(3)
C(37)-C(38)-C(39)-C(40)	0.5(7)
C(38)-C(37)-C(42)-C(41)	0.3(7)
C(38)-C(39)-C(40)-C(41)	-0.7(7)
C(39)-C(40)-C(41)-C(42)	0.7(7)
C(40)-C(41)-C(42)-C(37)	-0.5(7)
C(42)-C(37)-C(38)-C(39)	-0.3(7)
C(43)-P(4)-C(37)-C(38)	-51.3(4)
C(43)-P(4)-C(37)-C(42)	130.5(4)
C(43)-P(4)-C(49)-C(50)	-142.8(3)
C(43)-C(44)-C(45)-C(46)	-1.9(9)
C(44)-C(43)-C(48)-C(47)	-0.3(8)
C(44)-C(45)-C(46)-C(47)	1.7(9)
C(45)-C(46)-C(47)-C(48)	-0.8(10)
C(46)-C(47)-C(48)-C(43)	0.1(10)
C(48)-C(43)-C(44)-C(45)	1.2(8)
C(49)-P(4)-C(37)-C(38)	61.0(4)
C(49)-P(4)-C(37)-C(42)	-117.1(4)
C(49)-P(4)-C(43)-C(44)	143.5(4)
C(49)-P(4)-C(43)-C(48)	-37.6(5)
C(50)-P(5)-C(51)-C(52)	166.3(3)
C(50)-P(5)-C(53)-C(54)	-137.7(4)
C(50)-P(5)-C(53)-C(58)	41.4(5)
C(51)-P(5)-C(50)-C(49)	-174.6(3)
C(51)-P(5)-C(53)-C(54)	100.7(4)
C(51)-P(5)-C(53)-C(58)	-80.2(5)
C(52)-P(6)-C(59)-C(60)	-127.6(4)
C(52)-P(6)-C(59)-C(64)	53.2(4)
C(52)-P(6)-C(65)-C(66)	178.1(4)
C(52)-P(6)-C(65)-C(70)	-0.9(5)
C(53)-P(5)-C(50)-C(49)	66.5(3)
C(53)-P(5)-C(51)-C(52)	-75.3(3)
C(53)-C(54)-C(55)-C(56)	-2.4(9)
C(54)-C(53)-C(58)-C(57)	-0.7(9)
C(54)-C(55)-C(56)-C(57)	-0.3(10)
C(55)-C(56)-C(57)-C(58)	2.6(11)
C(56)-C(57)-C(58)-C(53)	-2.1(11)
C(58)-C(53)-C(54)-C(55)	2.9(9)
C(59)-P(6)-C(52)-C(51)	159.0(3)
C(59)-P(6)-C(65)-C(66)	-69.5(4)
C(59)-P(6)-C(65)-C(70)	111.5(5)
C(59)-C(60)-C(61)-C(62)	1.6(7)
C(60)-C(59)-C(64)-C(63)	0.1(7)
C(60)-C(61)-C(62)-C(63)	-1.8(7)
C(61)-C(62)-C(63)-C(64)	1.1(8)
C(62)-C(63)-C(64)-C(59)	-0.2(8)
C(64)-C(59)-C(60)-C(61)	-0.8(7)
C(65)-P(6)-C(52)-C(51)	-89.3(3)
C(65)-P(6)-C(59)-C(60)	118.4(4)
C(65)-P(6)-C(59)-C(64)	-60.9(4)
C(65)-C(66)-C(67)-C(68)	0.8(8)
C(66)-C(65)-C(70)-C(69)	0.4(8)
C(66)-C(67)-C(68)-C(69)	-1.2(8)
C(67)-C(68)-C(69)-C(70)	1.3(9)
C(68)-C(69)-C(70)-C(65)	-0.8(10)
C(70)-C(65)-C(66)-C(67)	-0.3(8)

Symmetry transformations used to generate equivalent atoms.

C.3 References

(1) Dubois and Miedaner, *J Am. Chem. Soc.* **1987**, *109*, 113–117

(2) Sheldrick, G. M. *Acta Cryst*. **2015**, *A71*, 3–8

(3) Sheldrick, G. M. *Acta Cryst.* **2008**, *A64*, 112–122

(4) Sheldrick*, G. M. Acta Cryst.* **2015**, *C71*, 3–8

(5) O. V. Dolomanov, L. J. Bourhis, R. J. Gildea, J. A. K. Howard and H. Puschmann. *J. Appl. Cryst.* **2009** *42*, 339–341

Appendix D Spectroelectrochemistry of $[NEt_4][Cp^*Cr(CO)_3]$

D.1 Experimental

Spectroelectrochemical measurements were performed on $[NEt_4][Cp^*Cr(CO)_3]$ in THF using an optically transparent thin-layer electrochemical cell equipped with CaF_2 windows.[1] The electrode potential was controlled using the BAS 100B potentiostat described above. The applied potential was ramped at a slow rate (1 mV s^{-1}) across the redox couple of interest, during which time spectra were recorded at regular intervals. Data collection was halted after the spectrum showed no further change upon increasing potential.

The extinction coefficient for $[NEt_4][Cp^*Cr(CO)_3]$ was determined via serial dilution of a known concentration of compound, repeated twice and averaged. The extinction coefficient for $[Cp^*Cr(CO)_3]\bullet$ was determined assuming 100% conversion from the anion at the completion of the spectroelectrochemical experiment.

D.2 Results

The spectrum of the $[Cp^*Cr(CO)_3]\bullet$ radical exhibits two peaks not present in the anion, at 475 nm (ε = 570 M^{-1} cm^{-1}) and 549 nm (ε = 556 M^{-1} cm^{-1}). In addition, it exhibits a peak at 353 nm that is also present in the anion (λ_{max} = 358 nm, ε = 1664 M^{-1} cm^{-1}), though the extinction coefficient is slightly lower (ε = 1454 M^{-1} cm^{-1}). The spectrum is shown in Figure D.1.

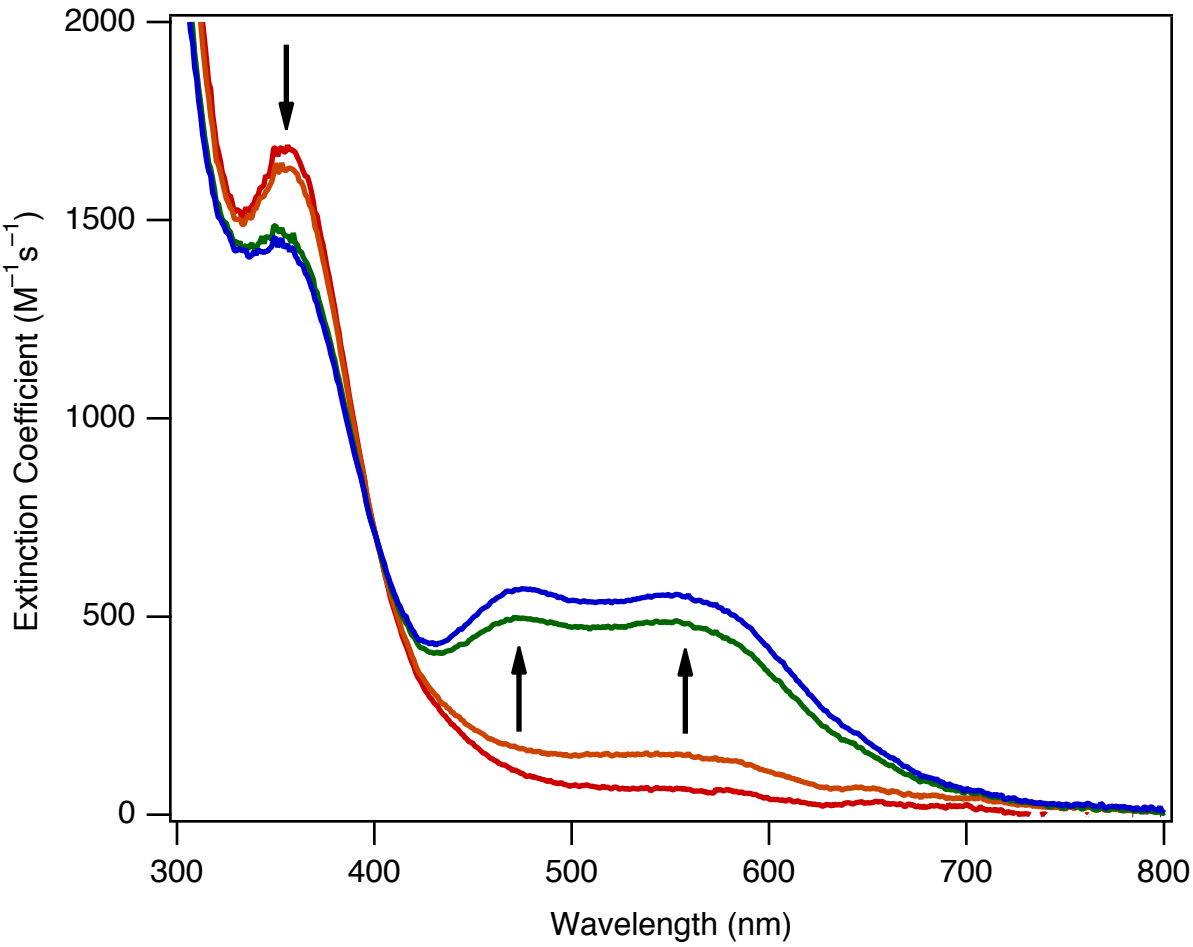

Figure D.1 Spectrum of [Cp*Cr(CO)$_3$] as potential is scanned across the [Cp*Cr(CO)$_3$]$^{-/0}$ couple.

D.3 References

(1) Krejčik M, Daněk M, & Hartl F *J Electroanal Chem Interfac Electrochem* **1991**, *317*(1–2), 1991, 179–187.